Tropical South Pacific Paleohydrology from Hydrogen Isotopes in Algal Lipids

Ashley E. Maloney

A dissertation

submitted in partial fulfillment of the

requirements for the degree of

Doctor of Philosophy

University of Washington

2018

Reading Committee:

Julian P Sachs, Chair

Anitra E Ingalls

Paul D Quay

Program Authorized to Offer Degree:

Oceanography

University of Washington

Abstract

Tropical South Pacific Paleohydrology from Hydrogen Isotopes in Algal Lipids

Ashley E. Maloney

Chair of Supervisory Committee:
Professor Julian Sachs, PhD
Oceanography

The tropics play a central role in global atmospheric moisture transport, however paleoclimate records of tropical precipitation are relatively scarce. Reconstructing pre-instrumental hydrological change requires the use of indirect indicators of rainfall such as hydrogen isotope ratios ($^{2}H/^{1}H$) of phytoplankton lipids preserved in sediments. In this thesis, I examine mechanisms of $^{2}H/^{1}H$ fractionation in phytoplankton lipids, develop a modern spatial calibration of biomarker hydrogen isotope ratios with instrumental precipitation rates, and quantitatively reconstruct Late Holocene precipitation across the tropical South Pacific. The lipid-water $^{2}H/^{1}H$ fractionation response to salinity in nutrient-replete continuous cultures of the centric diatom *Thalassiosira pseudonana* decreased linearly as salinity increased by 1.3‰ ppt^{-1} in fatty acids ($C_{14:0}$, $C_{16:0}$, $C_{16:1}$) and by 1.0‰ ppt^{-1} in the sterol 24-methyl-cholesta-5,24(28)-dien-3β-ol. A steady state flux balance model allowed further examination of the controls on lipid $^{2}H/^{1}H$ fractionation. The dinoflagellate biomarker dinosterol (4a, 23, 24-trimethyl-5a-cholest-22E-en-3β-ol) purified from tropical South Pacific freshwater lake surface sediments was correlated with precipitation rates, yielding a sensitivity of -12.1±2.6 ‰ $(mm\ d^{-1})^{-1}$. This empirical relationship, developed in the context of known controls on the isotopic composition of tropical precipitation, lake water, and algal lipid isotopes, provides a means of quantitatively reconstructing past precipitation. Sediment cores were collected from ten freshwater lakes on six

islands in the Solomon Islands, Vanuatu, Wallis, and Samoa. Down-core dinosterol $^{2}H/^{1}H$ measurements show wet Modern (1850-present) hydroclimate conditions and widespread dry conditions during the Little Ice Age (1450-1850) and Medieval Climate Anomaly (950-1250).

For my family, especially
Eddie Dragon (1941–2012)
who is dearly missed

Acknowledgements

Special thanks to my advisor, Julian Sachs, for introducing me to the world of isotopes and remote fieldwork and supporting this work. Julian's enthusiasm about paleoclimate and proxy development is contagious. I am grateful that I had the opportunity to join Julian in Wallis, Fiji, Palau, station ALOHA, and coastal Oregon, and as a teacher in Pohnpei and Kosrae.

My committee members have been amazing, they are great scientists and great teachers and I am glad I had the opportunity to learn from them. Tremendous thank you to Anitra Ingalls, Paul Quay, LuAnne Thompson, and Kate Huntington for their intellectual contributions throughout this project.

I benefited from collaborations with scientists from many institutions. This work advanced from input and samples provided by Jonathan Hassall, David Sear, Peter Langdon, Simon Haberle, Geoff Hope, and Matthew Prebble. Ursula Sichrowsky was a great help in Wallis. I enjoyed working with Jean Lynch-Stieglitz, Pratigya Polissar, and everyone on the Line Islands coring expedition.

I would also like to thank the UW Program on Climate Change, Terri Klinger and the IGERT Program on Ocean Change, Ginger Armbrust and the School of Oceanography, the UW Quaternary Research Center, my TA supervisor and friend Arthur Nowell, and Alyn Duxbury, all of whom offered advice and helped support parts of my research and/or conference travels. The assistance from Su Tipple, Kittie Tucker, April Timer, and Romeo Balagot, the Graduate School, and GPSS is greatly appreciated.

My lab mates were a terrific source of scientific support. I am fortunate to have Daniel Nelson, Nemiah Ladd, Julie Richey, and Alyssa Atwood as colleagues, they have helped me navigate this research journey and I am proud to follow their footsteps as we continue to piece

together Earth's story. Ines Mügler, Tessa McGee, Marta Wolfshorndl, Tess Clinkingbeard, Jiwoon Park, Josh Gregersen, Matthew Wolhowe, and Orest Kawka engaged in helpful discussions and instrument troubleshooting.

I especially want to thank the amazing students that helped purify so many of the samples in this thesis including Samantha Hing, Elise Baldwin, Amanda Witt, Polly Sobeck, and Becci Danford, and many helpers in the algae room including Christopher Paschall, Ryan D'Jay, Colton Skavicus, and Yashwant Meghare. I also want to thank the many impressive students that participated in the Pohnpei study abroad class and the Oceanography senior thesis classes.

I appreciate the support and encouragement from the Oceanography, Program on Climate Change, and IGERT communities. I learned a lot as part of the Emily Newsom, Andrea Fassbender, and Seth Bushinsky IGERT team. Pestering Katherine Heal, the sharpest chemical oceanographer I know, with questions about microbe metabolism on a regular basis was a highlight. Leah Johnson is a stellar source of sage and steady advice and I am grateful for her company during many late-night bike rides. I will always treasure the encouragement from Nancy Williams, Martina Brimmer, Angie Boysen, Jake Steinberg, Justin Penn, Max Showalter, and the OSB 5th floor scientists – thanks friends for pulling me through.

My co-instructors Susan Brittain, Chris Cerino, Jenny McColloch, and Gerry Santillan, and mentors and teachers at Stanford including Robert Dunbar, Adina Payton, and Josh Eagle helped me build a solid understanding of Earth science and pedagogy before I started at UW.

My parents Michael and Sandy and brothers Christopher and Andrew provided never-ending encouragement and confidence. My godparents Jeanie and Eddie Dragon played a key role in my training as an observer, especially of frogs, insects, and art.

Finally, thank you Ian Bystrom, I am lucky to have you.

Table of Contents

Chapter 1: Introduction

Spatial and temporal patterns of global rainfall regulate ecosystem structure, food security, and habitability. Modern instruments allow us to witness near real-time patterns of rainfall on a global scale. Observations together with sophisticated models help us dissect and forecast the weather, events, and climate that rule our world, and also detect human-caused disruptions (Power et al., 2017). However, our observational records are short which means that our ability to understand and predict future change in a warming world is limited.

Piecing together Earth's pre-instrumental story requires the use of indirect recorders of rainfall. Rain gauges, satellites, salinometers, and other instruments designed to detect hydrology are not the only objects that respond to the forces of nature. Nearly every aspect of Earth's skin reacts to rain or drought. For instance, heavy rains mobilize and transport fine materials and intermittently deposit them in catchments; drought-caused changes to vegetation are locked into tree ring histories. Furthermore, the hydrogen and oxygen isotopic compositions of environmental waters are linked to their fluxes though the hydrologic cycle (Craig, 1961; Craig and Gordon, 1965; Dansgaard, 1964; Gat, 1996). Processes such as these leave behind clues preserved in the right settings, allowing us to indirectly reconstruct pre-instrumental precipitation.

Despite the central role that tropical latitudes play in global climate (Chiang, 2009), reconstructions of past tropical precipitation are relatively scarce. Molecular paleohydrology from hydrogen isotope ratios of individual phytoplankton lipids preserved in sediments (Sachse et al., 2012), is a promising tool for reconstructing tropical hydrologic variability. This approach has been successfully applied to several timescales and locations (e.g. Atwood and Sachs, 2014; Leduc et al., 2013; Nelson and Sachs, 2016; Pahnke et al., 2007; Richey and Sachs, 2016; Sachs

et al., 2009; Smittenberg et al., 2011; van der Meer et al., 2008, 2007; Vasiliev et al., 2013; Zhang et al., 2014). My graduate work has focused on understanding, developing, and applying this tool to reconstruct the pre-instrumental precipitation in the tropical South Pacific.

In the tropics, the isotopic composition of precipitation is primarily influenced by the "amount effect" where higher precipitation rates are correlated with ^{2}H-depleted rain (Bony et al., 2008; Conroy et al., 2013; Dansgaard, 1964; Kurita et al., 2009; Risi et al., 2008). Changes in the hydrologic balance are reflected in lake water $^2H/^1H$ ratios and salinity. Hydrogen isotope ratios are expressed as δ^2H ($\delta = [R_{sample}/R_{VSMOW}] - 1$, where R is $^2H/^1H$ and VSMOW is Vienna Standard Mean Ocean Water). Culture experiments with a variety of microalgae species have shown that δ^2H_{lipid} is nearly perfectly correlated with δ^2H_{water} with R^2 values in excess of 0.99 (Englebrecht and Sachs, 2005; Zhang and Sachs, 2007). Therefore, well preserved algal lipids can provide a record of precipitation in sedimentary archives. Advances in gas chromatography-isotope ratio mass spectrometry (Burgoyne and Hayes, 1998; Sessions et al., 1999) and high performance liquid chromatography (Atwood and Sachs, 2012; Nelson and Sachs, 2013; Smittenberg and Sachs, 2007), enable us to use compound specific lipid biomarkers as indicators of past hydrological changes.

In Chapter 2 phytoplankton cultures and a mathematical model are used to investigate the cellular processes responsible for hydrogen isotope fractionation. The magnitude of phytoplankton lipid $^2H/^1H$ fractionation can be significantly influenced by several environmental parameters and physiological factors. This has implications for the proper interpretation of paleoclimate, prompting efforts to understand and characterize environmental impacts on lipid $^2H/^1H$ fractionation. For instance, $^2H/^1H$ fractionation in algal lipids increases at higher growth rates (M'Boule et al., 2014; Sachs and Kawka, 2015; Schouten et al., 2006; Zhang et al., 2009),

growth stage influences $^{2}H/^{1}H$ fractionation such that fractionation is decreased during exponential growth compare to stationary phase (Chivall et al., 2014; Wolhowe et al., 2009), light impacts $^{2}H/^{1}H$ fractionation (Sachs et al., 2017; van der Meer et al., 2015; Wolhowe et al., 2015), and temperature appears to influence $^{2}H/^{1}H$ fractionation (Estep and Hoering, 1980; Sachs, 2014; Stiller and Nissenbaum, 1980; Wolhowe et al., 2009; Zhang et al., 2009).

Several studies have established that salinity can have a significant influence on apparent $^{2}H/^{1}H$ fractionation in eukaryotic microalgae and cyanobacteria. Apparent fractionation in alkenones decreased ~3‰ per unit increase in salinity in *E. huxleyi* and *G. oceanica* batch cultures (Schouten et al., 2006). Apparent fractionation decreased ~0.7-1‰ per salinity unit increase in cyanobacteria lipids from several hypersaline ponds on Christmas Island (Sachse and Sachs, 2008), in the dinoflagellate lipid dinosterol along the Chesapeake Bay estuary (Sachs and Schwab, 2011), and in dinosterol and brassicasterol from a global survey of saline and hypersaline lakes (Nelson and Sachs, 2014). $^{2}H/^{1}H$ fractionation decreased ~1-2.6‰ per unit increase in salinity in alkenones from batch-cultured open ocean and coastal haptophytes in exponential phase (Chivall et al., 2014; M'Boule et al., 2014; Weiss et al., 2017), and by ~0.8-1‰ in alkenones from batch-cultured coastal haptophytes in stationary and decline phases (Chivall et al., 2014) although the different species displayed different absolute fractionations. It has been proposed that this nearly universal trend may be due to lower growth rates at sub-optimal salinity, less water transport across outer cell membranes, and/or increased production of small compatible solutes that might result in increased recycling of intracellular water to cause the intracellular water pool to become progressively enriched, a signal that is then passed onto lipids (Sachs and Schwab, 2011; Sachse and Sachs, 2008).

To investigate the mechanism responsible for the salinity fractionation effect, the estuarine diatom *Thalassiosira pseudonana* was continuously cultured in controlled conditions at different salinities. The lipid $^{2}H/^{1}H$ fractionation decreased by 1-1.3‰ per salinity unit increase. Maintaining the cultures at the same growth rate allowed us to rule out a previously proposed mechanism that suggested growth rate changes could indirectly cause decreased fractionation at increased salinity (Schwab and Sachs, 2011). The unique experimental design of this project justified the creation of a steady state model of hydrogen mass and isotope balances. The model provided evidence that increased equilibrium exchange or increased metabolic reduction of NADP+ to NADPH (instead of photosynthetically reduced NADPH) can cause the observed isotope fractionation in lipids. Chapter 2 confirmed that salinity has a significant influence on the fractionation of hydrogen isotopes in phytoplankton lipids, which is key information for the experimental design of the following chapters (which avoided field sites influenced greatly by salinity). Additionally, understanding the mechanisms responsible for variable fractionation gives us more confidence in the application of the lipid $^{2}H/^{1}H$ ratio proxy to paleoclimate reconstructions.

In Chapter 3 lake sediments and water samples were collected from multiple freshwater lakes in the South Pacific Convergence Zone (SPCZ), the Southern Hemisphere's largest precipitation feature (Vincent, 1994). Little is known about the SPCZ's location and intensity of rainfall prior to instrumental records, hindering attempts to predict precipitation changes. This chapter characterizes $\delta^{2}H$ values from rainwater, lake water, and the sedimentary dinoflagellate biomarker dinosterol (4a, 23, 24-trimethyl-5a-cholest-22E-en-3β-ol) from diverse lakes. Freshwater lake sediments and water samples were collected from lakes that spanned a 4.6 mm d^{-1} range in precipitation rates based on estimates from the Global Precipitation Climatology

Project (GPCP). $\delta^2H_{lakewater}$ values from 29 lakes ranged from -29 ‰ to 23 ‰ and were inversely correlated with precipitation rates, albeit with a steeper slope than the observed tropical Pacific "amount effect", owing to evaporation of lake water.

$\delta^2H_{dinosterol}$ values from core-top samples from 21 sites had a 69 ‰ range from -247 ‰ to -316 ‰ and were ^2H-depleted compared to $\delta^2H_{lakewater}$ values. The correlation between $\delta^2H_{dinosterol}$ and $\delta^2H_{lakewater}$ [$\delta^2H_{dinosterol} = 1.9(\pm0.3)* \delta^2H_{lakewater} -258(\pm5)$, $R^2=0.50$, $p<0.001$, $n=20$] emphasizes that environmental water isotopes are the first order control on algal lipid isotopes. This is in agreement with numerous studies that show microorganism lipids track the isotopes of their environmental water in the lab (Dirghangi and Pagani, 2013a, 2013b; Englebrecht and Sachs, 2005; Osburn et al., 2016; Paul, 2002; X. Zhang et al., 2009; Zhang and Sachs, 2007) and field (Huang et al., 2004; Polissar and Freeman, 2010; Sachs and Schwab, 2011; Sachse et al., 2012, 2004; Sauer et al., 2001; Schwab et al., 2015a; Schwab and Sachs, 2011). $\delta^2H_{dinosterol}$ was significantly correlated with GPCP precipitation rates [$\delta^2H_{dinosterol} = -12.1(\pm2.6)*P-211(\pm15)$, $R^2=0.59$, $p=0.0003$, $n=18$]. This empirical relationship, developed in the context of known controls on the isotopic composition of tropical precipitation, lake water, and algal lipid isotopes, provides a tool for calculating pre-instrumental rainfall in the SPCZ from lake sediment records.

Chapter 4 applies lipid biomarker hydrogen isotope molecular paleohydrology to well-dated sediment cores from several sites in the SPCZ. Compound specific measurements of purified dinosterol from these cores reveals a dynamic history of pre-instrumental rainfall during the last 2000 years. A total of 14 sediment cores from 10 freshwater lakes on 6 islands in the Solomon Islands, Vanuatu, Wallis, and Samoa show wet Modern (1850-present) hydroclimate conditions and widespread dry conditions during the Little Ice Age (1450-1850) and Medieval

Climate Anomaly (950-1250). To ensure proper interpretation of paleoclimate, multiple lake sites were investigated in each region whenever possible. Additionally, physical properties such as magnetic susceptibility support our interpretations of precipitation variability.

Changes in tropical precipitation in a warming climate will have profound implications for the global hydrologic balance and for societies that depend on rain to support subsistence lifestyles. Understanding how tropical precipitation changed in the past will help us understand the extent of natural variability and can inform hypothesis about past social and ecological change and assist with the validation of climate models for understanding past and future conditions.

Chapter 1 References

Atwood, A.R., Sachs, J.P., 2014. Separating ITCZ- and ENSO-related rainfall changes in the Galápagos over the last 3 kyr using D/H ratios of multiple lipid biomarkers. Earth Planet. Sci. Lett. 404, 408–419. doi:doi: 10.1016/j.epsl.2014.07.038

Atwood, A.R., Sachs, J.P., 2012. Purification of dinosterol from complex mixtures of sedimentary lipids for hydrogen isotope analysis. Org. Geochem. 48, 37–46. doi:10.1016/j.orggeochem.2012.04.006

Bony, S., Risi, C., Vimeux, F., 2008. Influence of convective processes on the isotopic composition (δ 18 O and δ D) of precipitation and water vapor in the tropics: 1. Radiative-convective equilibrium and Tropical Ocean–Global Atmosphere–Coupled Ocean-Atmosphere Response Experiment (TOGA-CO. J. Geophys. Res. 113, D19305. doi:10.1029/2008JD009942

Burgoyne, T.W., Hayes, J.M., 1998. Quantitative production of H2 by pyrolysis of gas chromatographic effluents. Anal. Chem. 70, 5136–5141. doi:10.1021/ac980248v

Chiang, J.C.H., 2009. The tropics in paleoclimate. Annu. Rev. Earth Planet. Sci. 37, 263–297. doi:10.1146/annurev.earth.031208.100217

Chivall, D., Boule, D.M., Sinke-Schoen, D., Sinninghe Damsté, J.S., Schouten, S., van der Meer, M.T.J., 2014. The effects of growth phase and salinity on the hydrogen isotopic composition of alkenones produced by coastal haptophyte algae. Geochim. Cosmochim. Acta 140, 381–390.

Conroy, J.L., Cobb, K.M., Noone, D., 2013. Comparison of precipitation isotope variability across the tropical Pacific in observations and SWING2 model simulations. J. Geophys. Res. Atmos. 118, 5867–5892. doi:10.1002/jgrd.50412

Craig, H., 1961. Isotopic variations in meteoric waters. Science (80-.). 133, 1702–1703.

Craig, H., Gordon, L., 1965. Deuterium and oxygen 18 variations in the ocean and the marine atmosphere, in: Tongiori, E. (Ed.), Proceedings of a Conference on Stable Isotopes in Oceanographic Studies and Paleotemperatures. CNR-Laboratorio di Geologia Nucleare, Pisa, pp. 9–130.

Dansgaard, W., 1964. Stable isotopes in precipitation. Tellus 16, 436–468.

Dirghangi, S.S., Pagani, M., 2013a. Hydrogen isotope fractionation during lipid biosynthesis by *Haloarcula marismortui*. Geochim. Cosmochim. Acta 119, 381–390. doi:10.1016/j.gca.2013.05.023

Dirghangi, S.S., Pagani, M., 2013b. Hydrogen isotope fractionation during lipid biosynthesis by *Tetrahymena thermophila*. Org. Geochem. 64, 105–111.

Englebrecht, A.C., Sachs, J.P., 2005. Determination of sediment provenance at drift sites using hydrogen isotopes and unsaturation ratios in alkenones. Geochim. Cosmochim. Acta 69, 4253–4265. doi:10.1016/j.gca.2005.04.011

Estep, M.F., Hoering, T.C., 1980. Biogeochemistry of the stable hydrogen isotopes. Geochim. Cosmochim. Acta 44, 1197–1206. doi:10.1016/0016-7037(80)90073-3

Gat, J.R., 1996. Oxygen and hydrogen isotopes in the hydrologic cycle. Annu. Rev. Earth Planet. Sci. 24, 225–262. doi:10.1146/annurev.earth.24.1.225

Huang, Y., Shuman, B., Wang, Y., Webb, T., 2004. Hydrogen isotope ratios of individual lipids in lake sediments as novel tracers of climatic and environmental change: A surface sediment test. J. Paleolimnol. 31, 363–375. doi:10.1023/B:JOPL.0000021855.80535.13

Kurita, N., Ichiyanagi, K., Matsumoto, J., Yamanaka, M.D., Ohata, T., 2009. The relationship between the isotopic content of precipitation and the precipitation amount in tropical regions. J. Geochemical Explor. 102, 113–122. doi:10.1016/j.gexplo.2009.03.002

Leduc, G., Sachs, J.P., Kawka, O.E., Schneider, R.R., 2013. Holocene changes in eastern equatorial Atlantic salinity as estimated by water isotopologues. Earth Planet. Sci. Lett. 362, 151–162. doi:10.1016/j.epsl.2012.12.003

M'Boule, D., Chivall, D., Sinke-Schoen, D., Sinninghe Damsté, J.S., Schouten, S., van der Meer, M.T.J., 2014. Salinity dependent hydrogen isotope fractionation in alkenones produced by coastal and open ocean haptophyte algae. Geochim. Cosmochim. Acta 130, 126–135.

Nelson, D.B., Sachs, J.P., 2016. Galápagos hydroclimate of the Common Era from paired microalgal and mangrove biomarker $^{2}H/^{1}H$ values. Proc. Natl. Acad. Sci. U. S. A. 113, 3476–3481. doi:10.1073/pnas.1516271113

Nelson, D.B., Sachs, J.P., 2014. The influence of salinity on D/H fractionation in dinosterol and brassicasterol from globally distributed saline and hypersaline lakes. Geochim. Cosmochim. Acta 133, 325–339. doi:10.1016/j.gca.2014.03.007

Nelson, D.B., Sachs, J.P., 2013. Concurrent purification of sterols, triterpenols and alkenones from sediments for hydrogen isotope analysis using high performance liquid chromatography. Org. Geochem. 64, 19–28. doi:10.1016/j.orggeochem.2013.09.005

Osburn, M.R., Dawson, K.S., Fogel, M.L., Sessions, A.L., 2016. Fractionation of hydrogen isotopes by sulfate- and nitrate-reducing bacteria. Front. Microbiol. 7, 1–16. doi:10.3389/fmicb.2016.01166

Pahnke, K., Sachs, J.P., Keigwin, L., Timmermann, A., Xie, S.-P., 2007. Eastern tropical Pacific hydrologic changes during the past 27,000 years from D/H ratios in alkenones. Paleoceanography 22. doi:10.1029/2007PA001468

Paul, H.A., 2002. Application of novel stable isotope methods to reconstruct paleoenvironments: Compound specific hydrogen isotopes and pore-water oxygen isotopes. Zürich: Swiss Federal Institute of Technology.

Polissar, P.J., Freeman, K.H., 2010. Effects of aridity and vegetation on plant-wax δD in modern lake sediments. Geochim. Cosmochim. Acta 74, 5785–5797. doi:10.1016/j.gca.2010.06.018

Power, S.B., Delage, F.P.D., Chung, C.T.Y., Ye, H., Murphy, B.F., 2017. Humans have already increased the risk of major disruptions to Pacific rainfall. Nat. Commun. 8, 14368. doi:10.1038/ncomms14368

Richey, J.N., Sachs, J.P., 2016. Precipitation changes in the western tropical Pacific over the past millennium. Geology 44, 671–674. doi:10.1130/G37822.1

Risi, C., Bony, S., Vimeux, F., 2008. Influence of convective processes on the isotopic composition (δ18O and δD) of precipitation and water vapor in the tropics: 2. Physical interpretation of the amount effect. J. Geophys. Res. 113, D19306. doi:10.1029/2008JD009943

Sachs, J.P., 2014. Hydrogen isotope signatures in the lipids of phytoplankton, in: Holland, H.D., Turekian, K.K. (Eds.), Treatise on Geochemistry. Elsevier Ltd, Oxford, pp. 79–94.

Sachs, J.P., Kawka, O.E., 2015. The influence of growth rate on $^{2}H/^{1}H$ fractionation in continuous cultures of the coccolithophorid *Emiliania huxleyi* and the diatom *Thalassiosira pseudonana*. PLoS One 10, e0141643. doi:10.1371/journal.pone.0141643

Sachs, J.P., Maloney, A.E., Gregersen, J., 2017. Effect of light on $^{2}H/^{1}H$ fractionation in lipids from continuous cultures of the diatom *Thalassiosira pseudonana*. Geochim. Cosmochim. Acta 209, 204–215. doi:10.1016/j.gca.2017.04.008

Sachs, J.P., Sachse, D., Smittenberg, R.H., Zhang, Z., Battisti, D.S., Golubic, S., 2009. Southward movement of the Pacific intertropical convergence zone. Nat. Geosci. 2, 519–525. doi:10.1038/NGEO554

Sachs, J.P., Schwab, V.F., 2011. Hydrogen isotopes in dinosterol from the Chesapeake Bay estuary. Geochim. Cosmochim. Acta 75, 444–459. doi:10.1016/j.gca.2010.10.013

Sachse, D., Billault, I., Bowen, G.J., Chikaraishi, Y., Dawson, T.E., Feakins, S.J., Freeman, K.H., Magill, C.R., McInerney, F.A., van der Meer, M.T.J., Polissar, P.J., Robins, R.J., Sachs, J.P., Schmidt, H.-L., Sessions, A.L., White, J.W., West, J.B., Kahmen, A., 2012. Molecular paleohydrology: Interpreting the hydrogen-isotopic composition of lipid biomarkers from photosynthesizing organisms. Annu. Rev. Earth Planet. Sci. 40, 221–249. doi:10.1146/annurev-earth-042711-105535

Sachse, D., Radke, J., Gleixner, G., 2004. Hydrogen isotope ratios of recent lacustrine sedimentary n-alkanes record modern climate variability. Geochim. Cosmochim. Acta 68, 4877–4889. doi:10.1016/j.gca.2004.06.004

Sachse, D., Sachs, J.P., 2008. Inverse relationship between D/H fractionation in cyanobacterial lipids and salinity in Christmas Island saline ponds. Geochim. Cosmochim. Acta 72, 793–806. doi:10.1016/j.gca.2007.11.022

Sauer, P.E., Eglington, T.I., Hayes, J.M., Schimmelmann, A., Sessions, A.L., 2001. Compound-specific D/H ratios of lipid biomarkers from sediments as a proxy for environmental and climatic conditions. Geochim. Cosmochim. Acta 65, 213–222.

Schouten, S., Ossebaar, J., Schreiber, K., Kienhuis, M.V.M., Langer, G., Benthien, A., Bijma, J., Burg, D., 2006. The effect of temperature, salinity and growth rate on the stable hydrogen isotopic composition of long chain alkenones produced by *Emiliania huxleyi* and *Gephyrocapsa oceanica*. Biogeosciences 3, 113–119.

Schwab, V.F., Garcin, Y., Sachse, D., Todou, G., Séné, O., Onana, J.M., Achoundong, G., Gleixner, G., 2015. Dinosterol δD values in stratified tropical lakes (Cameroon) are affected by eutrophication. Org. Geochem. 88, 35–49. doi:10.1016/j.orggeochem.2015.08.003

Schwab, V.F., Sachs, J.P., 2011. Hydrogen isotopes in individual alkenones from the Chesapeake Bay estuary. Geochim. Cosmochim. Acta 75, 7552–7565. doi:10.1016/j.gca.2011.09.031

Sessions, A.L., Burgoyne, T.W., Schimmelmann, A., Hayes, J.M., 1999. Fractionation of hydrogen isotopes in lipid biosynthesis. Org. Geochem. 30, 1193–1200. doi:10.1016/S0146-6380(99)00094-7

Smittenberg, R.H., Sachs, J.P., 2007. Purification of dinosterol for hydrogen isotopic analysis using high-performance liquid chromatography-mass spectrometry. J. Chromatogr. A 1169, 70–6. doi:10.1016/j.chroma.2007.09.018

Smittenberg, R.H., Saenger, C., Dawson, M.N., Sachs, J.P., 2011. Compound-specific D/H ratios of the marine lakes of Palau as proxies for West Pacific Warm Pool hydrologic variability. Quat. Sci. Rev. 30, 921–933. doi:10.1016/j.quascirev.2011.01.012

Stiller, M., Nissenbaum, A., 1980. Variations of stable hydrogen isotopes in plankton from a freshwater lake. Geochim. Cosmochim. Acta 44, 1099–1101. doi:10.1016/0016-7037(80)90064-2

van der Meer, M.T.J., Baas, M., Rijpstra, W.I.C., Marino, G., Rohling, E.J., Sinninghe Damsté, J.S., Schouten, S., 2007. Hydrogen isotopic compositions of long-chain alkenones record freshwater flooding of the Eastern Mediterranean at the onset of sapropel deposition. Earth Planet. Sci. Lett. 262, 594–600. doi:10.1016/j.epsl.2007.08.014

van der Meer, M.T.J., Benthien, A., French, K.L., Epping, E., Zondervan, I., Reichart, G.J., Bijma, J., Sinninghe Damsté, J.S., Schouten, S., Sinninghe Damst??, J.S., Schouten, S., 2015. Large effect of irradiance on hydrogen isotope fractionation of alkenones in *Emiliania huxleyi*. Geochim. Cosmochim. Acta 160, 16–24. doi:10.1016/j.gca.2015.03.024

van der Meer, M.T.J., Sangiorgi, F., Baas, M., Brinkhuis, H., Sinninghe Damsté, J.S., Schouten, S., 2008. Molecular isotopic and dinoflagellate evidence for Late Holocene freshening of the Black Sea. Earth Planet. Sci. Lett. 267, 426–434. doi:10.1016/j.epsl.2007.12.001

Vasiliev, I., Reichart, G.-J., Krijgsman, W., 2013. Impact of the Messinian Salinity Crisis on Black Sea hydrology—Insights from hydrogen isotopes analysis on biomarkers. Earth Planet. Sci. Lett. 362, 272–282. doi:10.1016/j.epsl.2012.11.038

Vincent, D.G., 1994. The South Pacific Convergence Zone (SPCZ): A review. Mon. Weather Rev. 122, 1949–1970.

Weiss, G.M., Pfannerstill, E.Y., Schouten, S., Sinninghe Damsté, J.S., van der Meer, M.T.J., 2017. Effects of alkalinity and salinity at low and high light intensity on hydrogen isotope fractionation of long-chain alkenones produced by *Emiliania huxleyi*. Biogeosciences Discuss. 14, 5693–5704. doi:10.5194/bg-2017-311

Wolhowe, M.D., Prahl, F.G., Langer, G., Oviedo, A.M., Ziveri, P., Maria, A., Ziveri, P., 2015. Alkenone δD as an ecological indicator: A culture and field study of physiologically-controlled chemical and hydrogen-isotopic variation in C37 alkenones. Geochim. Cosmochim. Acta 162, 166–182. doi:10.1016/j.gca.2015.04.034

Wolhowe, M.D., Prahl, F.G., Probert, I., Maldonado, M., 2009. Growth phase dependent hydrogen isotopic fractionation in alkenone-producing haptophytes. Biogeosciences 6, 1681–1694. doi:10.5194/bg-6-1681-2009

Zhang, X., Gillespie, A.L., Sessions, A.L., 2009. Large D/H variations in bacterial lipids reflect central metabolic pathways. Proc. Natl. Acad. Sci. U. S. A. 106, 12580–6. doi:10.1073/pnas.0903030106

Zhang, Z., Leduc, G., Sachs, J.P., 2014. El Niño evolution during the Holocene revealed by a biomarker rain gauge in the Galápagos Islands. Earth Planet. Sci. Lett. 404, 420–434. doi:http://dx.doi.org/10.1016/j.epsl.2014.07.013

Zhang, Z., Sachs, J.P., 2007. Hydrogen isotope fractionation in freshwater algae: I. Variations among lipids and species. Org. Geochem. 38, 582–608. doi:10.1016/j.orggeochem.2006.12.004

Zhang, Z., Sachs, J.P., Marchetti, A., 2009. Hydrogen isotope fractionation in freshwater and marine algae: II. Temperature and nitrogen limited growth rate effects. Org. Geochem. 40, 428–439. doi:10.1016/j.orggeochem.2008.11.002

Chapter 2: Exploring lipid $^{2}H/^{1}H$ fractionation mechanisms in response to salinity with continuous cultures of the diatom *Thalassiosira pseudonana*[1]

Abstract

The hydrogen isotopic ($^{2}H/^{1}H$) composition of lipids in microalgae is significantly depleted relative to extracellular water. While a variety of growth conditions influence the magnitude of ^{2}H-depletion, the effect of salinity is of particular interest due to the paleohydrological applications of lipid $^{2}H/^{1}H$. In previous studies, lipid-water $^{2}H/^{1}H$ fractionation was shown to decrease as salinity increased, a response largely independent of lipid type, species, or setting. The mechanism responsible for this response remains uncertain, primarily because salinity is rarely isolated as the sole variable in laboratory cultivation experiments investigating hydrogen isotope systematics in microalgae. Here we report the lipid-water $^{2}H/^{1}H$ fractionation response to salinity in nutrient-replete continuous cultures of the centric diatom *Thalassiosira pseudonana*. In six cultures with the same growth rate at salinities between 14-40 ppt, lipid-water $^{2}H/^{1}H$ fractionation decreased linearly as salinity increased by 1.3‰/ppt in fatty acids ($C_{14:0}$, $C_{16:0}$, $C_{16:1}$) and by 1.0‰/ppt in the sterol 24-methyl-cholesta-5,24(28)-dien-3β-ol. A constant growth rate between cultures reveals that the fractionation response to salinity is independent of growth rate. Sensitivity tests using a simple hydrogen flux model indicated that at high salinity a greater proportion of metabolic NAD(P)H in lipids at the expense of photosynthetic NADPH can cause ^{2}H-enrichment. Additionally, increased exudate release or decreased hydrogen transport can

[1] *Previously published as*: Maloney, A.E., Shinneman, A.L.C., Hemeon, K., Sachs, J.P., 2016. Exploring lipid $^{2}H/^{1}H$ fractionation mechanisms in response to salinity with continuous cultures of the diatom *Thalassiosira pseudonana*. *Organic Geochemistry* 101, 154–165. Reprinted with permission from Elsevier.

enrich both lipids and cell-water in ^2H. The 1.0-1.3‰/ppt increase in lipid-water $^2H/^1H$ fractionation observed in *T. pseudonana* is within the 0.8-2‰/ppt range observed in field studies and culture studies, supporting the application of algal lipid $^2H/^1H$ as a paleosalinity proxy.

Introduction

The $^2H/^1H$ ratio of individual phytoplankton lipids preserved in sediments (Sachse et al., 2012), is a promising tool for reconstructing past hydrologic variability (Atwood and Sachs, 2014; Kasper et al., 2014; Leduc et al., 2013; Nelson and Sachs, 2016; Pahnke et al., 2007; Petrick et al., 2015; Richey and Sachs, 2016; Sachs et al., 2009; Simon et al., 2015; Smittenberg et al., 2011; van der Meer et al., 2008, 2007; Vasiliev et al., 2013; Zhang et al., 2014). Hydroclimate reconstructions rely on the link between the hydrogen isotopic composition of environmental waters and fluxes of water though the hydrologic cycle (Craig, 1961; Craig and Gordon, 1965; Dansgaard, 1964; Gat, 1996). Deuterium/protium ($^2H/^1H$) ratios of environmental samples are expressed as δ^2H_{sample} ($\delta^2H_{sample} = [(^2H/^1H)_{sample}/(^2H/^1H)_{VSMOW}] - 1$) where VSMOW is Vienna Standard Mean Ocean Water. Molecular paleohydrology relies on the relationship between the δ^2H of photosynthetically produced lipids and that of their environmental source water. Culture experiments with a variety of microalgae species have shown that δ^2H_{lipid} is almost perfectly correlated with δ^2H_{water} with R^2 values in excess of 0.99 (Englebrecht and Sachs, 2005; Paul, 2002; Zhang and Sachs, 2007).

Phytoplankton lipids do not directly record the actual isotopic composition of source water. The offset between δ^2H_{lipid} and δ^2H_{water}, the lipid-water $^2H/^1H$ fractionation, represents the net isotopic effect of cellular processes associated with lipid biosynthesis. Fractionation is characterized by an apparent fractionation factor, $\alpha_{lipid\text{-}water}$ where $\alpha_{lipid\text{-}water} =$

$(^2H/^1H)_{lipid}/(^2H/^1H)_{water} = (\delta^2H_{lipid} + 1000)/(\delta^2H_{water} + 1000)$. Most biosynthetic and all photosynthetic products appear to be ^2H-depleted compared to ambient water resulting in $\alpha_{lipid\text{-}water} < 1$. Lipid-water $^2H/^1H$ fractionation factors can vary widely for different species of phytoplankton and different compounds (Sachse et al., 2012; Sessions et al., 1999; Zhang and Sachs, 2007), requiring the use of taxon-specific biomarkers.

The magnitude of $\alpha_{lipid\text{-}water}$ for any particular phytoplankton lipid can also be significantly influenced by several environmental and physiological parameters. This has important implications for proper interpretations of paleoclimate from molecular archives, prompting recent efforts to understand and characterize factors that impact microorganism $\alpha_{lipid\text{-}water}$ including growth rate (Schouten et al., 2006; Zhang et al., 2009; Sachs and Kawka, 2015), growth stage (Chivall et al., 2014; Heinzelmann et al., 2015a, 2015b, Wolhowe et al., 2015, 2009), irradiance (van der Meer et al., 2015), temperature (Estep and Hoering, 1980; Stiller and Nissenbaum, 1980; Wolhowe et al., 2009; Zhang et al., 2009), metabolism (Zhang et al., 2009; Osburn et al., 2011; Dirghangi and Pagani, 2013a, 2013b; Dawson et al., 2015; Heinzelmann et al., 2015a, 2015b), and salinity (Chivall et al., 2014; Heinzelmann et al., 2015a; Kasper, 2015; M'Boule et al., 2014; Nelson and Sachs, 2014; Sachs et al., 2016; Sachs and Schwab, 2011; Sachse and Sachs, 2008; Schouten et al., 2006)

Of particular concern for the application of molecular paleohydrology is the fact that increasing salinity can have a significant influence on $\alpha_{lipid\text{-}water}$ in eukaryotic microalgae and cyanobacteria. Apparent lipid-water $^2H/^1H$ fractionation in alkenones decreased ($\alpha_{lipid\text{-}water}$ increased) ~3‰/ppt in *Emiliania huxleyi* and *Gephyrocapsa oceanica* grown in batch cultures at different salinities (Schouten et al., 2006) (but also at different temperatures and growth rates as discussed in Zhang et al. (2009)). Apparent lipid-water $^2H/^1H$ fractionation decreased ~0.7-

1‰/ppt in cyanobacteria lipids from several hypersaline ponds on Christmas Island (Sachse and Sachs, 2008), in the dinoflagellate lipid dinosterol along the Chesapeake Bay estuary (Sachs and Schwab, 2011), and in dinosterol and brassicasterol from a global survey of saline and hypersaline lakes (Nelson and Sachs, 2014). In alkenones from batch-cultured open-ocean haptophytes $^{2}H/^{1}H$ fractionation decreased ~1-2‰/ppt in exponential phase (Chivall et al., 2014; M'Boule et al., 2014), and ~0.8-1‰/ppt in stationary and decline phases of the coastal species (Chivall et al., 2014). $C_{16:0}$ fatty acid from batch cultures in exponential, stationary, and decline phases all displayed decreasing $^{2}H/^{1}H$ fractionation of ~1.5‰/ppt (Heinzelmann et al., 2015a). $^{2}H/^{1}H$ fractionation decreased ~1.2-2.2‰/ppt in nitrogen-limited chemostats of *E. huxleyi* maintained at the same growth rate (Sachs et al., 2016). It has been proposed that this nearly-universal trend may be due to lower growth rates at sub-optimal salinity (Sachs and Schwab, 2011; Sachse and Sachs, 2008), decreased water transport across the outer cell membranes (Heinzelmann et al., 2015a; Sachs et al., 2016; Sachs and Schwab, 2011; Sachse and Sachs, 2008), increased production of small, compatible solutes (osmolytes) resulting in increased recycling of intracellular water and a progressively ^{2}H-enriched cell water pool (Sachs and Schwab, 2011; Sachse and Sachs, 2008), or an increase in the exudation of ^{2}H-depleted organic matter from cells at high salinity resulting in a ^{2}H-enriched cell water pool (Sachs et al., 2016).

In order to clarify the biochemical mechanisms responsible for the "salinity effect" we conducted nutrient-replete steady-state continuous culture experiments that had the same growth rate across a 26 ppt range of salinities with the diatom *T. pseudonana* to isolate the effect of salinity on $^{2}H/^{1}H$ fractionation in phytoplankton lipids. The diatom *T. pseudonana* was chosen because it is an extensively studied model organism (Armbrust et al., 2004) that can survive in a wide range of salinities (0-45 ppt). Continuous cultures are constant volume cultures that are

maintained indefinitely in exponential growth at a growth rate set by the media-supply rate. They provide an advantage over batch cultures (Bull, 2010) by allowing for reproducible, steady-state growth rates at several different salinities while maintaining constant temperature, light, nutrient, and chemical conditions. We present lipid-water $^{2}H/^{1}H$ fractionation values in three fatty acids and 24-methyl-cholesta-5,24(28)-dien-3β-ol (referred to as "sterol" for the remainder of the paper). This work complements a recent study using nitrogen-limited chemostats (Sachs et al., 2016) by investigating the effect of salinity on $\alpha_{lipid\text{-}water}$ in nutrient-replete continuously cultured microalgae; both studies support the universality of a 1-2‰/ppt sensitivity of $\alpha_{lipid\text{-}water}$ to salinity. A simple model of hydrogen fluxes indicated that lipid-water $^{2}H/^{1}H$ fractionation is sensitive to (i) proportionally more lipid hydrogen derived from the ^{2}H-enriched pool of metabolically reduced nicotinamide adenine dinucleotide phosphate (NADPH) or nicotinamide adenine dinucleotide (NADH) versus the ^{2}H-depleted pool of photosynthetically reduced NADPH, (ii) increased incorporation of cell-water-hydrogen into organic material, (iii) decreased transport of water in and out of cells, (iv) and increased extracellular release of organic hydrogen.

Methods

Continuous cultures

The diatom *T. pseudonana* (CCMP 1335) was grown in continuous cultures at a range of salinities chosen to ensure that approximately identical growth rates could be maintained across treatments: 14, 18, 27, 31, 36, and 40 ppt. An additional culture was attempted at 9 ppt which had a lower growth rate. Continuous cultures were grown in 5 l of f/2 media made from mixing MilliQ water with Instant Ocean aquarium salts (Spectrum Brands, Middleton, WI) and adding

trace metals, vitamins, and macronutrients to achieve concentrations of 882 μM NO_3^-, 36 μM $PO4^{-3}$, and 106 μM $Si(OH)_4$ (Guillard, 1975; Guillard and Ryther, 1962). Cultures were grown under 24-hr light (224 ± 54 μmol/m^2 s) at 20 °C with an inflow/outflow rate 4.7-5.0 ml/min. Detailed culture parameters are provided in Table S1. Cultures were monitored via *in vivo* fluorescence (IVF) twice daily. Steady-state conditions (taken as IVF varying less than 15% of the mean of all measurements) were maintained for 2-4 days before twice-daily subsampling for chlorophyll *a* (Chl *a*) and dissolved nutrients for a further 2-3 days. Chl *a* and nutrient subsamples were analyzed according to standard methods (UNESCO 1994). Additional 1 ml subsamples were preserved with formalin for cell density, cell diameter, and cell volume analyses on a Beckman Coulter Z2 Particle Count and Size Analyzer (Beckman Coulter, Fullerton CA, USA). For details of the cell enumeration, see the Supplementary material (Section 1). Growth rates in divisions per day (div/d) were estimated using dilution rate (flow-rate/volume) divided by ln(2) (Wood et al., 2005) and averaged over the 2-3 day steady-state sampling period. After 5-6 total days of steady-state growth, each entire culture was harvested onto a pre-combusted Whatman 142 mm diameter 0.7 μm pore size GF/F filter and immediately frozen at -20 °C.

Water and lipid δ^2H

Samples for isotopic analysis of the culture media were taken at the start and end of each continuous culture. δ^2H_{water} was measured six times per sample (the first three measurements were discarded to avoid memory effects) on a Picarro L2130-i Isotopic Liquid Water Analyzer with A0211 High-Precision Vaporizer (Picarro, Inc., Santa Clara, CA) and normalized to

VSMOW using three in-house water standards with δ^2H of -107.3 ± 0.5‰, -76.1 ± 0.3‰, and 14.8 ± 1.0‰. The average precision of sample measurements was 0.19‰.

Subsections of each frozen harvest filter were freeze-dried and cut into small pieces. Lipids were extracted by an Accelerated Solvent Extractor (ASE-200, Dionex Corp., Sunnyvale, CA, USA) using 9:1 dichloromethane:methanol (DCM:MeOH) at 1500 psi and 100 °C for three 5 min cycles. Total lipid extracts (TLEs) were saponified with 1N KOH at 70 °C for 12 h followed by liquid-liquid extractions with hexane. Aliquots of the saponified TLEs were silylated by dissolving them in 20 µl of pyridine and 20 µl of bis(trimethylsilyl)trifluoroacetamide (BSTFA, Sigma-Aldrich, St. Louis, MO, USA) and heating at 60 °C for 1 h. Lipid abundances were determined via gas chromatography-flame ionization (GC-FID) and recovery corrected using nC$_{36}$-alkane added to each sample prior to ASE extraction. Lipid identifications were made by comparing mass spectra generated by gas chromatography-mass spectrometry (GC-MS) to previously published mass spectra and laboratory standards (Zhang et al., 2009). GC-FID and GC-MS parameters were the same as in Sachs et al. (2016) and are provided in Table S5.

The remaining saponified TLEs were then purified using one-step column chromatography with a solid phase of 0.5 g aminopropyl gel (Supelco, Lot #2511301, Part # 5-7205). The sterol-containing fraction was eluted first in 8 ml of 3:1 DCM:isopropyl alcohol, followed by the fatty acids in 6 ml 4% acetic acid in diethyl ether. The fatty acid containing fractions were methylated by dissolving samples in 1 ml hexane with 2 ml 10:1 MeOH:acetyl chloride and heating for 12 h at 60 °C, followed by recovery via liquid-liquid extraction into hexane. Phthalic acid of known isotopic composition (-95.5 ± 2.2‰, Dr. Arndt Schimmelmann, Indiana University) was methylated via the same method to determine the isotopic composition

of the methylating agent. Sterol-containing fractions were acetylated by dissolving in 20 µl of pyridine plus 20 µl of acetic anhydride of known hydrogen isotopic composition (-123.8 ± 8.2‰) and heating at 70 °C for 0.5 hours.

Lipid δ^2H values were measured via gas-chromatography isotope-ratio mass spectrometry (GC-IRMS) according to the settings in Sachs et al. (2016) and provided in Table S5. Injections of external isotopic standards spanning a range of retention times and isotopic compositions of known hydrogen isotopic composition (Table S5) were injected separately after every 3-6 samples. Fatty acid and sterol data were evaluated and corrected using external standards as in Nelson and Sachs (2014b). Fatty acids were corrected for methylation and sterol for acetylation by mass balance calculations. The average $\delta^2H_{standard}$ precision of multiple injections for external and internal standards was 3.5‰.

Table 1. Linear regression results of culture parameters on salinity. Slopes with P values less than 0.05 are in bold.

Parameter	R^2	p level	Slope	Slope SE	Intcpt	Intcpt SE
Cell Density (x10^5 cells/ml)	0.01	0.86	0.00	0.02	1.2	0.5
Cell Diameter (µm)	0.54	0.09	0.02	0.01	3.0	0.2
Cell Volume (µm^3)	0.50	0.12	0.23	0.10	14	2
***in vivo* flouresence (fsu)**	0.60	0.07	5	2	117	54
Chl *a* (pg/cell)	0.44	0.15	0.04	0.02	-0.1	0.5
Fatty acid $C_{16:0}$ (µg/cell)	0.21	0.37	0.2	0.2	0	6
Fatty acid $C_{16:1}$ (µg/cell)	0.27	0.29	0.3	0.2	-3	6
Fatty acid $C_{14:0}$ (µg/cell)	0.21	0.36	0.10	0.09	1	3
Sterol (µg/cell)	0.47	0.13	0.02	0.01	-0.1	0.3
Residual NO_3^- (µM/cell)	0.11	0.52	8	11	359	1
Residual PO_4^{-3} (µM/cell)	0.05	0.67	0.1	0.3	13	2
Residual NO_2^- (µM/cell)	0.02	0.80	0.02	0.09	3	1
Residual NH_4^+ (µM/cell)	0.00	0.97	0.00	0.04	0.2	0.2
Residual $Si(OH)_4$ (µM/cell)	0.82	**0.01**	-1.0	0.2	46	7
$\alpha_{C16:0\text{-media}}$	0.95	**<0.001**	0.0013	0.0001	0.794	0.004
$\alpha_{C16:1\text{-media}}$	0.86	**<0.001**	0.0012	0.0002	0.809	0.007
$\alpha_{C14:0\text{-media}}$	0.99	**<0.001**	0.00125	0.00007	0.794	0.002
$\alpha_{sterol\text{-media}}$	0.85	**<0.001**	0.001	0.0002	0.641	0.006

Results

Continuous Cultures

None of the monitored culture parameters changed systematically with salinity except the siliceous acid remaining in the media after filtration (residual silica) (Table 1). Further details can be found in the Supplementary material (Sections 1 and 2). Continuous cultures at salinities 14, 18, 27, 31, 36, and 40 ppt could be maintained within a narrow range of growth rates between 1.90 and 1.99 div/d with a 1.97 ± 0.03 div/d mean while the fresher culture at salinity 9 ppt had a lower growth rate at 1.62 ± 0.03 div/d (Table 2).

Table 2. Average growth rate, *in vivo* fluorescence (IVF), cell density, cell diameter, and cell volume during the last 2-3 days of steady-state conditions.

Salinity	Growth rate (div/d)	SD	IVF (fsu)	SD	*n*	Cell density (x10^5 cells/ml)	SD	Cell diameter (µm)	SD	Cell volume (µm^3)	SD	*n*
9*	1.62	0.03	121	9	5	0.8	0.2	3.2	0.1	18	2	4
14	1.97	0.02	210	5	6	1.1	0.1	3.3	0.1	19	2	6
18	1.99	0.02	195	13	7	1.0	0.1	3.3	0.1	18	2	6
27	1.99	0.05	221	13	6	1.2	0.1	3.3	0.1	16	1	6
31	1.97	0.01	255	10	7	1.6	0.3	3.4	0.1	22	2	7
36	1.97	0.04	232	15	7	1.4	0.3	3.4	0.1	20	2	6
40	1.90	0.05	352	24	5	0.6	0.2	3.9	0.2	25	5	5

*Lower growth rate culture

δ^2H values of water and lipids

Isotope measurements and lipid concentrations are reported in Table 3. Concentrations of myristic ($C_{14:0}$), palmitic ($C_{16:0}$), and palmitoleic ($C_{16:1}$) fatty acids and the sterol were not linearly correlated with salinity (Table 1). The culture media that was sampled when the cells were harvested and had nearly constant δ^2H_{media} across all cultures averaging -74.4 ± 2.3‰ (Fig. 1). Two media samples taken at the start of steady-state conditions reveal that the isotopic composition of media during culture growth was constant with δ^2H_{media} values of -75.6 ± 0.12‰ (31 ppt) and -73.6 ± 0.42‰ (36 ppt). All lipids were ^2H-depleted compared to culture water,

δ^2H_{lipid} values increased as salinity increased, and were well correlated with salinity with R^2 values between 0.84 and 0.98 (Fig. 1). Fatty acids were the least depleted lipids. $\delta^2H_{C14:0}$ was between -248‰ and -218‰, a range of 30‰ with a mean of -234 ± 12‰. $\delta^2H_{C16:1}$ was between -234‰ and -206‰, a range of 29‰ with a mean of -221 ± 13‰. $\delta^2H_{C16:0}$ was between -247‰ and -218‰, a range of 28‰ with a mean of -232 ± 1‰. δ^2H_{sterol} values were more depleted than the fatty acids with a mean of -381± 11‰ and had a similar range (30‰) across the salinity treatments between -396‰ and -366‰. δ^2H_{lipid} values for all compounds from the low growth-rate 9 ppt culture were the most depleted samples and are included in Table 3 and Fig. 1.

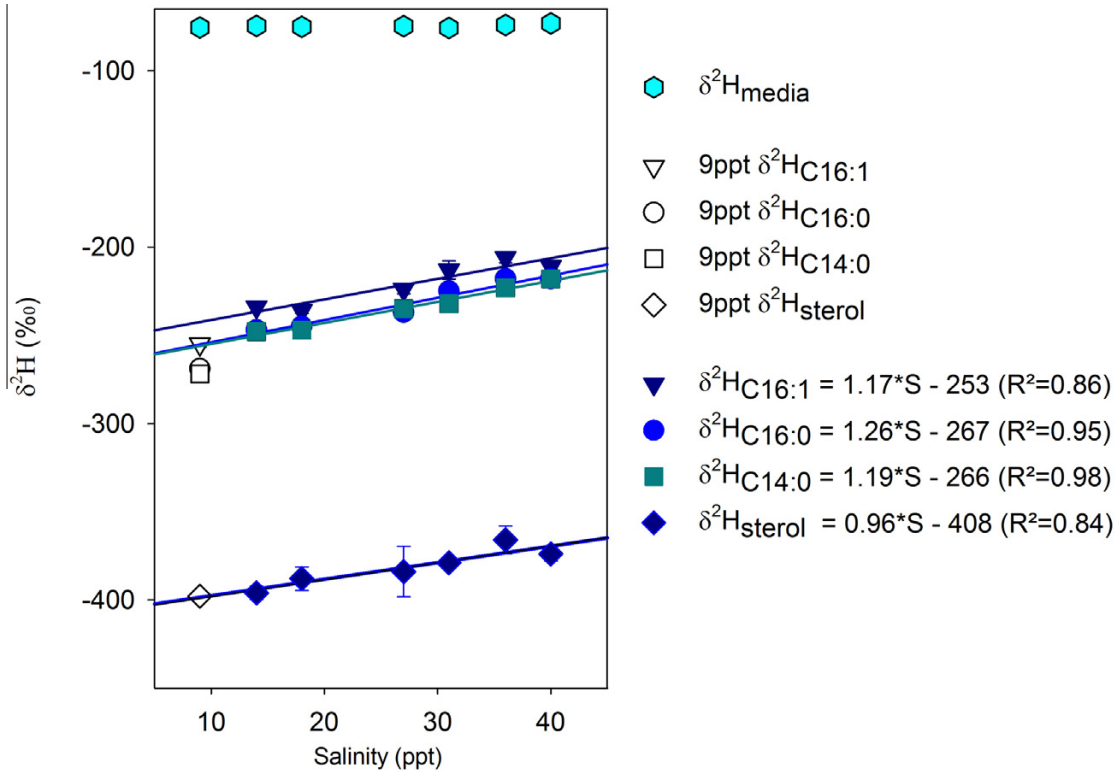

Fig. 1: Isotopic composition (δ^2H_{sample}) as a function of salinity for culture media, fatty acids, and a sterol in *T. pseudonana*. Fatty acids included myristic ($C_{14:0}$), palmitic ($C_{16:0}$) and palmitoleic ($C_{16:1}$) acids. The sterol was 24-methyl-cholesta-5,24(28)-dien-3β-ol. Lines are the linear regressions of δ^2H_{lipid} on salinity for the 14-40 ppt cultures and do not include the 9 ppt culture which had a lower growth rate. The 9 ppt data fall below the fatty acid regression lines but on the sterol regression line. Error bars represent standard deviations of three δ^2H_{media} measurements and 3-6 δ^2H_{lipid} measurements.

Table 3. Lipid concentrations and δ^2H values of media and lipids from continuous cultures of *T. pseudonana*. δ^2H_{media} is the average of 3 measurements. $\alpha_{lipid\text{-}media} = (1000 + \delta^2H_{lipid})/(1000 + \delta^2H_{media})$ is reported with propagated errors from δ^2H_{lipid} and δ^2H_{media}.

Salinity (ppt)		9*	14	18	27	31	36	40
Media	**δ^2H**	-75.5	-74.5	-75.1	-74.7	-75.7	-74.0	-73.2
	SD	0.1	0.5	0.2	0.2	0.1	0.1	0.3
C14:0	**[pg/cell]**	2.4	1.9	2.6	5.1	1.8	1.7	6.8
	δ^2H (‰)	-272	-248	-247	-235	-232	-223	-218
	n	3	3	3	3	5	3	4
	SD (‰)	2	4	4	2	4	3	2
	α	0.788	0.813	0.814	0.827	0.831	0.839	0.844
	SD	0.002	0.005	0.004	0.002	0.005	0.003	0.003
C16:0	**[pg/cell]**	2.5	3	3.9	8.5	2.9	1	15.1
	δ^2H (‰)	-269	-247	-245	-237	-225	-218	-218
	n	3	3	3	3	6	3	4
	SD (‰)	3	4	3	3	4	2	1
	α	0.791	0.813	0.817	0.825	0.838	0.844	0.844
	SD	0.003	0.004	0.003	0.003	0.004	0.002	0.001
C16:1	**[pg/cell]**	1.7	1.9	2.9	5.5	1.9	0.9	14.3
	δ^2H (‰)	-255	-234	-236	-224	-213	-206	-211
	n	3	3	3	3	3	3	4
	SD (‰)	2	3	2	3	5	3	2
	α	0.806	0.828	0.826	0.839	0.851	0.858	0.851
	SD	0.002	0.003	0.002	0.003	0.006	0.003	0.002
Sterol	**[pg/cell]**	0.6	0.2	0.4	0.4	0.3	0.4	1
	δ^2H (‰)	-398	-396	-388	-384	-379	-366	-374
	n	1	6	3	4	5	3	4
	SD (‰)	-	4	7	14	1	8	4
	α	0.652	0.653	0.662	0.666	0.672	0.684	0.676
	SD	-	0.004	0.007	0.015	0.001	0.009	0.004

*Lower growth rate culture

Fractionation factors increased, implying less $^2H/^1H$ fractionation, as salinity increased for all lipids (Table 3) and were highly correlated with salinity (R^2 was between 0.85 and 0.99) (Fig. 2 and Table 1). $\alpha_{C14:0\text{-}media}$ was between 0.813 and 0.844 with a 0.828 ± 0.013 mean, $\alpha_{C16:1\text{-}media}$ was between 0.826 and 0.858 with a 0.842 ± 0.013 mean, $\alpha_{C16:0\text{-}media}$ was between 0.813 and 0.844 with a 0.830 ± 0.014 mean, and $\alpha_{sterol\text{-}media}$ was between 0.653 and 0.684 with a 0.669 ± 0.011 mean. Since the hydrogen isotope fractionation response to salinity was the primary objective of these experiments, the freshest continuous culture (9 ppt) with a lower growth rate was not included in the linear regression analyses. If the low growth-rate data were included the α-salinity relationship became more sensitive to salinity

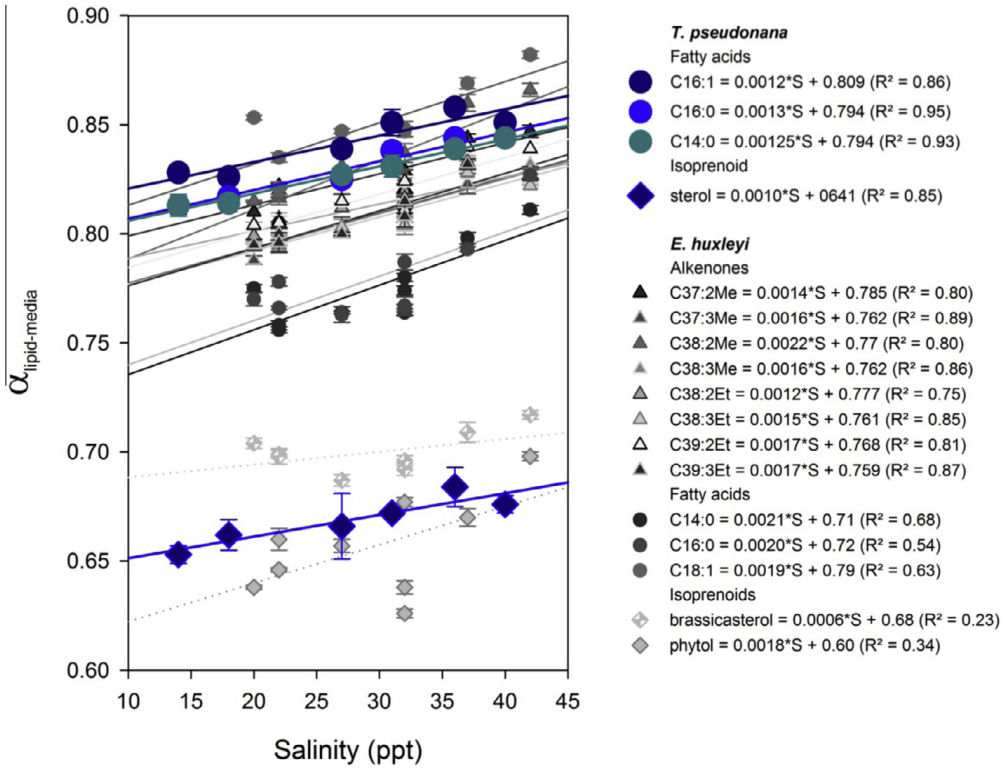

Fig. 2: Apparent fractionation factors, $\alpha_{lipid\text{-}media}$, as a function of salinity for three fatty acids and one sterol from nutrient-replete continuous cultures of *T. pseudonana*. Shown for comparison are fractionation factors for lipids from nitrogen-limited continuous cultures (chemostats) from the marine coccolithophorid *E. huxleyi* from Sachs et al. (2016) including eight alkenones, three fatty acids, one sterol, and phytol. Three separate chemostat cultures were conducted at 32 ppt and two at 22 ppt salinity for *E. huxleyi*. All values are averages of at least three measurements. Error bars represent propagated error for lipid and water measurements and are smaller than the symbols in some cases. Solid lines are linear regressions of data, dotted lines indicate linear regressions that were not significant below the P = 0.05 level.

for $\alpha_{C14:0\text{-}media}$ (0.0016±0.00012 instead of 0.0013±0.00007 ppt^{-1}) while the other lipids remained within the error of the estimated slopes (Supplementary material Fig. S3).

Model design and results

A coarse hydrogen flux model was used as a hypothesis development tool to test the sensitivity of $\alpha_{Lipids\text{-}Media}$ (capitalized to refer to model pools) to changes in hydrogen flux proportionality. The stationary model (Fig. 3) design included 6 boxes, 19 fluxes, the fractionation factor 0.4 associated with photosynthetic reduction of $NADP^+$ to NADPH via ferredoxin-$NADP^+$ reductase in photosystem 1 (PS1) (Luo et al., 1991; Schmidt et al., 2003), and an estimated fractionation factor 0.75 for the metabolic reduction of $NAD(P)^+$ to NAD(P)H using carbon-bound hydrogen (Sachs and Kawka, 2015; Schmidt et al., 2003). Fractionations associated with other processes were ignored ($\alpha = 1$) for most experiments both for simplicity and the fact that they are largely unknown (although some ranges of values were explored in the Supplementary material Fig. S6). The Cell Water pool, two organic hydrogen pools (Lipids and Other Organics), and two reductant pools (Photosynthetic NADPH and Metabolic NAD(P)H) had isotopic compositions determined by isotope mass balance equations (Supplementary material Section 3). The Media pool represented an infinite source of non-cellular hydrogen with constant $\delta^2H_{Media} = 0‰$. This model incorporated the key principals from a previously published 3-endmember model (Sachs et al., 2016; Sachs and Kawka, 2015). However, rather than prescribing endmember isotopic compositions, each hydrogen pool (except Media) was free to have variable isotopic compositions, which is important for testing the sensitivity of both Lipids and Cell Water.

Each flux represented an important biosynthetic, catabolic, or non-biosynthetic process responsible for moving hydrogen ($^2H + {}^1H$) between reservoirs. The sum of the

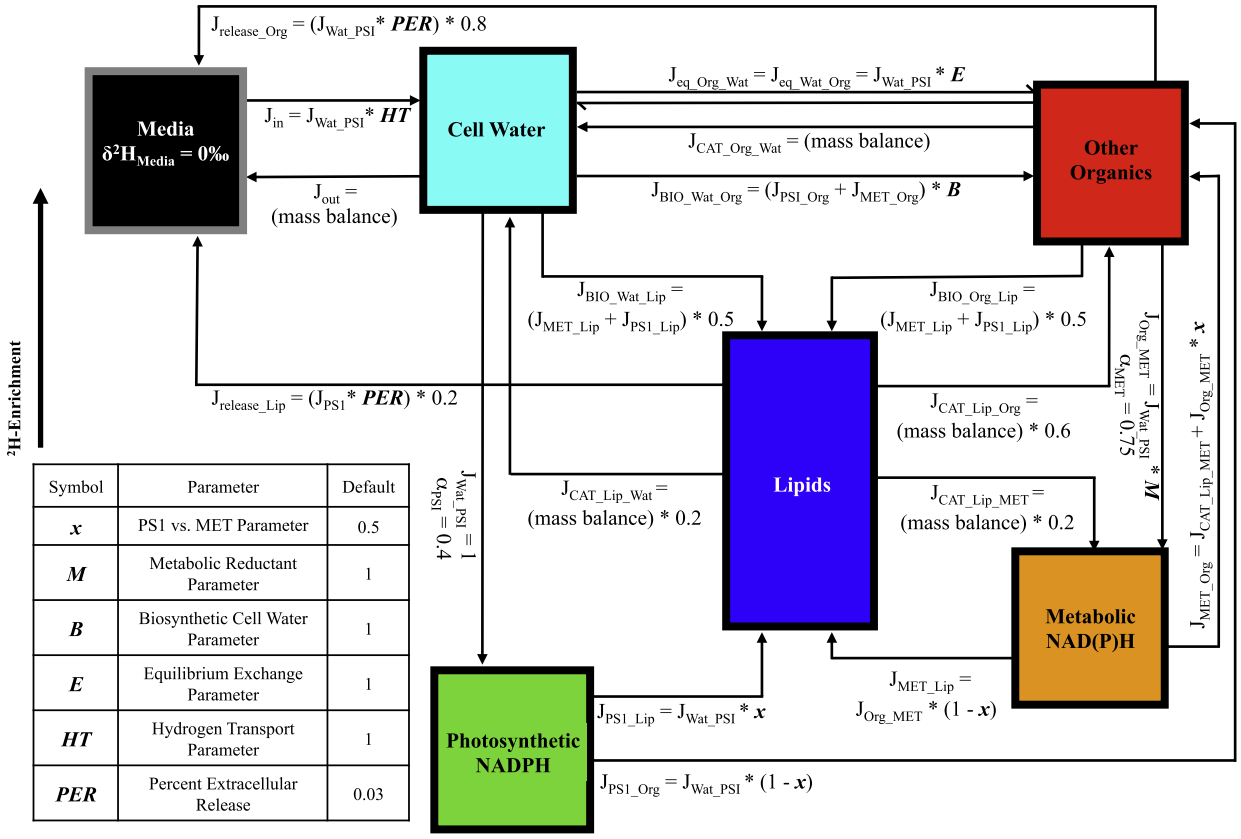

Symbol	Parameter	Default
x	PS1 vs. MET Parameter	0.5
M	Metabolic Reductant Parameter	1
B	Biosynthetic Cell Water Parameter	1
E	Equilibrium Exchange Parameter	1
HT	Hydrogen Transport Parameter	1
PER	Percent Extracellular Release	0.03

Fig. 3: Schematic for 6-box model of hydrogen mass and isotope fluxes in a population of phytoplankton cells. Fractionation factors associated with all fluxes are set to unity except for J_{Wat_PS1} ($\alpha_{PSI} = 0.4$) and J_{Org_MET} ($\alpha_{MET} = 0.75$).

fluxes into and out of each box was zero for the assumed steady-state conditions. Photosynthetic reduction of $NADP^+$ to NADPH was set to an arbitrary constant value ($J_{Wat\_PS1} = 1$) and a range of values was evaluated for six testable metabolic parameters that characterize the fluxes (Table S6). Assumed relationships between these metabolic parameters, J_{Wat_PS1}, and other fluxes (Table S7) make it possible to explore the sensitivity of $\alpha_{Lipids\text{-}Media}$ without the need to constrain or measure any individual flux.

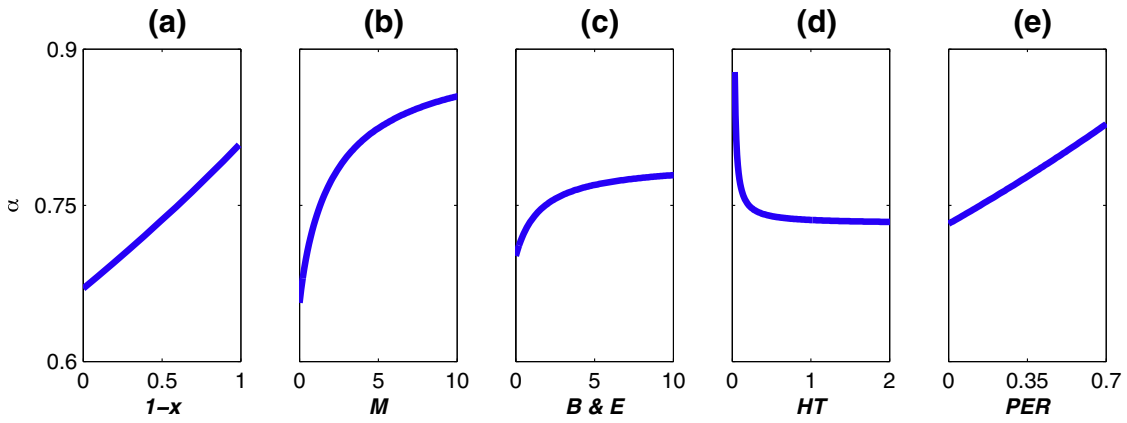

Fig. 4: Sensitivity of $\alpha_{Lipids\text{-}Media}$ to changes in metabolic parameters using default values where δ^2H_{Media} = 0‰. Lipid-Media $^2H/^1H$ fractionation decreases (i.e., $\alpha_{Lipids\text{-}Media}$ approaches unity) as (a) (1-*x*) (the amount of hydrogen from metabolic NAD(P)H vs. photosynthetic NADPH) increases, (b) *M* (size of the metabolic NAD(P)H flux relative to PS1) increases, (c) *B* and *E* increase (where *B* is the amount of organic-hydrogen source from cell-water-hydrogen relative to total NAD(P)H, and *E* is the equilibrium exchange between organic and cell-water-hydrogen), (d) *HT* (Hydrogen Transport) is less than photosynthesis and decreases, and (e) *PER* (Percent Extracellular Release) increases.

Fig. 4 illustrates how variations in each metabolic parameter influence $\alpha_{Lipids\text{-}Media}$. For individual metabolic parameter tests, all other metabolic parameters are set to default values specified in Table S6 and Fig. 3. Changes in the PSI vs. MET Parameter (*x*) (Sachs and Kawka, 2015) altered the proportion of Photosynthetic NADPH versus Metabolic NAD(P)H fluxes available for synthesis of Lipids and Other Organics. To achieve a 0.03 increase in $\alpha_{Lipids\text{-}Media}$ (the approximate range observed in our cultures), (1-*x*) must increase from 0.5 (default) to 0.7 (Fig. 4a), meaning Lipids received a larger flux of Metabolic NAD(P)H vs. Photosynthetic NADPH while Other Organics received a smaller flux of Metabolic NAD(P)H vs. Photosynthetic NADPH (Fig. S4). The Metabolic Reductant Parameter (*M*) determined the size of several fluxes (essentially the rate of catabolism) and also altered the proportion of Photosynthetic NADPH versus Metabolic NAD(P)H fluxes for synthesis of Lipids and Other Organics. To achieve a 0.03 increase in $\alpha_{Lipids\text{-}Media}$, *M* must increase from 1 (default) to 1.7 (Fig.

4b), meaning a larger flux of Metabolic NAD(P)H vs. Photosynthetic NADPH to Lipids and Other Organics (Fig. S4). The Biosynthetic Cell Water Parameter (*B*) determined the proportion of Cell Water-hydrogen used for synthesis of Other Organics (versus NAD(P)H) and the Equilibrium Exchange Parameter (*E*) set the amount of non-enzymatic equilibrium exchange between Cell Water and Other Organics. Increasing the flux of Cell Water-hydrogen to Other Organics by increasing *B* or *E* from 1 (default) to 4 ^{2}H-enriched Lipids enough to result in a 0.03 increase in $\alpha_{\text{Lipids-Media}}$ (Fig. 4c). The Hydrogen Transfer Parameter (*HT*) determined the flux sizes between Media and Cell Water. Decreasing *HT* from 1 (default) to 0.1, which restricted the fluxes between Media and Cell Water, resulted in a 0.03 increase in $\alpha_{\text{Lipids-Media}}$ (Fig. 4d). Percent Extracellular Release (*PER*) prescribed how much organic hydrogen was expelled from the cells. Increasing *PER* by 25% resulted in a 0.03 increase in $\alpha_{\text{Lipids-Media}}$. Decreasing *HT* or increasing *PER* were the only ways to ^{2}H-enrich Cell Water in this model (Fig. 5), whereas changes in *x*, *M*, *B*, and *E* resulted in Lipids that were ^{2}H-enriched without appreciably changing the isotopic composition of Cell Water (Fig. S5).

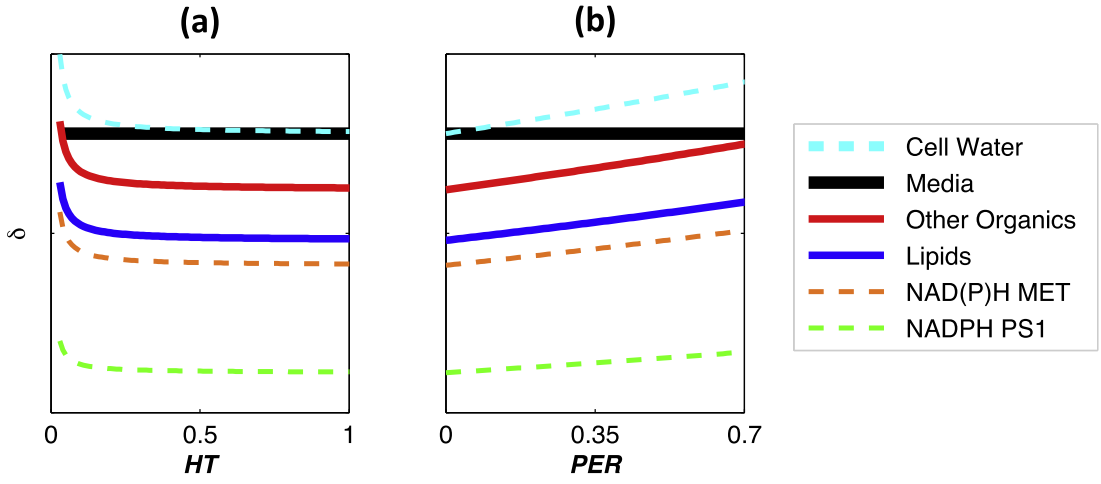

Fig. 5: Sensitivity of $\delta^{2}H_{\text{Resevoir}}$ to changes in metabolic parameters using default values and $\delta^{2}H_{\text{Media}}$ = 0‰. All non-media boxes become ^{2}H-enriched as (a) *HT* (Hydrogen Transport) decreases and (b) *PER* (Percent Extracellular Release) increases.

Discussion

Continuous cultures of *T. pseudonana* provide unequivocal evidence that $^{2}H/^{1}H$ fractionation decreases in lipids as salinity increases (Fig. 2). The 1.0-1.3‰/ppt salinity dependence observed in fatty acids and the predominant sterol in this species is similar to the sensitivity reported in field and batch culture studies with other species and lipids (Heinzelmann et al., 2015a; M'Boule et al., 2014; Sachs et al., 2016; Sachs and Schwab, 2011; Sachse and Sachs, 2008). Since the cultures were grown under steady-state conditions and at the same rate of growth across salinity treatments we can rule out the hypothesis put forth by Sachs & Schwab (2011) that the $^{2}H/^{1}H$ fractionation response in microalgal lipids is indirectly caused by salinity-induced changes in growth rate. This is further supported by a recent study of the coccolithophorid *E. huxleyi* maintained at the same growth rate using nitrogen-limited chemostats at a range of salinities (Sachs et al., 2016).

A six-box model was constructed to investigate the sensitivity of $\alpha_{Lipids\text{-}Media}$ to changes in basic cell physiology and metabolism. Several mechanisms emerge to explain salinity-induced variations in $\alpha_{Lipids\text{-}Media}$ as discussed below.

Varying proportions of reductant from Metabolic NAD(P)H versus Photosynthetic NADPH (x and M)

Photosynthetically produced NADPH is estimated to be ~600‰ depleted in ^{2}H relative to intracellular water (Luo et al., 1991; Schmidt et al., 2003) owing to the fact that electrolysis of water is associated with a large isotope effect. Reductant from other (metabolic) sources is expected to be less ^{2}H-depleted (Schmidt et al., 2003). Metabolic NAD(P)H can be generated in microalgae by $NADP^{+}$-reducing enzymes that participate in the oxidative pentose phosphate

(OPP) pathway including glucose-6-phosphate dehydrogenase (G6PDH) and 6-phosphogluconate dehydrogenase. In diatoms the OPP pathway is restricted to the cytosol (Gruber et al., 2009; Kroth et al., 2008; Michels et al., 2014; Wilhelm et al., 2006) but NAD(P)H can be generated by glycolytic enzymes in all cellular compartments (Smith et al., 2012) and the Entner-Doudoroff pathway in the mitochondria (Fabris et al., 2012). Additionally, NAD(P)H can be generated by isocitrate dehydrogenase and malate dehydrogenase in the TCA cycle, aldehyde dehydrogenase, pyruvate dehydrogenase, NAD(P)H-malic enzyme (Granum et al., 2005; Kroth et al., 2008), the membrane bound NADH-NADPH converting enzyme transhydrogenase, and other NAD^+ and $NADP^+$ reducing catabolic reactions (reviewed in Pollak et al., 2007; Spaans et al., 2015). Folate metabolism (Fan et al., 2014) may also contribute to metabolic NAD(P)H in diatoms (Hyde et al., 2008)

Separate pools of NAD(P)H with different isotopic compositions have been invoked to explain variable lipid-water $^2H/^1H$ fractionation in (i) microorganisms with heterotrophic, photoautotrophic, and chemoautrophic metabolisms (Zhang et al., 2009; Osburn et al., 2011; Dirghangi and Pagani, 2013a, 2013b; Dawson et al., 2015; Heinzelmann et al., 2015b), (ii) carbon-autonomous plant organs such as leaves (Gamarra and Kahmen, 2015), (iii) phytoplankton cells growing at different rates (Sachs and Kawka, 2015), and recently in (iv) the haptophyte *Emiliania huxleyi* grown at the same growth rate across a wide range of salinities (Sachs et al., 2016). We build on this line of reasoning and propose that similar mechanisms may play a role at high salinity in diatoms and other microalgae by (i) increasing the flux of Metabolic NAD(P)H (versus Photosynthetic NADPH) to Lipids while increasing the flux of Photosynthetic NADPH (versus Metabolic NAD(P)H) to Other Organics (increasing (1-*x*) in the model), or (ii) increasing the flux of hydrogen from Other Organics to Metabolic NAD(P)H and

thereby increasing the flux of Metabolic NAD(P)H (versus Photosynthetic NADPH) to Lipids and Other Organics (increasing *M* in the model) (Fig. S4).

In microalgae adjusting to salinity, changes in *M* or *x* might follow from physiological responses required to maintain osmotic and/or energy balances. Osmotic balance in microalge is achieved by the synthesis and accumulation of small organic molecules (osmolytes) which behave as non-toxic compatible solutes to help maintain vital cellular functions (Brown, 1978; Galinski, 1995; Kirst, 1989). Non-lipid biochemical constituents were not measured in these cultures so the hypothesis that increased production of osmolytes (and therefore a potential shift in biochemical composition) may "shuttle" light hydrogen to the osmolyte pool leaving intracellular water, NADPH, and lipids more enriched cannot be ruled out (Sachs and Schwab, 2011). This process was mimicked in the 6-box model by increasing the parameter (1-*x*) which caused the proportion of Lipid-hydrogen derived from Metabolic NAD(P)H and Other-Organic-hydrogen derived from Photosynthetic NADPH to increase. Increasing (1-*x*) in the 6-box model is analogous to increasing (1-*x*) in the 3-endmember model (Sachs et al., 2016; Sachs and Kawka, 2015) and has the same result, except that the Other Organics pool adds demand for NAD(P)H flux and all cellular pools of hydrogen are free to have variable isotopic compositions in the former. This analysis does not increase the total flux of reductant used in cells; it merely switches the relative proportion of ^{2}H-depleted reductant flux to Lipids vs. Other Organics. The result is a decrease in Lipid-Media $^{2}H/^{1}H$ fractionation (increase in $\alpha_{Lipid\text{-}Media}$) (Fig. 4a) with a concomitant increase in Organic-Media $^{2}H/^{1}H$ fractionation (decrease in $\alpha_{Organics\text{-}Media}$) (Fig. S5a) and could happen if osmolytes use a greater proportion of ^{2}H-depleted photosynthetic NADPH compared to lipids. Under high salt conditions osmolyte production required for cell survival might occur at the expense of lipid production, leaving lipids more ^{2}H-enriched. Increasing (1-*x*)

caused $\alpha_{Lipid\text{-}Media}$ to approach unity (Fig. 4a) but did not appreciably enrich NAD(P)H or intracellular water in ^{2}H as Sachs and Schwab (2011) hypothesized (Fig. S5). Therefore while our model supports their mechanism, it is perhaps more nuanced than originally proposed.

Alternatively, a similar result was accomplished by increasing *M* in the 6-box model. This sensitivity test is somewhat analogous to increasing (1-*x*) in the 3-endmember model (Sachs et al., 2016; Sachs and Kawka, 2015) except the 6-box model more realistically incorporates a source for metabolic NAD(P)H. When the flux of hydrogen from Other Organics to Metabolic NAD(P)H increased, the flux of Metabolic NAD(P)H to both Lipids and Other Organics also increased and $\alpha_{Lipid\text{-}Media}$ approached unity (Fig. 4b). This model analysis increased the total flux of reductant derived from metabolic NAD(P)H while the photosynthetic flux remained unchanged. Physically this might occur if cells have a greater demand for reducing power at high salinities. Importantly, previous investigations of protein activity and transcript abundance suggest that reduction of Metabolic NAD(P)H increases with salinity. For instance, increased expression levels of OPP enzymes have been observed in diatoms grown at high salinity (Cheng et al., 2014). Bacterial cells (Danevčič and Stopar, 2011), macroalgae (Huan et al., 2014), and cyanobacteria (Rai et al., 2014, 2013b) grown at high salinity showed increased OPP enzyme activity. Several higher plant studies imply that increased OPP activity or protein abundance occur in response to salinity changes (Gao et al., 2016; Huang et al., 2003; Nemoto and Sasakuma, 2000; Wang et al., 2008; Yang et al., 2014; Yu et al., 2011). In high salt conditions, $NAD(P)^{+}$ reducing proteins such as pyruvate dehydrogenase, malate dehydrogenase, and OPP enzymes were up-regulated in the halotolerant green alga *Dunaliella* (Liska, 2004). All of these studies indicate that phototrophs may require more reducing power at high salinities. Since growth performance was either different of not reported in salt treatments, it is not immediately

clear if the observed enzyme activities and transcript abundances are a direct response to salt or an indirect response to growth, highlighting the importance of continuous culture experiments.

If high salinity conditions result in either (i) ^{2}H-enriched NAD(P)H available for lipid synthesis when photosynthetically produced NADPH is preferentially shuttled to osmolytes, or (ii) overall more metabolically produced NAD(P)H flooding the reductant pool, then lipids should become ^{2}H-enriched. Indeed, heterotrophic bacteria and archaea don't have access to pools of photosynthetic NADPH and don't display δ^{2}H-enrichement at high salinity (Dirghangi and Pagani, 2013a; Heinzelmann et al., 2015a). If more metabolic NAD(P)H is used by photoautotrophs during lipid synthesis at high salinities, this could explain why salinity-dependent ^{2}H/^{1}H fractionation is observed in photoautotrophs but not heterotrophs. Increasing the flux of Metabolic NAD(P)H to just Lipids (1-*x*), or increasing the flux of metabolic NAD(P)H to both Lipids and Other Organics (*M*) are mechanisms that are likely to be directly linked to increased production of compatible solutes and/or energy balance, and as such are the most likely explanations for decreased ^{2}H/^{1}H fractionation at increased salinity.

Varying proportions of hydrogen from intracellular water (B and E)

NMR studies indicate acetogenic lipids derive about 50% of their hydrogen from NAD(P)H, 25% from intracellular water, and 25% from acetyl-CoA (Saito et al., 1980; Robins et al., 2003; Schmidt et al., 2003; Zhang et al., 2009). Isoprenoid lipids derive ~20-40% of their hydrogen from NADPH and the remainder from either acetyl-CoA when synthesized via the cytosolic MVA pathway, or pyruvate and glyceraldehyde-3-phosphate (GAP) when synthesized via the plastidic DOXP/MEP pathway (Sessions et al., 2002). Pyruvate, acetyl-CoA, and GAP are central metabolites under high demand by several competing cellular functions such as

carbohydrate, lipid, protein, and nucleic acid synthesis and catabolism (Hemmerlin et al., 2012; Oliver et al., 2009). One way salinity might influence the proportion of cell-water-derived hydrogen in biochemicals is by increasing the likelihood that carbon-bound hydrogen on the primary metabolite precursors pyruvate, acetyl-CoA, and GAP is derived from cell-water. For example, shifting demands on the primary metabolite pools could change the relative importance of different pyruvate synthesis pathways that impart different proportions of hydrogen derived from water versus metabolites on the lipid-destined methyl group (see Fig. 6 in Sachs et al., 2016), effectively changing the metabolic parameter *B*.

Additionally, hydrogen in pyruvate precursors can exchange with intracellular water through the presence or activity of isomerases at the glucose level (Katz and Crespi, 1970). The enzyme glucose-6 phosphate isomerase (which converts glucose-6-phosphate to fructose-6-phosphate and back) can facilitate both intramolecular and intermolecular exchange of hydrogen between the sugar and the aqueous solvent. Investigation of this enzyme in different cell types has revealed heterogeneity in the amount of back and forth conversion of sugars and suggests that environmental parameters can influence this exchange (Malaisse-Lagae et al., 1989). At high salinity, glucose-6 phosphate isomerase from *Dunaliella salina* was strongly induced by salinity at both the protein and gene level (Cui et al., 2010). Any associated fractionation effects aside (Fig. S6), it is plausible that salinity could increase the proportion of ^{2}H-enriched cell-water-derived hydrogen in lipid precursors, and by extension, lipids (akin to increasing the model metabolic parameter *B*) by altering the relative or absolute presence or activity of these enzymes.

Relatedly, preferences for specific lipid biosynthesis isoenzymes may modify the amount of cell-water-hydrogen in lipids (akin to increasing the model metabolic parameter *E*). There are numerous fatty acid synthesis isoenzymes responsible for incorporating hydrogen during lipid

synthesis. For instance, Zhang et al. (2009) noted that there are many variants of enoyl-ACP reductase enzymes involved in the second reductive step of fatty acid biosynthesis (Massengo-Tiassé and Cronan, 2009). The enzymes FabI and FabL directly transfer hydrogen from NAD(P)H to the growing fatty acid chain, but FabK involves the indirect transfer of H^- via a nitrogen-bound hydrogen on the flavin cofactor. Since N-bound hydrogen undergoes rapid exchange with water, flavoproteins that transfer hydrogen to organic material can indirectly enrich products in ^2H (Chisla and Massey, 1989; Schmidt et al., 2003; Simon and Kraus, 1976). For fatty acids at least, enhancement of FabK over FabI or FabL could incorporate more cell-water-hydrogen into lipids. While it is not yet known if FabK occurs in eukaryotic microalgae, or if salinity can induce a shift in Fab isoenzymes, the presence of the gene encoding for FabK was inferred from the transcriptome of the diatom *Nitzschia* sp. (see Table 1 in Cheng et al., 2014)). Since these enzymes are not involved in isoprenoid synthesis, an analogous process would need to be invoked to explain the similar salinity response of sterol δ^2H values to salinity in diatoms.

Finally, osmolytes in phytoplankton are typically small organic molecules with a large proportion of exchangeable hydrogen, such as amino acids and derivatives, polyols and sugars, methylamines, methylsulfonium compounds, and urea (Yancey, 2005). Sachs and Schwab (2011) proposed that osmolyte production might result in ^2H-enriched pools of cell water and NAD(P)H. If a normal fractionation factor (i.e., one that results in a product that is isotopically depleted compared to the reactant) characterizes the enzymatic or equilibrium exchange of hydrogen from Cell Water to Other Organics, the model yields ^2H-enriched lipids (Fig. S6). These mechanisms for incorporating additional cell-water-hydrogen into lipids (*B* and *E*) are less direct (and therefore more difficult to test) than changes in NAD(P)H related to *x* or *M* but cannot be ruled out.

Variations in Hydrogen Transport (HT):

Both $\delta^2H_{OtherOrganics}$ and $\delta^2H_{CellWater}$ become more ^2H-enriched as *HT* approaches zero, likely the result of recycling of intracellular water without full replenishment from the media (Fig. 4). One widely proposed mechanism for decreased fractionation at elevated salinity is "increased recycling" of cell water resulting from diminished transport of environmental water into cells (Heinzelmann et al., 2015a; Sachs et al., 2016; Sachs and Schwab, 2011; Sachse and Sachs, 2008). Investigations of intracellular water from both prokaryotic and mammalian cells (Kreuzer-Martin et al., 2006, 2005; Kreuzer et al., 2012) indicate that the isotopic composition of cell-water-hydrogen and oxygen can differ from that of growth media. Since the permeability of the lipid bilayer is high and the residence time of water inside a cell is short (García-Martín et al., 2001) decreasing transport of environmental water across the cell membrane might be achieved by transcriptional down-regulation of aquaporins or adjustment of the probability that aquaporins are open (Boursiac et al., 2005; Hasegawa et al., 2000; Horie et al., 2011). The model indicates that a hydrogen flux across the cell membrane that is smaller than the photosynthetic flux of hydrogen increases $\alpha_{Lipid\text{-}Media}$ and causes intracellular water to become ^2H-enriched relative to external water (Fig. 4a). Reduced transport of environmental water (to fluxes smaller than the total flux of hydrogen required for biosynthesis) therefore remains a viable mechanism for explaining decreased fractionation at increased salinity, but a hypothetical one pending demonstration of changes in $\delta^2H_{CellWater}$ in photoautotrophs.

Variations in the release of organic hydrogen (PER)

Depending on growth conditions and species, phytoplankton cells can exude 2-76% of their photosynthetically fixed carbon (Thornton, 2014; Van Oostende et al., 2013). Phytoplankton *PER* is considered to be a normal physiological function of healthy cells and likely plays a protective role in stressful environments (Thornton, 2014). Several studies indicate that both phytoplankton and bacteria increase *PER* and alter its chemical composition (Abdullahi et al., 2006) in response to suboptimal growth conditions (Alcoverro et al., 2000; Zlotnik and Dubinsky, 1989) such as elevated salinity (Abdullahi et al., 2006; Aslam et al., 2012; Liu and Buskey, 2000; Maršálek and Rojíčkovâ, 2015; Steele et al., 2014; Zhang et al., 2011). Experiments with diatom cultures at high salinity showed increased frustule-bound exopolysaccharides but decreased transparent exopolysaccharides (Bussard et al., 2017). The model sensitivity analysis indicated that increasing *PER* causes $\alpha_{Lipid\text{-}Media}$ to approach unity (Fig. 4e) when more ^{2}H-depleted organic material is expelled from the cell. This was the only model process besides restricted uptake of extracellular water (low *HT*) that caused significant changes in modeled $\delta^{2}H_{CellWater}$ (Fig. 4b), supporting the hypothesis recently put forward in Sachs et al. (2016) that increased exudation of ^{2}H-depleted organic matter may lead to ^{2}H-enriched cell-water. Investigations of the isotopic composition of intracellular water and exudate fluxes could help elucidate whether changes in *HT* or *PER* can explain decreased fractionation with increased salinity.

Model limitations

Interestingly, the 9 ppt data fell below the α-salinity trends for the fatty acids (Fig. S3a-c) but on the α-salinity trend for the sterol (Fig. S3d). In previous studies comparing *T. pseudonana*

nutrient-replete (higher growth rate) continuous cultures to nutrient-limited (lower growth rate) chemostats, $\alpha_{fattyacids\text{-}media}$ was not influenced by growth rate while $\alpha_{sterol\text{-}media}$ displayed increased fractionation at increased growth rate (Sachs and Kawka, 2015; Z. Zhang et al., 2009). Thus the 9 ppt treatment in this study behaved as the previous works would predict: presumably the decreased growth rate pushed the sample onto the trend for the sterol α-salinity relationship while there was no "bolstering effect" for the fatty acid α-salinity relationships since acetogenic lipids do not seem to be influenced by growth rate in *T. pseudonana* (Sachs and Kawka, 2015; Z. Zhang et al., 2009).

The stationary model presented is inadequate for evaluating the effect of changes in growth rate or growth phase on $\alpha_{Lipids\text{-}Media}$. Because catabolism equaled anabolism in a single population of cells, the model is more representative of a culture in "stationary phase". The 6-box model is not directly comparable to the continuous cultures that were held in steady-state by dilution with a constantly overturning population of cells. However, because a nearly identical salinity effect was observed in batch cultures that were in exponential, stationary, and death phases (Heinzelmann et al., 2015a), the 6-box model represents a first step in determining the mechanisms underlying the sensitivity of $\alpha_{Lipids\text{-}Media}$ to salinity.

Adding other hydrogen reservoirs to the model and additional isotopically distinct pool of metabolic NAD(P)H might reveal nuances governing the H isotopic composition of lipids. For instance, measured fatty acid δ^2H was more sensitive to salinity than the sterol in this study, and recent culture studies with haptophytes revealed different $\alpha_{lipid\text{-}water}$ sensitivities in isoprenoid and acetogenic lipids (Kasper, 2015; Sachs et al., 2016). Since it has been suggested that *n*-alkyl ^2H-enrichement relative to isoprenoid lipids might be due to isotopically different pools of NAD(P)H (Sachse and Sachs, 2008; Sessions et al., 1999), a more complex model might inform

unexplained patterns of hydrogen isotope fractionation in microorganisms. While the *n*-alkyl lipid precursor acetyl-CoA is synthesized in the chloroplast (e.g. Shtaida et al., 2015), the precursor to isoprenoid compounds (isopentenyl pyrophosphate, IPP) is synthesized either in the cytoplasm via the "eukaryotic" mevalonic acid (MVA) pathway or in the plastid via the "prokaryotic" 1-deoxy-D-xylulose-5-phosphate/2-methyl-erythroyl-4-phosphate pathway (DOXP/MEP) (Lohr et al., 2012). In diatoms, sterol synthesis has characteristics of bacterial, higher plant, and fungal biosynthetic pathways, possibly a result of their unique evolutionary origin (Desmond and Gribaldo, 2009; Fabris et al., 2014) likely resulting in steroidal precursors from both the MVA and DOXP/MEP pathways (Lohr et al., 2012 and references therein). Therefore, incorporating compartmentalization into a model could further illuminate differences in $^{2}H/^{1}H$ fractionation between fatty acids and isoprenoids and differences between species.

From the sensitivity analyses of the 6-box hydrogen flux model we hypothesize that (i) variations in the source of NAD(P)H and/or increased production of Metabolic NAD(P)H versus Photosynthetic NADPH is the most likely mechanism responsible for the salinity sensitivity of $\alpha_{Lipids\text{-}Media}$, with (ii) increased incorporation of Cell Water-hydrogen into Other Organics a viable second mechanism. Two additional mechanisms caused a significant ^{2}H-enrichment of both lipids and intracellular water, including (iii) restricted hydrogen transport from media into cells, and (iv) increased extracellular release of organic material, insight that could not be obtained from the previous 3-endmember model (Sachs et al., 2016; Sachs and Kawka, 2015). These might contribute to ^{2}H-enrichement of lipids at high salinities if it can be shown that intracellular water can be isotopically distinct from media in photoautotrophs. Considering these mechanisms separately is useful for the purposes of sensitivity analysis, but it is important to

note that a combination of these mechanisms may well be responsible for the observed salinity effect on lipid fractionation.

Conclusions

The diatom *T. pseudonana* was grown at steady-state in nutrient-replete continuous cultures at six salinities between 14-40 ppt and at a lower growth rate at 9 ppt. Over the 26 ppt salinity range in which the cultures had equivalent growth rates, δ^2H values increased by 1.3‰/ppt in $C_{14:0}$, $C_{16:0}$, and $C_{16:1}$ fatty acids, and by 1.0‰/ppt in 24-methyl-cholesta-5,24(28)-dien-3β-ol. Growth rate differences, previously hypothesized to contribute to the observed sensitivity of lipid δ^2H to salinity, can be ruled out as a causal mechanism in both *T. pseudonana* and *E. huxleyi* (Sachs et al., 2016). A 6-box model revealed four mechanisms that might contribute to ^2H-enrichment in lipids as salinity increases: (i) increases in the relative contribution of metabolic NAD(P)H (vs. photosynthetic NADPH), (ii) increased incorporation of cell-water-hydrogen into organic material, (iii) restricted exchange of water between cells and the environment, and (iv) increased release of organic exudates. Although each mechanism could potentially impact $\alpha_{lipid\text{-}water}$, shifts in the relative supply of metabolic NAD(P)H, at the expense of photosynthetic NADPH, is the most parsimonious mechanism.

Irrespective of the underlying cause of diminished $^2H/^1H$ fractionation in microalgal lipids under increased salinity, there is strong empirical support from field, batch cultures, nitrogen limited chemostats, and now nutrient-replete continuous cultures that this response is robust and likely universal. In virtually all lipids and species $^2H/^1H$ fractionation decreases with salinity by 1-2‰/ppt. The consistency of these observations implies that biomarker lipid δ^2H values may be used to reconstruct salinity in paleoclimate and paleoenvironmental studies.

Acknowledgements

This material is based upon work supported by the National Science Foundation under Grant No. OCE-1027079 (J.P.S.). The University of Washington Program on Climate Change Fellowship and IGERT Ocean Change Fellowship award #NSF1068839 provided partial support for A.E.M. We would like to thank P. MacCready for lending lab space, E. V. Armbrust and A. Ingalls for lending equipment, F. Ribolet, G. Hennon, L. Fisher, and O. Kawka for assisting with culture data interpretation, A. Chomos and N. Kato for assisting with culture maintenance, J.A. Gregersen for assisting with water isotope measurements, C. Paschall and R. D'Jay for assisting with Coulter Counter measurements, R.A. Cattolico and H. Hunsperger for assisting with flow cytometry measurements, D.B. Nelson and J.N. Richey for assisting with lipid analysis, and S.G. Warren and M.D. Wolhowe for writing edits. Thanks to K.A. Krogslund and A. Morello who analyzed nutrient and chlorophyll samples. Valuable discussions with S.R. Smith, J. Levering, A. Gruber, M.J. Behrenfeld, G. Rocap, E.V. Armbrust, P.D. Quay, L.A. Thompson, A. Ingalls, K.R. Heal, C. Deutch, N.S. Banas, A.E. Shao, C. Saenger, and L. Johnson aided model development. The comments of two anonymous reviewers and Associate Editor S. Schouten improved this manuscript.

Chapter 2 Appendix A. Supplementary data

Culturing and instrumental details

All culture conditions are given in **Table S1**. In order to establish the maximum salinity range in which *T. pseudonana* could sustain similar division rates in nutrient replete continuous cultures, several semi-continuous batch cultures were grown in triplicate at a range of salinities (9-45 ppt) (**Fig S1**). Once acclimated to their respective salinity levels for 6-10 generations, these cultures were then used as starter cultures for the continuous cultures. Continuous cultures maintained the same growth rate in the salinity range 14-40 ppt. To ensure that IVF was an appropriate proxy for cell density, 1 ml aliquots preserved with Lugols fixative were taken twice daily from 2-4 generations per salinity and enumerated using a hemacytometer with a Leica DM1000 microscope. In 2010 and 2011 continuous culture cell density was estimated using a hemacytometer using subsamples preserved in Lugols fixative. In 2013, continuous culture subsamples preserved with formalin were analyzed for cell density and cell diameter by injecting 100 µL into a BD Accuri C6 flow cytometer (BD Biosciences, San Jose, CA, USA) and comparing data contained in the same gate on the forward versus side scatter plots for all culture samples. Diameter was calculated using the relationship obtained from non-fluorescent polystyrene F-13838 size calibration beads (Thermo Fisher Scientific, Molecular Probes, Carlsbad, CA, USA). In 2013 the same formalin-treated subsamples were also used to measure cell diameter, density, and volume on a Beckman Coulter Z2 Particle Count and Size Analyzer (Beckman Coulter, Fullerton CA, USA). The different cell counting methods gave different absolute results (**Table S2**), not a new problem in phytoplankton science (Hallegraeff, 1977), but

did not give different relationships to salinity. The main text adopts the cell counts from the Coulter Counter for all calculations.

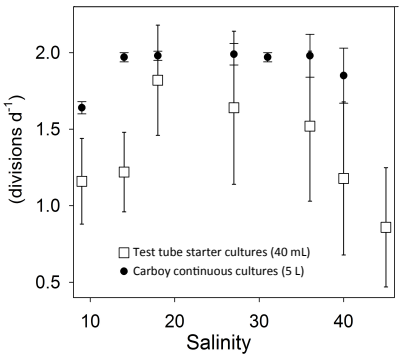

Fig. S1. Average division rates achieved in batch culture test tubes (40 ml volume) compare to continuous culture carboys (5 l volume). Average growth rate (div/d) of several (n = 20-40) semi-continuous batch cultures at salinities 9, 14, 18, 27, 36, 40, 45 ppt (open squares) and average growth rate (specific growth rate divided by ln(2)) of individual continuous cultures at salinities 9, 14, 18, 27, 31, 36, and 40 during the last 2-3 days of steady state (closed circles). The freshest continuous culture (9 ppt) could not be maintained at a similar growth rate and was therefore not included in linear regression analyses.

Table S1. Nutrient replete continuous culture settings

Parameter	Details/Settings	Notes/Source
Strain	CCMP 1335	Provasoli-Guillard National Center for Marine Algae and Microbiota (NCMA)
Environment	1.12 m^2 foam chamber cooled with household AC unit	Grown in 2010 and 2011 at the University of Washington
Temperature	20 ± 1 °C	
Light Cycle	24 h	Provided by one 40 W cool-white fluorescent bulb on each side of chamber
Light Intensity	224 ± 54 µmol/m^2 s (average measured at 8 locations in the chamber)	QSL-2100 probe (Biospherical Instruments, San Diego, CA, USA)
Media	Milli-Q water mixed with Instant Ocean® aquarium salts then 0.7 µm and 0.2 µm filtered on Whatman GF/F and Supor membrane filter	(Spectrum Brands, Middleton, WI, USA); (GE Healthcare Bio-Sciences, Pittsburgh, PA, USA); (Pall Life Sciences, Port Washington, NY, USA)
Nutrient regime	f/2; stock solutions of macronutrients, trace metals, and vitamins were 0.2 µm filtered; concentrations were 882 µM NO_3^-, 36 µM $PO4^{-3}$, and 106 µM $Si(OH)_4$	(Guillard, 1975; Guillard and Ryther, 1962); SFCA 0.2 µm membrane syringe filters (Thermo Fisher Scientific, Waltham, MA, USA)
Salinity (ppt)	9, 14, 18, 27, 31, 36, 40; measured with a calibrated Orion 3-Star Plus conductivity meter and checked daily in cultures with a refractometer	(Thermo Fisher Scientific, Waltham, MA, USA)
Culture volume and vessel	5 l (grown in 12 l paddle-stirred polycarbonate carboys); all plastic and glassware was acid-washed, rinsed with Milli-Q water, and autoclaved before use.	Thermo Scientific Nalgene #2600-0012
Air	Bubbled with 0.2 µm filtered medical grade air	SFCA 0.2 µm membrane syringe filters (Thermo Fisher Scientific, Waltham, MA, USA)
Flow rate	Inflow/outflow rate 4.7-5.0 ml/min	
Growth rate	Specific growth rate, µ (/d) estimated using dilution rate (D = flow-rate/volume) and divide by ln(2) for division rate (div/d)	(Wood et al., 2005)
Steady state assessment	Continuous cultures steady state was when *in vivo* fluorescence (IVF) was always within 15% of the mean	
Continuous culture preparation	~ 130 ml of exponentially growing starter culture added to 1 l media in carboys; after sufficiently large increase in biomass (>100 fsu), volume was increased to 5 l	
Continuous culture initiation	Once the 5 l culture was in early to mid-exponential phase (between 250-350 fsu), continuous cultures were initiated	IVF was monitored 1-2 times daily by extracting 40 ml of culture material (then discarded to avoid contamination)
Chl *a*	Subsampled twice daily during last 2-4 days of continuous culture steady state growth	Extracted in 90% acetone for a minimum of 24 hours at -20 °C analyzed on a TD-700 fluorometer (Turner Designs)
Nutrient subsamples	Subsampled twice daily during last 2-4 days of continuous culture steady state growth	Continuous flow photometry: Technicon AAII autoanalyser (Seal Analytical, Mequon, WI, USA).
Starter culture design	Semi-continuous batch cultures: acclimated in triplicate to respective salinity levels for 6-14 transfers	1 ml of cell culture was added to 39 ml sterile f/2 media at the end of exponential phase
Starter culture vessels	25x150 mm round borosilicate glass test tubes plugged with sterilized cotton	Swirled gently 2-3 times per day
Starter culture growth	Calculated by $k = \log_2(N_1/N_0)/(T_1-T_0)$: N_1 & N_0 = IVF or cell counts at start and end of exponential growth; T_1 & T_0 = corresponding times (div/d)	(Adolf et al., 2003)
In vivo fluorescence (IVF)	Monitored 1-2 times daily by inserting test tube culture in fluorometer for test tube batch cultures or extracting 40 ml of continuous culture	TD-700 (Turner Designs, Sunnyvale, CA, USA) fitted with a 340-500 nm wavelength excitation filter and a >665 nm wavelength emission filter. All readings were adjusted to a solid standard and are reported in Fluorescent Signal Units (fsu)

Table S2. Average cell density determined by 3 different methods and cell diameter determined by 2 different methods. The average of 4-6 subsamples (*n*) taken during steady state is reported with standard deviations.

	Salinity	Coulter Counter	SD	*n*	Flow Cytometer	SD	*n*	Hema-cytometer	SD	*n*
Cell density ($x10^5$ cells/ml)	14	1.1	0.1	6	4.4	0.5	6	5.9	1.2	6
	18	1.0	0.1	6	2.7	0.2	6	3.5	3.3	6
	27	1.2	0.1	6	2.3	0.7	6	11.1	1.3	5
	31	1.6	0.3	7	5.1	0.7	7	6.8	1.2	6
	36	1.4	0.3	6	4.6	0.9	6	14.1	1.2	6
	40	0.6	0.2	5	2.7	1.0	5	10.5	1.9	5
Cell diameter (μm)	14	3.3	0.1	6	4.3	0.1	6			
	18	3.3	0.1	6	4.2	0.1	6			
	27	3.3	0.1	6	4.3	0.1	6			
	31	3.4	0.1	7	4.9	0.2	7			
	36	3.4	0.1	6	4.5	0.1	6			
	40	3.9	0.2	5	4.4	0.1	5			

Continuous cultures in steady-state at salinities 14, 18, 27, 31, 36, and 40 ppt had similar growth rates that were between 1.90 and 1.99 div/d with a 1.97 ± 0.03 div/d mean but the culture at 9 ppt had a lower growth rate of 1.62 div/d. The averages of several steady-state IVF readings for the 14 to 40 ppt cultures were not significantly correlated with salinity (main text Table 1) and were between 195 ± 13 and 352 ± 24 fsu with a 244 ± 57 fsu mean (main text Table 2). The averages of 4 to 7 steady-state subsamples for cell density, diameter, and volume did not show any correlation with salinity (main text Table 1). Average steady-state cell density ranged from 0.6 - 1.5 x 10^5 cells/ml with a 1.2 ± 0.3 x 10^5 cells/ml mean. Average steady-state cell diameter was between 3.3 - 3.9 μm with a 3.4 ± 0.2 μm mean. Average steady-state cell volume was between 16 -25 μm^3 with a 20 ± 3 μm^3 mean (main text Table 2). The average steady-state per cell Chl *a* content ranged from 0.6 - 1.9 pg/cell with a 0.9 ± 0.2 pg/cell mean and was uncorrelated to salinity (main text Table 1).

The averages of 4 steady-state subsamples for residual nutrient concentrations in the culture media (**Table S3**) were 591 ± 42 μM for NO_3^-, 18 ± 1 μM for PO_4^{-3}, 3 ± 1 μM for NO_2^-,

and 0.3 ± 0.1 μM for NH_4^-, and were uncorrelated with salinity (main text Table 1, **Table S4**). Average concentrations of residual $Si(OH)_4$ in the media decreased significantly with salinity (R^2=0.87, P=0.01) (**Table S4**) and were between 37 and 6 μM (**Table S3**). Per cell residual $Si(OH)_4$ calculations were also significantly correlated with salinity (main text Table 1, **Fig. S2**) and averages ranged from 9.8 to 36.1 μg/cell with a 20 ± 11 μg/cell mean.

Per cell lipid concentrations (pg/cell) were uncorrelated with salinity (main text Table 1). The sterol (24-methyl-cholesta-5,24(28)-dien-3β-ol) was the least abundant compound ranging from 0.2 - 1.0 pg/cell with a 0.5 ± 0.25 pg/cell mean. Fatty acids were approximately an order of magnitude more abundant, palmitic acid ($C_{16:0}$) content ranged from 1.0 - 15.1 pg/cell with a 5.3 ± 4.92 pg/cell mean; palmitoleic acid ($C_{16:1}$) content ranged from 0.9 - 14.3 pg/cell with a 4.2 ± 4.73 pg/cell mean; myristic acid ($C_{14:0}$) content ranged from 1.7 - 6.8 pg/cell averaged 3.2 ± 2.00 pg/cell mean (main text Table 3). Trace amounts of C_{15} and C_{18} fatty acids and 24-methylcholesterol were detected in some samples.

As discussed in the main text, the $\alpha_{lipid\text{-}water}$-salinity relationship changed slightly for fatty acids when the lower growth rate culture grown at 9ppt was added. The $\alpha_{lipid\text{-}water}$-salinity relationship remained the same for the sterol (**Fig. S3**). Instrument settings for quantification, identification, and lipid hydrogen isotope ratios (Sachs et al., 2016) are provided in **Table S5**.

Residual silica

All the residual nutrient concentrations taken during the last 2-3 days of steady-state from the continuous cultures are reported in **Table S3**. Residual silica changed significantly with salinity (**Fig. S2**) when normalized to cell density (main text Table 1) and also when not normalized (**Table S4**). The significant decrease in residual $Si(OH)_4$ suggests that cells grown in

higher salinity treatments used more silica. It is unlikely that high salinity media caused silica to precipitate out (Morris et al., 1976). Since cell volume or diameter did not significantly change (**Table S4**), cellular silica must have accumulated as intracellular soluble silica, or must have been incorporated in thicker (but not larger) frustules at higher salinities.

Table S3. Average residual nutrients for each continuous culture salinity treatment. The average of 4 subsamples taken during steady state is reported with standard deviations. Compare to feed media concentrations 882 µM NO_3^-, 36 µM PO_4^{-3}, and 106 µM $Si(OH)_4$.

Salinity	NO_3^- (µM)	SD	PO_4^{-3} (µM)	SD	NO_2^- (µM)	SD	NH_4^+ (µM)	SD	$Si(OH)_4$ (µM)	SD
14	571	133	19	5	5	1	0.5	0.3	34	7
18	601	161	20	5	3	1	0.2	0.2	37	6
27	651	102	18	4	3	1	0.3	0.3	19	6
31	522	133	19	5	3	1	0.2	0.1	20	3
36	598	116	18	4	3	0	0.3	0.3	19	7
40	604	57	17	2	4	1	0.3	0.4	6	3

Several studies of higher plants (Liang et al., 2007) suggest that silica may alleviate salinity stress. Diatoms grown at high salinity might likewise accumulate more soluble silica if their cellular processes can be enhanced or protected. It has been proposed that diatoms may use internal soluble silica to assist with cellular processes (Medlin, 2002), so it is conceivable that increased silica uptake at higher salinity treatments is due to an increased demand for internal cellular silica. Additionally, a greater concentration of Na^+ ions is present in high salinity media and silicate transport relies on Na^+ gradient, at least in the diatom *Nitzschia alba* (Bhattacharyya and Volcani, 1980), thus more silica may be transported into intracellular space regardless of demand.

Alternatively diatoms may incorporate more silica into their frustules at higher salinities. Salinity has been shown to influence frustule morphology and rigidity (Bussard et al., 2017; La Vars et al., 2013; Vrieling et al., 2007). Several diatom batch culture studies suggest that frustules are built denser or with more silica in fresher water (Leterme et al., 2010; Olsen and

Paasche, 1986; Tuchman et al., 1984; Vrieling et al., 2007, 1999), or get longer-but not wider (Hildebrand et al., 2006), all contrary to the findings of this study. Since it is impossible to achieve steady state growth conditions in batch culture format, continuous culture results are not comparable to previous batch cultures especially since a study using chemostats (Paasche, 1973) found a different silica-frustule relationship compared to a study using batch cultures (Olsen and Paasche, 1986).

Although our cultures had less residual silica in the media at high salinity, this is not likely related to the lipid-media $^{2}H/^{1}H$ fractionation because non-siliceous species also had decreased fractionation at increased salinity (Chivall et al., 2014; Heinzelmann et al., 2015a; Kasper, 2015; M'Boule et al., 2014; Nelson and Sachs, 2014; Sachs et al., 2016; Sachs and Schwab, 2011; Sachse and Sachs, 2008; Schouten et al., 2006). Furthermore, silica metabolism is independent of other major metabolic pathways and not necessarily related to the hydrogen isotopic composition of organic matter.

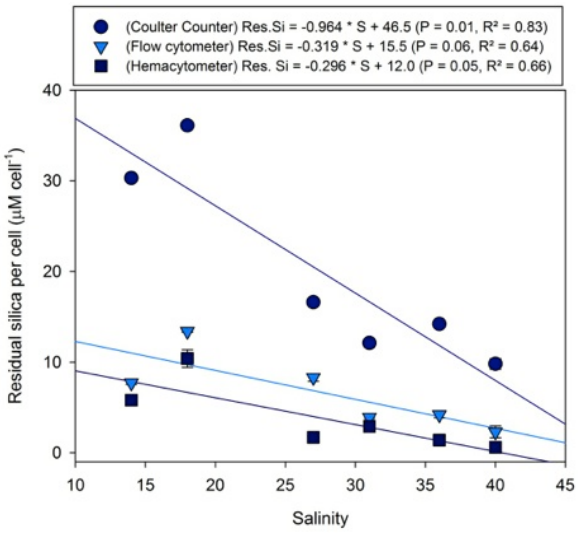

Fig. S2. Residual silica/cell versus salinity calculated with three different cell density measurements.

Table S4. Linear regression slope coefficients of culture parameters on salinity and their standard error (SE). Slopes with P values less than 0.05 are in bold.

Parameter	R^2	Slope	SE	P
Specific Growth Rate (/d)	0.40	0.0	0.0	0.18
Cell Density Coulter Counter ($x10^5$ cells/ml)	0.01	0.00	0.02	0.86
Cell Density Flow Cytometer ($x10^5$ cells/ml)	0.00	0.00	0.06	0.98
Cell Density Hemacytometer ($x10^5$ cells/ml)	0.56	0.3	0.1	0.09
Cell Diameter Coulter Counter (μm)	0.54	0.02	0.01	0.09
Cell Diameter Flow Cytometer (μm)	0.26	0.01	0.01	0.30
Cell Volume (μm^3)	0.50	0.23	0.01	0.12
Chl *a* (μg/l)	0.88	2.10	0.40	**0.01**
Residual NO_3^- (μM)	0.00	0	2	0.92
Residual PO_4^{-3} (μM)	0.54	-0.07	0.03	0.10
Residual NO_2^- (μM)	0.12	-0.03	0.05	0.51
Residual NH_4 (μM)	0.14	0.00	0.01	0.46
Residual $Si(OH)_4$ (μM)	0.87	-1.0	0.2	**0.01**

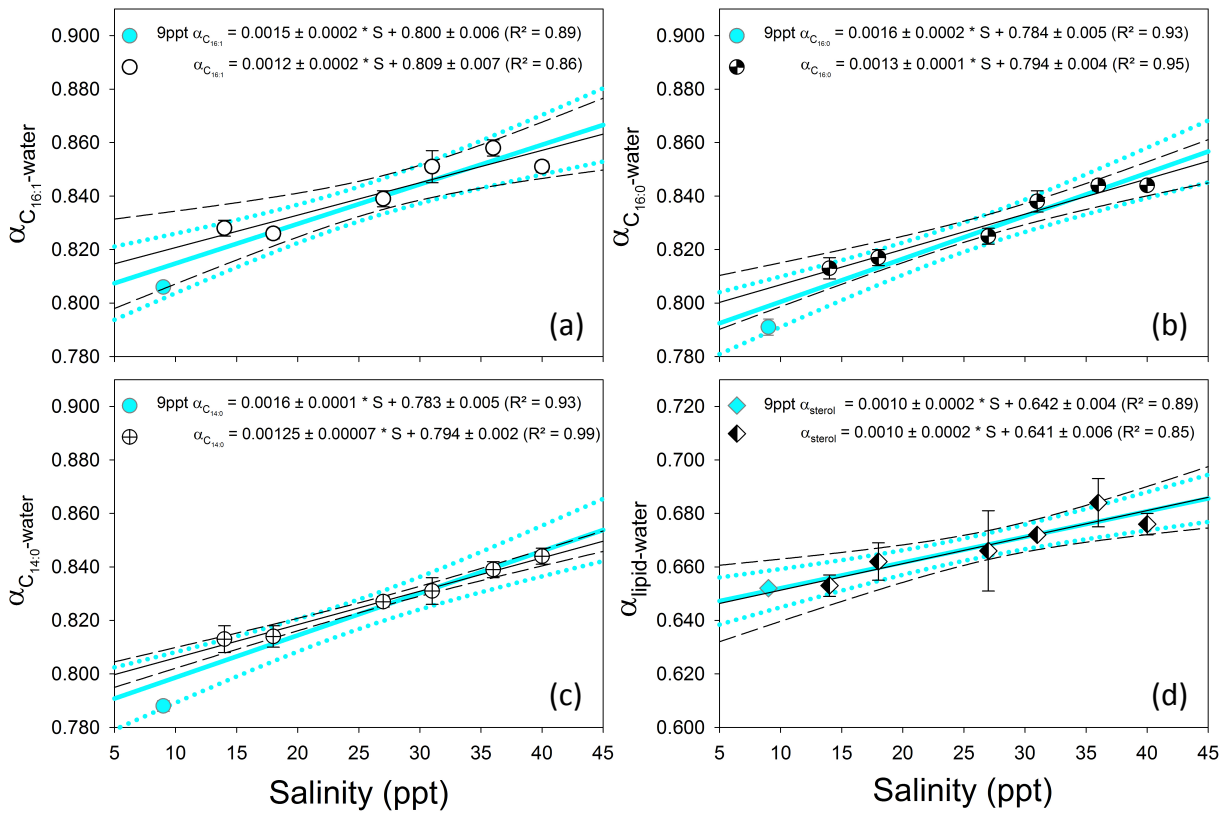

Fig. S3: Apparent fractionation factors, $\alpha_{lipid\text{-}water}$, for *T. pseudonana.* Linear regressions are for all cultures 9 to 40 ppt (cyan symbols, cyan lines, and cyan dotted 95% confidence interval, n = 7) and for just the 14 to 40 ppt cultures (black symbols, black lines, and black dashed 95% confidence interval, n = 6). Error bars represent propagated standard deviations of 3 δ^2H_{water} and 3-6 δ^2H_{lipid} injections (except for the 9 ppt sterol data point which only had one injection).

Table S5. Settings for GC-FID (a), GC-MS (b), and GC-IRMS (c) used in this study.

(a) Identification: Gas chromatography-flame ionization (GC-FID) settings		
Gas chromatograph	Agilent GC 6890N	(Agilent Tech., Santa Clara, CA, USA)
Autosampler	Agilent 7683 autosampler	
Inlet	Programmable temperature vaporization inlet operated in splitless mode, 300 °C	
Carrier gas	He (1.3 ml/min)	
Column	Agilent DB-5 ms capillary column (60 m × 0.32 mm × 0.25 μm)	(Agilent Tech., Santa Clara, CA, USA)
Detector	Flame ionization detector	
Oven Program	Hold 110 °C 4 min; ramp to 150 °C at 15 °C/min; ramp to 320 °C at 6 °C/min; hold 28 min	
(b) Quantification: Gas chromatography-mass spectrometry (GC-MS) settings		
Gas chromatograph	Agilent GC 6890N	(Agilent Tech., Santa Clara, CA, USA)
Autosampler	Agilent 7683 autosampler	
Inlet	Programmable temperature vaporization inlet operated in splitless mode, 300 °C	
Carrier gas	He (1.5 ml/min)	
Column	VF-17 ms capillary column (60 m × 0.32 mm × 0.25 μm column (60 m × 0.32 mm × 0.25 μm)	(Agilent Tech., Santa Clara, CA, USA formally Varian Inc.)
Detector	Agilent 5975 inert mass selective detector	(Agilent Tech., Santa Clara, CA, USA)
Oven Program (non-polar fractions)	Ramp from 110 °C to 280 °C at 15 °C/min; hold 40 min; ramp to 320 °C at 3 °C/min; hold 10 min	
Oven Program (polar fractions)	Ramp from 110 °C to 150 °C at 15 °C/min; ramp to 320 °C at 6 °C/min; hold 24 min	
(c) Isotopic Composition: Gas-chromatography isotope-ratio mass spectrometry (GC-IRMS) settings		
Gas chromatograph	Trace Ultra GC II	(Thermo Fisher Scientific, Waltham, MA, USA)
Autosampler	Thermo TRIPLUS	
Inlet	Split-splitless injector operated in splitless mode at 325 °C	
Carrier gas	He (1.5 ml/min)	
Pyrolysis	1400 °C ceramic reactor	(1.5 mm OD x 0.55 mm ID x 320 mm long)
IRMS	Thermo DELTA V PLUS IRMS	
Column (non-polar fractions)	VF-17 ms capillary column (60 m × 0.32 mm × 0.25 μm)	(Agilent Tech., Santa Clara, CA, USA formally Varian Inc.)
Oven Program (non-polar fractions)	Hold 120 °C for 10 min; ramp to 220 °C at 20 °C/min; ramp to 300 °C at 2 °C/min; ramp to 325 °C at 10 °C/min; hold 5 min	
H_3^+ factor (non-polar fractions)	4.2±0.1 ppm/mV (n = 8 days)	(Sessions et al., 2001)
Column (polar fractions)	Agilent DB-5 ms capillary column (60 m × 0.32 mm × 0.25 μm)	
Oven Program (polar fractions)	Hold 120 °C for 10 min; ramp to 180 °C at 20 °C/min; ramp to 325 °C at 3 °C/min; hold 11 min	
H_3^+ factor (polar fractions)	4.9±0.1 ppm/mV (n = 5 days)	(Sessions et al., 2001)
External Standards	*n*C21-alkane (-214.7±2.0‰), *n*C23-alkane (-48.8±1.4‰), *n*C26-alkane (-54.9±1.5‰), *n*C32-alkane (-212.4±1.0‰), *n*C34-alkane (-231.8±1.4‰), and *n*C38-alkane (-102.6±1.3‰)	Dr. Arndt Schimmelmann

MODEL DETAILS

The reduction of $NADP^+$ to NADPH via ferredoxin-$NADP^+$ reductase in photosystem 1 (PS1) uses hydrogen from intracellular water and is associated with a large normal isotope effect and an estimated fractionation factor of 0.4 (Luo et al., 1991; Schmidt et al., 2003). The metabolic reduction of $NADP^+$ to NADPH uses carbon-bound hydrogen and is likely associated with a normal isotope effect with a fractionation factor estimated to be 0.75 (Sachs and Kawka, 2015; Schmidt et al., 2003). Biosynthetic hydrogen sourced from isotopically distinct pools of NAD(P)H has been identified as a key mechanism responsible for lipid-water $^2H/^1H$ variations in microbes with different metabolisms (Dawson et al., 2015; Dirghangi and Pagani, 2013a, 2013b; Heinzelmann et al., 2015b; Osburn et al., 2011; X. Zhang et al., 2009) and between green and non-photosynthesizing plant organs (Gamarra and Kahmen, 2015). Sachs and Kawka (2015) extended this principal to explain decreased lipid-water $^2H/^1H$ fractionation at low growth rates and Sachs et al. (2016) suggested that high salinities could also influence biosynthetic preferences for isotopically distinct pools of NAD(P)H. A 3-endmember model (Sachs et al., 2016; Sachs and Kawka, 2015) demonstrated that photoautotroph δ^2H_{Lipid} is sensitive to the relative proportions of hydrogen from water, photosynthetically reduced NADPH, and metabolically reduced NADPH. The model illustrated that for lipids (i) more hydrogen from water versus NADPH results in ^2H-enrichment and (ii) more metabolic versus photosynthetic NADPH results in ^2H-enrichement.

Using these starting principles we developed a 6-box stationary model that characterizes basic hydrogen cycling in a population of photoautotrophic cells grown in 24-hr light. The only "endmember" in this model is the Media pool with a constant isotopic composition. All 5 cellular pools of hydrogen are free to vary in response to changes in flux sizes. Steady-state in this model

physiologically means that catabolic processes are as important as biosynthetic processes for moving hydrogen in and out of the "Other Organics" and "Lipids" boxes. This section outlines the assumptions and design of the new 6-box model and explains in detail the fluxes and the metabolic parameters that are tested to examine the sensitivity of cellular pools of hydrogen. The default values and ranges of the six testable metabolic parameters are summarized in **Table S6** and the calculated fluxes are summarized in **Table S7**.

All the fluxes represent biosynthetic, equilibrium exchange, or catabolic processes responsible for moving hydrogen in and out of cellular pools or in and out of cells. "Lipids" synthesis is modeled after fatty acids where 50% hydrogen is from NAD(P)H, 25% from cell water, and 25% from acetyl-CoA (Robins et al., 2003; Saito et al., 1980; Schmidt et al., 2003). Some fatty acid synthesis enzymes use either NADH or NADPH (Marrakchi et al., 2002), which is why we include NADH in the "Metabolic NAD(P)H" box. For "Other Organics" (synthesized via a number of processes using cell water, photosynthetic NADPH, and metabolic NAD(P)H) a large variety of catabolic reactions reduce $NAD(P)^+$ and return hydrogen to cell water. Lipid catabolism during the β-oxidation process is represented by 3 fluxes of total hydrogen to "Cell Water", "Metabolic NAD(P)H", and "Other Organics" according to set stoichiometric proportions (Buchanan et al., 2015).

PS1 vs. MET Parameter (x)

The flux of hydrogen from "Cell Water" to "Photosynthetic NADPH" during photosynthesis (J_{Wat_PS1}) is balanced by biosynthesis of "Lipids" and "Other Organics". The proportions of these biosynthetic fluxes are determined by the PS1 vs. MET parameter *x* such that $J_{PS1\_Lip} = J_{Wat\_PS1} * x$ and $J_{PS1\_Org} = J_{Wat\_PS1} * (1-x)$. Likewise catabolic production of

"Metabolic NAD(P)H" is balanced by two fluxes proportional to x such that $J_{MET\_Lip} = J_{Org\_MET} * (1\text{-}x)$ and $J_{MET\_Org} = J_{Org\_MET} * x + J_{CAT\_Lip\_Met}$. We adopt a default value $x = 0.5$ so "Lipids" and "Other Organics" receive equal fluxes of hydrogen from "Photosynthetic NADPH" and "Metabolic NAD(P)H" (with the exception of "Other Organics" which has a slightly larger flux from metabolic NAD(P)H to balance lipid β-oxidation). An increase in $1\text{-}x$ (or decrease in x) results in a larger flux of hydrogen from metabolic NAD(P)H to "Lipids" and more photosynthetic NADPH to "Other Organics" (**Fig. S4**). This causes lipid-media $^2H/^1H$ fractionation to decrease ($\alpha_{Lipids\text{-}Media}$ approaches unity) as δ^2H_{Lipids} becomes ^2H-enriched and causes organics-media $^2H/^1H$ fractionation to decrease ($\alpha_{OtherOrganics\text{-}Media}$ moves away from unity) as $\delta^2H_{OtherOrganics}$ becomes ^2H-depleted. $\delta^2H_{CellWater}$ is not significantly changed as $1\text{-}x$ varies from zero to unity (**Fig. S5a**).

Metabolic Reductant Parameter (M)

The metabolic production of NAD(P)H (J_{Org_MET}) is related to photosynthesis (J_{Wat_PS1}) by the "Metabolic Reductant Parameter" ($J_{Org\_MET} = J_{Wat\_PS1} * M$). We adopt a default value of $M = 1$, implying that the flux of metabolic NAD(P)H is equal photosynthetic NADPH, while exploring the range $0 < M < 10$. As M increases, so does any flux related to J_{Org_MET} including synthesis of "Lipids" and "Other Organics" using metabolic NAD(P)H (J_{MET_Lip} and J_{MET_Org}), cell water ($J_{BIO\_Wat\_Org}$, $J_{BIO\_Wat\_Lip}$), and organics ($J_{BIO\_Org\_Lip}$), and also catabolism to maintain steady-state ($J_{CAT\_Org\_Wat}$, $J_{CAT\_Lip\_Wat}$, $J_{CAT\_Lip\_Met}$, $J_{CAT\_Lip\_Org}$) (**Fig. S4**). Therefore, increasing M is analogous to increasing metabolic recycling without a change in photosynthesis. **Figure S5b** illustrates that as M increases, fractionation decreases ($\alpha_{Organics\text{-}Media}$ approaches unity) and changing M has very little influence on $\delta^2H_{CellWater}$.

Biosynthetic Cell Water Parameter (B)

$J_{BIO\_Wat\_Org}$ represents enzymatic transfer of hydrogen from "Cell Water" to "Other Organics" during biosynthesis. The biosynthetic incorporation of cell-water-hydrogen is related to the combined NAD(P)H fluxes by *B*, the "Biosynthetic Cell Water Parameter" ($J_{BIO\_Wat\_Org} = (J_{PS1\_Org} + J_{MET\_Org}) * B$). Since half of the hydrogen in 3-C sugars (i.e., glyceraldehyde-3-phosphate (GAP)) emanating from the Calvin-Benson cycle appears to come directly from intracellular water (Buchanan et al., 2015) a default value of $B = 1$ is used to indicate that equal amounts of cell-water-hydrogen and combined NAD(P)H hydrogen are incorporated into organics. To maintain steady-state, changing *B* also changes the mass balance catabolism flux ($J_{CAT\_Org\_Wat}$).

Equilibrium Exchange Parameter (E)

Equilibrium exchange between cell-water-hydrogen and organic-hydrogen is related to photosynthesis by the "Equilibrium Exchange Parameter" ($J_{eq\_Org\_Wat} = J_{eq\_Wat\_Org} = J_{Wat\_PS1} * E$). Equilibrium exchange of hydrogen between intracellular water and organic material occurs readily with hydrogen in carboxyl, hydroxyl, amide, amine, thiol and sulfide groups, as well as with the alpha hydrogen of carbonyl groups via keto-enol tautomerism. This exchange can be relatively fast compared to biosynthetic processes (García-Martín et al., 2001). A default value of $E = 1$ represents what we consider to be the lower limit of equilibrium exchange and means that the equilibrium exchange fluxes are the same size as the total photosynthetic flux. Increasing *E* has the same impact as increasing *B* (**Fig. S5c**), but is a chemically distinct way to incorporate cell-water-hydrogen into biochemicals. Changes in both *B* and *E* have minimal impact on

$\delta^2H_{CellWater}$ (**Fig. S5c**). **Figure S6** illustrates how $\alpha_{Lipids\text{-}Media}$ can be influenced if equilibrium exchange or biosynthetic incorporation of cell water were associated with fractionation factors.

Table S6. Metabolic parameters

Tested metabolic parameters	*Symbol*	*Range*	*Default*	*Notes*
PSI versus MET NAD(P)H Parameter	***x***	0 - 1	0.5	Determines amount of lipid-hydrogen and other-organic-hydrogen sourced from photosynthetic NADPH (vs. metabolic NAD(P)H); analogous to "*x*" (Sachs and Kawka, 2015; Sachs et al. 2016)
Metabolic Reductant Parameter	***M***	0 - 10	1	Determines flux size of metabolic NAD(P)H relative to the flux of photosynthesis
Biosynthetic Cell Water Parameter	***B***	0 - 10	1	Determines amount of organic-hydrogen sourced from cell-water-hydrogen relative to photosynthetic and metabolic NAD(P)H; comparable to "1-*f*" (Sachs and Kawka, 2015; Sachs et al. 2016)
Equilibrium Exchange Parameter	***E***	0 - 10	1	Determines size of equilibrium hydrogen flux between cell-water-hydrogen and organic-hydrogen relative to the flux of photosynthesis
Hydrogen Transport Parameter	***HT***[a]	0.03 - 1	1	Determines flux of media-hydrogen (as water or protons) into cells relative to the flux of photosynthesis
Percent Extracellular Release	***PER***	0 - 0.7	0.03	Determines percent of hydrogen release relative to the flux of photosynthesis (Sharp, 1977; Smith and Platt, 1984)

[a] *HT* can't be smaller than *PER* otherwise fluxes become negative if more organic-hydrogen is released than is taken in from media

Hydrogen Transport Parameter (HT)

The "Hydrogen Transport Parameter" ($J_{in} = J_{Wat\_PS1} * HT$) determines the flux size of hydrogen from "Media" to "Cell Water" compare to photosynthesis. Hydrogen enters cells as water (via diffusion or aquaporin transport) or as protons via Na^+/H^+ antiport proteins (Rai et al., 2013a). A default value $HT = 1$ indicates that the flux of hydrogen entering cells is equal to photosynthesis. Changing *HT* also changes the amount of hydrogen exiting cells (J_{out}) to maintain steady-state. When the exchange flux of hydrogen between cells and the environment is restricted to less than the photosynthetic flux of hydrogen (i.e. when $HT < 1$), lipid-water $^2H/^1H$

fractionation decreases ($\alpha_{Organics\text{-}Media}$ approached unity) and both $\delta^2H_{OtherOrganics}$ and $\delta^2H_{CellWater}$ get more ^{2}H-enriched as *HT* approaches zero (**Fig. S5d**).

Table S7. Fluxes calculated according to assumed relation to metabolic parameters and steady-state mass balance

Process	*Hydrogen Flux*	*Equation*
Biosynthetic & catabolic:		
Photosynthetic production of NADPH	J_{Wat_PSI}	= 1 (arbitrary constant)
Metabolic production of NAD(P)H	J_{Org_MET}	= J_{Wat_PSI} * ***M***
Lipid biosynthesis using photosynthetic NADPH	J_{PS1_Lip}	= J_{Wat_PSI} * ***x***
Other biosynthesis using photosynthetic NADPH	J_{PS1_Org}	= J_{Wat_PSI} * (1 − ***x***)
Lipid biosynthesis using metabolic NAD(P)H	J_{MET_Lip}	= $J_{CAT\_Lip\_MET}$ + J_{Org_MET} * (1 − ***x***)
Other biosynthesis using metabolic NAD(P)H	J_{MET_Org}	= J_{Org_MET} * ***x***
Lipid biosynthesis using cell-water-hydrogen	$J_{BIO\_Wat\_Lip}$	= (J_{PS1_Lip} + J_{MET_Lip}) * 0.5
Other biosynthesis using cell-water-hydrogen	$J_{BIO\_Wat\_Org}$	= (J_{PS1_Org} + J_{MET_Org}) * ***B***
Lipid biosynthesis using organic-hydrogen	$J_{BIO\_Org\_Lip}$	= (J_{PS1_Lip} + J_{MET_Lip}) * 0.5
H^+ produced during β-carboxylation	$J_{CAT\_Lip\_Wat}$	= ($J_{BIO\_Org\_Lip}$ + J_{MET_Lip} + J_{PSI_Lip} + $J_{BIO\_Wat\_Lip}$ − $J_{release\_Lip}$) * 0.2
NADH produced during β-carboxylation	$J_{CAT\_Lip\_MET}$	= ($J_{BIO\_Org\_Lip}$ + J_{MET_Lip} + J_{PSI_Lip} + $J_{BIO\_Wat\_Lip}$ − $J_{release\_Lip}$) * 0.2
Organics produced during β-carboxylation	$J_{CAT\_Lip\_Org}$	= ($J_{BIO\_Org\_Lip}$ + J_{MET_Lip} + J_{PSI_Lip} + $J_{BIO\_Wat\_Lip}$ − $J_{release\_Lip}$) * 0.6
Water produced during catabolism	$J_{CAT\_Org\_Wat}$	= J_{MET_Org} + $J_{CAT\_Lip\_Org}$ + $J_{BIO\_Wat\_Org}$ + J_{PS1_Org} − $J_{release\_Org}$ − $J_{release\_Lip}$ − $J_{BIO\_Org\_Lip}$
Non-biosynthetic:		
Equilibrium exchange from cell-water to organics	$J_{eq\_Wat\_Org}$	= J_{Wat_PSI} * ***E***
Equilibrium exchange from organics to cell-water	$J_{eq\_Org\_Wat}$	= J_{Wat_PSI} * ***E***
Release of lipid-hydrogen as exudates	$J_{release\_Lip}$	= (J_{Wat_PSI} * ***PER***) * 0.2
Release of organic-hydrogen as exudates	$J_{release\_Org}$	= (J_{Wat_PSI} * ***PER***) * 0.8
Transport/diffusion of media-H into cells	J_{in}	= J_{Wat_PSI} * ***HT***
Transport/diffusion of cell-H out of cells	J_{out}	= J_{in} + $J_{CAT\_Org\_Wat}$ + $J_{CAT\_Lip\_Wat}$ − J_{Wat_PSI} − $J_{BIO\_Wat\_Org}$ − $J_{BIO\_Wat\_Lip}$

Percent Extracellular Release (PER)

Finally, $J_{release\_Org}$ and $J_{release\_Lip}$ represent the loss of lipid and organic hydrogen via exudation. "Percent Extracellular Release" is a parameter that determines how much organic material is expelled by the culture ($J_{release\_Org}$ + $J_{release\_Lip}$ = J_{Wat_PS1} * *PER*). Compiled reports from several exponentially growing cultures found that on average *PER* is 5% of autotrophically produced products (Nagata, 2000). Two reports for *T. pseudonana* indicated slightly lower percentages of 1.2-4% (Sharp, 1977; Smith and Platt, 1984) prompting the use of 3% as the default value in the model. A value of *PER* = 0.03 indicates that the flux of organic hydrogen

that leaves the cells is 3% the flux of hydrogen used to make photosynthetic NADPH. Of this we estimate that 20% of the exudates are derived from the lipid pool (Emerson and Hedges, 2008; Thornton, 2014). As cellular hydrogen loss via exudates (*PER*) increases, $^{2}H/^{1}H$ fractionation decreases ($\alpha_{Organics\text{-}Media}$ approaches unity) with a concomitant ^{2}H-enrichment of intracellular water (**Fig. S5e**).

Model Equations

The following six steady-state equations describe the mass balance of the nineteen fluxes of total hydrogen ($^{2}H+^{1}H$) between the six boxes:

$$\frac{\partial h_{Media}}{\partial t} = J_{out} + J_{release\_Org} + J_{release\_Lip} - J_{in} = 0 \quad (1)$$

$$\frac{\partial h_{Wat}}{\partial t} = J_{in} + J_{eq\_Org\_Wat} + J_{CAT\_Org\_Wat} + J_{CAT\_Lip\_Wat} - J_{out} - J_{eq\_Wat\_Org} - J_{BIO\_Wat\_Org} - J_{BIO\_Wat\_Lip} - J_{Wat\_PS1} = 0 \quad (2)$$

$$\frac{\partial h_{Org}}{\partial t} = J_{eq\_Wat\_Org} + J_{BIO\_Wat\_Org} + J_{CAT\_Lip\_Org} + J_{PS1\_Org} + J_{MET\_Org} - J_{eq\_Org\_Wat} - J_{CAT\_Org\_Wat} - J_{Org\_MET} - J_{release\_Org} = 0 \quad (3)$$

$$\frac{\partial h_{Lip}}{\partial t} = J_{BIO\_Org\_Lip} + J_{BIO\_Wat\_Lip} + J_{PS1\_Lip} + J_{MET\_Lip} - J_{CAT\_Lip\_Org} - J_{CAT\_Lip\_Wat} - J_{CAT\_Lip\_MET} - J_{release\_Lip} = 0 \quad (4)$$

$$\frac{\partial h_{PS1}}{\partial t} = J_{Wat\_PS1} - J_{PS1\_Lip} - J_{PS1\_Org} = 0 \quad (5)$$

$$\frac{\partial h_{MET}}{\partial t} = J_{Org\_MET} + J_{CAT\_Lip\_MET} - J_{MET\_Lip} - J_{MET\_Org} = 0 \quad (6)$$

Where h_{Media}, h_{Wat}, h_{Org}, h_{Lip}, h_{PS1}, and h_{MET} indicate the mass of hydrogen in each box. The next six equations describe the steady state isotopic composition of each box where R is the $^{2}H/^{1}H$ ratio and each flux is paired with a fractionation factor, α:

$$\frac{\partial R_{Media}}{\partial t} * h_{Media} = J_{out}\alpha_{out}R_{Wat} + J_{release\_Org}\alpha_{release\_Org}R_{Org} + J_{release\_Lip}\alpha_{release\_Lip}R_{Lip} - J_{in}\alpha_{in}R_{Media} = 0 \quad (7)$$

$$\frac{\partial R_{Wat}}{\partial t} * h_{Wat} = J_{in}\alpha_{in}R_{Media} + J_{eq\_Org\_Wat}\alpha_{eq\_Org\_Wat}R_{Org} + J_{CAT\_Org\_Wat}\alpha_{CAT\_Org\_Wat}R_{Org} + J_{CAT\_Lip\_Wat}\alpha_{CAT\_Lip\_Wat}R_{Lip} - R_{Wat} * (J_{out}\alpha_{out} + J_{eq\_Wat\_Org}\alpha_{eq\_Wat\_Org} + J_{BIO\_Wat\_Org}\alpha_{BIO\_Wat\_Org} + J_{BIO\_Wat\_Lip}\alpha_{BIO\_Wat\_Lip} + J_{Wat\_PS1}\alpha_{PS1}) = 0 \quad (8)$$

$$\frac{\partial R_{Org}}{\partial t} * h_{Org} = J_{eq\_Wat\_Org}\alpha_{eq\_Wat\_Org}R_{Wat} + J_{BIO\_Wat\_Org}\alpha_{BIO\_Wat\_Org}R_{Wat} + J_{CAT\_Lip\_Org}\alpha_{CAT\_Lip\_Org}R_{Lip} + J_{PS1\_Org}\alpha_{PS1\_Org}R_{PS1} + J_{MET\_Org}\alpha_{MET\_Org}R_{MET} - R_{Org} * (J_{BIO\_Org\_Lip}\alpha_{BIO\_Org\_Lip} + J_{eq\_Org\_Wat}\alpha_{eq\_Org\_Wat} + J_{CAT\_Org\_Wat}\alpha_{CAT\_Org\_Wat} + J_{Org\_MET}\alpha_{MET} + J_{release\_Org}\alpha_{release\_Org}) = 0 \quad (9)$$

$$\frac{\partial R_{Lip}}{\partial t} * h_{Lip} = J_{BIO\_Org\_Lip}\alpha_{BIO\_Org\_Lip}R_{Org} + J_{BIO\_Wat\_Lip}\alpha_{BIO\_Wat\_Lip}R_{Wat} + J_{PS1\_Lip}\alpha_{PS1\_Lip}R_{PS1} + J_{MET\_Lip}\alpha_{MET\_Lip}R_{MET} - R_{Lip} * (J_{CAT\_Lip\_Org}\alpha_{CAT\_Lip\_Org} + J_{CAT\_Lip\_Wat}\alpha_{CAT\_Lip\_Wat} + J_{release\_Lip}\alpha_{release\_Lip} + J_{Cat\_Lip\_MET}\alpha_{Cat\_Lip\_MET}) = 0 \quad (10)$$

$$\frac{\partial R_{PS1}}{\partial t} * h_{PS1} = J_{Wat\_PS1}\alpha_{PS1}R_{Wat} - R_{PS1} * (J_{PS1\_Org}\alpha_{PS1\_Org} + J_{PS1\_Lip}\alpha_{PS1\_Lip}) = 0 \quad (11)$$

$$\frac{\partial R_{MET}}{\partial t} * h_{MET} = J_{Org\_MET}\alpha_{MET}R_{Org} + J_{Cat\_Lip\_MET}\alpha_{Cat\_Lip\_MET}R_{Lip} - R_{MET} * (J_{MET\_Org}\alpha_{MET\_Org} + J_{MET\_Lip}\alpha_{MET\_Lip}) = 0 \quad (12)$$

Since $\delta^2H_{Media} = 0‰$, $R_{Media} = (155.76 \pm 0.05) \times 10^{-6}$ (Hagemann et al., 1970). To determine R_{Wat}, R_{PS1}, R_{MET}, R_{Lip}, and R_{Org}, the fluxes were calculated algebraically (using eqns. 1-6 and the assumptions described in **Table S7** using default values in **Table S6**) and then the linear system of equations describing the isotope composition of each box (eqns. 7-12) was solved using standard matrix solving procedures in MATLAB™. Finally R_{Wat}, R_{PS1}, R_{MET}, R_{Lip}, and R_{Org} were converted to $\delta^2H_{CellWater}$, δ^2H_{PS1}, δ^2H_{MET}, δ^2H_{Lipids}, and $\delta^2H_{OtherOrganics}$. Code for this model can be found at: https://doi.org/10.5281/zenodo.153986.

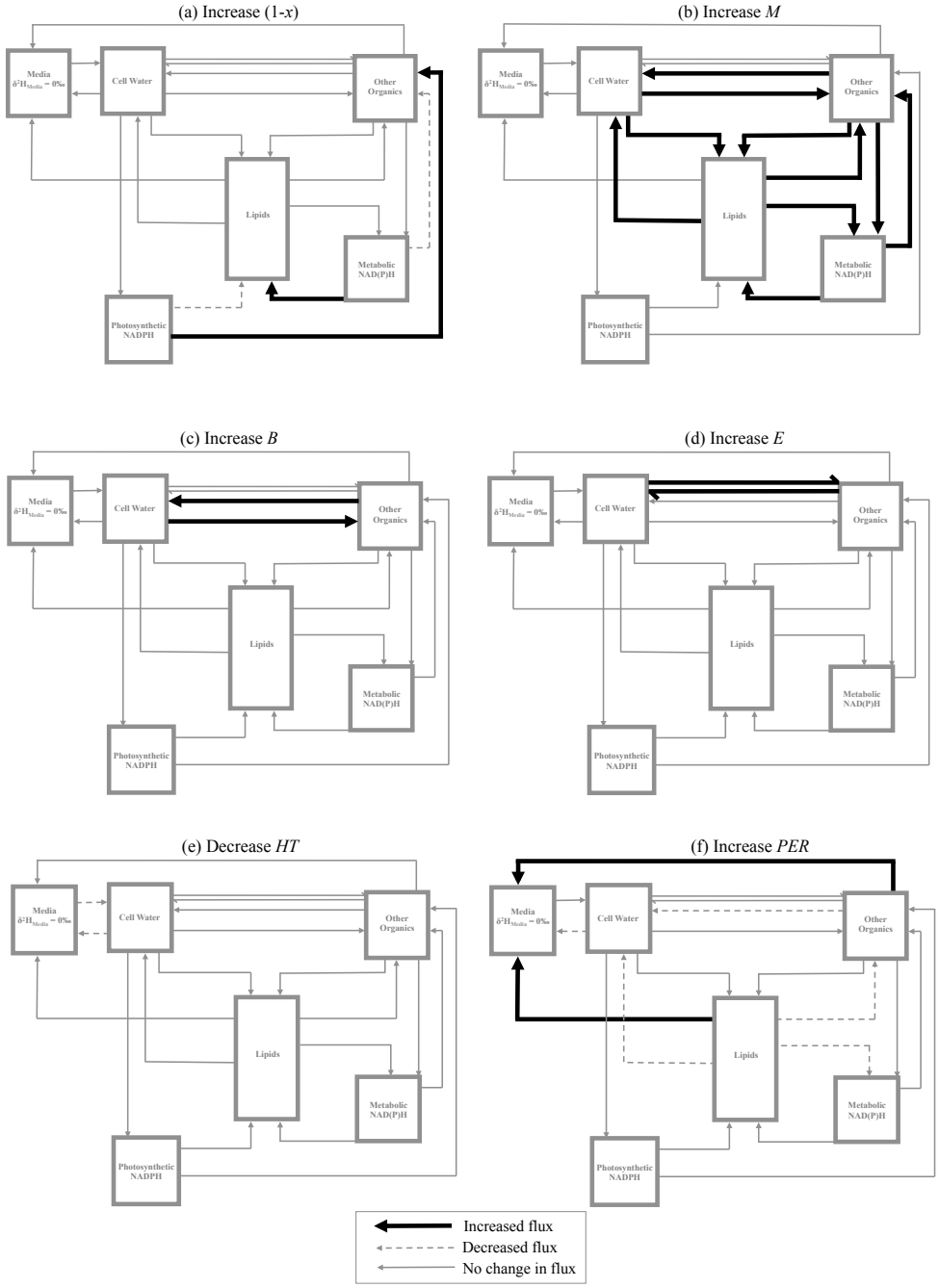

Fig. S4. Schematic that shows sign of change (increase in bold, decrease in dotted, and no change in grey) when the metabolic parameters vary: (a) 1-*x* = PSI vs MET NAD(P)H Parameter, (b) *M* = Metabolic Reductant Parameter, (c) *B* = Biosynthetic Cell Water Parameter, (d) *E* = Equilibrium Exchange Parameter, (e) *HT* = Hydrogen Transport Parameter, (f) *PER* = Percent Exudate Release.

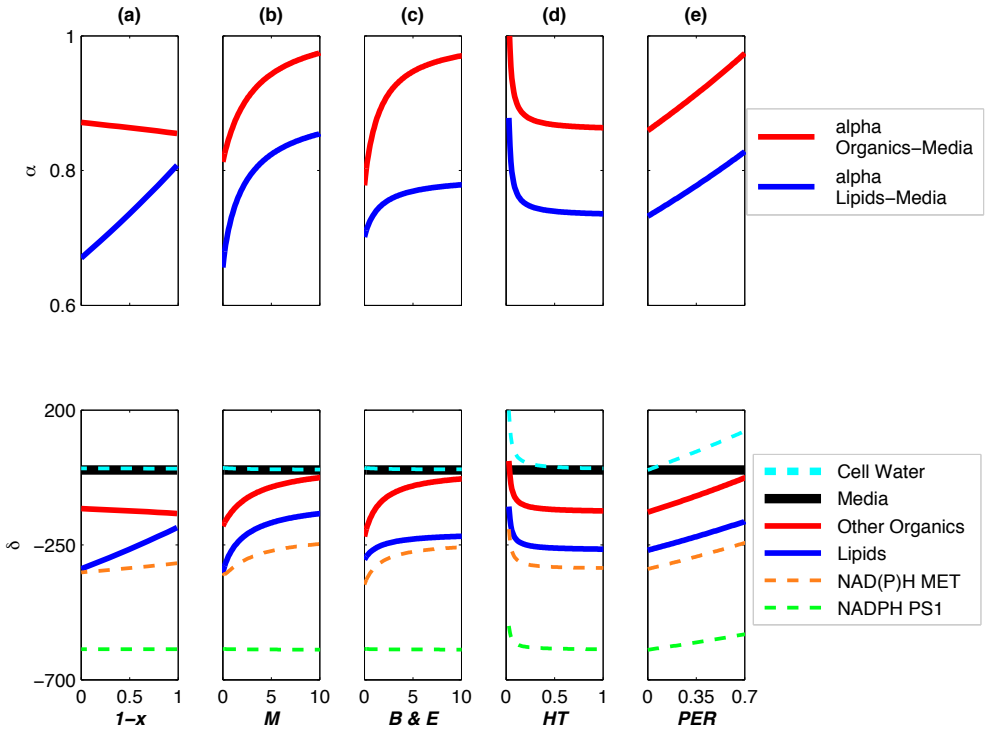

Fig. S5. Changes in $\delta^2H_{Resevoir}$, $\alpha_{Lipid\text{-}Media}$, and $\alpha_{Organics\text{-}Media}$ as metabolic parameters vary: (a) 1-*x* = PSI vs MET NAD(P)H Parameter, (b) *M* = Metabolic Reductant Parameter, (c) *B* = Biosynthetic Cell Water Parameter and *E* = Equilibrium Exchange Parameter, (d) *HT* = Hydrogen Transport Parameter, (e) *PER* = Percent Exudate Release.

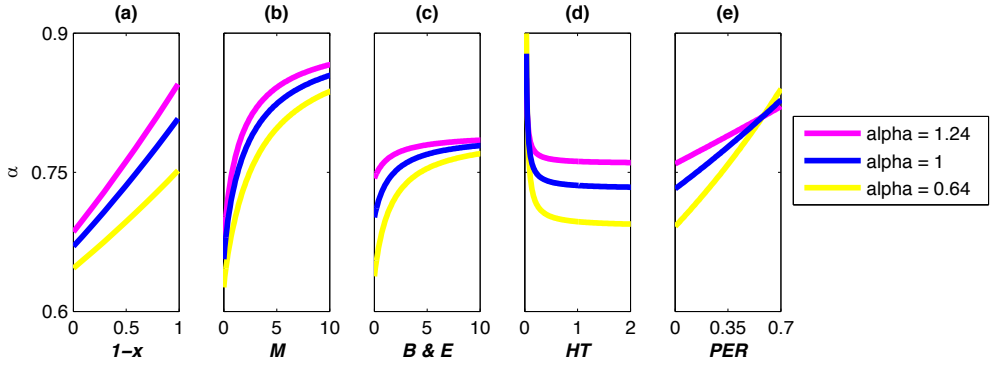

Fig. S6. The sensitivity of $\alpha_{Lipids\text{-}Media}$ to changes in the fractionation factor associated with the biosynthetic incorporation of hydrogen from water into organic compounds or equilibrium exchange. The blue lines are the same as in Fig. 3 from the main text and the top panels of Fig. S5. Lipid-Media $^{2}H/^{1}H$ fractionation decreases as fractionation factors associated with these fluxes increases. Cook and Cleland (2007) (Table 9.1 page 269) compiled metabolite-water fractionation factors for various molecules involved in enzyme mediated C-H exchange with water that range from 0.64 to 1.24. Isotope effects for specific hydrogen positions involved in water exchange during keto-enol tautomerism (applicable to α_{cW_O}) have been measured (Wang et al., 2009). The temperature dependent equilibrium hydrogen isotope effect between water and linear ketones for the alpha hydrogen position ranged from 0.83 to 0.85 (Wang et al., 2009). 1-*x* = PSI vs MET NAD(P)H Parameter (a), *M* = Metabolic Reductant Paramter (b), *B* = Biosynthetic Cell Water Parameter and *E* = Equilibrium Exchange Parameter (c), *HT* = Hydrogen Transport Parameter (d), *PER* = Percent Exudate Release (e).

Chapter 2 References

Abdullahi, A.S., Underwood, G.J.C., Gretz, M.R., 2006. Extracellular matrix assembly in diatoms (Bacillariophyceae). V. Environmental effects on polysaccharide synthesis in the model diatom, *Phaeodactylum tricornutum*. J. Phycol. 42, 363–378. doi:10.1111/j.1529-8817.2006.00193.x

Adolf, J.E., Stoecker, D.K., Harding, L.W., 2003. Autotrophic growth and photoacclimation in *Karlodinium micrum* (Dinophyceae) and *Storeatula major* (Cryptophyceae). J. Phycol. 39, 1101–1108.

Alcoverro, T., Conte, E., Mazzella, L., 2000. Production of mucilage by the adriatic epipelic diatom *Cylindrotheca closterium* (Bacillariophyceae) under nutrient limitation. J. Phycol. 36, 1087–1095. doi:10.1046/j.1529-8817.2000.99193.x

Armbrust, E.V., Berges, J.A., Bowler, C., Green, B.R., Martinez, D., Putnam, N.H., Zhou, S., Allen, A.E., Apt, K.E., Bechner, M., Brzezinski, M.A., Chaal, B.K., Chiovitti, A., Davis, A.K., Demarest, M.S., Detter, J.C., Glavina, T., Goodstein, D., Hadi, M.Z., Hellsten, U., Hildebrand, M., Jenkins, B.D., Jurka, J., Kapitonov, V. V, Kröger, N., Lau, W.W.Y., Lane, T.W., Larimer, F.W., Lippmeier, J.C., Lucas, S., Medina, M., Montsant, A., Obornik, M., Parker, M.S., Palenik, B., Pazour, G.J., Richardson, P.M., Rynearson, T.A., Saito, M.A., Schwartz, D.C., Thamatrakoln, K., Valentin, K., Vardi, A., Wilkerson, F.P., Rokhsar, D.S., 2004. The genome of the diatom *Thalassiosira pseudonana*: ecology, evolution, and metabolism. Science 306, 79–86. doi:10.1126/science.1101156

Aslam, S.N., Cresswell-Maynard, T., Thomas, D.N., Underwood, G.J.C., 2012. Production and characterization of the intra- and extracellular carbohydrates and polymeric substances (EPS) of three sea-ice diatom species, and evidence for a cryoprotective role for EPS. J. Phycol. 48, 1494–1509. doi:10.1111/jpy.12004

Atwood, A.R., Sachs, J.P., 2014. Separating ITCZ- and ENSO-related rainfall changes in the Galápagos over the last 3 kyr using D/H ratios of multiple lipid biomarkers. Earth Planet. Sci. Lett. 404, 408–419. doi:10.1016/j.epsl.2014.07.038

Bhattacharyya, P., Volcani, B.E., 1980. Sodium-dependent silicate transport in the apochlorotic marine diatom *Nitzschia alba*. Proc. Natl. Acad. Sci. 77, 6386–6390.

Boursiac, Y., Chen, S., Luu, D., Sorieul, M., Dries, N. van den, Maurel, C., 2005. Early effects of salinity on water transport in Arabidopsis roots. Molecular and cellular features of aquaporin expression. Plant Physiol. 139, 790–805. doi:10.1104/pp.105.065029.water

Brown, A.D., 1978. Compatible solutes and extreme water stress in eukaryotic micro-organisms. Adv. Microb. Physiol. 17, 181–242.

Buchanan, B.B., Gruissem, W., Jones, R.L., 2015. Biochemsitry and Molecular Biology of Plants, 2nd ed. Wiley, West Sussex.

Bull, A.T., 2010. The renaissance of continuous culture in the post-genomics age. J. Ind. Microbiol. Biotechnol. 37, 993–1021. doi:10.1007/s10295-010-0816-4

Bussard, A., Corre, E., Hubas, C., Duvernois-Berthet, E., Le Corguillé, G., Jourdren, L., Coulpier, F., Claquin, P., Lopez, P.J., 2017. Physiological adjustments and transcriptome reprogramming are involved in the acclimation to salinity gradients in diatoms. Environ. Microbiol. 19, 909–925. doi:10.1111/1462-2920.13398

Cheng, R., Feng, J., Zhang, B.-X., Huang, Y., Cheng, J., Zhang, C.-X., 2014. Transcriptome and gene expression analysis of an oleaginous diatom under different salinity conditions. BioEnergy Res. 7, 192–205. doi:10.1007/s12155-013-9360-1

Chisla, S., Massey, V., 1989. Mechanisms of flavoprotein-catalyzed reactions. Eur. J. Biochem. 181, 1–17.
Chivall, D., Boule, D.M., Sinke-Schoen, D., Sinninghe Damsté, J.S., Schouten, S., van der Meer, M.T.J., 2014. The effects of growth phase and salinity on the hydrogen isotopic composition of alkenones produced by coastal haptophyte algae. Geochim. Cosmochim. Acta 140, 381–390.
Cook, P.F., Cleland, W.W., 2007. Enzyme kinetics and mechanism. Garland Science, New York.
Craig, H., 1961. Isotopic variations in meteoric waters. Science 133, 1702–1703.
Craig, H., Gordon, L., 1965. Deuterium and oxygen 18 variations in the ocean and the marine atmosphere, in: Tongiori, E. (Ed.), Proceedings of a Conference on Stable Isotopes in Oceanographic Studies and Paleotemperatures. CNR-Laboratorio di Geologia Nucleare, Pisa, pp. 9–130.
Cui, L., Chai, Y., Li, J., Liu, H., Zhang, L., Xue, L., 2010. Identification of a glucose-6-phosphate isomerase involved in adaptation to salt stress of *Dunaliella salina*. J. Appl. Phycol. 22, 563–568. doi:10.1007/s10811-009-9494-x
Danevčič, T., Stopar, D., 2011. Asymmetric response of carbon metabolism at high and low salt stress in *Vibrio* sp. DSM14379. Microb. Ecol. 62, 198–204. doi:10.1007/s00248-011-9870-3
Dansgaard, W., 1964. Stable isotopes in precipitation. Tellus 16, 436–468.
Dawson, K.S., Osburn, M.R., Sessions, A.L., Orphan, V.J., 2015. Metabolic associations with archaea drive shifts in hydrogen isotope fractionation in sulfate-reducing bacterial lipids in cocultures and methane seeps. Geobiology 13, 462–477. doi:10.1111/gbi.12140
Desmond, E., Gribaldo, S., 2009. Phylogenomics of sterol synthesis: Insights into the origin, evolution, and diversity of a key eukaryotic feature. Genome Biol. Evol. 1, 364–81. doi:10.1093/gbe/evp036
Dirghangi, S.S., Pagani, M., 2013a. Hydrogen isotope fractionation during lipid biosynthesis by *Haloarcula marismortui*. Geochim. Cosmochim. Acta 119, 381–390. doi:10.1016/j.gca.2013.05.023
Dirghangi, S.S., Pagani, M., 2013b. Hydrogen isotope fractionation during lipid biosynthesis by *Tetrahymena thermophila*. Org. Geochem. 64, 105–111.
Emerson, S., Hedges, J., 2008. Chemical oceanography and the marine carbon cycle. Cambridge University Press, New York, N.Y.
Englebrecht, A.C., Sachs, J.P., 2005. Determination of sediment provenance at drift sites using hydrogen isotopes and unsaturation ratios in alkenones. Geochim. Cosmochim. Acta 69, 4253–4265. doi:10.1016/j.gca.2005.04.011
Estep, M.F., Hoering, T.C., 1980. Biogeochemistry of the stable hydrogen isotopes. Geochim. Cosmochim. Acta 44, 1197–1206. doi:10.1016/0016-7037(80)90073-3
Fabris, M., Matthijs, M., Carbonelle, S., Moses, T., Pollier, J., Dasseville, R., Baart, G.J.E., Vyverman, W., Goossens, A., 2014. Tracking the sterol biosynthesis pathway of the diatom *Phaeodactylum tricornutum*. New Phytol. 204, 521–535. doi:10.1111/nph.12917
Fabris, M., Matthijs, M., Rombauts, S., Vyverman, W., Goossens, A., Baart, G.J.E., 2012. The metabolic blueprint of *Phaeodactylum tricornutum* reveals a eukaryotic Entner-Doudoroff glycolytic pathway. Plant J. 70, 1004–14. doi:10.1111/j.1365-313X.2012.04941.x
Fan, J., Ye, J., Kamphorst, J.J., Shlomi, T., Thompson, C.B., Rabinowitz, J.D., 2014. Quantitative flux analysis reveals folate-dependent NADPH production. Nature 510, 298–302. doi:10.1038/nature13236
Galinski, E.A., 1995. Osmoadaptation in bacteria. Adv. Microb. Physiol. 37, 273–328.

Gamarra, B., Kahmen, A., 2015. Concentrations and δ^2H values of cuticular *n*-alkanes vary significantly among plant organs, species and habitats in grasses from an alpine and a temperate European grassland. Oecologia 1–18. doi:10.1007/s00442-015-3278-6

Gao, S., Zheng, Z., Huan, L., Wang, G., 2016. G6PDH activity highlights the operation of the cyclic electron flow around PSI in Physcomitrella patens during salt stress. Sci. Rep. 6, 21245. doi:10.1038/srep21245

García-Martín, M.L., Ballesteros, P., Cerdán, S., 2001. The metabolism of water in cells and tissues as detected by NMR methods. Prog. Nucl. Magn. Reson. Spectrosc. 39, 41–77.

Gat, J.R., 1996. Oxygen and hydrogen isotopes in the hydrologic cycle. Annu. Rev. Earth Planet. Sci. 24, 225–262. doi:10.1146/annurev.earth.24.1.225

Granum, E., Raven, J.A., Leegood, R.C., 2005. How do marine diatoms fix 10 billion tonnes of inorganic carbon per year? Can. J. Bot. 83, 898–908. doi:10.1139/b05-077

Gruber, A., Weber, T., Bártulos, C.R., Vugrinec, S., Kroth, P.G., 2009. Intracellular distribution of the reductive and oxidative pentose phosphate pathways in two diatoms. J. Basic Microbiol. 49, 58–72. doi:10.1002/jobm.200800339

Guillard, R.R.L., 1975. Culture of phytoplankton for feeding marine invertebrates, in: Culture of Marine Invertebrate Animals. pp. 26–60.

Guillard, R.R.L., Ryther, J.H., 1962. Studies of marine planktonic diatoms. I. *Cyclotella nana* Hustedt and *Detonula confervacea* Cleve. Can. J. Microbiol. 8, 229–239.

Hagemann, R., Nief, G., Roth, E., 1970. Absolute isotopic scale for deuterium analysis of natural waters. Absolute D/H ratio for SMOW. Tellus 22, 712–715.

Hallegraeff, G.M., 1977. A comparison of different methods used for the quantitative evaluation of biomass of freshwater phytoplankton. Hydrobiologia 55, 145–165.

Hasegawa, P.M., Bressan, R.A., Zhu, J.-K., Bohnert, H.J., 2000. Plant cellular and molecular responses to high salinity. Annu. Rev. Plant Physiol. Plant Mol. Biol. 51, 463–499.

Heinzelmann, S.M., Chivall, D., M'Boule, D., Sinke-Schoen, D., Villanueva, L., Sinninghe Damsté, J.S., Schouten, S., van der Meer, M.T.J., 2015a. Comparison of the effect of salinity on the D/H ratio of fatty acids of heterotrophic and photoautotrophic microorganisms. FEMS Microbiol. Lett. 362, fnv065. doi:10.1093/femsle/fnv065

Heinzelmann, S.M., Villanueva, L., Sinke-Schoen, D., Sinninghe Damsté, J.S., Schouten, S., van der Meer, M.T.J., 2015b. Impact of metabolism and growth phase on the hydrogen isotopic composition of microbial fatty acids. Front. Microbiol. 6, 1–11. doi:10.3389/fmicb.2015.00408

Hemmerlin, A., Harwood, J.L., Bach, T.J., 2012. A raison d'être for two distinct pathways in the early steps of plant isoprenoid biosynthesis? Prog. Lipid Res. 51, 95–148. doi:10.1016/j.plipres.2011.12.001

Hildebrand, M., York, E., Kelz, J.I., Davis, A.K., Frigeri, L.G., 2006. Nanoscale control of silica morphology and three-dimensional structure during diatom cell wall formation. J. Mater. Res. 21, 2689–2698.

Horie, T., Kaneko, T., Sugimoto, G., Sasano, S., Panda, S.K., Shibasaka, M., Katsuhara, M., 2011. Mechanisms of water transport mediated by PIP aquaporins and their regulation via phosphorylation events under salinity stress in barley roots. Plant Cell Physiol. 52, 663–675.

Huan, L., Xie, X., Zheng, Z., Sun, F., Wu, S., Li, M., Gao, S., Gu, W., Wang, G., 2014. Positive correlation between PSI response and oxidative pentose phosphate pathway activity during salt stress in an intertidal macroalga. Plant Cell Physiol. 55, 1395–1403.

Huang, J., Zhang, H., Wang, J., Yang, J., 2003. Molecular cloning and characterization of rice 6-phosphogluconate dehydrogenase gene that is up-regulated by salt stress. Mol. Biol. Rep. 30, 223–7.

Hyde, J.E., Dittrich, S., Wang, P., Sims, P.F.G., Crécy-Lagard, V. de, Hanson, A.D., 2008. *Plasmodium falciparum*: a paradigm for alternative folate biosynthesis in diverse microorganisms? Trends Parasitol. 24, 502–508. doi:10.1016/j.pt.2008.08.004.Plasmodium

Kasper, S., 2015. Reconstruction of past changes in ocean salinity – a compound specific stable hydrogen isotope approach.

Kasper, S., van der Meer, M.T.J., Mets, A., Zahn, R., Sinninghe Damsté, J.S., Schouten, S., 2014. Salinity changes in the Agulhas leakage area recorded by stable hydrogen isotopes of C37 alkenones during Termination I and II. Clim. Past 10, 251–260. doi:10.5194/cp-10-251-2014

Katz, J.J., Crespi, H.L., 1970. Isotope effects in biological systems, in: Collins, C.J., Bowman, N.S. (Eds.), Isotope Effects in Chemical Reactions, ACS Monograph 167. Van Nostrand Reinhold Co, New York, pp. 286–363.

Kirst, G.O., 1989. Salinity tolerance of eukaryotic marine algae. Annu. Rev. Plant Physiol. Plant Mol. Biol. 40, 21–53.

Kreuzer-Martin, H.W., Ehleringer, J.R., Hegg, E.L., 2005. Oxygen isotopes indicate most intracellular water in log-phase Escherichia coli is derived from metabolism. Proc. Natl. Acad. Sci. 102, 17337–41. doi:10.1073/pnas.0506531102

Kreuzer-Martin, H.W., Lott, M.J., Ehleringer, J.R., Hegg, E.L., 2006. Metabolic processes account for the majority of the intracellular water in log-phase *Escherichia coli* cells as revealed by hydrogen isotopes. Biochemistry 45, 13622–13630.

Kreuzer, H.W., Quaroni, L., Podlesak, D.W., Zlateva, T., Bollinger, N., McAllister, A., Lott, M.J., Hegg, E.L., 2012. Detection of metabolic fluxes of O and H atoms into intracellular water in mammalian cells. PLoS One 7, e39685. doi:10.1371/journal.pone.0039685

Kroth, P.G., Chiovitti, A., Gruber, A., Martin-Jezequel, V., Mock, T., Parker, M.S., Stanley, M.S., Kaplan, A., Caron, L., Weber, T., Maheswari, U., Armbrust, E.V., Bowler, C., 2008. A model for carbohydrate metabolism in the diatom *Phaeodactylum tricornutum* deduced from comparative whole genome analysis. PLoS One 3, e1426. doi:10.1371/journal.pone.0001426

La Vars, S.M., Johnston, M.R., Hayles, J., Gascooke, J.R., Brown, M.H., Leterme, S.C., Ellis, A. V, 2013. 29Si{1H} CP-MAS NMR comparison and ATR-FTIR spectroscopic analysis of the diatoms *Chaetoceros muelleri* and *Thalassiosira pseudonana* grown at different salinities. Anal. Bioanal. Chem. 405, 3359–65. doi:10.1007/s00216-013-6746-z

Leduc, G., Sachs, J.P., Kawka, O.E., Schneider, R.R., 2013. Holocene changes in eastern equatorial Atlantic salinity as estimated by water isotopologues. Earth Planet. Sci. Lett. 362, 151–162. doi:10.1016/j.epsl.2012.12.003

Leterme, S.C., Ellis, A. V, Mitchell, J.G., Buscot, M.-J., Pollet, T., Schapira, M., Seuront, L., 2010. Morphological flexibility of *Cocconeis placentula* (Bacillariophyceae) nanostructure to changing salinity levels. J. Phycol. 46, 715–719. doi:10.1111/j.1529-8817.2010.00850.x

Liang, Y., Sun, W., Zhu, Y.-G., Christie, P., 2007. Mechanisms of silicon-mediated alleviation of abiotic stresses in higher plants: A review. Environ. Pollut. 147, 422–8. doi:10.1016/j.envpol.2006.06.008

Liska, A.J., 2004. Enhanced photosynthesis and redox energy production contribute to salinity tolerance in *Dunaliella* as revealed by homology-based proteomics. Plant Physiol. 136, 2806–2817. doi:10.1104/pp.104.039438

Liu, H., Buskey, E.J., 2000. Hypersalinity enhances the production of extracellular polymeric substance (EPS) in the Texas brown tide alga, *Aureoumbra lagunensis* (Pelagophyceae). J. Phycol. 36, 71–77. doi:10.1046/j.1529-8817.2000.99076.x

Lohr, M., Schwender, J., Polle, J.E.W., 2012. Isoprenoid biosynthesis in eukaryotic phototrophs: A spotlight on algae. Plant Sci. 185–186, 9–22. doi:10.1016/j.plantsci.2011.07.018

Luo, Y.-H., Sternberg, L., Suda, S., Kumazawa, S., Mitsui, A., 1991. Extremely low D/H ratios of photoproduced hydrogen by cyanobacteria. Plant Cell Physiol. 32, 897–900.

M'Boule, D., Chivall, D., Sinke-Schoen, D., Sinninghe Damsté, J.S., Schouten, S., van der Meer, M.T.J., 2014. Salinity dependent hydrogen isotope fractionation in alkenones produced by coastal and open ocean haptophyte algae. Geochim. Cosmochim. Acta 130, 126–135.

Malaisse-Lagae, F., Liemans, V., Yaylali, B., Sener, A., Malaisse, W.J., 1989. Phosphoglucoisomerase-catalyzed interconversion of hexose phosphates; comparison with phosphomannoisomerase. Biochim. Biophys. Acta 998, 118–125. doi:10.1016/0885-4505(91)90052-M

Marrakchi, H., Zhang, Y.-M., Rock, C.O.O., 2002. Mechanistic diversity and regulation of Type II fatty acid synthesis. Biochem. Soc. 30, 1050–1055. doi:10.1042/BST0301050

Maršálek, B., Rojíčkovâ, R., 2015. Stress factors enhancing production of algal exudates: a potential self-protective mechanism? Zeitschrift für Naturforsch. C 51, 646–650.

Massengo-Tiassé, R.P., Cronan, J.E., 2009. Diversity in enoyl-acyl carrier protein reductases. Cell. Mol. Life Sci. 66, 1507–1517. doi:10.1016/j.biotechadv.2011.08.021.Secreted

Medlin, L.K., 2002. Why silica or better yet why not silica? Speculations as to why the diatoms utilise silica as their cell wall material. Diatom Res. 17, 453–459.

Michels, A.K., Wedel, N., Kroth, P.G., Germany, A.K.M., 2014. Diatom plastids possess a phosphoribulokinase with an altered regulation and no oxidative pentose phosphate pathway. Plant Physiol. 137, 911–920. doi:10.1104/pp.104.055285.plasts

Morris, A.W., Bale, A.J., Howland, R.J.M., 1976. Nutrient distributions in an estuary: Evidence of chemical precipitation of dissolved silicate and phosphate. Estuar. Coast. Shelf Sci. 12, 205–216.

Nagata, T., 2000. Production mechanisms of dissolved matter, in: Kirchmann, D.L. (Ed.), Microbial Ecology of the Oceans. Wiley-Liss, New York, pp. 121–152.

Nelson, D.B., Sachs, J.P., 2016. Galápagos hydroclimate of the Common Era from paired microalgal and mangrove biomarker $^{2}H/^{1}H$ values. Proc. Natl. Acad. Sci. U. S. A. 113, 3476–3481. doi:10.1073/pnas.1516271113

Nelson, D.B., Sachs, J.P., 2014. The influence of salinity on D/H fractionation in dinosterol and brassicasterol from globally distributed saline and hypersaline lakes. Geochim. Cosmochim. Acta 133, 325–339. doi:10.1016/j.gca.2014.03.007

Nemoto, Y., Sasakuma, T., 2000. Specific expression of glucose-6-phosphate dehydrogenase (G6PDH) gene by salt stress in wheat (*Triticum aestivum* L.). Plant Sci. 158, 53–60. doi:S0168945200003058 [pii]

Oliver, D.J., Nikolau, B.J., Wurtele, E.S., 2009. Acetyl-CoA-Life at the metabolic nexus. Plant Sci. 176, 597–601. doi:10.1016/j.plantsci.2009.02.005

Olsen, S., Paasche, E., 1986. Variable kinetics of silicon-limited growth in *Thalassiosira pseudonana* (Bacillariophyceae) in response to changed chemical composition of the growth medium. Br. Phycol. J. 21, 183–190. doi:10.1080/00071618600650211

Osburn, M.R., Sessions, A.L., Pepe-Ranney, C., Spear, J.R., 2011. Hydrogen-isotopic variability in fatty acids from Yellowstone National Park hot spring microbial communities. Geochim. Cosmochim. Acta 75, 4830–4845. doi:10.1016/j.gca.2011.05.038

Paasche, E., 1973. Silicon and the ecology of marine plankton diatoms. I. *Thalasssiosira pseudonana (Cyclotella nana)* grown in a chemostat with silicate as limiting nutrient. Mar. Biol. 19, 117–126.

Pahnke, K., Sachs, J.P., Keigwin, L., Timmermann, A., Xie, S.-P., 2007. Eastern tropical Pacific hydrologic changes during the past 27,000 years from D/H ratios in alkenones. Paleoceanography 22. doi:10.1029/2007PA001468

Paul, H.A., 2002. Application of novel stable isotope methods to reconstruct paleoenvironments: Compound specific hydrogen isotopes and pore-water oxygen isotopes. Zürich: Swiss Federal Institute of Technology.

Petrick, B.F., McClymont, E.L., Marret, F., van der Meer, M.T.J., 2015. Changing surface water conditions for the last 500ka in the Southeast Atlantic: Implications for variable influences of Agulhas leakage and Benguela upwelling. Paleoceanography 30, 1153–1167. doi:10.1002/2015PA002787

Pollak, N., Dölle, C., Ziegler, M., 2007. The power to reduce: pyridine nucleotides – small molecules with a multitude of functions. Biochem. J. 402, 205–218. doi:10.1042/BJ20061638

Rai, S., Agrawal, C., Shrivastava, A.K., Singh, P.K., Rai, L.C., 2014. Comparative proteomics unveils cross species variations in *Anabaena* under salt stress. J. Proteomics 98, 254–270. doi:10.1016/j.jprot.2013.12.020

Rai, S., Pandey, S., Shrivastava, A.K., Singh, P.K., Agrawal, C., Rai, L.C., 2013a. Understanding the mechanisms of abiotic stress management in cyanobacteria with special reference to proteomics, in: Srivastava, A.K., Rai, A.N., Neilan, B.A. (Eds.), Stress Biology of Cyanobacteria. Taylor and Francis Group, Boca Raton, Fl, pp. 93–112.

Rai, S., Singh, S., Shrivastava, A.K., Rai, L.C., 2013b. Salt and UV-B induced changes in *Anabaena* PCC 7120: physiological, proteomic and bioinformatic perspectives. Photosynth. Res. 118, 105–14. doi:10.1007/s11120-013-9931-1

Richey, J.N., Sachs, J.P., 2016. Precipitation changes in the western tropical Pacific over the past millennium. Geology 44, 671–674. doi:10.1130/G37822.1

Robins, R.J., Billault, I., Duan, J., Guiet, S., Pionnier, S., Zhang, B.-L., 2003. Measurement of ^{2}H distribution in natural products by quantitative ^{2}H NMR: An approach to understanding metabolism and enzyme mechanism? Phytochem. Rev. 2, 87–102.

Sachs, J.P., Kawka, O.E., 2015. The influence of growth rate on $^{2}H/^{1}H$ fractionation in continuous cultures of the coccolithophorid *Emiliania huxleyi* and the diatom *Thalassiosira pseudonana*. PLoS One 10, e0141643. doi:10.1371/journal.pone.0141643

Sachs, J.P., Maloney, A.E., Gregersen, J., Paschall, C., 2016. Effect of salinity on $^{2}H/^{1}H$ fractionation in lipids from continuous cultures of the coccolithophorid *Emiliania huxleyi*. Geochim. Cosmochim. Acta 189, 96–109. doi:10.1016/j.gca.2016.05.041

Sachs, J.P., Sachse, D., Smittenberg, R.H., Zhang, Z., Battisti, D.S., Golubic, S., 2009. Southward movement of the Pacific intertropical convergence zone. Nat. Geosci. 2, 519–525. doi:10.1038/NGEO554

Sachs, J.P., Schwab, V.F., 2011. Hydrogen isotopes in dinosterol from the Chesapeake Bay estuary. Geochim. Cosmochim. Acta 75, 444–459. doi:10.1016/j.gca.2010.10.013

Sachse, D., Billault, I., Bowen, G.J., Chikaraishi, Y., Dawson, T.E., Feakins, S.J., Freeman, K.H., Magill, C.R., McInerney, F.A., van der Meer, M.T.J., Polissar, P.J., Robins, R.J., Sachs, J.P., Schmidt, H.-L., Sessions, A.L., White, J.W., West, J.B., Kahmen, A., 2012. Molecular paleohydrology: Interpreting the hydrogen-isotopic composition of lipid biomarkers from photosynthesizing organisms. Annu. Rev. Earth Planet. Sci. 40, 221–249. doi:10.1146/annurev-earth-042711-105535

Sachse, D., Sachs, J.P., 2008. Inverse relationship between D/H fractionation in cyanobacterial lipids and salinity in Christmas Island saline ponds. Geochim. Cosmochim. Acta 72, 793–806. doi:10.1016/j.gca.2007.11.022

Saito, K., Kawaguchi, A., Okuda, S., Seyama, Y., Yamakawa, T., Nakamura, Y., Yamada, M., 1980. Stereospecificity of hydrogen transfer by pyridine nucleotide-dependent enoyl reductases in fatty acid synthesis: Studies with enzymes obtained from developing castor bean seeds and *Chlorella vulgaris*. Plant Cell Physiol. 21, 9–19.

Schmidt, H.-L., Werner, R.A., Eisenreich, W., 2003. Systematics of ^{2}H patterns in natural compounds and its importance for the elucidation of biosynthetic pathways. Phytochem. Rev. 2, 61–85. doi:10.1023/B:PHYT.0000004185.92648.ae

Schouten, S., Ossebaar, J., Schreiber, K., Kienhuis, M.V.M., Langer, G., Benthien, A., Bijma, J., Burg, D., 2006. The effect of temperature, salinity and growth rate on the stable hydrogen isotopic composition of long chain alkenones produced by *Emiliania huxleyi* and *Gephyrocapsa oceanica*. Biogeosciences 3, 113–119.

Sessions, A.L., Burgoyne, T.W., Hayes, J.M., 2001. Determination of the H3 factor in hydrogen isotope ratio monitoring mass spectrometry. Anal. Chem. 73, 200–207.

Sessions, A.L., Burgoyne, T.W., Schimmelmann, A., Hayes, J.M., 1999. Fractionation of hydrogen isotopes in lipid biosynthesis. Org. Geochem. 30, 1193–1200. doi:10.1016/S0146-6380(99)00094-7

Sessions, A.L., Jahnke, L.L., Schimmelmann, A., Hayes, J.M., Essions, A.L.E.X.L.S., Ahnke, L.I.L.J., Chimmelmann, A.R.S., Ayes, J.O.H.N.M.H., 2002. Hydrogen isotope fractionation in lipids of the methane-oxidizing bacterium Methylococcus capsulatus. Geochim. Cosmochim. Acta 66, 3955–3969.

Sharp, J.H., 1977. Excretion of organic matter by marine phytoplankton: Do healthy cells do it? Limnol. Oceanogr. 22, 381–399. doi:10.4319/lo.1977.22.3.0381

Shtaida, N., Khozin-Goldberg, I., Boussiba, S., 2015. The role of pyruvate hub enzymes in supplying carbon precursors for fatty acid synthesis in photosynthetic microalgae. Photosynth. Res. 125, 407–422. doi:10.1007/s11120-015-0136-7

Simon, H., Kraus, A., 1976. Hydrogen isotope transfer in biological processes, in: Buncel, E., Lee, C. (Eds.), Isotopes in Organic Chemistry. Elsevier Science, Amsterdam, pp. 153–229.

Simon, M.H., Gong, X., Hall, I.R., Ziegler, M., Barker, S., Knorr, G., van der Meer, M.T.J., Kasper, S., Schouten, S., 2015. Salt exchange in the Indian-Atlantic Ocean Gateway since the Last Glacial Maximum: A compensating effect between Agulhas Current changes and salinity variations? Paleoceanography 30, 1318–1327. doi:10.1002/2015PA002842

Smith, R.E.H., Platt, T., 1984. Carbon exchange and ^{14}C tracer methods in a nitrogen-limited diatom, *Thalassiorsira pseudonana*. Mar. Ecol. Prog. Ser. 16, 75–87.

Smith, S.R., Abbriano, R.M., Hildebrand, M., 2012. Comparative analysis of diatom genomes reveals substantial differences in the organization of carbon partitioning pathways. Algal Res. 1, 2–16. doi:10.1016/j.algal.2012.04.003

Smittenberg, R.H., Saenger, C., Dawson, M.N., Sachs, J.P., 2011. Compound-specific D/H ratios of the marine lakes of Palau as proxies for West Pacific Warm Pool hydrologic variability. Quat. Sci. Rev. 30, 921–933. doi:10.1016/j.quascirev.2011.01.012

Spaans, S.K., Weusthuis, R.A., van der Oost, J., Kengen, S.W.M.S.W.M., 2015. NADPH-generating systems in bacteria and archaea. Front. Microbiol. 6, 1–27. doi:10.3389/fmicb.2015.00742

Steele, D.J., Franklin, D.J., Underwood, G.J.C., 2014. Protection of cells from salinity stress by extracellular polymeric substances in diatom biofilms. Biofouling 30, 987–998. doi:10.1080/08927014.2014.960859

Stiller, M., Nissenbaum, A., 1980. Variations of stable hydrogen isotopes in plankton from a freshwater lake. Geochim. Cosmochim. Acta 44, 1099–1101. doi:10.1016/0016-7037(80)90064-2

Thornton, D.C.O., 2014. Dissolved organic matter (DOM) release by phytoplankton in the contemporary and future ocean. Eur. J. Phycol. 49, 20–46. doi:10.1080/09670262.2013.875596

Tuchman, M.L., Theriot, E., Stoermer, E.F., 1984. Effects of low level salinity concentrations on the growth of *Cyclotella meneghiniana* Kütz. (Bacillariophyta). Arch. für Protistenkd. 128, 319–326. doi:10.1016/S0003-9365(84)80003-2

van der Meer, M.T.J., Baas, M., Rijpstra, W.I.C., Marino, G., Rohling, E.J., Sinninghe Damsté, J.S., Schouten, S., 2007. Hydrogen isotopic compositions of long-chain alkenones record freshwater flooding of the Eastern Mediterranean at the onset of sapropel deposition. Earth Planet. Sci. Lett. 262, 594–600. doi:10.1016/j.epsl.2007.08.014

van der Meer, M.T.J., Benthien, A., French, K.L., Epping, E., Zondervan, I., Reichart, G.-J., Bijma, J., Sinninghe Damsté, J.S., Schouten, S., 2015. Large effect of irradiance on hydrogen isotope fractionation of alkenones *in Emiliania huxleyi*. Geochim. Cosmochim. Acta 160, 16–24. doi:10.1016/j.gca.2015.03.024

van der Meer, M.T.J., Sangiorgi, F., Baas, M., Brinkhuis, H., Sinninghe Damsté, J.S., Schouten, S., 2008. Molecular isotopic and dinoflagellate evidence for Late Holocene freshening of the Black Sea. Earth Planet. Sci. Lett. 267, 426–434. doi:10.1016/j.epsl.2007.12.001

Van Oostende, N., Moerdijk-Poortvliet, T.C.W., Boschker, H.T.S., Vyverman, W., Sabbe, K., 2013. Release of dissolved carbohydrates by *Emiliania huxleyi* and formation of transparent exopolymer particles depend on algal life cycle and bacterial activity. Environ. Microbiol. 15, 1514–31. doi:10.1111/j.1462-2920.2012.02873.x

Vasiliev, I., Reichart, G.-J., Krijgsman, W., 2013. Impact of the Messinian Salinity Crisis on Black Sea hydrology—Insights from hydrogen isotopes analysis on biomarkers. Earth Planet. Sci. Lett. 362, 272–282. doi:10.1016/j.epsl.2012.11.038

Vrieling, E.G., Poort, L., Beelen, T.P.M., Gieskes, W.W.C., 1999. Growth and silica content of the diatoms *Thalassiosira weissflogii* and *Navicula salinarum* at different salinities and enrichments with aluminium. Eur. J. Phycol. 34, 307–316.

Vrieling, E.G., Sun, Q., Tian, M., Kooyman, P.J., Gieskes, W.W.C., van Santen, R.A., Sommerdijk, N.A.J.M., 2007. Salinity-dependent diatom biosilicification implies an important role of external ionic strength. Proc. Natl. Acad. Sci. U. S. A. 104, 10441–6. doi:10.1073/pnas.0608980104

Wang, X., Ma, Y., Huang, C., Wan, Q., Li, N., Bi, Y., 2008. Glucose-6-phosphate dehydrogenase plays a central role in modulating reduced glutathione levels in reed callus under salt stress. Planta 227, 611–23. doi:10.1007/s00425-007-0643-7

Wang, Y., Sessions, A.L., Nielsen, R.J., Goddard, W.A., 2009. Equilibrium $^{2}H/^{1}H$ fractionations in organic molecules: I. Experimental calibration of ab initio calculations. Geochim. Cosmochim. Acta 73, 7060–7075. doi:10.1016/j.gca.2009.08.019

Wilhelm, C., Büchel, C., Fisahn, J., Goss, R., Jakob, T., Laroche, J., Lavaud, J., Lohr, M., Riebesell, U., Stehfest, K., Valentin, K., Kroth, P.G., 2006. The regulation of carbon and nutrient assimilation in diatoms is significantly different from green algae. Protist 157, 91–124. doi:10.1016/j.protis.2006.02.003

Wolhowe, M.D., Prahl, F.G., Langer, G., Oviedo, A.M., Ziveri, P., Maria, A., Ziveri, P., 2015. Alkenone δD as an ecological indicator: A culture and field study of physiologically-controlled chemical and hydrogen-isotopic variation in C37 alkenones. Geochim. Cosmochim. Acta 162, 166–182. doi:10.1016/j.gca.2015.04.034

Wolhowe, M.D., Prahl, F.G., Probert, I., Maldonado, M., 2009. Growth phase dependent hydrogen isotopic fractionation in alkenone-producing haptophytes. Biogeosciences 6, 1681–1694. doi:10.5194/bg-6-1681-2009

Wood, M.A., Everroad, R.C., Wingard, L.M., 2005. Measuring growth rates in microalgal cultures, in: Andersen, R.A. (Ed.), Algal Culturing Techniques. Elsevier Academic Press, Amsterdam, pp. 269–285.

Yancey, P.H., 2005. Organic osmolytes as compatible, metabolic and counteracting cytoprotectants in high osmolarity and other stresses. J. Exp. Biol. 208, 2819–2830. doi:10.1242/jeb.01730

Yang, Y., Fu, Z., Su, Y., Zhang, X., Li, G., Guo, J., Que, Y., Xu, L., 2014. A cytosolic glucose-6-phosphate dehydrogenase gene, *ScG6PDH*, plays a positive role in response to various abiotic stresses in sugarcane. Sci. Rep. 4, 7090. doi:10.1038/srep07090

Yu, J., Chen, S., Zhao, Q., Wang, T., Yang, C., Diaz, C., Sun, G., Dai, S., 2011. Physiological and proteomic analysis of salinity tolerance in *Puccinellia tenuiflora*. J. Proteome Res. 10, 3852–3870. doi:10.1021/pr101102p

Zhang, X., Gillespie, A.L., Sessions, A.L., 2009. Large D/H variations in bacterial lipids reflect central metabolic pathways. Proc. Natl. Acad. Sci. U. S. A. 106, 12580–6. doi:10.1073/pnas.0903030106

Zhang, Z., Leduc, G., Sachs, J.P., 2014. El Niño evolution during the Holocene revealed by a biomarker rain gauge in the Galápagos Islands. Earth Planet. Sci. Lett. 404, 420–434. doi:http://dx.doi.org/10.1016/j.epsl.2014.07.013

Zhang, Z., Sachs, J.P., 2007. Hydrogen isotope fractionation in freshwater algae: I. Variations among lipids and species. Org. Geochem. 38, 582–608. doi:10.1016/j.orggeochem.2006.12.004

Zhang, Z., Sachs, J.P., Marchetti, A., 2009. Hydrogen isotope fractionation in freshwater and marine algae: II. Temperature and nitrogen limited growth rate effects. Org. Geochem. 40, 428–439. doi:10.1016/j.orggeochem.2008.11.002

Zhang, Z.J., Chen, S.H., Wang, S.M., Luo, H.Y., 2011. Characterization of extracellular polymeric substances from biofilm in the process of starting-up a partial nitrification process under salt stress. Appl. Microbiol. Biotechnol. 89, 1563–1571. doi:10.1007/s00253-010-2947-y

Zlotnik, I., Dubinsky, Z., 1989. The effect of light and temperature on DOC excretion by phytoplankton. Limnol. Oceanogr. 34, 831–839. doi:10.4319/lo.1989.34.5.0831

Chapter 3: A method for reconstructing precipitation in the tropical South Pacific from dinosterol $^{2}H/^{1}H$ ratios in lake sediment[2]

Abstract

The South Pacific Convergence Zone (SPCZ) is the largest precipitation feature in the Southern Hemisphere supplying freshwater to 11 million people. Despite its significance, little is known about the location and intensity of SPCZ precipitation prior to instrumental records, hindering attempts to predict precipitation changes in a warming world. Here we use sedimentary molecular fossils to establish a tool for extending the historical record of SPCZ precipitation. Freshwater lake sediments and water samples were collected from lakes that spanned a 4.6 mm d^{-1} range in precipitation rates based on estimates from the Global Precipitation Climatology Project (GPCP). $\delta^{2}H_{lakewater}$ values from 29 lakes ranged from -29 ‰ to +23 ‰ and were inversely correlated with precipitation rates, albeit with a steeper slope than the observed tropical Pacific "amount effect", owing to evaporation. The biomarker dinosterol was purified from core-top lake sediments to test dinosterol $^{2}H/^{1}H$ ratios ($\delta^{2}H_{dinosterol}$) as a proxy for hydroclimate variability in the SPCZ region. Lake-averaged $\delta^{2}H_{dinosterol}$ values from 21 lakes tracked $\delta^{2}H_{lakewater}$ and ranged from -245 ‰ in French Polynesia to -316 ‰ in the Solomon Islands and were correlated with precipitation rates with a sensitivity of -12.1 ±2.6 ‰ $(mm\ d^{-1})^{-1}$. The empirical SPCZ GPCP-$\delta^{2}H_{dinosterol}$ relationship provides a means of quantitatively reconstructing past SPCZ precipitation with uncertainties up to ±3 mm d^{-1}, about twice that of the satellite-gauge GPCP product itself.

[2] *In preparation for submission as*: Maloney, A.E., Nelson, D.B., Prebble, M., Sear, D.A., Hassall, J.D., Langdon, P.G., Croudace, I.W., Sachs, J.P. (*in prep*). A method for reconstructing precipitation in the tropical South Pacific from dinosterol $^{2}H/^{1}H$ ratios in lake sediment.

Introduction

The South Pacific Convergence Zone (SPCZ) is the Southern Hemisphere's largest precipitation feature (Vincent, 1994) supplying freshwater to 11 million people on 3,975 islands (Power et al., 2011; WHO, 2016). The majority of coupled climate models suggest a larger and wetter SPCZ in the future with a more extreme zonal structure during ENSO events (Borlace et al., 2014; Brown et al., 2012, 2011; Cai et al., 2012). It is difficult to validate these model results because little is known about the extent of natural variability in SPCZ migration due to the short satellite (40 years) and gauge (130 years) records of SPCZ precipitation.

Long continuous records of SPCZ precipitation variability are needed to understand natural variability prior to the instrumental record. Coral archives (Linsley et al., 2008, 2006) and speleothems (Maupin et al., 2014; Partin et al., 2013) from the SPCZ region do not extend beyond 600 years ago. Sediment archives have successfully recorded longer-term changes in tropical vegetation and human activity (Combettes et al., 2015; Hope and Pask, 1998; Parkes, 1994; Prebble et al., 2013; Prebble and Wilmshurst, 2009; Rull et al., 2015; Southern, 1986; Stevenson and Hope, 2005; Wirrmann et al., 2006), and large scale precipitation during the past 10,000 years (Hassall, 2017). Here we present an organic biomarker-based proxy to quantify precipitation changes across tropical south Pacific islands using sediment archives to extend the record of precipitation observations well beyond the instrumental records.

In the tropics, precipitation hydrogen isotope ratios, expressed as δ^2H ($\delta = [R_{sample}/R_{VSMOW}] - 1$, where R is $^2H/^1H$ and VSMOW is Vienna Standard Mean Ocean Water), are principally controlled by precipitation amount (Dansgaard, 1964; Kurita et al., 2009; Risi et al., 2008; Rozanski et al., 1993). Tropical lake water δ^2H values are largely influenced by

precipitation δ^2H values and evaporative enrichment (Garcin et al., 2012; Issa et al., 2015). Lipids from algae track the isotopic composition of environmental water (Englebrecht and Sachs, 2005; Paul, 2002; Sachse et al., 2012; Schouten et al., 2006; Zhang and Sachs, 2007), and their preservation in sediments offers a window into past lake hydrology and by extension past precipitation.

Phytoplankton produce a variety of taxon-specific lipids (Volkman, 2005; Volkman et al., 1998) that can be exploited to infer environmental conditions. Dinosterol (4α,23,24-trimethyl-5α-cholest-22E-en-3β-ol) is produced almost exclusively by dinoflagellates, although it has also been detected in a single marine diatom species (Volkman et al., 1993). Source-specificity is important since the same lipid produced by different species of algae grown under the same conditions can have δ^2H values that differ by over 100‰ (Sachs, 2014; Sessions et al., 1999; Zhang and Sachs, 2007).

Algal lipid δ^2H values are sensitive to other environmental parameters including salinity (Maloney et al., 2016; Nelson and Sachs, 2014a; Sachs et al., 2016; Sachs and Schwab, 2011; Sachse and Sachs, 2008; Schouten et al., 2006; Weiss et al., 2017), growth rate and phase (Chivall et al., 2014; Sachs and Kawka, 2015; Wolhowe et al., 2015, 2009; Z. Zhang et al., 2009), temperature (Ladd et al., 2017; Wolhowe et al., 2009; Z. Zhang et al., 2009), light (Sachs et al., 2017; van der Meer et al., 2015), and redox environment or metabolism (Schwab et al., 2015a). To limit potential influences from salinity and temperature, this study sampled freshwater tropical lakes spanning a small range of seasonally stable temperatures (<4 °C, **Table A.1**). To capture less controllable parameters such as species composition, growth rate, metabolism, and light, multiple sites were sampled in each region.

Previous lake sediment core-top studies demonstrate that δ^2H values of sedimentary molecular fossils largely reflect modern spatial climate gradients. Sampling regions include global (Nelson and Sachs, 2014a, 2014b) and continental transects across Europe (Sachse et al., 2004), the Americas (Polissar and Freeman, 2010), eastern North America (Huang et al., 2004; Sauer et al., 2001), southwest United States (Hou et al., 2008), Cameroon (Garcin et al., 2012; Schwab et al., 2015a, 2015b), and the Tibetan Plateau (Aichner et al., 2010; Mügler et al., 2008; Xia et al., 2008). However, the fidelity to which lacustrine δ^2H values track climate across the vast expanse of the South Pacific Ocean has not yet been tested.

The goals of this study are to 1) characterize δ^2H values from lake water and purified sedimentary dinosterol from diverse lakes in the understudied SPCZ region and 2) explore the empirical relationship between modern precipitation and the lipid biomarker dinosterol as a tool for calculating pre-instrumental precipitation in the SPCZ.

Methods

Sample Collection

Sediment core-top samples were collected from 21 lakes (**Table B.1**). Most were from 6.604 cm diameter sediment cores collected in 2011-2012 with a universal corer device (Aquatic Research), the sample from Lake Wanum was collected in 1999. The uppermost portion (typically 20-50 cm) was sectioned in the field at 0.5 or 1 cm intervals to a depth at which the sediment was sufficiently consolidated to transport and store without disturbance to stratigraphy. Lake Emaotul was sampled in 1995 when it was dry with a D-section peat borer (Hope, 1996) and again in 2015 with a 8.6 cm diameter UWITEC (UWITEC, Mondsee, Austria) gravity corer. Samoa and New Caledonia were sampled in 2013 and Samoa again in 2014 with the UWITEC

gravity corer. Samoa and New Caledonia samples obtained in 2013 were subsampled in the field at 0.5 or 1 cm intervals, whereas Samoa samples obtained in 2014 were subsampled in the laboratory; interface integrity was maintained using Zorbitrol in the field. Samples from Tetiaroa were collected in March and/or October 2015 by hand. Sediment cores from the deepest (88 m) part of Lac Lalolalo (Wallis) had disturbed sediment water interfaces (15-20 cm) due to vigorous degassing upon recovery, therefore additional cores were collected from shallower depths (24 m) to obtain surface sediments that did not experience mixing.

At all lakes except Lake Wanum and the 1995 visit to Emaotul lake, water samples were collected and stored in glass or plastic vials and sealed to prevent evaporation. Additional water samples were collected from 9 lakes in Nauru, Vanuatu, Wallis, and the Solomon Islands (unique from those with sediment samples). Several non-lake water samples were collected for hydrogen and oxygen isotope analysis from streams, channels, lagoons, ocean, tap water, rain barrels, and cave drip water (**Table B.2**). Salinity was measured in the field with a refractometer to ±1 ppt. Local precipitation events were sampled whenever possible with a cup or bag, or with a rain water collector containing mineral oil to prevent evaporation.

Lake water temperature, pH, conductivity, and dissolved oxygen (DO) % were measured on-site using a portable data sonde (Hydrolab) at most lakes (**Fig. A.1**). Lake areas were determined with the Google Earth Pro polygon tool or from literature if available. Lake elevation was determined by topographical maps, hand held GPS, and literature if available (**Table A.1**).

Water Isotope Analyses

$\delta^{2}H$ and $\delta^{18}O$ were measured at the University of Washington, School of Oceanography 6-14 times per sample (the first three measurements were discarded to avoid memory effects) on

a Picarro L2130-i Isotopic Liquid Water Analyzer (Picarro, Inc., Santa Clara, CA) in high precision mode and normalized to VSMOW using three in house lab standards with hydrogen isotopic compositions -107.3 ± 0.5 ‰, -76.1 ± 0.3 ‰, and 14.8 ± 1.0 ‰. A subset of 32 samples were reanalyzed 2-4 times between 2014 and 2017 to give injection-weighted mean standard deviation of 1.3‰ for δ^2H and 0.3 ‰ for $\delta^{18}O$, characterizing the analytical stability.

Samples collected on Wallis were measured at University of Hawaii on a Picarro L1102-*i* WS-CRDS with analytical precision of 0.5‰ for δ^2H and 0.04‰ for $\delta^{18}O$ determined using an in-house standard run after every 10th sample. Water samples collected on New Caledonia and Samoa were measured at Natural Environmental Research Council Isotope Geosciences Facility with a GV Isoprime with Multiprep and EuroPyrOH.

Dinosterol hydrogen isotope analyses

Lipid extracts were obtained from freeze-dried sediment samples with an Accelerated Solvent Extractor (ASE-200, Dionex Corp., Sunnyvale, CA, USA) using 9:1 dichloromethane:methanol (DCM:MeOH) at 1500 psi and 100 °C for three 5 min cycles. Lipid extracts were base-hydrolyzed with 1N KOH at 70 °C for 6-12 h followed by liquid-liquid extractions in hexane. Column chromatography was used to separate dinosterol from other major lipid classes. A solid phase of 0.5 g amino propyl gel (Supelco) and 8 mL of 3:1 DCM:isopropyl alcohol eluted the non-polar fraction containing dinosterol. This fraction was further purified using 1.0 g deactivated silica gel with 6 ml of hexane (HEX), followed by 6 ml 1:1 HEX:DCM, and finally 8 ml 4:1 HEX:Ethyl acetate to elute an alcohol fraction containing dinosterol.

Dinosterol was purified from neighboring sterols by High Performance Liquid Chromatography according to Nelson & Sachs (2013). Prior to HPLC, samples were acetylated

using acetic anhydride with a known hydrogen isotopic composition (-123.8 ± 8.2 ‰) by dissolving in 40 uL of 1:1 pyridine:acetic anhydride and heating at 70 °C for 0.5 h. Identifications were performed on an Agilent GC 6890N connected to an Agilent quadrupole MSD5975 detector and equipped with an Agilent 7683 autosampler, a split-splitless injector operated in splitless mode, and an Agilent VF-17 ms capillary column (60 m × 0.25 mm × 0.25 μm) used with He carrier gas at 1.5 mL min^{-1}. The oven was ramped from 110 °C to 280 °C at 15 °C min^{-1} and held for 40 min, then ramped to 320 °C at 3 °C min^{-1} and held for 10 min. HPLC-purified dinosterol samples were quantified against a 5α-cholestane external standard on an Agilent 6890N GC equipped with a Flame Ionization Detector (FID), using methods similar to the GCMS.

$\delta^2H_{dinosterol}$ values were measured via gas-chromatography isotope-ratio mass spectrometry (GC-IRMS). Samples were injected into a Thermo Trace Ultra GC II (Thermo Fisher Scientific, Waltham, MA, USA) gas chromatograph via a Thermo TRIPLUS autosampler operated in splitless mode at 330 °C with a constant flow (1.1 mL min^{-1}) of He carrier gas. Eluting compounds were pyrolyzed in a 1400 °C ceramic reactor for introduction on a Thermo DELTA V PLUS IRMS. The GC was equipped with a VF-17ms capillary column (60 m × 0.25 mm × 0.25 μm), the oven was programmed to hold at 120 °C for 2 min, increase to 260 °C at 20 °C min^{-1}, increase to 310 °C at 1 °C min^{-1}, increase to 325 °C at 20 °C min^{-1}, and hold 325 °C for 15 min. The H_3^+ factor (Sessions et al., 2001) was measured prior to every sequence and was 2.00 ± 0.27 ppm nA^{-1} during the 38 months that 27 sequences were run for this study. External standards of known hydrogen isotopic composition including *n*-C_{21}-alkane (-214.7‰ CAS #629-94-7), *n*-C23-alkane (-48.8‰ CAS #638-67-5), *n*-C26-alkane (-54.9‰ CAS #630-01-3), *n*-C32-alkane (-212.4‰ CAS #544-85-4), *n*-C34-alkane (-231.8‰ CAS #14167-59-0), and *n*-C38-

alkane (-102.6‰ CAS #7194-85-6) (Dr. Arndt Schimmelmann, Indiana University, http://mypage.iu.edu/~aschimme/compounds.html) were injected throughout each run. Any peak areas less than 11 Vs were not considered to avoid size dependent δ^2H effects (Polissar and D'Andrea, 2014) and isotopic compositions were evaluated in the Isodat 2.0 software relative to calibrated H_2 reference gas. Dinosterol δ^2H values were corrected using the regression of known versus Isodat-reported *n*-alkane standard δ^2H values. Dinosterol δ^2H values were then corrected for hydrogen added during acetylation by a mass balance calculation as in Nelson and Sachs, (2014a).

TABLE 1. Lake location, rainfall rate (GPCPv2.3 1979-2016), P-E (GPCP-OAFlux), and lake-average isotope values.

Freshwater Site	Latitude	Longitude	GPCP	σ	P-E	σ	$\delta^2H_{lakewater}$	σ	n	$\delta^2H_{dinosterol}$	σ	n
	°	°	mm d^{-1}	mm d^{-1}	mm d^{-1}	mm d^{-1}	‰	‰		‰	‰	
Rimatu'u Pond, Tetiaroa, French Polynesia	-17.0249	210.4417	3.77	1.10	-0.25	1.15	16.0	4.1	3	-247	15	3
Oroatera Pond, Tetiaroa, French Polynesia	-16.9958	210.4591	3.77	1.10	-0.27	1.15	23.0		2	-251	33	2
Onetahi Pond, Tetiaroa, French Polynesia[#,^]	-17.0207	210.4081	3.78	1.10	-0.26	1.15	2.7		2	-284		1
Lake Tagamaucia, Teveuni, Fiji[#]	-16.8163	180.0601	5.03	1.08	1.00	1.14	-16.2	0.9	6	-284	3	2
Grand Lac, Grande Terre, New Caledonia	-22.2703	166.9094	3.53	0.63	-1.10	0.73	-15.5	0.1	2	-284		1
Lake Hut, Grande Terre, New Caledonia	-22.2609	166.9526	3.52	0.64	-1.12	0.74	-15.2		1	-267		1
Otas Lake, Efate, Vanuatu	-17.6945	168.5850	4.90	0.94	0.04	1.02	-8.0		1	-262	4	2
Emaotul Lake, Efate, Vanuatu[$]	-17.7342	168.4151	4.82	0.94	-0.06	1.02	-15.4	14.4	2	-266	7	3
Small Pond, Efate, Vanuatu[#]	-17.7342	168.4531	4.84	0.94	-0.04	1.02	-20.1		1			
Red Lake, Thion, Vanuatu	-15.0326	167.0901	5.48	1.24	1.30	1.30	-16.3	0.7	2	-251	12	3
White Lake, Thion, Vanuatu	-15.0410	167.0892	5.47	1.24	1.30	1.30	-10.0	0.2	2	-268	4	3
Waérowa East Lake, Espiritu Santo, Vanuatu[#]	-15.5950	167.0788	5.25	1.16	0.91	1.22	-27.2		1	-292		1
Waérowa West Lake, Espiritu Santo, Vanuatu[#]	-15.5951	167.0726	5.25	1.16	0.91	1.22	-19.5		1			
Bellmolle North Lake, Espiritu Santo, Vanuatu[#]	-15.5830	167.1118	5.25	1.16	0.92	1.22	-20.7		1			
Bellmolle Swamp, Espiritu Santo, Vanuatu[#]	-15.5839	167.1016	5.25	1.16	0.92	1.22	-22.7		1			
Bellmolle South Lake, Espiritu Santo, Vanuatu	-15.5884	167.1019	5.25	1.16	0.92	1.22	-15.3		1			
Buada Pond, Nauru[$]	-0.5347	166.9223	5.37	1.31	1.83	1.37	-19.7	0.1	2			
Lake Lanoto'o, Upolu, Samoa	-13.9109	188.1726	5.56	1.37	1.22	1.41	-17.5	1.8	4	-286	8	3
Lac Lalolalo, Wallis	-13.3017	183.7662	5.97	1.43	1.43	1.47	-12.3	0.5	6	-292	5	4
Lac Lanutavake, Wallis	-13.3212	183.7860	5.96	1.43	1.42	1.47	-5.8	0.2	6	-287	6	4
Lac Lano, Wallis	-13.2942	183.7597	5.97	1.43	1.43	1.48	-2.4		1			
Lake Wanum, Papua New Guinea	-6.6391	146.7872	7.44	1.13	3.98	1.20				-292		1
Barora Pond, Tetepare, Solomon Islands	-8.7223	157.6005	7.90	1.52	4.24	1.55	-24.2	0.9	2	-296	16	2
Lake Tavara Tetepare, Solomon Islands	-8.7029	157.4503	7.94	1.52	4.27	1.55	-25.4	0.6	2	-314	4	2
Lake Rano, Rendova, Solomon Islands	-8.6879	157.3243	7.97	1.52	4.25	1.56	-12.1	1.3	3	-275	8	2
Harai Lake #1, Rendova, Solomon Islands	-8.5622	157.3556	7.99	1.52	4.36	1.56	-28.5		1	-316		1
Harai Lake #2, Rendova, Solomon Islands	-8.5684	157.3683	7.98	1.52	4.36	1.56	-12.1		1	-296		1
Harai Lake #3, Rendova, Solomon Islands	-8.5648	157.3651	7.99	1.52	4.36	1.56	-27.2		1	-312	13	2
Arundel Lake #1, Arundel, Solomon Islands	-8.1917	157.1793	8.10	1.53	4.47	1.57	-21.0		1			
Arundel Lake #2, Arundel, Solomon Islands	-8.2060	157.1824	8.10	1.53	4.46	1.57	-3.9		1			

[#]High vegetation cover
[^]Manufactured
[$]Ephemeral

All 44 core-top samples and the standard deviations of multiple injections are reported in **Table B.1**. The pooled uncertainty for replicate analyses was 6.2 ‰ (Polissar and D'Andrea, 2014) and represents the overall analytical uncertainty. Included in this table is a cyanobacterial mat sample growing atop floating peat sedge on lake Tagimaucia that was not included in the lake-averaged sediment core-top value. For lakes with multiple core-top samples, lake-averaged $\delta^2H_{dinosterol}$ values were determined by averaging all core-top samples and the standard deviation of multiple lake core-tops represents lake-averaged $\delta^2H_{dinosterol}$ uncertainty (**Table 1**). A pooled uncertainty of 10.4 ‰ was determined from lakes with multiple core-tops and applied to lakes with only a single core-top sample and used for all graphs and statistics.

Statistics, data, and models

Large errors in independent variables in this study required the use of a maximum likelihood estimate method (York et al., 2004) incorporating bivariate analytical uncertainty for all linear regressions (Cantrell, 2008; Reed, 1989; Thirumalai et al., 2011; York, 1969; York et al., 2004), which were performed using published Matlab™ code (Thirumalai et al., 2011). Since most previous studies of algal lipid isotopes with respect to environmental variables did not have large x-errors (culture studies) or the x-errors were not accounted for (field studies), the results of ordinary least squares regressions are also provided in the figure captions. In all cases the biased ordinary least squares regressions slopes are smaller than the maximum likelihood method slopes, as was the case in a rigorous study of calibration techniques for corals as sea surface temperature proxies (Xu et al., 2015).

Monte Carlo error propagation, mapping, and data extraction was done in R (R Core Team, 2017). Smoothed data extraction from netcdf files used R's extract function with the "bilinear" method to average the 4 grid cells nearest to the lake sites.

The Global Precipitation Climatology Project (GPCPv2.3) dataset (Adler et al., 2017, 2003) was used to compute long-term mean annual precipitation rates for the 1979-2016 period (**Table 1**). The dataset is based on gauge and satellite observations and is gridded at a 2.5 ° x 2.5 ° scale. Estimates of precipitation uncertainty (Adler et al., 2012) accompany precipitation data. Data are provided by the National Oceanic & Atmospheric Administration/Oceanic & Atmospheric Research/Earth System Research Laboratory Physical Sciences Division (NOAA/OAR/ESRL PSD), Boulder, Colorado, USA, from their Web site at http://www.esrl.noaa.gov/psd/.

Long term mean air temperature data for the 1948-2016 period are from the National Centers for Environmental Protection (NCEP) reanalysis data (Kalnay et al., 1996) gridded at a 2.5 ° x 2.5 ° scale (**Table A.1**) and provided by the NOAA/OAR/ESRL PSD, Boulder, Colorado, USA, from their web site at http://www.esrl.noaa.gov/psd/.

Long term mean evaporation data for the 1958-2016 period and evaporation error estimates averaged over the 1985-2016 period gridded at a 1 ° x 1 ° scale (**Table A.1**) are from the Woods Hole Oceanographic Institution Objectively Analyzed air-sea Fluxes (OAFlux) for the Global Oceans project (http://oaflux.whoi.edu) funded by the NOAA Climate Observations and Monitoring (COM) program (Yu et al., 2008).

Mean annual amount weighted station values of observed precipitation isotopes (δ^2H_{rain}) and mean annual local gauge precipitation rates (**Table A.2; Fig. A.2**) are from the Global Network of Isotopes in Precipitation (GNIP) (IAEA/WMO, 2006)

(https://nucleus.iaea.org/wiser/) and from the Japan Agency for Marine-Earth Science and Technology (Kurita et al., 2009) (http://www.jamstec.go.jp/iorgc/cgi-bin/database/v01/browse_summary.cgi?program=hcorp&group=CRHCG&cat=Isotope&id=Isotope_Palau).

Online Isotope Precipitation Calculator (OIPC) precipitation δ^2H estimates ($\delta^2H_{OIPCrain}$) (**Table B.3; Fig. A.2**) are from the OIPC which uses the IAEA database and interpolation algorithms with a set of predictor parameters to calculate precipitation isotopes (Bowen and Revenaugh, 2003). The OIPC is accessible at http://wateriso.utah.edu/waterisotopes/pages/data_access/oipc.html.

Precipitation δ^2H estimates from the second Stable Water Isotope INtercomparison Group (SWING2) (Sturm et al., 2010) ($\delta^2H_{SWING2rain}$) (**Table B.3; Fig. A.2; Fig. A.3**) were calculated from nudged isotope enabled global circulation models (Hoffmann et al., 1998; Risi et al., 2010; Schmidt et al., 2007; Yoshimura et al., 2008). Mean annual results for LMDZ, ECHAM, and GISS models are from https://data.giss.nasa.gov/swing2/. Mean monthly results from IsoGSM are from http://hydro.iis.u-tokyo.ac.jp/~kei/?IsoGSM1#j9fb954c and averaged. Model details are given in (**Table A.3**).

Study sites

The lakes in this study (**Fig. 1; Table 1; Table A.1**) were chosen to create a modern spatial calibration between $\delta^2H_{dinosterol}$ and SPCZ precipitation. The lakes span 123.7 ° of longitude, 21.4 ° of latitude, and a narrow 23-27 °C range of NCEP/NCAR reanalysis mean annual air temperature where the largest (smallest) seasonal/inter-annual variability is 8.3 (3.7) °C in New Caledonia (Wallis) over the last 69 years (**Fig. A.4**). The lakes are all less than 250 m

above sea level with the exception of Lake Lanoto'o, Samoa (762 m) and Tagimaucia Lake, Fiji (820 m).

Across the study sites the mean annual GPCP precipitation rates for the 1979-2016 period vary from to 8.1 mm d^{-1} in the Solomon Islands to 3.5 mm d^{-1} in New Caledonia (**Fig. 1**). Seasonal variability (**Fig. A.5**) results in greater SPCZ precipitation extent during the austral summer (Vincent, 1994) and ENSO variability results in a northeast shift to a more zonal position during El Niño events (Widlansky et al., 2011). Without wind speed, site-specific evaporation rates cannot be calculated. However, mean annual ocean evaporation rates from each study site for the 1958-2016 period from OAFlux indicate the lowest evaporation rates in the Solomon Islands, Papua New Guinea, and Nauru (3.5-3.6 mm d^{-1}) and the highest evaporation rates in Vanuatu (4.9 mm d^{-1}) (**Table A.1; Fig. A.6; Fig. A.7**).

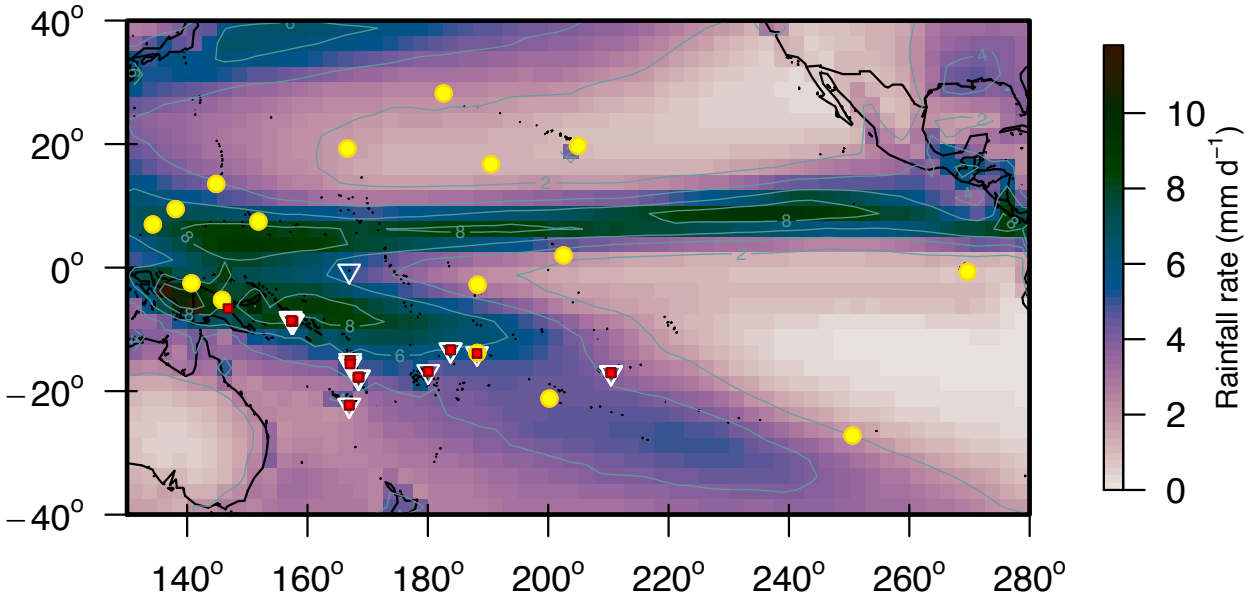

Fig. 1. Location of 29 SPCZ freshwater lake water samples (open white triangles), 21 freshwater lake sediment samples (red squares), and 16 tropical Pacific GNIP or JAMSTEK (Palau) stations (yellow circles). Contours and color scale show mean GPCPv2.3 precipitation rate (mm d^{-1}) on a 2.5 ° x 2.5 ° grid for the 1979-2016 period (http://www.esrl.noaa.gov/psd/).

Notably, the lakes in this study do not have rain gauges on site, and the effects of topography on localized mean annual precipitation rate are not captured by the 2.5 ° x 2.5 ° grid scale used in GPCP data. Rain gauge data at nearby locations indicate that GPCP underestimates actual precipitation rates in the SPCZ region. For instance, a rain gauge on Tetepare, Solomon Islands recorded a mean annual precipitation rate of ~13 mm d^{-1} between July 2003-July 2009 (Read et al., 2010) while the GPCP estimate is 8.4±1.1 mm d^{-1} for the same period. Likewise, precipitation at Lake Tagimaucia (Taveuni, Fiji) was estimated to be somewhere between 15-26 mm d^{-1} based on rain gauges from other parts of the island recorded in 1976-83 and 1913-74 (Southern et al., 1986) while the GPCP estimate is 4.6±1.2 mm d^{-1} for the 1979-2016 period. Despite these disagreements GPCP offers the most temporally and spatially comprehensive data available for understanding modern precipitation in the maritime tropical Pacific.

The largest lake in this study is Lake Wanum in Papua New Guinea (405 hectares) and the deepest is Lake Lalolalo on Wallis (88 m). The lakes on Grande Terre, New Caledonia are large flat bottom doline formations (Jeanpert et al., 2016). Most other lakes are small coastal ponds or crater lakes. Seven of the shallowest lakes had extensive vegetation cover. Five lakes from Vanuatu and the manufactured Onetahi Pond (Tetiarora, French Polynesia) had species of *Nymphaea* and *Nymphoides* covering up to ~50 % of the water's surface, and Lake Tagimaucia (Fiji) had extensive (92.5 %) floating mats of peat sedge (Southern et al., 1986). Profiles of salinity, temperature, DO%, and pH were recorded for many of the sites in Fiji, Vanuatu, Wallis, Samoa, and the Solomon Islands (**Fig. A.1**). The bathymetry and some physio-chemical properties of other sites has been further described for Lake Wanum in Papua New Guinea (Garrett-Jones, 1979), Lake Tagimaucia in Fiji (Southern, 1986; Southern et al., 1986), Lanoto'o

in Samoa (Hassall, 2017; Parkes, 1994; Schabetsberger et al., 2009), and Lake Lalolalo and Lanutavake on Wallis (Schabetsberger et al., 2009; Sichrowsky et al., 2014).

All lakes were fresh at the time of sampling with the exception of Rimatu'u pond (Tetiaroa, French Polynesia) and the deepest part of Lake Lalolalo (Wallis). Rimatu'u pond was observed to be brackish (5 ppt) in 1997 (Che et al., 2001), since then the shoreline that separates the lake from the sea water lagoon has been growing (Le Cozannet et al., 2013), presumably assisting the freshening of the pond. It was fresh when sampled in March 2015 but had a salinity of 2 ppt when sampled at the end of the dry season in October 2015. The effect of salinity on δ^2H values of algal lipids is about 1 ‰ ^2H-enrichement per salinity unit (Maloney et al., 2016; Nelson and Sachs, 2014a; Sachs et al., 2016; Sachs and Schwab, 2011; Sachse and Sachs, 2008; Weiss et al., 2017), so while a 5 ppt increase in salinity could cause a ^2H-enrichment of ~5‰, it is within the analytical error of $\delta^2H_{dinosterol}$ measurements. Lake Lalolalo contained freshwater (<1 ppt) in the oxygenated photic zone (a secchi disk reading revealed that light penetrated only 3.4 m), but below 10 m salinity gradually increased reaching 3 ppt at 50 m and finally, 31 ppt at 80 m (Sichrowsky et al., 2014) (see **Fig. A.1**). Given the strong gradient in light and oxygen, it is unlikely that dinoflagellates lived outside the fresh region of Lake Lalolalo. Other lakes near the coast may occasionally experience brackish salinities due to storm over wash events. After our 2012 visit, Lake Otas on Efate Island experienced a flooding event in 2015 during cyclone Pam (Hong et al., 2017), but it is unknown how this event affected the salinity or water isotope values.

Some lakes such as Barora Pond (Tetepare, Solomon Islands), Red lake (Thion, Vanuatu), and Lake Otas (Efate, Vanuatu) (**Fig. A.1**) were supersaturated in oxygen at the surface indicating high productivity rates at the time of sampling. Many lakes also had low/zero

oxygen at the sediment-water interface, particularly those with supersaturation at the surface. Most of the lakes in this study have not been examined for algal species composition but dinosterol was found in all sediments collected indicating dinoflagellates were present. Lalolalo and Lanutavke crater lakes on Wallis Island have been relatively well studied and contain the dinoflagellates of the genera *Gymnodinium* and *Peridinium* (Schabetsberger et al., 2009; Sichrowsky et al., 2014), the latter a known producer of dinosterol (c.f. Atwood et al., 2014). Lake Tagimaucia (Fiji) hosts at least four of species of dinoflagellates from the genera *Gymnodinium*, *Gyrodinium*, and *Peridinium*, and Lake Lanoto'o (Samoa) has at least one species of *Peridinium* (Schabetsberger et al., 2009).

The sediment in most lakes was highly unconsolidated algal gytta. Sediment in Grand Lac (Grande Terre, New Caledonia) and Barora Pond (Tetepare, Solomon Islands) had high amounts of lithogenous material and sediments in Harai Lake #2 (Rendova, Solomon Islands) had sandy material. Onetahi Pond (Tetiarora, French Polynesia) was manufactured in the early 2010s so sediment has only been accumulating for a few years. Radiometric dating in 15 lakes verifies that core-top sediments are not older than 1960 (**Table A.4; Table A.5**). We estimate that the core-top sediments in this study incorporate several years of accumulation ranging from 0.4±3 years to 20±50 years, further details are provided in the Supplemental Information (**Table A.1**).

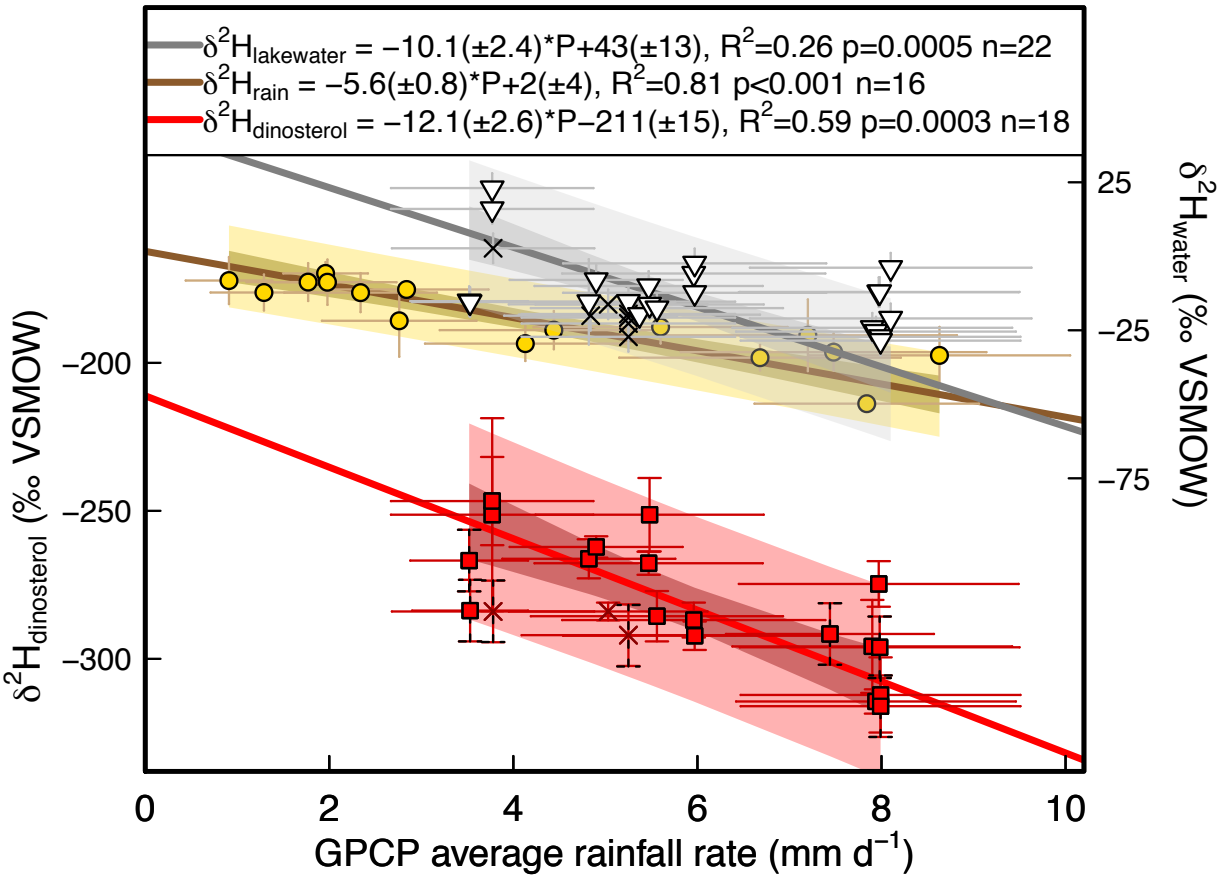

Fig. 2. The relationship between GPCPv2.3 mean annual precipitation rate (mm d^{-1}) for the 1979-2016 period and $\delta^2H_{dinosterol}$, $\delta^2H_{lakewater}$, and δ^2H_{rain}. Lake-averaged $\delta^2H_{dinosterol}$ values (red squares) from 18 lakes are plotted on the left axis. Also plotted are 3 lakes with high vegetation cover (dark red crosses) that are not included in the regression. On the right axis: lake-averaged $\delta^2H_{lakewater}$ values (white triangles) from 22 lakes in addition to 7 lakes with high vegetation cover (black crosses) that are not included in the regression, and GNIP/JAMSTEK δ^2H_{rain} values (yellow circles) from 16 stations (same as **Fig. A.2b**). X-axis errors are precipitation rate errors provided by GPCP. $\delta^2H_{lakewater}$ error bars are the estimated standard error of tropical lake water (±5 ‰, except 14 ‰ at Lake Emaotul, see text), δ^2H_{rain} error bars are weighted standard deviations, and $\delta^2H_{dinosterol}$ error bars are the standard deviations of multiple core-top values. When only one core-top was measured the pooled standard deviation is shown (±10.4 ‰ indicated by error bars with black dashes). The dark and light shaded bands around the regression lines are the 95% confidence and prediction intervals. To account for large errors in both axes, linear fits were determined using the maximum likelihood estimate method (York et al., 2004) (solid red, gray, and brown lines) incorporating bivariate analytical uncertainty (Thirumalai et al., 2011). *Not shown* ordinary least squares regressions:
$\delta^2H_{lakewater}$ = -3.9(±1.4)*P+11(±9), R^2=0.27, p=0.01, n=22
δ^2H_{rain} =-3.5(±0.7)*P-6(±3), R^2=0.67, p=0.0001, n=16
$\delta^2H_{dinosterol}$ = -9.6(±2.0)*P-223(±12), R^2=0.58, p=0.0002, n=18

Results

Amount effect

There are 15 IAEA/GNIP stations and 1 JAMSTEC station (Palau) (**Fig. 1**) on tropical Pacific islands between 30°N and 30°S with at least 23 δ^2H measurements from at least 3 years (**Table A.2**). The 9 mm d^{-1} range in precipitation rates vs. the 44 ‰ range in mean annual amount-weighted δ^2H_{rain} yields a tropical Pacific "amount effect" of [y= -4.5(±0.6)x+1(±4), R^2=0.42, p<0.001, n=16], where the Hilo station data fell well above the 95 % prediction interval (**Fig. A.2a**). Even though most GNIP station sample collection dates (many in the 1960's) did not overlap with the GPCP 1979-2016 period, δ^2H_{rain} was better correlated with regional GPCP precipitation data (**Fig. A.2b; Fig. 2**), and had a statistically indistinguishable "amount effect" of [y= -5.6(±0.8)x+2(±4), R^2=0.81, p<0.001, n=16].

At the 30 SPCZ sampling locations used in this study, multi-model mean $\delta^2H_{SWINGrain}$ data from four nudged isotope-enabled global circulation models (**Fig. A.3; Table B.3**) had a small 22 ‰ range and multi-model mean precipitation rates had a 7.3 mm d^{-1} range. $\delta^2H_{SWINGrain}$ vs. multi-model mean precipitation rates gave a smaller "amount effect" of [y= -2.9(±0.6)x-14(±4), R^2=0.66, p<0.001, n=30] (**Fig. A.2c**) about half the size as that from GNIP/JAMSTEK observation data. $\delta^2H_{OIPCrain}$ values from this study's 30 sample sites had a 34 ‰ range with very large uncertainties at several lake sites, especially Vanuatu (**Table B.3**). $\delta^2H_{OIPCrain}$ values vs. GPCP precipitation rates gave an "amount effect" of [y= -8.6(±2.4)x+16(±14), R^2=0.72, p=0.002, n=30] (**Fig. A.2d**) ~two times larger than GNIP/JAMSTEK observation data.

Regional meteoric water line

δ^2H_{water} and $\delta^{18}O_{water}$ of 38 rain events collected in Nauru, Fiji, Wallis, Solomon Islands, Vanuatu, and Tetiaroa between 2010-2016 (**Table B.2**) gave a SPCZ-RMWL [RMWL= 7.6(±0.3)x+11.5(±0.9), R^2=0.93, p=<0.001, n=38] with a slope similar to South Pacific tropical IAEA/GNIP data (GNIP slopes ranged from 6.4 to 8.1 (with a 7.3±0.1 mean)), but with a larger intercept than GNIP data (GNIP intercepts ranged from 0.0 to 10.4 (with a 6.7± 0.3 mean) (**Fig. 3; Fig. A.8**). Water samples from Fiji, Wallis, and Vanuatu representative of long-term precipitation from rain tanks, bottled and tap water, streams, and cave drip water, in addition to published precipitation isotope data from Tahiti (Hildenbrand et al., 2005) and Papua New Guinea (Ferguson, 2007; Ferguson et al., 2011) agree with the SPCZ-RMWL (**Fig. 3; Fig. A.8**). As expected for samples containing seawater, brackish and salty water samples from lakes, channels, lagoons, and ocean water with salinities between 2-35 ppt fell off the RMWL (**Fig. 3**).

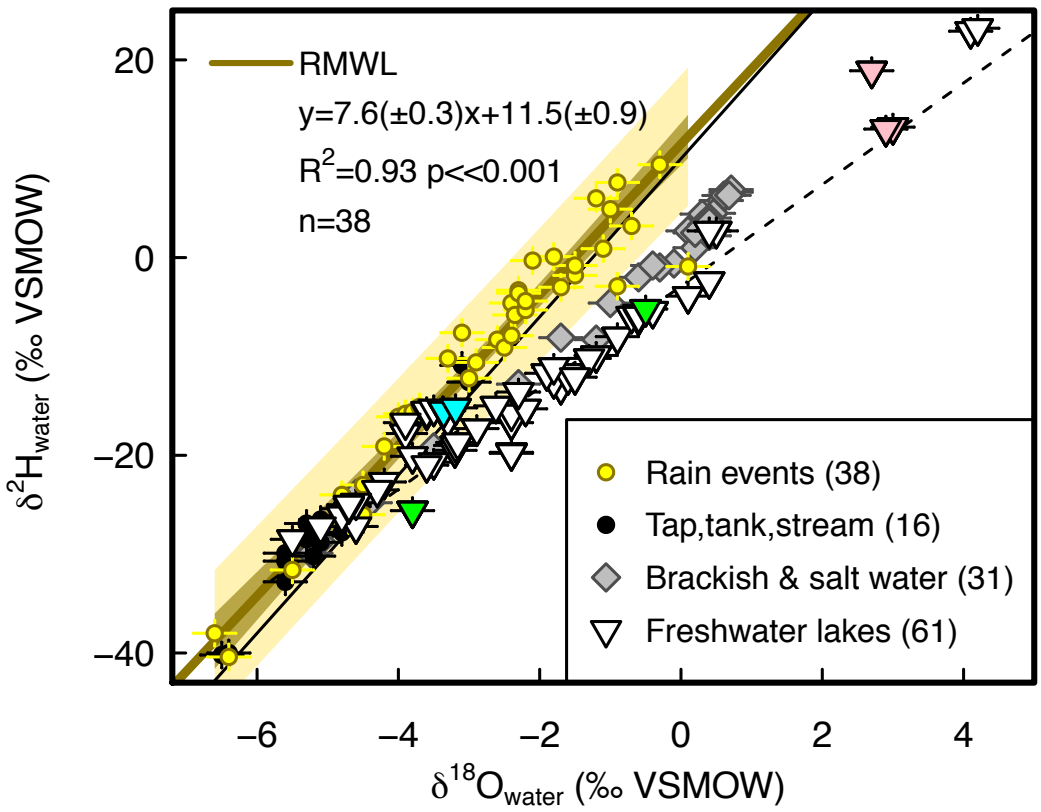

Fig. 3. Hydrogen and oxygen isotope values from SPCZ surface waters. The GMWL (y=8x+10) is shown for reference (thin black line). Error bars represent analytical uncertainty and are smaller than symbols in some cases. Samples from 38 local rain events (yellow circles) create a regional meteoric water line (RMWL) represented by the thick brown line, dark and light shading indicates the 95 % confidence and prediction intervals, the linear fit was determined using the maximum likelihood estimate method (York et al., 2004) incorporating bivariate analytical uncertainty (Thirumalai et al., 2011). Water samples from rain tanks, bottled or tap water, streams, and cave drip water (black dots) presumably average over multiple rain events during longer timescales than discrete rain samples and generally fall along the RMWL. Gray diamonds represent 31 samples collected from brackish coastal ponds, inlets, lagoons, and the ocean at salinities from 2 to 35 ppt. 61 individual freshwater lake samples (triangles) from 31 lakes fall along the RMWL at sites with high precipitation rate or high altitudes, and away from the RMWL at sites with low precipitation rates and form a SPCZ local evaporation line (dashed line determined using maximum likelihood estimate method y=5.1(±0.1)x-2.9(±0.2), R^2=0.95, p<<0.001, n=61). Highlighted in cyan are samples from lake on Grande Terre (New Caledonia) which are meteoric compare to other locations with similar evaporation and rainfall rates. Highlighted in green is Lake Emaotul (Efate, Vanuatu) with a sample that was ^{2}H-enriched by 20 ‰ in September 2015 compared to May 2017. Highlighted in pink is Rimatu'u Pond (Tetiarora, French Polynesia) with a sample that was 5 ‰ ^{2}H-enriched with salinity=2 ppt in October 2015 compared to duplicate samples when salinity=0 ppt in March 2015. *Not shown* ordinary least squares regressions: RMWL: y=7.2(±0.3)x+10.4(±1.0), R^2=0.93, p<<0.001, n=38; SPCZ LEL: y=5.1(±0.1)x-1.7(±0.4), R^2=0.95, p<<0.001, n=61

Lake water

Figure 3 shows individual $\delta^2H_{lakewater}$ samples that form a SPCZ-wide local evaporation line with a smaller slope in relation to the RMWL determined by the relative humidity of the air (and assumed kinetic and equilibrium isotope effect) (Henderson and Shuman, 2009). Solomon Islands lakes had the most isotopically depleted water and plotted closest to the RMWL while Tetiaroa lakes (pink trianles) showed the greatest extent of evolution along the LEL due to greater extend of evaporation. Samples from Lake Tagimaucia (Fiji), Lake Lanoto'o (Samoa), and both lakes on New Caledonia (New Caledonia lakes are highlighted in cyan) fell on/near the RMWL indicating these lakes experienced little evaporation, at least at the time of sampling. Only three lakes were sampled at 2 different time points. Lake Lanoto'o (Samoa) was sampled in July 2013 and September 2014 and surface $\delta^2H_{lakewater}$ differed by 4 ‰ (Hassall, 2017). Rimatu'u Pond (Tetiaroa) was sampled in March 2015 and at the end of the dry season in October 2015. The October sample was 7 ‰ ^{2}H-enriched and salinity increased from 0 to 2 ppt (highlighted in pink in **Fig. 3**). Emaotul Lake (Efate, Vanuatu) was sampled in September 2015 and again May 2017 when it was 20 ‰ more ^{2}H-depleted (highlighted in green in **Fig. 3**). Because the seasonal variation in lake water isotopes is otherwise unknown, we adopt an estimated δ^2H error value of 5 ‰ for each lake-averaged value (Nelson and Sachs, 2014a). However, due to the large observed change in water isotopes in Lake Emaotul, the standard deviation of its two measurements is used in all statistics and regressions (±14.4 ‰). Lake Wanum (Papua New Guinea) was the only lake with a sediment sample but no water sample. All water sample data is available in **Table B.2**.

The lake-averaged $\delta^2H_{lakewater}$ samples had a 52 ‰ range from -29.4 ‰ to 23.0 ‰ (**Table 1**). $\delta^2H_{lakewater}$ varied by 25 ‰ between 8 nearby Solomon Islands lakes, 20 ‰ between 3 nearby

Tetiarora lakes, 19 ‰ between 10 Vanuatu lakes, and 10 ‰ between 3 nearby Wallis Islands lakes. The 20 ‰ range between 3 nearby Tetiarora lakes was highly influenced by ^{2}H-depleted Onetahi Pond that is extensively covered in vegetation. Likewise, the 19 ‰ range in $\delta^{2}H_{lakewater}$ between 10 Vanuatu lakes becomes only 8 ‰ if 5 lakes with extensive vegetation cover are removed. Accordingly, these high vegetation cover sites, in addition to Lake Tagimaucia (Fiji) which is covered in floating peat sedge (Southern et al., 1986), were not included in $\delta^{2}H_{lakewater}$ vs. environmental regressions owing to their attenuated evaporative ^{2}H-enrichement.

$\delta^{2}H_{lakewater}$ values were significantly correlated with GPCP precipitation rates [$\delta^{2}H_{lakewater}$ = -10.1(±2.4)*P+43 (±13), R^{2}=0.26, p=0.0005, n=22] (**Fig. 2**). $\delta^{2}H_{lakewater}$ values did not show a strong correlation with OAFlux evaporation rates [$\delta^{2}H_{lakewater}$ = 75(±34)*E-319 (±141), R^{2}=0.05, p=0.04, n=22] (**Fig. A.7**), but were significantly correlated with P-E [$\delta^{2}H_{lakewater}$ = -8.1(±1.7)*(P-E)+0(±12), R^{2}=0.23, p=0.0001, n=22] (**Fig. A.9**). $\delta^{2}H_{lakewater}$ values were also significantly correlated with $\delta^{2}H_{rain}$ values calculated from the tropical pacific "amount effect" equation using GPCP rain rates at each lake site [$\delta^{2}H_{lakewater}$ = 2.6(±1.1)*$\delta^{2}H_{rain}$ +63(±30), R^{2}=0.28, p=0.02, n=22] (**Fig. A.10**). Note these regressions did not include $\delta^{2}H_{lakewater}$ values from seven lakes with high vegetation cover since the effects of local evaporation were inhibited.

$\delta^{2}H_{dinosterol}$ values

All 44 $\delta^{2}H_{dinosterol}$ values from core-top samples were ^{2}H-depleted compared to $\delta^{2}H_{lakewater}$ values (**Table B.1**). Lake-averaged $\delta^{2}H_{dinosterol}$ core-top values from 21 sites had a 69 ‰ range from -247 ‰ to -316 ‰ (**Table 1**) and were correlated with $\delta^{2}H_{lakewater}$ values [$\delta^{2}H_{dinosterol}$ = 1.9(±0.3)* $\delta^{2}H_{lakewater}$ -258(±5), R^{2}=0.50, p<0.001, n=20] (**Fig. 4**), where the regression includes

lakes with high vegetation cover to demonstrate the fidelity to which algal lipids track changes in their source water. $\delta^2H_{dinosterol}$ was significantly correlated with GPCP precipitation rates [$\delta^2H_{dinosterol}$ = -12.1(±2.6)*P-211(±15), R^2=0.59, p=0.0003, n=18] (**Fig. 2**) and OAFlux evaporation rates [$\delta^2H_{dinosterol}$ = 47(±18)*E-478(±75), R^2=0.24, p=0.004, n=18] (**Fig. A.7**). The relationship between GPCP precipitation minus OAFlux evaporation (P-E) and $\delta^2H_{dinosterol}$ was also significant [$\delta^2H_{dinosterol}$ = -9.7(±1.8)*(P-E)-265(±4), R^2=0.54, p=0.0001, n=18] (**Fig. A.9**), and similar to the $\delta^2H_{dinosterol}$-GPCP relationship. $\delta^2H_{dinosterol}$ was also significantly correlated with δ^2H_{rain} values calculated from the tropical Pacific "amount effect" equation using GPCP rain rates at each lake site [$\delta^2H_{dinosterol}$ = 2.5(±0.8)*(δ^2H_{rain})-206(±23), R^2=0.59, p=0.005, n=18] (**Fig. A.10**) (these regressions did not include $\delta^2H_{dinosterol}$ values from three lakes with high vegetation cover since the effects of local evaporation were inhibited).

Discussion

$\delta^2H_{dinosterol}$ values

The slope of the $\delta^2H_{dinosterol}$-GPCP relationship (-12.1±2.6 ‰ (mm d^{-1})$^{-1}$) is similar to the $\delta^2H_{lakewater}$-GPCP relationship (-10.1±2.4 ‰ (mm d^{-1})$^{-1}$), both of which are steeper than the "amount effect" (-5.6±0.8 ‰ (mm d^{-1})$^{-1}$) (**Fig. 2**) due to the enriching effects of evaporation. This aptly demonstrates how hydrologic conditions are reflected in the biomarker proxy dinosterol via the links between precipitation rate, evaporation, lake water isotopes, and algal lipid isotopes.

The $\delta^2H_{dinosterol}$-GPCP relationship [$\delta^2H_{dinosterol}$ = -12.1(±2.6)*P-211(±15), R^2=0.59, p=0.0003, n=18] (**Fig. 2**) was very similar to $\delta^2H_{dinosterol}$-P-E relationship [$\delta^2H_{dinosterol}$ = -

9.7(±1.8)*(P-E)-265(±4), R^2=0.54, p=0.0001, n=18] (**Fig. A.9**). This similarity is likely a result of the small range of OAFlux evaporation rates (3.5 to 4.9 mm d^{-1}) compare to GPCP precipitation rates (3.5 to 8.1 mm d^{-1}) across the sample sites. Indeed, the P-E spatial pattern is dominated by P in this region (Fig. 4 in Schanze et al., 2010). We propose that the $\delta^2H_{dinosterol}$-GPCP relationship can be used to calculate precipitation in the SPCZ region.

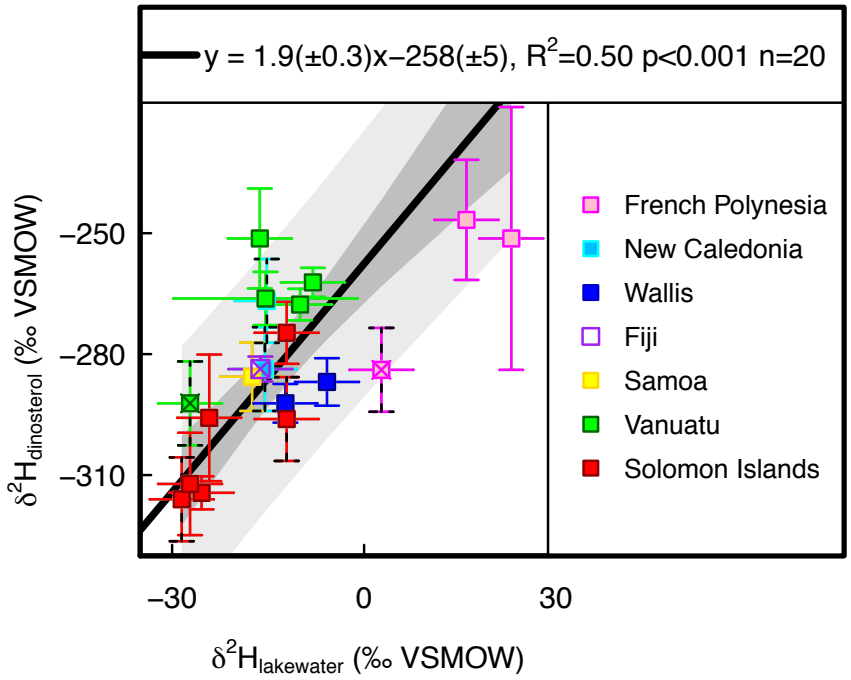

Fig. 4. $\delta^2H_{lakewater}$ vs. $\delta^2H_{dinosterol}$ from 20 SPCZ lakes. Lakes in French Polynesia (pink) have the most ^{2}H-enriched $\delta^2H_{lakewater}$ and $\delta^2H_{dinosterol}$ values. New Caledonia (light blue), Wallis Island (blue), Fiji (open purple), Samoa (yellow), and Vanuatu (green) lakes are less ^{2}H-enriched. Lakes in the Solomon Islands (red) have the most ^{2}H-depleted $\delta^2H_{lakewater}$ and $\delta^2H_{dinosterol}$ values. $\delta^2H_{lakewater}$ error bars are the estimated standard error of tropical lake water (±5 ‰, except 14 ‰ at Lake Emaotul, see text), $\delta^2H_{dinosterol}$ error bars are the standard deviations of multiple core-top values. Where only one core-top was measured, the pooled standard deviation is shown (±10.4 ‰ indicated by error bars with black dots). The dark and light shaded region represent the 95 % confidence and prediction intervals. Samples from lakes with high vegetation cover are indicated with crosses, and they are included in the regression (black line). To account for large errors in both axes, linear fits were determined using the maximum likelihood estimate method (York et al., 2004) incorporating bivariate analytical uncertainty (Thirumalai et al., 2011).
Not shown ordinary least squares regression: y=1.1(±0.3)x-268(±5), R^2=0.49, p=0.0005, n=20

The correlation between $\delta^2H_{dinosterol}$ and $\delta^2H_{lakewater}$ (**Fig. 4**) emphasizes that environmental water isotopes are the first order control on algal lipid isotopes. This is in agreement with numerous studies that show microorganism lipids track the isotopes of their environmental water in the lab (Dirghangi and Pagani, 2013a, 2013b; Englebrecht and Sachs, 2005; Osburn et al., 2016; Paul, 2002; X. Zhang et al., 2009; Zhang and Sachs, 2007) and field (Huang et al., 2004; Polissar and Freeman, 2010; Sachs and Schwab, 2011; Sachse et al., 2012, 2004; Sauer et al., 2001; Schwab et al., 2015a; Schwab and Sachs, 2011).

The slope of the SPCZ $\delta^2H_{lakewater}$ - $\delta^2H_{dinosterol}$ relationship (1.9±0.3) is steeper than various (non-dinosterol) lipids from freshwater cultures of Chlorophyceae and Trebouxiophyceae which ranged from 0.7 to 1.0 (Zhang and Sachs, 2007). It is also steeper than the relationship of $\delta^2H_{dinosterol}$ between suspended particles and $\delta^2H_{lakewater}$ of freshwater lakes across Cameroon (0.7±0.2) and Cameroon lake sediments (1.5±0.3) (Schwab et al., 2015a). The Cameroon sediment samples were correlated with lake eutrophic conditions and hypothesized to be influenced by increased dinoflagellate heterotrophy or post-depositional $\delta^2H_{dinosterol}$ alterations (Schwab et al., 2015a). We note however, that if errors in SPCZ $\delta^2H_{lakewater}$ were ignored and a simple ordinary least squares regression was used for the freshwater SPCZ lakes, the relationship would be within error of both freshwater culture and Cameroon suspended particle data (1.1±0.3). Since sedimentary aquatic lipids incorporate several years of accumulation, better estimates of long-term mean values for $\delta^2H_{lakewater}$ and knowledge about the timing of dinosterol production in relation to $\delta^2H_{lakewater}$ could indicate if the SPCZ $\delta^2H_{lakewater}$ - $\delta^2H_{dinosterol}$ relationship is different than other freshwater algal lipids, or if it is a product of the regression technique used.

Non-hydrologic environmental factors including metabolism, growth rate or growth stage, irradiance, and species composition may contribute to the scatter in the SPCZ $\delta^2H_{lakewater}$ - $\delta^2H_{dinosterol}$ relationship. Differences in metabolic state can have a large impact on $^2H/^1H$ ratios in lipids, at least in prokaryotes (Heinzelmann et al., 2015; Osburn et al., 2016; X. Zhang et al., 2009). Heterotrophic dinoflagellates can contribute to the sedimentary record (Amo et al., 2007) and the extent to which dinoflagellates utilize photoautotrophy versus heterotrophy to support cellular function could potentially influence $\delta^2H_{dinosterol}$ values at some sites more than others. In addition, differences in growth rate and phase (Chivall et al., 2014; Heinzelmann et al., 2015; Sachs and Kawka, 2015; Wolhowe et al., 2015, 2009; Z. Zhang et al., 2009) and irradiance (Sachs et al., 2017; van der Meer et al., 2015) are known to influence lipid-water $^2H/^1H$ fractionation so monitoring productivity and turbidity of lake waters could indicate if these factors play a role in SPCZ freshwater lakes. Furthermore, given the large diversity in dinosterol producing dinoflagellates (Janouškovec et al., 2016), it is likely that the large spatial and environmental distributions in this study harbor distinct species assemblages. While it isn't possible to fully characterize any of these potential influences in our data, many lakes with diverse physical and chemical properties were targeted to capture the range of species, heterotrophy, light, and growth rate effects. Despite these influences that may be responsible for the scatter, the SPCZ $\delta^2H_{lakewater}$ - $\delta^2H_{dinosterol}$ relationship together with the robust empirical relationship between $\delta^2H_{dinosterol}$ and precipitation rates, supports the use of $\delta^2H_{dinosterol}$ as a proxy for hydrologic variations.

δ^2H_{rain} values and the amount effect

Tropical precipitation isotope observations are sparse in space and time, but characterizing spatial variability in modern δ^2H_{rain} values is important for understanding controls on the isotopic composition of lake water and dinosterol. Several studies have already established a strong inverse relationship between precipitation amount and δ^2H_{rain} values in the tropics (Araguás-Araguás et al., 1998; Conroy et al., 2013; Dansgaard, 1964; Kurita et al., 2009; Rozanski et al., 1993), a relationship that is most robust over annual timescales (Conroy et al., 2013) and when isotope data are compared to regional (as opposed to local) precipitation rates (Kurita et al., 2009).

Multiple approaches specific to this study's SPCZ lake sites demonstrate that the "amount effect" is a robust feature of precipitation isotopes. The SWING2 "amount effect" is about two times smaller (-2.3±0.6 ‰ (mm d^{-1})$^{-1}$ (**Fig. A.2c**)), while the OIPC "amount effect" is about two times larger (-8.1±2.2 ‰ (mm d^{-1})$^{-1}$ (**Fig. A.2d**)) than the relationship from GNIP/JAMSTEK station data across the entire tropical Pacific (-4.5±0.6 ‰ to -5.6±0.8 ‰ (mm d^{-1})$^{-1}$) depending if local or regional precipitation rates are used **Fig. A.2a,b**). Recent advancements in isotope-incorporated general circulation models have greatly improved understanding of the behavior of water isotopes (Yoshimura, 2015) and advances in interpolation algorithms have aided prediction of water isotopes in remote areas (Bowen, 2010). Irrespective of the true relationship for the SPCZ "amount effect", all three approaches indicate that higher mean SPCZ precipitation rates are associated with ^{2}H-depleted precipitation.

$\delta^2H_{lakewater}$ values

$\delta^2H_{lakewater}$ is correlated with GPCP precipitation rates with a steeper slope than GPCP-δ^2H_{rain} due to evaporative enrichment (**Fig. 2**). The effects of evaporation are also apparent from the evolution of lakes along the SPCZ-wide LEL (**Fig. 3**). However, $\delta^2H_{lakewater}$ values are not well-correlated with mean ocean evaporation rates (**Fig. A7**). The dinosterol samples were better correlated with OAFlux evaporation (R^2=0.24) than lake water samples (R^2=0.05), which could indicate that the ocean evaporation product is not applicable to the lake sites in this study, or be a result of the greater timespan represented by dinosterol in core-top sediment (years) than lake water (weeks-months).

Most of the lake water samples in this study represent snapshots in time and likely do not reflect mean annual $\delta^2H_{lakewater}$. Additional sampling at these sites could help reveal true long term mean $\delta^2H_{lakewater}$ values. For instance, two visits to Lake Emaotul (Efate, Vanuatu) revealed a surprisingly large 20‰ change in $\delta^2H_{lakewater}$ values; the 2015 sample coincided with El Niño drought and the 2017 sample was collected shortly after Cyclone Donna which increased lake depth from 6 to 6.4 m.

Some of the local variability in $\delta^2H_{lakewater}$ is related to lake catchment area and residence time (Henderson and Shuman, 2009; Leng and Marshall, 2004). The $\delta^2H_{lakewater}$ value from (aquatic vegetation-free) Red Lake (Thion, Vanuatu) was -17 ‰ but it's larger neighbor White Lake (also aquatic vegetation-free) was ^{2}H-enriched with a value of -10 ‰ (**Table 1**). The difference may be a due to Red Lake's small volume, and potentially shorter residence time, responding more readily to sporadic ^{2}H-depleted rain events, especially cyclones. On Wallis Island three nearby lakes, Lake Lalolalo, Lake Lanutavake, and Lake Lano were all vegetation free and had a 10 ‰ range in $\delta^2H_{lakewater}$ correlated with lake volume, reflecting the greater

impact that evaporation has on lakes with larger surface area to volume ratios. $\delta^2H_{lakewater}$ values vary by ~25 ‰ among 8 nearby Solomon Islands lakes; Rendova Island Harai lakes to the north were more ^2H-depleted compared to the large Lake Rano in the south. This is likely due to the highlands in the north that contribute to the watershed for many of the Harai lakes compare to the lower-altitude catchment for Lake Rano. Clearly, several secondary factors influence $\delta^2H_{lakewater}$ values, and may partially obscure the relationship between OAFlux and $\delta^2H_{lakewater}$. Nevertheless, the strong correlation between precipitation rates and $\delta^2H_{lakewater}$ and values (**Fig. 2**) and between δ^2H_{rain} and $\delta^2H_{lakewater}$ values (**Fig. A.10**) indicates that δ^2H_{rain} (via precipitation rate) and evaporative enrichment are the primary influences on $\delta^2H_{lakewater}$.

Paleoclimate applications

The ultimate goal of this study is to develop an empirical relationship between modern satellite precipitation and the lipid biomarker dinosterol as a tool for calculating pre-instrumental precipitation in the SPCZ from lake sediment records. $\delta^2H_{dinosterol}$ values have a remarkably strong empirical relationship with GPCP precipitation rates across the SPCZ (**Fig. 2**) despite potential sources of variability in lake water and lipid isotopes. Three steps are required to get from 1) precipitation rate to δ^2H_{rain}, 2) δ^2H_{rain} to $\delta^2H_{lakewater}$, and 3) $\delta^2H_{lakewater}$ to $\delta^2H_{dinosterol}$. Despite the indirect connection, the major hydrological patterns of the SPCZ are clearly reflected in the dinosterol biomarker from recent sediments and create a useful empirical relationship that can be applied at several sites. We propose that the SPCZ GPCP-$\delta^2H_{dinosterol}$ relationship from freshwater lakes in the SPCZ can be used as a transfer function for quantifying past regional precipitation rates in the SPCZ making the assumptions that the relationships between precipitation rates, precipitation isotopes, and evaporation rates remained constant through time.

The most straightforward approach to applying this calibration is re-arrangement of the modern GPCP-$\delta^2H_{dinosterol}$ relationship (**Fig. 2**) to calculate paleoprecipitation downcore:

$$\mathbf{Pp} = \delta^2H_{sample} - \mathbf{I} / \mathbf{S} \qquad \text{[Eq. 1]}$$

where **Pp** is the calculated paleoprecipitation, δ^2H_{sample} is a downcore measurement, **I** is the intercept of the regression (-211), and **S** is the sensitivity of the regression (-12.1).

Figure 5 quantifies the uncertainties of reconstructed precipitation rates to uncertainties in the slope and intercept errors from the calibration regression from Eq. 1 as well as analytical uncertainty in downcore δ^2H_{sample} measurements. Propagating these uncertainties using a Monte Carlo approach results in calculated precipitation errors about twice as large (±1.5 to 3.1 mm d^{-1}) as errors in the modern SPCZ GPCP precipitation rates (±0.3 to 1.5 mm d^{-1}).

The GPCP-$\delta^2H_{dinosterol}$ calibration offers the opportunity to extend estimates of large scale mean precipitation into the past within the SPCZ region. The best application would make use of sediment cores from multiple lakes from different areas of the SPCZ to map spatial patterns of precipitation changes through time.

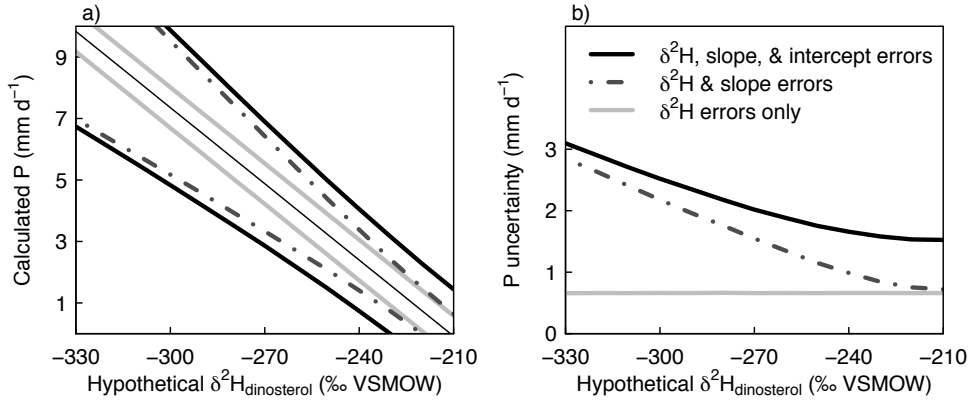

Fig. 5. Uncertainties in calculated precipitation. Calculated P (a) (thin black line) is shown for a range of hypothetical $\delta^2H_{dinosterol}$ values with uncertainties from three sources. Panel b) summarizes the magnitude of uncertainty in calculated P. Uncertainties were calculated using a Monte Carlo approach with 100,000 iterations with normally distributed errors from analytical uncertainty in $\delta^2H_{dinosterol}$ measurements (±8 ‰) (thick gray lines), plus calibration error in the slope (±2.6) (dark gray dashed lines), plus intercept errors (±15) (thick black lines).

Conclusions

This work investigated the environmental controls on the $^{2}H/^{1}H$ ratios of SPCZ lake waters and the dinoflagellate sterol dinosterol purified from recent freshwater lake sediments. The lakes in this study represent diverse freshwater ecosystems with varying physical and chemical parameters. The main controls on $\delta^{2}H_{lakewater}$ were precipitation rate and evaporation. Additional lake-specific environmental properties such as lake volume, water residence time, and catchment area likely contribute to $\delta^{2}H_{lakewater}$ variability in each region. While environmental and growth parameters such as light, growth rate, metabolism, and species composition likely contribute to $\delta^{2}H_{dinosterol}$ variability, we conclude that the main control on $\delta^{2}H_{dinosterol}$ was $\delta^{2}H_{lakewater}$. The breadth of physical parameters that impact $\delta^{2}H_{lakewater}$, combined with the range of environmental/growth processes that impact $\delta^{2}H_{dinosterol}$, highlight the importance of sampling multiple lakes in each region. The empirical SPCZ GPCP-$\delta^{2}H_{dinosterol}$ relationship provides a method to quantitatively reconstruct past precipitation rates with uncertainties about 2-fold greater than GPCP uncertainties.

Acknowledgements

The authors would like to thank G. Hope for providing sediment from his 1995 visit to Lake Emaotul, S. Haberle for providing sediment from his 1998 visit to Lake Wanum, and R. Smittenberg for extracting lipids from the Lake Wanum sample. We are grateful for permission from all civic and traditional authorities and assistance on Wallis Island from J.N. Richey, U. Sichrowsky, J.-Y. Meyer, A. Malau, K. Manufeki, S. Tauvale, C. Manry and others from Service de L'Environment, M. Fotuaika, J.-F. Poncet, P. Nicomette, S. Felomaki, P. Tauvale, C. Chauvet, and the planning assistance from R. Schabetsberger, C. Lique, M. Bridoux, and C. Altman. We would like to thank T. Thomas and the Tetepare Descendants' Association Rangers

for helping with sample collection in the Solomon Islands. We thank Cerillo Balo from the Vanuatu Kaljarol Senta at Port Olry for assisting with sample collection in Vanuatu (2012). Thanks to Msr. François Le Borgne and the Department of Pollution Prevention and Risk, New Caledonia for permission to core Grand Lac and Lake Hut and to Olivier for field assistance. Field work in Upolu, Samoa was kindly permitted by Taule'ale'ausmai Laavasa Malua, Chief Executive Officer, Niualuga Evaimalo and staff in Ministry Natural Resources and Environment. Field assistance was provided by Josie Hill, Lucy, Tinifu, Solomano and Ai. In Vanuatu (2015 & 2017) we would like to thank Esline Garaebiti and Philip Malsale of the Geo-Hazards Division, Government of Vanuatu for permission to undertake fieldwork in Efate, Lake Emoatul, and to Fabienne, Maurice and Hugo for assistance with construction of the coring platform. We are grateful for the assistance of C. Seanger, I. Baldon, A. Gagnon, J. Gregerson, and L. Brandkamp for collection of samples from Tetiarora. S. Hing, E. Baldwin, A. Witt, and P Sobeck provided careful assistance in the lab. M. Wolfshorndl, T. Magee, and S. N. Ladd, assisted with splitting cores at LacCore. We thank C. Kaapu-Lyons, N. Wallsgrove, and B. Popp for analyzing Wallis Island water samples. Conversations with L. Thompson, S. PoChedley, R. Echols, J. Scheff, S. Rushley, D. Battisti, R. Wood, K. Thirumalai and constructive comments from A.E. Ingalls and P. Quay greatly improved this manuscript.

Funding: This work was supported by the U.S. National Science Foundation [grant #1502417] to J.P.S; a University of Washington Program on Climate Change Fellowship and IGERT Ocean Change Fellowship [grant #NSF1068839] provided partial support for A.E.M; radiometric dating was supported by AINSE (The Australian Institute of Nuclear Science and Engineering) [Award No ALNGRA14513] to M.P.; IGERT Ocean Change mini-research awards and a University of Washington Quaternary Research Center research award to A.E.M; University of Washington

Quaternary Research Center and Tetiarora Society assisted with travel; The Explorers Club Exploration Fund Grant, Gilchrist Expedition Grant and Royal Geographical Society (with IBG) Monica Cole Grant assisted with travel to Samoa. Analysis of water samples from Samoa and New Caledonia were undertaken at the NERC Isotope Geosciences Laboratory. Funding was provided for Lake Emoatul through NERC Urgent grant NE/N006674/1.

Lake Lanoto'o and New Caledonia data was funded under a NERC Studentship to J.D. Hassall. All Radioisotope dating for lake Emoatul, Lanoto'o, Grand Lac and Lake Hut were undertaken by GAU.

Chapter 3 Appendix A. Supplementary data

Table A.1. Estimated sediment accumulation time, elevation, depth, area, mean annual air temperature (NCEP/NCAR 1958-2016), evaporation rate (OAFlux 1958-2016), and precipitation isotope values cacluated from the tropical Pacific "amount effect" using GPCP precipiation rates.

Freshwater Site	Acc. time	σ	Elevation	Max. depth	Area	MAT	OAFlux	σ	δ^2H_{rain}	σ
	years	years	m	m	hector	°C	mm d^{-1}	mm d^{-1}	‰	‰
Rimatu'u Pond, Tetiaroa, French Polynesia	~0.5[a]		1	<1	9.0	25.8	4.03	0.35	-19.1	8.0
Oroatera Pond, Tetiaroa, French Polynesia			1	<1	0.3	25.8	4.04	0.35	-19.1	8.0
Onetahi Pond, Tetiaroa, French Polynesia[#,^]	< 10		1	<1	0.4	25.8	4.04	0.35	-19.2	8.0
Lake Tagamaucia, Teveuni, Fiji[#]	23	47	820	2.1	1.3*	25.8	4.03	0.36	-26.2	8.4
Grand Lac, Grande Terre, New Caledonia			~180-250	5	180	23.0	4.63	0.37	-17.8	6.1
Lake Hut, Grande Terre, New Caledonia			~180-250	2	4.4	23.1	4.64	0.37	-17.7	6.1
Otas Lake, Efate, Vanuatu			1	2.5	23	25.3	4.87	0.39	-25.5	7.8
Emaotul Lake, Efate, Vanuatu[$]	4		119	10	59	25.2	4.89	0.39	-25.0	7.7
Small Pond, Efate, Vanuatu[#]			85	2.5	4.0	25.2	4.88	0.39	-25.1	7.7
Red Lake, Thion, Vanuatu	12	25	9	2.5	4.0	26.2	4.18	0.38	-28.7	9.2
White Lake, Thion, Vanuatu	13	38	9	17	6.5	26.2	4.18	0.38	-28.7	9.2
Waérowa East Lake, Espiritu Santo, Vanuatu[#]	1	3	11	1.8	11	26.0	4.34	0.39	-27.4	8.8
Waérowa West Lake, Espiritu Santo, Vanuatu[#]			11		7.5	26.0	4.34	0.39	-27.4	8.7
Bellmolle North Lake, Espiritu Santo, Vanuatu[#]			14		3.4	26.0	4.33	0.38	-27.4	8.8
Bellmolle Swamp, Espiritu Santo, Vanuatu[#]			10		0.4	26.0	4.33	0.38	-27.4	8.8
Bellmolle South Lake, Espiritu Santo, Vanuatu			8		1.1	26.0	4.33	0.38	-27.4	8.8
Buada Pond, Nauru[$]			1	<1	5.3	27.7	3.54	0.41	-28.1	9.5
Lake Lanoto'o, Upolu, Samoa	5[b]		762	16	12	26.9	4.34	0.33	-29.1	9.8
Lake Lalolalo, Wallis	10	12	1	89	18	27.1	4.54	0.35	-31.4	10.2
Lake Lanutavake, Wallis	21	53	13	25	5.3	27.1	4.54	0.35	-31.4	10.2
Lake Lano, Wallis			3	4	1.9	27.1	4.54	0.35	-31.4	10.2
Lake Wanum, Papua New Guinea	10[c]		34	19	406	23.9	3.46	0.38	-39.7	9.6
Barora Pond, Tetepare, Solomon Islands	0.4	3	7	2.5	0.7	27.1	3.66	0.34	-42.2	11.4
Lake Tavara Tetepare, Solomon Islands	2	4	11	3.7	3.2	27.1	3.67	0.34	-42.4	11.4
Lake Rano, Rendova, Solomon Islands	3	6	34	11	54	27.1	3.72	0.34	-42.6	11.5
Harai Lake #1, Rendova, Solomon Islands	22	56	30	3	0.8	27.1	3.63	0.34	-42.7	11.4
Harai Lake #2, Rendova, Solomon Islands			10	5.3	1.5	27.1	3.63	0.34	-42.7	11.5
Harai Lake #3, Rendova, Solomon Islands	8	24	9	1.4	0.6	27.1	3.63	0.34	-42.7	11.4
Arundel Lake #1, Arundel, Solomon Islands			40		1.8	27.1	3.63	0.34	-43.4	11.5
Arundel Lake #2, Arundel, Solomon Islands			50		7.1	27.1	3.63	0.34	-43.3	11.6

[#]High vegetation cover

[^]Manufactured

[$]Ephemeral

[a]Trichet et al. 2013

[b]Hassall 2017

[c]Haberle 2002 (Tibito tephra dated to ~1660 at 30cm depth)

*Likely connected to the other water bodies with a total of 16 hectors (Southern et al. 1985)

Table A.2. List of GNIP and JAMSTEK stations with at least 20 samples, 3 years, b/t 30N and 30S, Pacific Island only.

Site Name	Lat	Lon	Elevation (m)	Station (mm/d)	SD (mm/d)	GPCP (mm/d)	SD (mm/d)	Wt.Mean δ^2H (‰)	SD (‰)	Wt.Mean δ^{18}O (‰)	SD (‰)	n δ^2H	Years sampled	Total years
Midway Island	28.22	-177.37	13	2.9	0.8	4.0	0.3	-12.27	6.59	-2.77	0.82	275	1962; '64; '66-69; '73-76; '78-80; '82-91	30
Hilo	19.72	-155.07	9	9.1	1.9	2.4	0.9	-5.78	3.84	-2.22	0.6	85	1962-64;67-69;	14
Wake Island	19.28	166.65	3	2.5	0.7	1.8	0.7	-8.71	6.4	-1.96	0.89	132	1962-69; '73; '75-76	11
Johnston Island	16.73	-169.52	2	1.9	0.6	1.3	0.6	-12.23	6.07	-2.48	0.73	90	1962-65; '73-76	8
Taguac	13.55	144.83	110	7.1	1.4	4.2	1.1	-29.5	5.88	-5	0.83	106	1962-66; '73-76	9
Yap	9.49	138.09	23	8.2	1.3	7.1	1.6	-34.25	4.31	-5.56	0.63	65	1969; '73-76	5
Truk	7.47	151.85	2	9.8	1.2	8.7	1.8	-32.38	6.29	-5.3	0.65	72	1968-69; '73-75	6
Palau (JAMSTEK)	7.0	134.3	2	7.0	4	2.0	0.7	-26.69	12.11	-4.52	1.56	48	2002-06	4
Chrsitmas Island	1.98	-157.46	3	1.0	0.8	7.2	1.6	-11.21	2.78	-2.41	0.36	23	1962-64	3
Bellavista	-0.69	-90.32	194	3.1	2.1	0.8	0.4	-8.19	7.95	-2.25	1.07	143	1995-2005; '07-08	13
Jayapura	-2.53	140.72	3	6.2	1.5	10.1	1.4	-33.47	9.61	-5.46	1.37	275	1962-63; 69-70; 73; 75-80; 82-83; 89	28
Canton Island	-2.77	-171.72	2	2.1	1.0	2.9	0.9	-21.78	12.14	-3.69	1.74	50	1962-65	4
Madang	-5.22	145.8	4	9.5	1.1	7.4	1.0	-49.79	2.81	-7.75	0.48	105	1969-70; '73-76; '78	13
Apia	-13.8	-171.78	2	8.4	1.6	5.6	1.4	-23.9	5.55	-4.56	0.7	108	1963-66; '73-77	9
Rarotonga Island	-21.2	-159.8	6	5.5	1.4	4.5	1.2	-24.94	6.46	-4.4	0.66	132	1980-83; '86-91	10
Easter Island	-27.17	-109.43	41	3.0	0.7	1.6	0.7	-8.75	7.66	-2.23	1.07	286	1969; 1991-2009; '11-14	24

Table A.3. Nudged SWING2 models with reference, simulation, and grid resolution.

Model	Key Reference	Simulations	Grid Resolution
ECHAM4	Hoffmann et al. 1998	Nudged ith ECMWF	2.8° x 2.8°
LMDZ4	Risi et al. 2010	Nudged with ECMWF	2.5° x 3.75°
GISS	Schmidt et al. 2007	Nudged with NCEP	2° x 2.5°
GSM	Yoshimura et al. 2008	Nudged with NCEP	1.9° x 1.9°

Dating Methods

Sediment cores were split at the University of Washington or LacCore. Age models for select cores were developed using radiocarbon and Lead-210 (^{210}Pb) analysis. Terrestrial leaf fossils from the top 70 cm of 13 sediment cores were analyzed for radiocarbon ages with accelerator mass spectrometry. Leaf fossils were pre-treated with an acid-base-acid procedure (Brock et al., 2010) at the University of Washington before analyses at Direct AMS (Seattle, WA), or pretreated and analyzed at Australian National University or CAMS (LLNL, Livermore, CA) (**Table A4**). Radiocarbon ages were calibrated using SHCAL13 (Hogg et al., 2013) and the SH1-2 bomb curve extension (Hua et al., 2013).

Selected sediment intervals from the uppermost portion (12 to 90 cm) of eight sediment cores were analyzed for abundance of atmosphere derived ^{210}Pb at Flett Research Ltd. or ANTSO (Australian Nuclear Science and Organization) facilities (**Table A5**). Detailed procedures are available in Atahan et al., (2014). Alpha spectrometry was used to measure total ^{210}Pb indirectly from Polonium-210 (^{210}Po) (the granddaughter of ^{210}Pb which is in secular equilibrium with ^{210}Pb within two years of deposition). Supported ^{210}Pb was measured indirectly from Radium-226 measurements. Atmospheric-derived unsupported ^{210}Pb was calculated by subtracting supported ^{210}Pb from total ^{210}Pb. A constant rate of supply (CRS) model (Appleby and Oldfield, 1978) was used to construct ^{210}Pb chronologies by relating exponential ^{210}Pb decay profiles to the cumulative dry mass-depth profiles as determined using bulk density measurements. Uncertainty in ages from the CRS model were conservatively estimated to be 20% of the age in years (Binford, 1990), with a minimum uncertainty of ±1 yr. The ^{210}Pb models were not validated with the independent tracer Cesium-137 due to limited sediment in these cores. Age-depth relationships were constructed using CRS modeled ages and radiocarbon ages using BACON v2.2 software (Blaauw and Christen, 2011). For all cores the topmost 0 cm age was assumed to be the same as collection date. The BACON chronologies were used and estimate the number of years and uncertainty in the 0-1cm section of these cores (**Table A1**). If age models were constructed for multiple cores from a lake, the average accumulation age and average uncertainty is reported. The uncertainties account for the fact that sediments could not accumulate after the collection date.

Dating Results

Leaf fossils picked from sediment core samples in the top 0-5cm show modern radiocarbon activity, confirming that the surface sediments in these lakes are recent. Leaf fossils from deeper in the sediments had older radiocarbon ages, indicating the cores are chronologically harmonious (**Table A4**). Unsupported ^{210}Pb had decreasing profiles in most cores tested and CRS models allowed for the estimation of recent sediment ages (**Table A5**). ^{210}Pb activity was not detected in core SHAR2UC1 from Lake Harai #2 (Rendova, Solomon Islands), potentially due to high sand content or lack of recent accumulation. ^{210}Pb activity was very low in core LATVKUC1 from Lake Lanutavake (Wallis), apart from the sample from 7-8cm, indicating fluctuations in grain size or potential mixing in the top of the core. Core SRANUC1 from Lake Rano (Rendova, Solomon Islands) had a decreasing ^{210}Pb activity profile from 6-16cm. The non-decreasing profile in the top 4cm was assumed to be due to rapid sedimentation rate (which acts to dilute ^{210}Pb activity) for the purposes of estimating sediment ages with the CRS model, however there is a possibility that the upper sediments were mixed. Accumulation time in years ranged from 0.4±3 years in Barora Pond (Tetepare, Solomon Islands), to ~ 20±50 years in Lake Tagimaucia (Taveuni, Fiji), Lake Lanuatavake (Wallis), and Harai Lake #1 (Rendova, Solomon Islands). Trichet et al., (2013) suggest that modern accumulation rates were around 2 cm per year in 1995 in Rimatu'u Pond (Tetiarora, French Polynesia), although sedimentation has been interrupted in the past during periods of high storm activity. Nearby Onetahi pond was manufactured in ~2010. Two radiocarbon dates from Emaotul indicate the 0-1 cm sample could contain 20 years of accumulation (Hope, 1996). Tagimaucia dates indicate sedimentation rates of 6-10 cm/yr (Southern, 1986). The presence of tephra in Lake Wanum sediment at 30cm assists with accumulation time estimate (Haberle, 2002).

Table A.4. Radiocarbon ages of fossil leafs from sediment cores. D=Direct AMS, C=CAMS, S=ANU

Freshwater site	Core ID	Depth (cm)	Percent modern carbon	±	^{14}C Age	±	LAB
Lake Tagimaucia, Taveuni, Fiji	TAG UC4	2.5	100.16	0.34	>Modern		D
Lake Tagimaucia, Taveuni, Fiji	TAG UC4	71.5	82.06	0.31	1588	30	D
Red Lake, Thion, Vanuatu	VTR UC3	17.5	100.69	0.45	>Modern		D
Red Lake, Thion, Vanuatu	VTR UC3	5.5	122.8	1.2	>Modern		D
Red Lake, Thion, Vanuatu	VTR UC3	4.5	100.54	0.23	>Modern		D
White Lake, Thion, Vanuatu	VTW UC2	3.5	139.09	0.31	>Modern		D
White Lake, Thion, Vanuatu	VTW UC2	31.5	96.53	0.64	284	53	D
Lac Lalolalo, Wallis	LALO UC22	1.5	106.45	0.26	>Modern		D
Lac Lalolalo, Wallis	LALO UC22	13.5	99.3	0.24	56	19	D
Lac Lalolalo, Wallis	LALO UC5	41	97.58	0.32	197	26	D
Lac Lanutavake, Wallis	LATVK UC1	14.5	96.88	0.52	255	43	D
Lac Lanutavake, Wallis	LATVK UC1	36.5	92.34	0.35	640	30	D
Lac Lanutavake, Wallis	LATVK UC4	3.25	142.38	0.51	>Modern		C
Lac Lanutavake, Wallis	LATVK UC4	26	94.9	0.25	420	21	D
Barora Pond, Tetepare, Solomon Islands	SBAR UC2	1	113.26	0.43	>Modern		C
Lake Tavara Tetepare, Solomon Islands	STAV UC4	3.5	100.53	0.37	>Modern		D
Lake Tavara Tetepare, Solomon Islands	STAV UC2	0-5	103.34		>Modern		S
Lake Rano, Rendova, Solomon Islands	SRAN UC1	1	103.98	0.56	>Modern		C
Lake Rano, Rendova, Solomon Islands	SRAN UC1	15	97.55	0.3	199	25	D
Harai Lake #1, Rendova, Solomon Islands	SHARI UC2	2	101.13	0.45	>Modern		C
Harai Lake #1, Rendova, Solomon Islands	SHARI UC2	24.5	95.52	0.34	368	29	D
Harai Lake #3, Rendova, Solomon Islands	SHAR3 UC2	2	113.69		>Modern		S
Harai Lake #3, Rendova, Solomon Islands	SHAR3 UC2	44.5	95.08		405	25	S
Harai Lake #3, Rendova, Solomon Islands	SHAR3 UC2	70.1	97.13		235	25	S
Harai Lake #3, Rendova, Solomon Islands	SHAR3 UC2	70.1	96.64		275	25	S

Table A.5. 210-Pb results

CORE	Lab	Depth (cm)	210Pb activity (Bq/kg) unsupported	Cumulative dry mass (g cm-2)	Modeled age (yr AD)
Lac Lalolalo, Wallis					
LALOUC22	F	2	53.5	0.047	2007.2
LALOUC22	A	3.5	57.2	0.092	2002.0
LALOUC22	F	5.5	53.9	0.172	1991.0
LALOUC22	A	7	51.1	0.292	1962.8
LALOUC22	F	8	43.0	0.356	1930.9
LALOUC22	F	9	14.3	0.423	1902.2
LALOUC22	F	10	5.3	0.516	1858.5
LALOUC22	A	11		0.576	
LALOUC22	F	12		0.647	
LALOUC22	F	13.5		0.872	
LALOUC22	A	20.5		1.208	
LALOUC22	A	30		2.538	
LALOUC22	A	35		3.638	
LALOUC24	F	3.5	54.7	0.105	1972.4
LALOUC24	F	5.5	21.7	0.165	1947.6
LALOUC24	F	7	12.1	0.225	1913.8
LALOUC24	F	8	5.1	0.255	1898.0
LALOUC24	F	9.5		0.3	
LALOUC24	F	11.5		0.38	
LALOUC24	F	13.5		0.46	
LALOUC24	F	16.5		0.58	
LALOUC24	F	20.5		0.78	
LALOUC24	F	24.5		0.98	
LALOUC24	F	27		1.13	
Lac Lanutavake, Wallis					
LATVKUC1	A	4	9		
LATVKUC1	A	8	98		
LATVKUC1	A	12	10		
LATVKUC1	A	16	15		
Waérowa East Lake, Espiritu Santo, Vanuatu					
VSWUC1	A	3.5	45	0.2	2008.9
VSWUC1	A	6.5	38	0.4	2006.0
VSWUC1	A	11.5	29	0.8	2000.0
VSWUC1	A	19.5	20	2.1	1977.8

Table A.5. *continued*

Barora Pond, Tetepare, Solomon Islands					
SBARUC2	A	1.5	47	0.2	2011.2
SBARUC2	A	3.5	46	0.4	2010.8
SBARUC2	A	5.5	44	0.8	2010.2
SBARUC2	A	13.5	43	3.0	2006.1
SBARUC2	A	24.5	37	6.8	1998.3
SBARUC2	A	30.5	30	8.7	1994.4
SBARUC2	A	40.5	19	11.6	1989.4
SBARUC2	A	50.5	18	14.8	1984.3
SBARUC2	A	70.5	18	22.1	
SBARUC2	A	90.5	14	29.7	
Lake Tavara Tetepare, Solomon Islands					
STAVUC4	A	2.5	142	0.3	2006.9
STAVUC4	A	4.5	132	0.5	2003.0
STAVUC4	A	6.5	123	0.7	1998.8
STAVUC4	A	10.5	111	1.1	1989.4
STAVUC4	A	16.5	67	1.7	1974.0
STAVUC4	A	20.5	46	2.1	1963.6
STAVUC4	A	24.5	23	2.6	1952.4
STAVUC4	A	32.5	18	3.9	1922.5
Lake Rano, Rendova, Solomon Islands					
SRANUC1	A	1.5	17	0.2	2010.6
SRANUC1	A	3.5	48	0.5	2007.7
SRANUC1	A	5.5	136	0.8	1991.4
SRANUC1	A	9.5	32	1.2	1964.9
SRANUC1	A	12.5	16	1.7	1944.1
SRANUC1	A	15.5	9	2.3	1911.8
SRANUC1	A	22.5	7	4.4	
SRANUC1	A	30.5	14	7.6	
Harai Lake #2, Rendova, Solomon Islands					
SHAR2UC1	A	0.5	2	0.5	
SHAR2UC1	A	6.5	not detected	6.5	
SHAR2UC1	A	11.5	0.4	11.5	

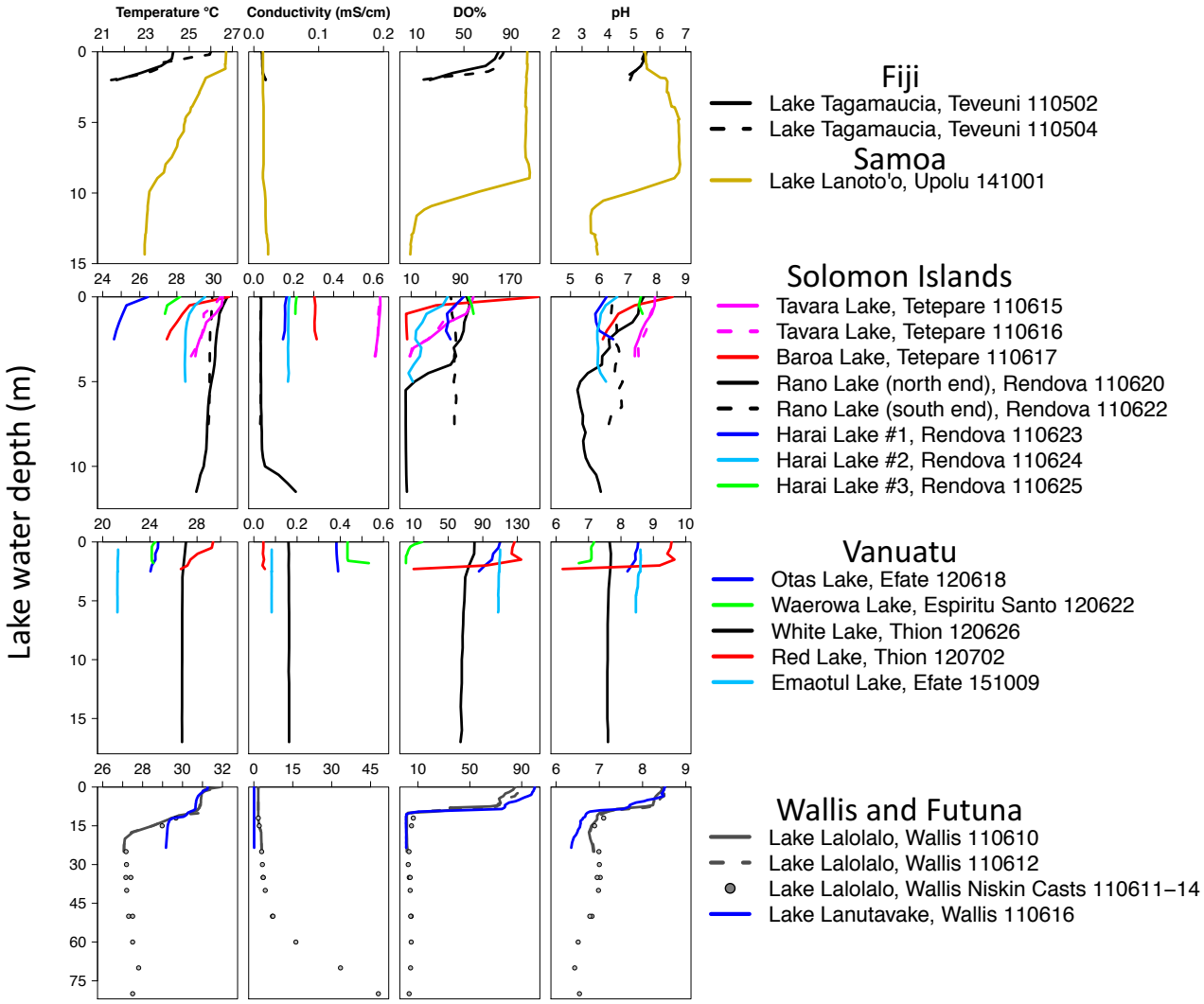

Fig. A.1. Depth profiles of in situ measurements of temperature, conductivity, dissolved oxygen, and pH for several lakes in this study. Dates for each profile are listed in the legend in YYMMDD format. Dashed lines indicate duplicate lake profiles taken on different days and points for Lake Lalolalo represent data taken from water retrieved with a Niskin bottle and measured at the surface. Note different scales. Data from Wallis and Futuna from (Sichrowsky et al., 2014) and data from Samoa from (Hassall, 2017).

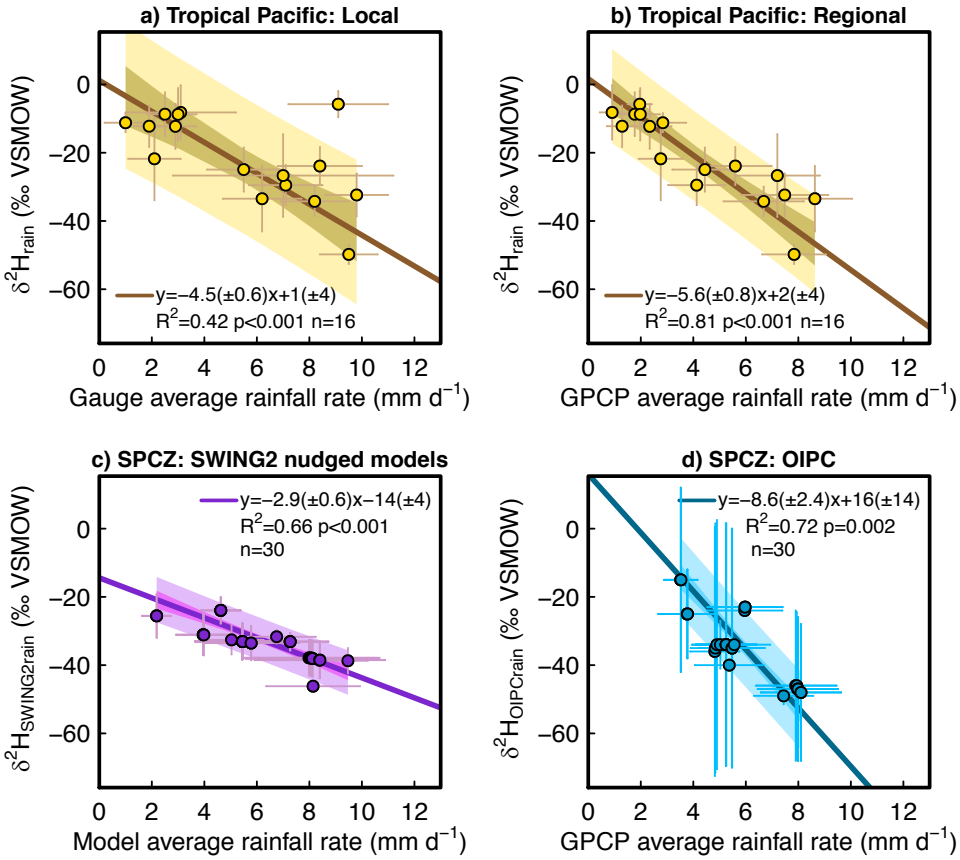

Fig. A.2. Precipitation rate (mm d^{-1}) vs. δ^2H_{rain} from tropical Pacific observations (a-b), and SPCZ lakes sites in (c) models, or (d) the OIPC interpolation algorithm. (a) Amount-weighted IAEA-GNIP and JAMSTEK δ^2H_{rain} vs. IAEA-GNIP and JAMSTEK local gauge precipitation rates. Error bars represent amount-weighed standard deviations in δ^2H_{rain} and standard deviations in precipitation rate measurements. Station data is from 16 tropical Pacific islands between 30°N and 30°S with 23 or more $^2H/^1H$ measurements spanning 3 or more years. (b) IAEA-GNIP and JAMSTEK $\delta^2H_{OBSERVrain}$ vs. GPCPv2.3 mean annual Precipitation rate for the 1979-2016 period, x-axis errors are precipitation rate errors provided by GPCP. (c) Nudged SWING2 multi-model mean $\delta^2H_{SWING2rain}$ vs. SWING2 multi-model mean annual precipitation rates at all 30 lake sites. Errors indicate standard deviations between mean values from the four models. (d) $\delta^2H_{OIPCrain}$ from the OIPC interpolation algorithm with 95 % confidence interval error bars (±47.5 %) vs. GPCP. To account for large errors in both axes, linear fits were determined using the maximum likelihood estimate method (York et al., 2004) incorporating bivariate analytical uncertainty (Thirumalai et al., 2011). Regressions are shown with 95 % confidence and prediction intervals (dark and light shading).

Not shown ordinary least squares regressions:

a) y=-2.7(±0.8)x-7(±5), R^2=0.43, p=0.005, n=16

b) y =-3.5(±0.7)x-6(±3), R^2=0.67, p=0.0001, n=16

c) y =-2.2(±0.3)x-20(±2), R^2=0.68, p<<0.001, n=30

d) y =-5.5(±0.6)x-3(±4), R^2=0.72, p<<0.001, n=30

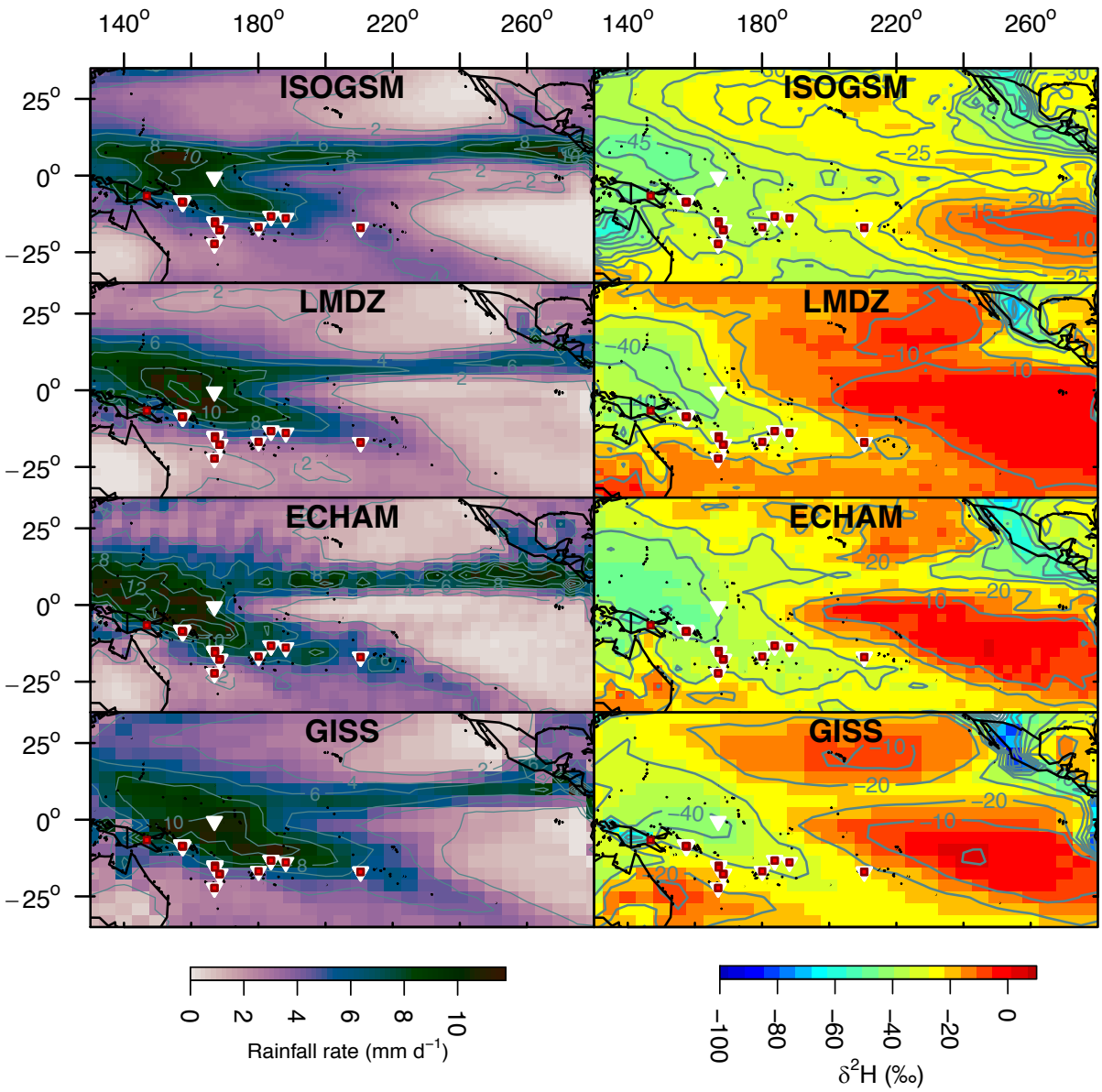

Fig. A.3. Maps of IsoGSM, LMDZ, ECHAM, and GISS (https://data.giss.nasa.gov/swing2/ & http://hydro.iis.u-tokyo.ac.jp/~kei/tmp/isogsm2/) nudged model mean precipitation rates (mm d^{-1}) (left panels) and $\delta^2H_{SWING2rain}$ (right panels) with locations of 29 SPCZ freshwater lake water samples (white triangles) and 21 freshwater lake sediment samples (red squares).

a)

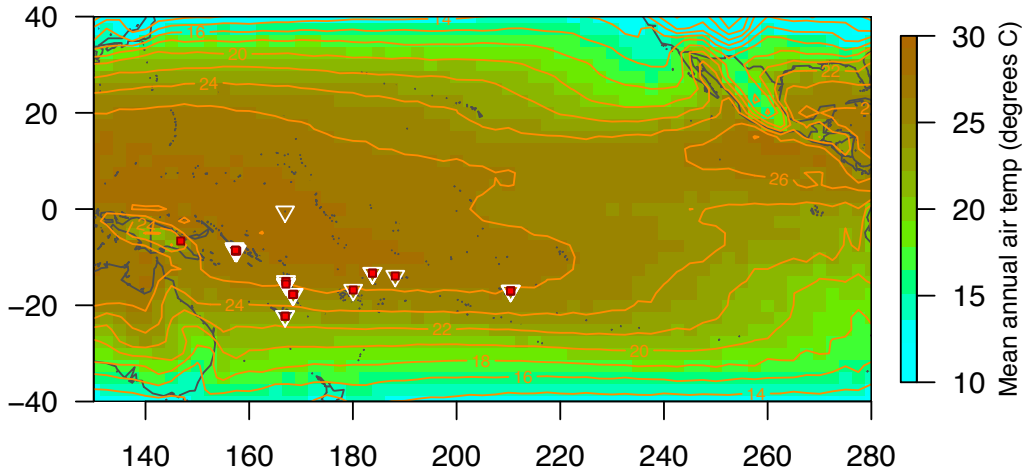

b)

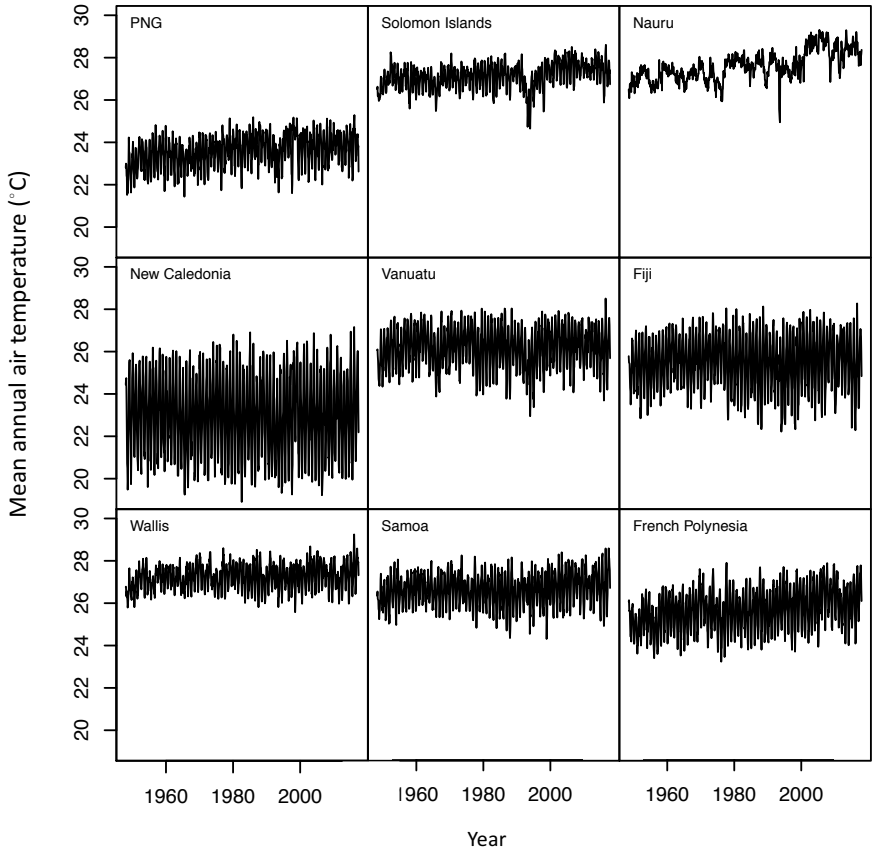

Fig. A.4. Mean annual NCAR reanalysis air temperature for the 1958-2016 period on a 2.5 ° x 2.5 ° grid (http://www.esrl.noaa.gov/psd/). (a) Locations of 29 SPCZ freshwater lake water samples (open white triangles) and 22 freshwater lake sediment samples (red squares); contours and shading show mean annual air temperature. (b) Mean annual air temperature time series from lake sites in each major SPCZ area arranged roughly from west to east.

a)

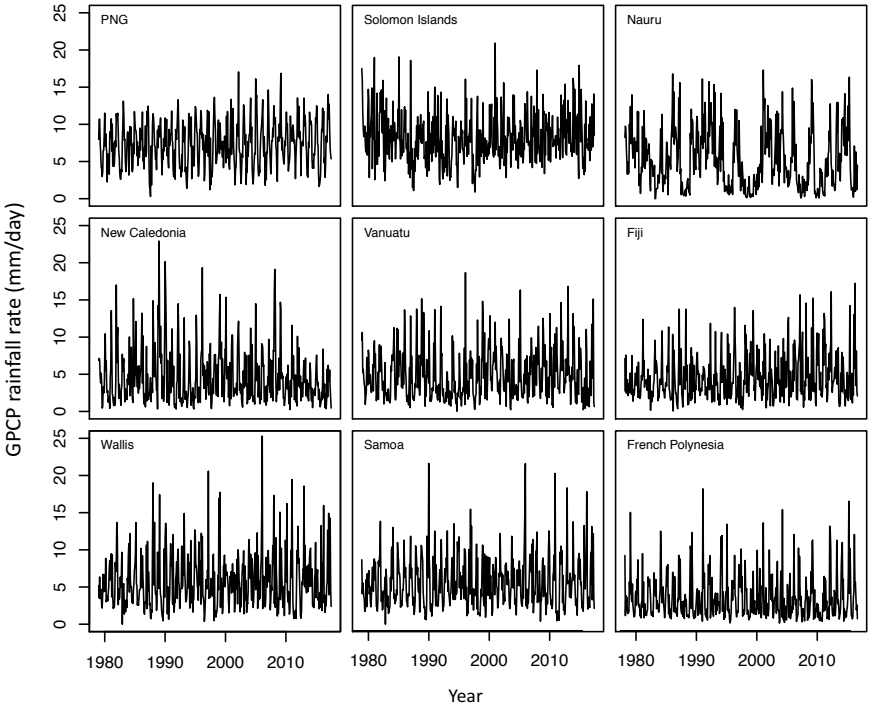

b)

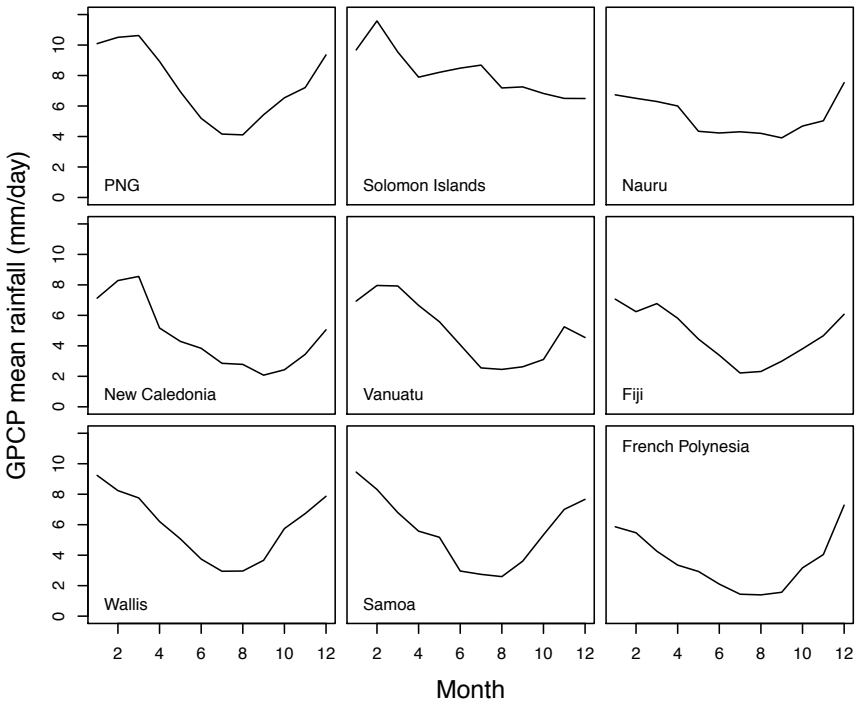

Fig. A.5. GPCPv2.3 precipitation (http://www.esrl.noaa.gov/psd/). (a) Precipitation rate (mm d^{-1}) at lake sites in each major SPCZ area in this study arranged roughly from west to east (b) monthly means during the 1979-2017 period.

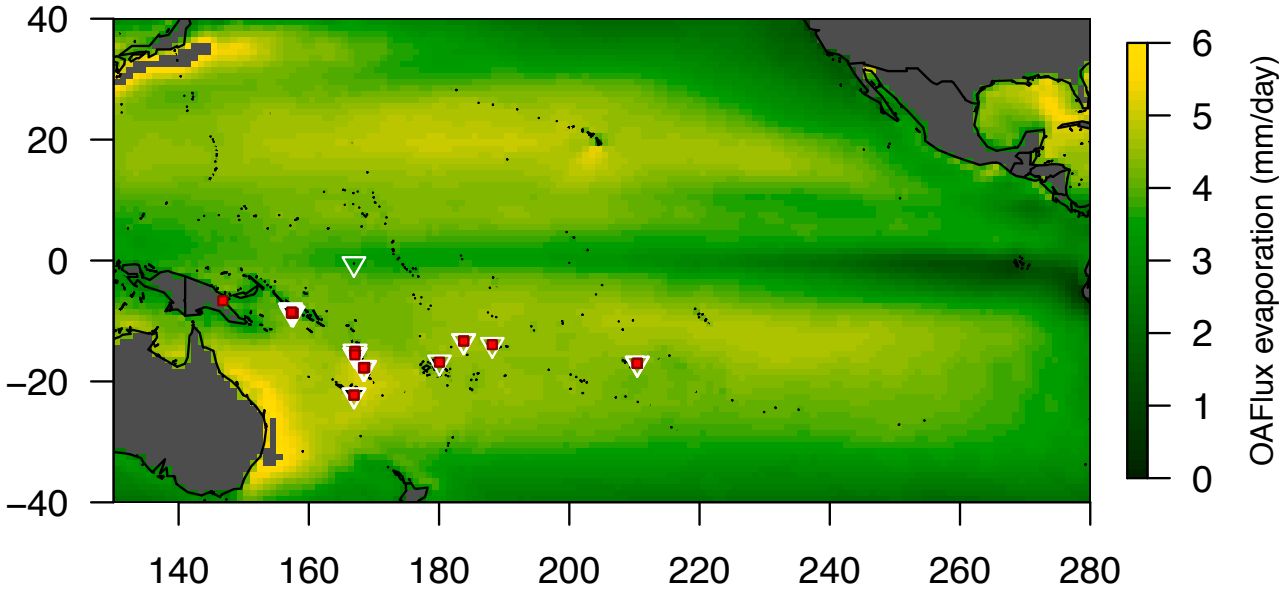

Fig. A.6. Mean annual ocean evaporation rates for the 1958-2016 period from OAFlux (Yu et al., 2008) on a 1 ° x 1 ° grid (http://oaflux.whoi.edu/evap.html) with locations of 29 SPCZ freshwater lake water samples (open white triangles) and 21 freshwater lake sediment samples (red squares).

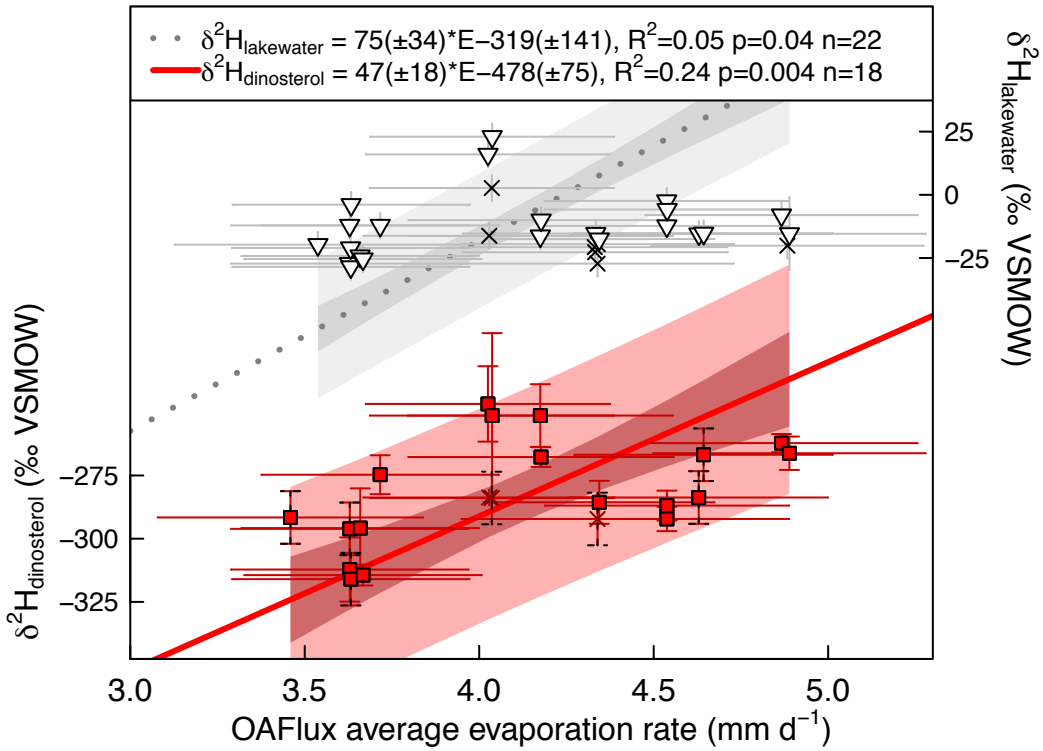

Fig. A.7. Relationships between mean annual evaporation rate (mm d^{-1}) for the 1958-2016 period from OAFlux (Yu et al., 2008) (http://oaflux.whoi.edu/evap.html) and $\delta^2H_{lakewater}$ or $\delta^2H_{dinosterol}$. Plotted on the left-axis is lake-averaged $\delta^2H_{dinosterol}$ (red squares) from 18 lakes. Also shown are 3 lakes with high vegetation cover not included in regressions (red crosses). On the right axis: lake-averaged $\delta^2H_{lakewater}$ (white triangles) from 22 lakes. Also shown are 7 lakes with high vegetation cover (black crosses) that are not included in regressions. X-axis error bars represent estimated systematic mean errors in evaporation provided by OAFlux. $\delta^2H_{lakewater}$ error bars are the estimated standard error of tropical lake water (±5 ‰, except 14 ‰ at Lake Emaotul), and $\delta^2H_{dinosterol}$ error bars are the standard deviations of multiple core-top values, except when only one core-top was measured then the pooled standard deviation calculated from lakes with multiple core-tops is shown (±10.4 ‰ indicated by error bars with black dashes). To account for large errors in both axes, linear fits were determined using the maximum likelihood estimate method (York et al., 2004) incorporating bivariate analytical uncertainty (Thirumalai et al., 2011) (solid red line and dotted gray line which was significant below the p=0.05 level but not using an ordinary least squares regression). Regressions are shown with 95 % confidence and prediction intervals (dark and light shading).

Not shown ordinary least squares regressions:

$\delta^2H_{lakewater}$ = 6(±6)*E-38(±24), R^2=0.05, p=0.3, n=22

$\delta^2H_{dinosterol}$ = 22(±10)*E-374(±40), R^2=0.24, p=0.04, n=18

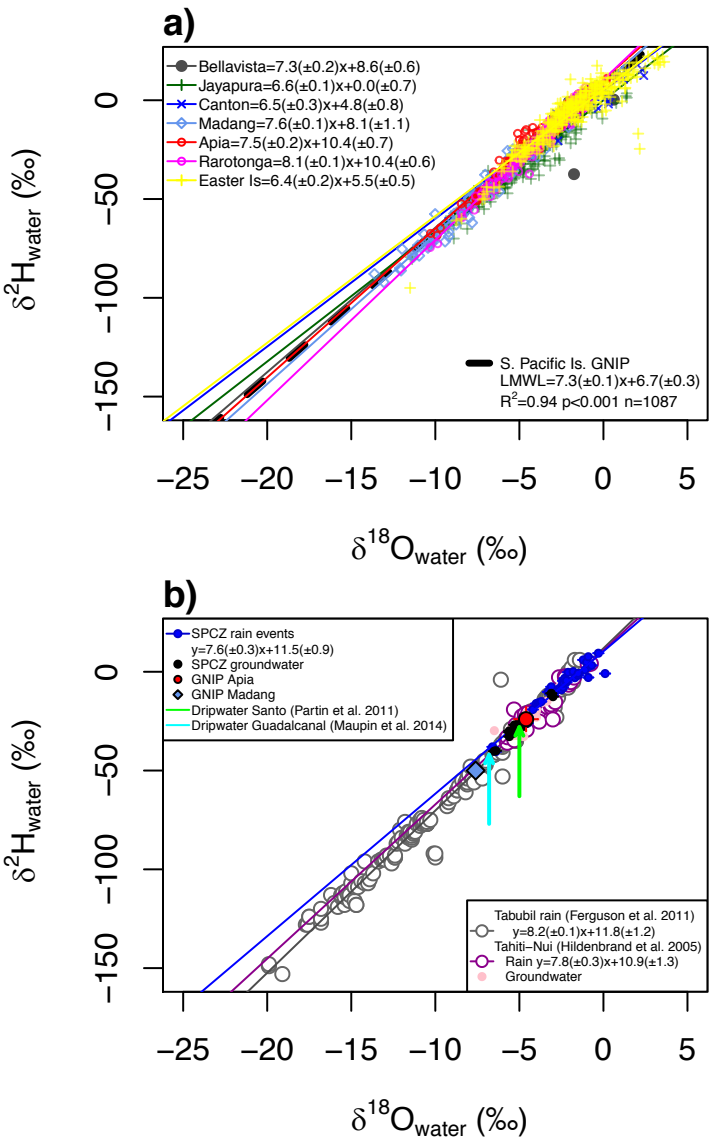

Fig. A.8. The hydrogen and oxygen isotope composition of precipitation isotopes in (a) the south tropical Pacific from IAEA/GNIP (https://nucleus.iaea.org/wiser/) station monthly data and (b) from islands in this study and published data from nearby SPCZ islands. SPCZ rain events (blue circles) and SPCZ groundwater (black circles) are as in **Fig. 3** in the main text. The red (light blue) GNIP Apia (Madang) circle (diamond) in (b) is the amount-weighted mean of all monthly rain samples. The open gray circles are rainfall samples collected in Tabubil, Papua New Guinea between 2003-2006 from Ferguson et al. (2011) (data available in Ferguson 2007). The dark pink open circles are from rain samples and closed pink circles are ground waters collected on Tahiti-Nui between 2000-2001 from Hildenbrand et al. (2005). The bright green arrow indicates the estimated δ^2H value given the $\delta^{18}O$ value of cave drip water from Espirato Santo, Vanuatu collected in 2011 (Partin et al. 2011), and the cyan arrow indicates the estimated δ^2H value given the mean $\delta^{18}O$ value of 3 cave drip water samples collected in 2010 from 2 caves on Guadalcanal, Solomon Islands (Maupin et al. 2014).

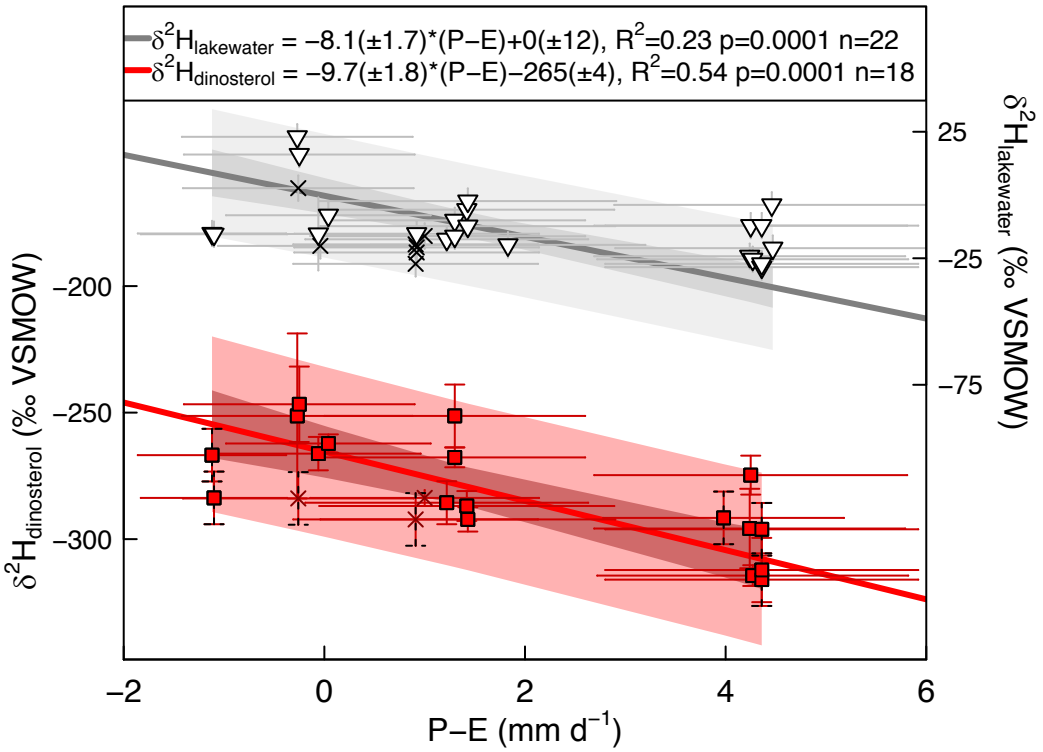

Fig. A.9. Relationships between P-E (mm d^{-1}) and $\delta^2H_{lakewater}$ or $\delta^2H_{dinosterol}$ (P-E = GPCP mean annual precipitation rate for the 1979-2016 period - OAFlux mean annual evaporation rate for the 1958-2016 period). Plotted on the left-axis is lake-averaged $\delta^2H_{dinosterol}$ (red squares) from 18 lakes. Also shown are 3 lakes with high vegetation cover not included in regressions (red crosses). On the right axis: lake-averaged $\delta^2H_{lakewater}$ (white triangles) from 22 lakes. Also shown are 7 lakes with high vegetation cover (black crosses) that are not included in regressions. X-axis error bars are propagated errors provided by GPCP and OAFlux. $\delta^2H_{lakewater}$ error bars are the estimated standard error of tropical lake water (±5 ‰, except 14 ‰ at Lake Emaotul), and $\delta^2H_{dinosterol}$ error bars are the standard deviations of multiple core-top values, except when only one core-top was measured then the pooled standard deviation calculated from lakes with multiple core-tops is shown (±10.4 ‰ indicated by error bars with black dashes). To account for large errors in both axes, linear fits were determined using the maximum likelihood estimate method (York et al., 2004) incorporating bivariate analytical uncertainty (Thirumalai et al., 2011). Regressions (sold red or gray lines) are shown with 95 % confidence and prediction intervals (dark and light shading). *Not shown* ordinary least squares regressions: $\delta^2H_{lakewater}$ = -3.0(±1.2)*E-6(±3), R^2=0.23, p=0.02, n=22 & $\delta^2H_{dinosterol}$ = -7.6(±1.7)*E-267(±5), R^2=0.54, p=0.0004, n=18

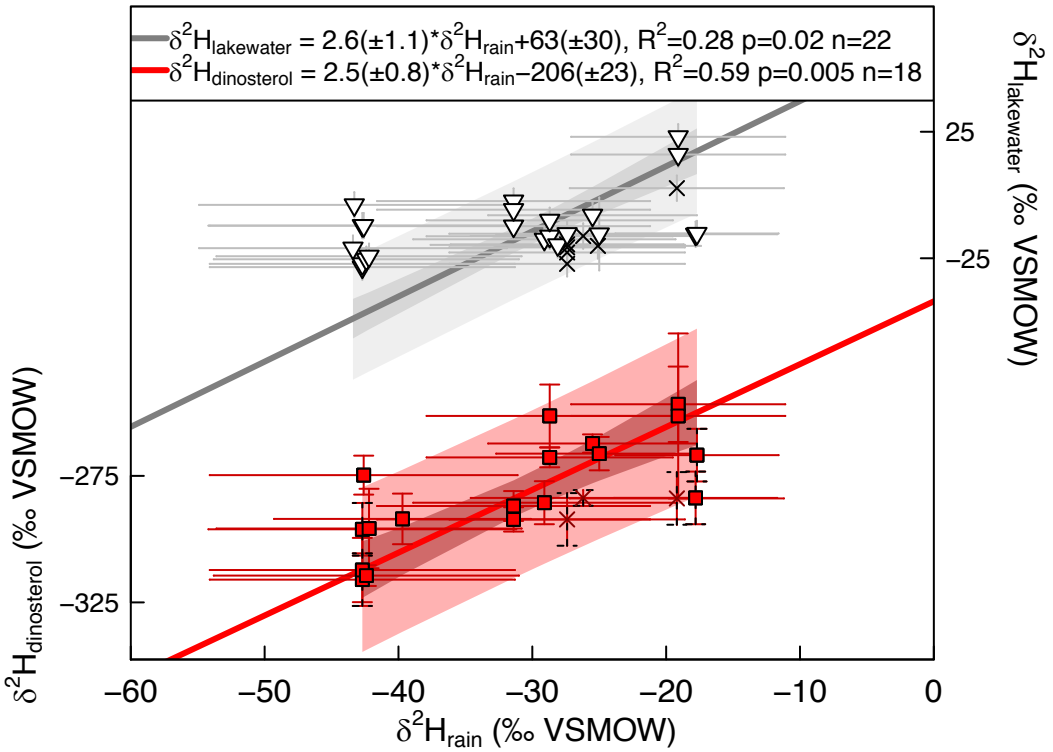

Fig. A.10. Relationships between δ^2H_{rain} and $\delta^2H_{lakewater}$ or $\delta^2H_{dinosterol}$. δ^2H_{rain} was calculated using the GPCP rainfall at each lake site and the Tropical Pacific "amount effect" relationship between GNIP/JAMSTEK station data and GPCP rainfall rates [δ^2H_{rain} = -5.6(±0.8)*P+2(±4), R^2=0.81, p<0.001, n=16 (**Fig. A.2** and main text **Fig. 2**). Plotted on the left-axis is lake-averaged $\delta^2H_{dinosterol}$ (red squares) from 18 lakes. Also shown are 3 lakes with high vegetation cover not included in regressions (red crosses). On the right axis: lake-averaged $\delta^2H_{lakewater}$ (white triangles) from 22 lakes. Also shown are 7 lakes with high vegetation cover (black crosses) that are not included in regressions. X-axis error bars were calculated using a Monte Carlo approach with 10000 iterations and account for errors from GPCP rainfall estimates plus errors in the slope and intercept of the "amount effect" relationship. $\delta^2H_{lakewater}$ error bars are the estimated standard error of tropical lake water (±5 ‰, except 14 ‰ at Lake Emaotul), and $\delta^2H_{dinosterol}$ error bars are the standard deviations of multiple core-top values, except when only one core-top was measured then the pooled standard deviation calculated from lakes with multiple core-tops is shown (±10.4 ‰ indicated by error bars with black dashes). To account for large errors in both axes, linear fits were determined using the maximum likelihood estimate method (York et al., 2004) incorporating bivariate analytical uncertainty (Thirumalai et al., 2011). Regressions (sold red or gray lines) are shown with 95 % confidence and prediction intervals (dark and light shading).

Not shown ordinary least squares regressions:

$\delta^2H_{lakewater}$ = 0.7(±0.3)*δ^2H_{rain}+10 (±8), R^2=0.27, p=0.01, n=22

$\delta^2H_{dinosterol}$ = 1.7(±0.4)*δ^2H_{rain}-227(±12), R^2=0.58, p=0.0002, n=18

Chapter 3 Appendix B. Supplementary data

Table B1. Individual sediment samples

#	Site Name	δ^2H	SD	n	Core Section ID	Collection Date	Sediment Depth	Technique	Water Depth (m)	Latitude	Longitude
1	Rimatu'u Pond, Tetiaroa, French Polynesia	-240	3	3	RimPond	150328	0-0.5cm	Hand grab	~0.5	-17.02489	210.441721
2	Rimatu'u Pond, Tetiaroa, French Polynesia	-236	17	2	wpt 36	151021	0-2cm	Hand grab	~0.5	-17.02489	210.441721
3	Rimatu'u Pond, Tetiaroa, French Polynesia	-264	5	2	wpt 37	151021	0-2cm	Hand grab	~0.5	-17.02431	210.441626
4	Oroatera Pond, Tetiaroa, French Polynesia	-274	6	4	wpt 33	151021	0-2cm	Hand grab	~0.5	-16.99580	210.459125
5	Oroatera Pond, Tetiaroa, French Polynesia	-228	8	2	wpt 35	151021	0-2cm	Hand grab	~0.5	-16.99563	210.459061
6	Onetahi Pond, Tetiaroa, French Polynesia	-284	8	3	SpaPond	151026	0-2cm	Hand grab	~0.5	-17.02074	210.408133
7	Lake Tagamaucia, Teveuni, Fiji	-281	4	3	TAG UC3	110504	0-1cm	Universal Corer	2.2	-16.81630	180.060124
8	Lake Tagamaucia, Teveuni, Fiji	-286	1	3	TAG UC4	110504	0-1cm	Universal Corer	2.2	-16.81630	180.060140
9	Lake Tagamaucia, Teveuni, Fiji*	-253	6	4	algal matt	110502	0-1cm	Hand grab	0	-16.81486	180.059138
10	Grand Lac, Grande Terre, New Caledonia	-284	1	3	GRL-U1	130723	0-1cm	UWITEC gravity core	2.9	-22.27033	166.909367
11	Lake Hut, Grande Terre, New Caledonia	-273	1	3	LHT-U2	130724	0-1cm	UWITEC gravity core	4.7	-22.26085	166.952550
11	Lake Hut, Grande Terre, New Caledonia (replicate)	-261	4	3	LHT-U2	130724	0-1cm	UWITEC gravity core	4.7	-22.26085	166.952550
12	Otas Lake, Efate, Vanuatu	-260	6	4	VEO UC6	120620	0-1cm	Universal Corer	2.3	-17.69450	168.584950
13	Otas Lake, Efate, Vanuatu	-265	8	4	VEO UC7	120620	0-1cm	Universal Corer	2.3	-17.69738	168.584423
14	Emaotul Lake, Efate, Vanuatu	-259	2	3	VTEFVR	950107	0-1cm	D-section peat borer	0	-17.73160	168.414850
15	Emaotul Lake, Efate, Vanuatu	-271	2	3	VAN G5	150910	0-2cm	UWITEC gravity core	6	-17.7299	168.415462
16	Emaotul Lake, Efate, Vanuatu	-268	4	3	VAN G7	150910	0-2cm	UWITEC gravity core	6.4	-17.7299	168.415462
17	Red Lake, Thion, Vanuatu	-255	20	3	VTR UC1	120627	0-1cm	Universal Corer	2.4	-15.03245	167.090017
18	Red Lake, Thion, Vanuatu	-262	14	5	VTR UC3	120627	0-1cm	Universal Corer	2.5	-15.03283	167.089917
19	Red Lake, Thion, Vanuatu	-238	6	3	VTR UC5	120702	0-1cm	Universal Corer	2.3	-15.03257	167.090133
20	White Lake, Thion, Vanuatu	-265	8	3	VTW UC1	120626	0-1cm	Universal Corer	17.3	-15.04103	167.089150
21	White Lake, Thion, Vanuatu	-272	9	5	VTW UC2	120626	0-1cm	Universal Corer	17.1	-15.04105	167.089133
22	White Lake, Thion, Vanuatu	-266	5	6	VTW UC5	120702	0-1cm	Universal Corer	17	-15.04118	167.089217
23	Wairowa Lake, Espiritu Santo, Vanuatu	-292	2	4	VSW UC1	120622	0-1cm	Universal Corer	1.6	-15.59503	167.078750
24	Lake Lanoto'o, Upolu, Samoa	-290	1	4	LAN13	130717	0-2cm	UWITEC gravity core	17?	-13.91033	188.172700
25	Lake Lanoto'o, Upolu, Samoa	-276	10	10	LAN14 U1	140930	0-1cm	UWITEC gravity core	17?	-13.91088	188.172600
26	Lake Lanoto'o, Upolu, Samoa	-291	7	4	LAN14 U2	140930	0-1cm	UWITEC gravity core	17?	-13.91088	188.172600
27	Lac Lalolalo, Wallis	-300	4	3	LALO UC5	110511	0-1cm	Universal Corer	17	-13.30245	183.766533
27	Lac Lalolalo, Wallis (replicate)	-297	1	3	LALO UC5	110511	0-1cm	Universal Corer	17	-13.30245	183.766533
28	Lac Lalolalo, Wallis	-293	6	4	LALO UC16	110514	0-1cm	Universal Corer	26	-13.30157	183.768134
29	Lac Lalolalo, Wallis	-289	5	6	LALO UC22	110519	0-1cm	Universal Corer	23	-13.30168	183.768083
30	Lac Lalolalo, Wallis	-288	3	3	LALO UC24	110519	0-1cm	Universal Corer	24	-13.30168	183.768039
31	Lac Lanutavake, Wallis	-295	4	3	LATVK UC1	110518	0-1cm	Universal Corer	23.3	-13.32118	183.786021
32	Lac Lanutavake, Wallis	-287	5	6	LATVK UC3	110519	0-1cm	Universal Corer	23.2	-13.32110	183.786139
33	Lac Lanutavake, Wallis	-280	4	3	LATVK UC4	110519	0-1cm	Universal Corer	23.2	-13.32115	183.786132
34	Lac Lanutavake, Wallis	-286	5	3	LATVK UC6	110519	0-1cm	Universal Corer	22.9	-13.32102	183.786298
35	Lake Wanum, Papua New Guinea	-292	12	3	WB 0-1	1999 May	0-1cm	Universal Corer	6	-6.63348	146.796589
36	Barora Pond, Tetepare, Solomon Islands	-307	7	4	SBAR UC2	110617	0-1cm	Universal Corer	2.4	-8.72232	157.600450
37	Barora Pond, Tetepare, Solomon Islands	-285	1	3	SBAR UC3	110617	0-1cm	Universal Corer	2.5	-8.72232	157.600450
38	Lake Tavara Tetepare, Solomon Islands	-312	3	3	STAV UC1	110615	0-1cm	Universal Corer	3.7	-8.70287	157.450267
39	Lake Tavara Tetepare, Solomon Islands	-317	2	3	STAV UC4	110615	0-1cm	Universal Corer	3.7	-8.70277	157.450167
40	Lake Rano, Rendova, Solomon Islands	-269	3	6	SRAN UC1	110620	0-1cm	Universal Corer	11.8	-8.68793	157.324267
41	Lake Rano, Rendova, Solomon Islands	-280	4	6	SRAN UC8	110621	0-1cm	Universal Corer	8	-8.69518	157.319067
42	Harai Lake #2, Rendova, Solomon Islands	-287	3	3	SHAR2 UC1	110624	0-1cm	Universal Corer	5.3	-8.56840	157.368383
43	Harai Lake #2, Rendova, Solomon Islands	-305	5	3	SHAR2 UC2	110624	0-1cm	Universal Corer	5.2	-8.56842	157.368300
44	Harai Lake #3, Rendova, Solomon Islands	-312	5	3	SHAR3 UC2	110625	0-1cm	Universal Corer	1.4	-8.56481	157.365120
45	Harai Lake #1, Rendova, Solomon Islands	-316	8	3	SHAR1 UC2	110623	0-1cm	Universal Corer	3.4	-8.56218	157.355550

*microbial matt ontop floating peat sedge, no gps, position estimated, not used in regression or lake average

Table B2. Individual water samples

Sample type	Site	Sample ID	Depth (m)	Salinity	Date	Lat	Lon	$\delta^{18}O$	SD	$\delta^{2}H$	SD
Freshwater Lake	Rimatu'u Pond, Tetiaroa, French Polynesia	T_1	0	0	150328	-17.02489	210.44172	2.9	0.3	13.0	1.3
Freshwater Lake	Rimatu'u Pond, Tetiaroa, French Polynesia (replicate)	T_2	0	0	150328	-17.02489	210.44172	3.0	0.3	13.2	1.3
Freshwater Lake	Rimatu'u Pond, Tetiaroa, French Polynesia	T_37	0	0	151021	-17.02431	210.44163	2.7	0.3	18.9	1.3
Freshwater Lake	Oroatera Pond, Tetiaroa, French Polynesia	T_33	0	0	151021	-16.99580	210.45913	4.1	0.3	22.9	1.3
Freshwater Lake	Oroatera Pond, Tetiaroa, French Polynesia (replicate)	T_35	0	0	151021	-16.99563	210.45906	4.2	0.3	23.2	1.3
Freshwater Lake	Onetahi Pond, Tetiaroa, French Polynesia	T_a	0	0	151026	-17.02074	210.40813	0.5	0.3	2.7	1.3
Freshwater Lake	Onetahi Pond, Tetiaroa, French Polynesia (replicate)	T_b	0	0	151026	-17.02074	210.40813	0.4	0.3	2.7	1.3
Freshwater Lake	Lake Tagamaucia, Teveuni, Fiji	F_4	0	0	110502	-16.81433	180.05865	-3.6	0.3	-15.7	1.3
Freshwater Lake	Lake Tagamaucia, Teveuni, Fiji	F_13	0	0	110502	-16.81610	180.05991	-3.3	0.3	-16.4	1.3
Freshwater Lake	Lake Tagamaucia, Teveuni, Fiji	F_15	1.5	0	110502	-16.81637	180.06004	-3.6	0.3	-15.5	1.3
Freshwater Lake	Lake Tagamaucia, Teveuni, Fiji	F_8	0	0	110502	-16.81637	180.06004	-3.5	0.3	-15.3	1.3
Freshwater Lake	Lake Tagamaucia, Teveuni, Fiji	F_30	1.9	0	110505	-16.81610	180.05991	-3.9	0.3	-17.8	1.3
Freshwater Lake	Lake Tagamaucia, Teveuni, Fiji	F_31	0	0	110504	-16.81610	180.05991	-3.9	0.3	-16.7	1.3
Freshwater Lake	Grand Lac, Grande Terre, New Caledonia	NC_a	0	0	130723	-22.27033	166.90937	-3.37	0.3	-15.4	1.3
Freshwater Lake	Grand Lac, Grande Terre, New Caledonia	NC_b	0	0	130723	-22.27033	166.90937	-3.36	0.3	-15.5	1.3
Freshwater Lake	Lake Hut, Grande Terre, New Caledonia	NC_c	0	0	130724	-22.26085	166.95255	-3.19	0.3	-15.2	1.3
Freshwater Lake	Otas Lake, Efate, Vanuatu	V_5	0	0	120618	-17.69652	168.58430	-0.9	0.3	-8.0	1.3
Freshwater Lake	Emaotul Lake, Efate, Vanuatu	VAN_1	0	0	170516	-17.73421	168.41546	-3.8	0.3	-25.6	1.3
Freshwater Lake	Emaotul Lake, Efate, Vanuatu	VAN_2	0	0	150920	-17.73213	168.41360	-0.5	0.3	-5.2	1.3
Freshwater Lake	Small Pond, Efate, Vanuatu	V_6	0	0	120619	-17.73417	168.45307	-3.8	0.3	-20.1	1.3
Freshwater Lake	Red Lake, Thion, Vanuatu	V_31	0	0	120702	-15.03272	167.09013	-2.4	0.3	-16.7	1.3
Freshwater Lake	Red Lake, Thion, Vanuatu	V_24	0	0	120625	-15.03370	167.08907	-2.4	0.3	-15.8	1.3
Freshwater Lake	White Lake, Thion, Vanuatu	V_30	0	0	120702	-15.04127	167.08897	-1.2	0.3	-9.9	1.3
Freshwater Lake	White Lake, Thion, Vanuatu	V_23	0	0	120625	-15.04008	167.08830	-1.3	0.3	-10.2	1.3
Freshwater Lake	Waćrowa East Lake, Espiritu Santo, Vanuatu	V_13	0	0	120622	-15.59505	167.07878	-4.6	0.3	-27.2	1.3
Freshwater Lake	Waćrowa West Lake, Espiritu Santo, Vanuatu	V_12	0	0	120621	-15.59510	167.07257	-3.2	0.3	-19.5	1.3
Freshwater Lake	Bellmolle North Lake, Espiritu Santo, Vanuatu	V_9	0	0	120621	-15.58297	167.11178	-3.5	0.3	-20.7	1.3
Freshwater Lake	Bellmolle Swamp, Espiritu Santo, Vanuatu	V_10	0	0	120621	-15.58390	167.10162	-4.2	0.3	-22.7	1.3
Freshwater Lake	Bellmolle South Lake, Espiritu Santo, Vanuatu	V_11	0	0	120621	-15.58842	167.10190	-2.2	0.3	-15.3	1.3
Freshwater Lake	Nauru, Badua Pond	N_a	0	0	100215	-0.53467	166.92228	-2.4	0.3	-19.7	1.3
Freshwater Lake	Nauru, Badua Pond (replicate)	N_b	0	0	100215	-0.53467	166.92228	-2.4	0.3	-19.8	1.3
Freshwater Lake	Lake Lanoto'o, Upolu, Samoa	2013 A	0	0	130717	-13.91033	188.17270	-3.19	0.3	-19.0	1.3
Freshwater Lake	Lake Lanoto'o, Upolu, Samoa	2013 B	0	0	130717	-13.91033	188.17270	-3.16	0.3	-18.7	1.3
Freshwater Lake	Lake Lanoto'o, Upolu, Samoa	2014 S	0	0	140930	-13.91088	188.17260	-2.62	0.3	-15	1.3
Freshwater Lake	Lake Lanoto'o, Upolu, Samoa	2014 B	16.4	0	140930	-13.91088	188.17260	-2.89	0.3	-17.3	1.3
Freshwater Lake	Lac Lalolalo, Wallis	W_25	0	0	110510	-13.30153	183.76512	-1.6	0.04	-12.1	0.53
Freshwater Lake	Lac Lalolalo, Wallis	W_26	0	0	110510	-13.29928	183.76617	-1.7	0.04	-13.1	0.53
Freshwater Lake	Lac Lalolalo, Wallis	W_52	0	0	110512	-13.30082	183.76583	-1.8	0.04	-12.4	0.53
Freshwater Lake	Lac Lalolalo, Wallis	W_48	0	0	110514	-13.30053	183.76615	-1.8	0.04	-12.5	0.53
Freshwater Lake	Lac Lalolalo, Wallis	W_121	0	0	110517	-13.30123	183.76832	-1.6	0.04	-11.7	0.53
Freshwater Lake	Lac Lalolalo, Wallis	W_133	0	0	110522	-13.30000	183.76512	-1.6	0.04	-12.1	0.53
Freshwater Lake	Lac Lanutavake, Wallis	W_35	0	0	110516	-13.32073	183.78508	-0.7	0.04	-5.9	0.53
Freshwater Lake	Lac Lanutavake, Wallis	W_113	0	0	110516	-13.32143	183.78592	-0.6	0.04	-5.9	0.53
Freshwater Lake	Lac Lanutavake, Wallis	W_108	0	0	110516	-13.32143	183.78592	-0.6	0.04	-6.1	0.53
Freshwater Lake	Lac Lanutavake, Wallis	W_169	0	0	110517	-13.32143	183.78592	-0.6	0.04	-5.7	0.53
Freshwater Lake	Lac Lanutavake, Wallis	W_180	0	0	110519	-13.32143	183.78592	-0.6	0.04	-5.9	0.53
Freshwater Lake	Lac Lanutavake, Wallis	W_136	0	0	110520	-13.32143	183.78592	-0.4	0.04	-5.4	0.53
Freshwater Lake	Lac Lano, Wallis	W_188	0	0	110518	-13.29423	183.75974	0.4	0.04	-2.4	0.53
Freshwater Lake	Barora Pond, Tetepare, Solomon Islands	SI_6	0	0	110617	-8.72203	157.60068	-4.3	0.3	-23.5	1.3
Freshwater Lake	Barora Pond, Tetepare, Solomon Islands	SI_8	2.5	0	110618	-8.72232	157.60045	-4.6	0.3	-24.8	1.3
Freshwater Lake	Lake Tavara Tetepare, Solomon Islands	SI_1	0	0	110615	-8.70153	157.44993	-4.8	0.3	-26.1	1.3
Freshwater Lake	Lake Tavara Tetepare, Solomon Islands	SI_2	0	0	110615	-8.70287	157.45027	-4.7	0.3	-25.2	1.3
Freshwater Lake	Lake Tavara Tetepare, Solomon Islands	SI_34	3.4	0	110615	-8.70287	157.45027	-4.7	0.3	-25.0	1.3
Freshwater Lake	Lake Rano, Rendova, Solomon Islands	SI_12	0	0	110620	-8.69552	157.31818	-1.9	0.3	-11.7	1.3
Freshwater Lake	Lake Rano, Rendova, Solomon Islands	SI_13	0	0	110620	-8.69530	157.31873	-1.8	0.3	-11.1	1.3
Freshwater Lake	Lake Rano, Rendova, Solomon Islands	SI_15	11	0	110622	-8.68852	157.32480	-2.3	0.3	-13.6	1.3
Freshwater Lake	Harai Lake #2, Rendova, Solomon Islands	SI_23	0	0	110624	-8.56857	157.36827	-1.5	0.3	-12.1	1.3
Freshwater Lake	Harai Lake #3, Rendova, Solomon Islands	SI_27	0	0	110625	-8.56473	157.36515	-5.1	0.3	-27.2	1.3
Freshwater Lake	Harai Lake #1, Rendova, Solomon Islands	SI_18	0	0	110623	-8.56215	157.35557	-5.5	0.3	-28.5	1.3
Freshwater Lake	Arundel Lake #1, Arundel, Solomon Islands	SI_29	0	0	110628	-8.19168	157.17925	-3.6	0.3	-21.0	1.3
Freshwater Lake	ArundelLake #2, Arundel, Solomon Islands	SI_30	0	0	110628	-8.20597	157.18235	0.1	0.3	-3.9	1.3

Table B2. Individual water samples *continued*

Sample type	Site	Sample ID	Depth (m)	Salinity	Date	Lat	Lon	$\delta^{18}O$	SD	$\delta^{2}H$	SD
Rain event	Tetiaroa, French Polynesia	Train.1		0	150222	-17.01638	210.41048	-2.9	0.3	-10.6	1.3
Rain event	Tetiaroa, French Polynesia (duplicate)	Train.2		0	150222	-17.01380	210.41048	-2.8	0.3	-9.7	1.3
Rain event	Tetiaroa, French Polynesia	Train.3		0	160130	-17.01380	210.41048	-4.7	0.3	-26.6	1.3
Rain event	Teveuni, Fiji	F_1		0	110502	-16.81237	180.05475	-3.8	0.3	-15.6	1.3
Rain event	Teveuni, Fiji (duplicate)	F_11		0	110502	-16.81237	180.05475	-3.9	0.3	-15.8	1.3
Rain event	Teveuni, Fiji	F_14		0	110502	-16.81423	180.05852	-3.7	0.3	-15.1	1.3
Rain event	Teveuni, Fiji	F_16		0	110502	-16.80032	179.99201	-4.8	0.3	-24.0	1.3
Rain event	Teveuni, Fiji	F_19		0	110502	-16.81423	180.05852	-4.0	0.3	-16.1	1.3
Rain event	Teveuni, Fiji	F_45		0	110503	-16.80032	179.99201	-6.4	0.3	-40.4	1.3
Rain event	Teveuni, Fiji	F_22		0	110504	-16.81423	180.05852	-5.5	0.3	-31.6	1.3
Rain event	Teveuni, Fiji	F_23		0	110505	-16.81423	180.05852	-4.2	0.3	-19.1	1.3
Rain event	Lakeba, Fiji	F_124		0	110530	-18.24095	181.19001	-2.2	0.3	-5.3	1.3
Rain event	Lakeba, Fiji	F_159		0	110530	-18.24095	181.19001	-2.35	0.3	-5.8	1.3
Rain event	Lakeba, Fiji	F_208		0	110530	-18.24095	181.19001	0.1	0.3	7.2	1.3
Rain event	Lakeba, Fiji	F_128		0	110530	-18.17611	181.19723	-0.7	0.3	3.2	1.3
Rain event	Vanua Balavu, Fiji	F_189		0	110603	-17.30316	181.01141	-3.3	0.3	-10.2	1.3
Rain event	Vanua Balavu, Fiji	F_185		0	110604	-17.30316	181.01141	-2.4	0.3	-4.6	1.3
Rain event	Vanua Balavu, Fiji	F_139		0	110606	-17.30316	181.01141	-2.2	0.3	-4.4	1.3
Rain event	Efate, Vanuatu	V_7		0	120620	-17.74493	168.31699	-0.9	0.3	7.6	1.3
Rain event	Efate, Vanuatu	V_8		0	120620	-17.74493	168.31699	-6.6	0.3	-38.0	1.3
Rain event	Espiritu Santo, Vanuatu	V_16		0	120622	-15.51346	167.17253	-1.7	0.3	-3.0	1.3
Rain event	Espiritu Santo, Vanuatu	V_26		0	120626	-15.04670	167.07257	-1.0	0.3	4.9	1.3
Rain event	Espiritu Santo, Vanuatu	V_27		0	120627	-15.04670	167.07257	-2.1	0.3	-0.3	1.3
Rain event	Espiritu Santo, Vanuatu	V_28		0	120628	-15.04670	167.07257	-1.2	0.3	6.0	1.3
Rain event	Wallis Island	W_3		0	110510	-13.28060	183.81482	-4.5	0.3	-26.0	1.3
Rain event	Wallis Island	W_34		0	110510	-13.29883	183.76603	-4.5	0.3	-23.0	1.3
Rain event	Wallis Island	W_101		0	110512	-13.28060	183.81481	-0.9	0.3	-2.9	1.3
Rain event	Wallis Island	W_102		0	110512	-13.28060	183.81481	-0.3	0.3	9.4	1.3
Rain event	Wallis Island	W_37		0	110515	-13.28060	183.81481	-2.3	0.3	-3.3	1.3
Rain event	Wallis Island	W_104		0	110516	-13.28060	183.81481	-1.1	0.3	0.9	1.3
Rain event	Wallis Island	W_42		0	110517	-13.28292	183.82768	-1.5	0.3	-1.8	1.3
Rain event	Wallis Island	W_160		0	110517	-13.28060	183.81481	-1.5	0.3	-0.8	1.3
Rain event	Tetepare, Solomon Islands	SI_7		0	110618	-8.72193	157.44376	-1.8	0.3	0.1	1.3
Rain event	Tetepare, Solomon Islands	SI_11		0	110619	-8.72193	157.44376	-3.1	0.3	-7.6	1.3
Rain event	Tetepare, Solomon Islands	SI_14		0	110621	-8.72193	157.44376	-2.6	0.3	-8.3	1.3
Rain event	Tetepare, Solomon Islands	SI_16		0	110622	-8.72193	157.44376	-3.0	0.3	-12.2	1.3
Rain event	Tetepare, Solomon Islands	SI_19		0	110623	-8.72193	157.44376	-2.5	0.3	-9.1	1.3
Rain event	Tetepare, Solomon Islands	SI_28		0	110626	-8.72193	157.44376	-2.3	0.3	-3.6	1.3
Rain event	Nauru	nauru rain 3		0	100215	-0.53820	166.91120	0.1	0.3	-0.9	1.3
Rain event	Nauru	nauru rain 4		0	100215	-0.53820	166.91120	-2.4	0.3	-7.9	1.3
Stream	Teveuni, Fiji	F_21	0	0	110504	-16.81235	180.05466	-5.3	0.3	-26.9	1.3
Rain tank	Nasaqalau village, Lakeba, Fiji	F_187		0	110530	-18.17829	181.19043	-3.0	0.3	-12.6	1.3
Cave drip	Lakeba, Fiji	F_182		0	110530	-18.18749	181.17047	-5.2	0.3	-28.0	1.3
Rain tank	Vanua Balavu, Fiji	F_183		0	110605	-17.30316	181.01141	-3.1	0.3	-10.9	1.3
Tap	Vanua Balavu, Fiji	F_181		0	110605	-17.30316	181.01141	-4.8	0.3	-25.4	1.3
Tap	Wallis Island	W_44		0	110509	-13.28060	183.81482	-4.8	0.3	-27.8	1.3
Bottled water	Vanuatu	V_2		0	120617	na	na	-6.4	0.3	-40.0	1.3
Rain tank	Port Vila, Efate, Vanuatu	V_1		0	120617	-17.74493	168.31699	-5.6	0.3	-32.8	1.3
Stream	Efate, Vanuatu	V_4	0	0	120617	-17.71423	168.56863	-5.1	0.3	-28.8	1.3
Stream	Espiritu Santo, Vanuatu	V_15	0	0	120622	-15.37777	167.17490	-5.6	0.3	-30.7	1.3
Stream	Espiritu Santo, Vanuatu	V_21	0	0	120623	-15.59628	167.06698	-5.2	0.3	-30.2	1.3
Rain Tank	Port Orly, Espiritu Santo, Vanuatu	V_25		0	120625	-15.04670	167.07257	-6.5	0.3	-40.2	1.3
Stream	Tetepare, Solomon Islands	SI_10	0	0	110618	-8.70441	157.54490	-5.1	0.3	-26.5	1.3
Stream	Redova, Solomon Islands	SI_17	0	0	110623	-8.56287	157.35505	-5.6	0.3	-29.9	1.3
Stream	Redova, Solomon Islands	SI_25	0	0	110625	-8.56443	157.36315	-5.3	0.3	-28.5	1.3
Stream	Redova, Solomon Islands	SI_26	0	0	110625	-8.56467	157.36428	-5.2	0.3	-28.0	1.3
Lagoon	Tetiaroa, French Polynesia	T_S12IW2(	0	34	150126	-17.01589	210.40267	0.57	0.3	5.77	1.3
Lagoon	Tetiaroa, French Polynesia	T_T29IW1	0	34	150130	-17.00747	210.42011	0.46	0.3	4.48	1.3
Lagoon	Tetiaroa, French Polynesia	T_T19IW2{	0	35	150220	-17.01569	210.40172	0.61	0.3	6.28	1.3
Lagoon	Tetiaroa, French Polynesia	T_T19IW2{	0	35	150223	-17.01569	210.40172	0.71	0.3	6.62	1.3
Lagoon	Tetiaroa, French Polynesia	T_T31IW2	0	35	150325	-17.00058	210.40717	0.71	0.3	6.88	1.3
Lagoon	Tetiaroa, French Polynesia	T_T36-2IW	0	35	150328	-16.02611	210.44156	0.68	0.3	6.30	1.3
Sea shore	Teveuni, Fiji	F_17	0	32	110502	-16.79919	179.99191	0.1	0.3	2.7	1.3
Sea shore	Teveuni, Fiji (replicate)	F_18	0	33	110502	-16.79919	179.99191	0.2	0.3	1.0	1.3
Sea shore	Lakeba, Fiji	F_126	0	34	110530	-18.17592	181.19724	0.3	0.3	4.4	1.3
Canal	Lakeba, Fiji	F_129	0	5	110530	-18.17802	181.19148	-4.5	0.1	-25.5	1.3
Inlet	Lakeba, Fiji	F_6	0	2	110530	-18.17798	181.19268	-5.1	0.1	-28.7	1.3
Ocean	Lau Group, Fiji	Lau_210	0	34	110531	-18.44889	181.45785	0.4	0.3	4.0	1.3
Ocean	Lau Group, Fiji	F_105	0	34	110601	-17.89570	181.00233	0.3	0.3	3.3	1.3
Lagoon	Vanuau Balavu, Fiji	F_130	0	33	110602	-17.31638	181.01668	0.4	0.3	3.6	1.3
Sea shore	Wallis Island	W_135	0	31	110513	13.28900	183.95162	0.4	0.3	2.2	1.3
Inlet	Espiritu Santo, Vanuatu	V_14	0	25	120622	-15.59707	167.10373	-1.0	0.3	-4.6	1.3
Brackish lake outflow	Espiritu Santo, Vanuatu	V_22	0	20	120623	-15.59827	167.06692	-2.3	0.3	-12.8	1.3
Ocean	Espiritu Santo, Vanuatu	V_17	0	34	120623	-15.60000	167.10325	0.3	0.3	3.1	1.3
Brackish lake	Malo, Vanuatu	V_20	0	2	120623	-15.63812	167.17918	-5.24	0.3	-29.9	1.3
Inlet	Malo, Vanuatu	V_18	0	25	120623	-15.62480	167.17975	0.4	0.3	3.6	1.3
Brackish lake outflow	Malo, Vanuatu	V_19	0	12	120623	-15.63513	167.18130	-3.5	0.3	-19.2	1.3
Lagoon	Tetepare, Solomon Islands	SI_4	0	34	110617	-8.72105	157.59887	0.2	0.3	2.5	1.3
Lagoon	Tetepare, Solomon Islands	SI_3	0	29	110617	-8.701453	157.45045	-0.6	0.3	-2.0	1.3
Lagoon	Redova, Solomon Islands	SI_21	0	31	110624	-8.56768	157.36427	-0.1	0.3	-0.6	1.3
Lagoon	Redova, Solomon Islands	SI_22	0	30	110624	-8.56837	157.36592	-0.3	0.3	-1.0	1.3
Sea shore	Redova, Solomon Islands	SI_24	0	26	110625	-8.56280	157.35963	-0.4	0.3	-0.8	1.3
Inlet	Tetpare, Solomon Islands	SI_5	0	22	110617	-8.72112	157.59882	-1.7	0.3	-8.1	1.3
Swamp river	Tetepare, Solomon Islands	SI_9	0	5	110618	-8.70305	157.53712	-4.6	0.3	-23.9	1.3
Mangrove swamp	New Georgia, Solomon Islands	SI_31	0	8	110628	-8.20199	157.27382	-4.4	0.3	-24.8	1.3
Coastal pond	New Georgia, Solomon Islands	SI_32	0	6	110628	-8.20257	157.27525	-4.7	0.3	-26.3	1.3
Coastal pond	Sasevele, Solomon Islands	SI_33	0	14	110629	-8.32874	157.33878	-1.2	0.3	-8.3	1.3

Table B.3. SWING2 and OIPC precipitation rate and isotope composition at SPCZ lake sites.

Freshwater Site	SWING2 precipitation rate mm d^{-1}						$\delta^2H_{SWING2rain}$ ‰						$\delta^2H_{OIPCrain}$	95% CI
	ISOGSM	ECHAM	GISS	LMDZ	AVG	SD	ISOGSM	ECHAM	GISS	LMDZ	AVG	SD	‰	‰
Rimatu'u Pond, Tetiaroa, French Polynesia	4.2	5.0	5.5	3.8	4.6	0.8	-28	-27	-22	-19	-24	4	-25	26
Oroatera Pond, Tetiaroa, French Polynesia	4.2	5.0	5.5	3.8	4.6	0.8	-28	-27	-22	-19	-24	4	-25	26
Onetahi Pond, Tetiaroa, French Polynesia[#,^]	4.2	5.0	5.5	3.8	4.6	0.8	-28	-27	-22	-19	-24	4	-25	26
Lake Tagamaucia, Teveuni, Fiji[#]	4.8	6.4	5.4	3.5	5.0	1.2	-36	-36	-29	-28	-33	4	-34	14
Grand Lac, Grande Terre, New Caledonia	2.5	2.0	2.8	1.5	2.2	0.6	-33	-29	-21	-20	-26	6	-15	54
Lake Hut, Grande Terre, New Caledonia	2.5	2.0	2.8	1.5	2.2	0.6	-33	-29	-21	-20	-26	6	-15	54
Otas Lake, Efate, Vanuatu	3.5	5.3	4.3	2.9	4.0	1.0	-37	-35	-24	-28	-31	6	-34	73
Emaotul Lake, Efate, Vanuatu[$]	3.5	5.2	4.3	2.9	4.0	1.0	-36	-36	-24	-28	-31	6	-36	73
Small Pond, Efate, Vanuatu[#]	3.5	5.2	4.3	2.9	4.0	1.0	-37	-36	-24	-28	-31	6	-35	73
Red Lake, Thion, Vanuatu	4.9	8.1	6.3	3.9	5.8	1.8	-36	-38	-27	-32	-34	5	-35	70
White Lake, Thion, Vanuatu	4.9	8.1	6.3	3.9	5.8	1.8	-36	-38	-27	-32	-34	5	-35	70
Waérowa East Lake, Espiritu Santo, Vanuatu[#]	4.6	7.8	5.8	3.6	5.4	1.8	-36	-38	-26	-32	-33	5	-34	71
Waérowa West Lake, Espiritu Santo, Vanuatu[#]	4.6	7.8	5.8	3.6	5.4	1.8	-36	-38	-26	-32	-33	5	-34	71
Bellmolle North Lake, Espiritu Santo, Vanuatu[#]	4.6	7.8	5.9	3.6	5.5	1.8	-36	-38	-26	-32	-33	5	-34	71
Bellmolle Swamp, Espiritu Santo, Vanuatu[#]	4.6	7.8	5.8	3.6	5.5	1.8	-36	-38	-26	-32	-33	5	-34	71
Bellmolle South Lake, Espiritu Santo, Vanuatu	4.6	7.8	5.8	3.6	5.5	1.8	-36	-38	-26	-32	-33	5	-34	71
Buada Pond, Nauru[$]	8.7	9.0	10.4	9.7	9.5	0.8	-41	-39	-41	-33	-39	4	-40	3
Lake Lanoto'o, Upolu, Samoa	6.5	6.2	8.9	5.4	6.8	1.5	-33	-33	-32	-29	-32	2	-34	3
Lac Lalolalo, Wallis	7.3	6.8	9.2	5.8	7.3	1.5	-34	-36	-33	-30	-33	3	-23	1
Lac Lanutavake, Wallis	7.2	6.8	9.2	5.8	7.3	1.5	-34	-36	-33	-30	-33	3	-24	2
Lac Lano, Wallis	7.3	6.8	9.3	5.8	7.3	1.5	-34	-36	-33	-30	-33	3	-23	2
Lake Wanum, Papua New Guinea	6.3	6.9	9.3	10.0	8.1	1.8	-47	-45	-44	-48	-46	2	-49	5
Barora Pond, Tetepare, Solomon Islands	6.5	11.9	7.4	6.5	8.1	2.6	-39	-44	-32	-37	-38	5	-46	44
Lake Tavara Tetepare, Solomon Islands	6.5	11.8	7.4	6.4	8.0	2.6	-39	-44	-31	-37	-38	5	-46	43
Lake Rano, Rendova, Solomon Islands	6.5	11.7	7.4	6.4	8.0	2.5	-39	-44	-31	-37	-38	5	-47	42
Harai Lake #1, Rendova, Solomon Islands	6.5	11.9	7.5	6.6	8.1	2.5	-39	-44	-32	-37	-38	5	-47	42
Harai Lake #2, Rendova, Solomon Islands	6.5	11.9	7.5	6.6	8.1	2.5	-39	-44	-32	-37	-38	5	-47	42
Harai Lake #3, Rendova, Solomon Islands	6.5	11.9	7.5	6.6	8.1	2.5	-39	-44	-32	-37	-38	5	-47	42
Arundel Lake #1, Arundel, Solomon Islands	6.8	12.1	7.8	6.9	8.4	2.5	-39	-45	-32	-38	-39	5	-48	40
Arundel Lake #2, Arundel, Solomon Islands	6.8	12.0	7.8	6.9	8.4	2.5	-39	-45	-32	-38	-39	5	-48	40

[#]High vegetation cover

[^]Manufactured

[$]Ephemeral

Chapter 3 References

Adler, R.F., Gu, G., Huffman, G.J., 2012. Estimating climatological bias errors for the global precipitation climatology project (GPCP). J. Appl. Meteorol. Climatol. 51, 84–99. doi:10.1175/JAMC-D-11-052.1

Adler, R.F., Gu, G., Sapiano, M., Wang, J.J., Huffman, G.J., 2017. Global precipitation: Means, variations and trends during the Satellite Era (1979–2014). Surv. Geophys. 38, 679–699. doi:10.1007/s10712-017-9416-4

Adler, R.F., Huffman, G.J., Chang, A., Ferraro, R., Xie, P.-P., Janowiak, J., Rudolf, B., Schneider, U., Curtis, S., Bolvin, D., Gruber, A., Susskind, J., Arkin, P., Nelkin, E., 2003. The Version-2 Global Precipitation Climatology Project (GPCP) Monthly Precipitation Analysis (1979–Present). J. Hydrometeorol. 4, 1147–1167. doi:10.1175/1525-7541(2003)004<1147:TVGPCP>2.0.CO;2

Aichner, B., Herzschuh, U., Wilkes, H., Vieth, A., Böhner, J., 2010. δD values of n-alkanes in Tibetan lake sediments and aquatic macrophytes - A surface sediment study and application to a 16ka record from Lake Koucha. Org. Geochem. 41, 779–790. doi:10.1016/j.orggeochem.2010.05.010

Amo, M., Suzuki, N., Kawamura, H., Yamaguchi, A., Takano, Y., Horiguchi, T., 2007. Biomarker compositions of dinoflagellates and their applications for paleoenvironmental proxies, in: Okada, H., Mawatari, S., Suzuki, N., Gautam, P. (Eds.), Proceedings of International Symposium "The Origin and Evolution of Natural Diversity." pp. 223–226.

Appleby, P.G., Oldfield, F., 1978. The calculation of lead-210 dates assuming a constant rate of supply of unsupported 210Pb to the sediment. Catena 5, 1–8. doi:10.1016/S0341-8162(78)80002-2

Araguás-Araguás, L., Froehlich, K., Rozanski, K., 1998. Stable isotope composition of precipitation over southeast Asia. J. Geophys. Res. 103, 721–728. doi:10.1029/98JD02582

Atahan, P., Heijnis, H., Dodson, J., Grice, K., Le Métayer, P., Taffs, K., Hembrow, S., Woltering, M., Zawadzki, A., 2014. Pollen, biomarker and stable isotope evidence of late Quaternary environmental change at Lake McKenzie, southeast Queensland. J. Paleolimnol. 53, 139–156. doi:10.1007/s10933-014-9813-3

Atwood, A.R., Volkman, J.K., Sachs, J.P., 2014. Characterization of unusual sterols and long chain diols, triols, keto-ols and n-alkenols in El Junco Lake, Galápagos. Org. Geochem. 66, 80–89. doi:10.1016/j.orggeochem.2013.11.004

Binford, M.W., 1990. Calculation and uncertainty analysis of 210Pb dates for PIRLA project lake sediment cores. J. Paleolimnol. 3, 253–267.

Blaauw, M., Christen, J.A., 2011. Flexible paleoclimate age-depth models using an autoregressive gamma process. Bayesian Anal. 6, 457–474. doi:10.1214/11-BA618

Borlace, S., Santoso, A., Cai, W., Collins, M., 2014. Extreme swings of the South Pacific Convergence Zone and the different types of El Niño events. Geophys. Res. Lett. 41, 4695–4703. doi:10.1002/2014GL060551

Bowen, G.J., 2010. Isoscapes: Spatial Pattern in Isotopic Biogeochemistry. Annu. Rev. Earth Planet. Sci. 38, 161–187. doi:10.1146/annurev-earth-040809-152429

Bowen, G.J., Revenaugh, J., 2003. Interpolating the isotopic composition of modern meteoric precipitation. Water Resour. Res. 39, 1–13. doi:10.1029/2003WR002086

Brock, F., Higham, T., Ditchfield, P., Ramsey, C.B., 2010. Current pretreatment methods for AMS radiocarbon dating at the Oxford Radiocarbon Accelerator Unit (ORAU). Radiocarbon 52, 103–112. doi:10.1017/S0033822200045069

Brown, J.R., Moise, A.F., Colman, R.A., 2012. The South Pacific Convergence Zone in CMIP5 simulations of historical and future climate. Clim. Dyn. 41, 2179–2197. doi:10.1007/s00382-012-1591-x

Brown, J.R., Moise, A.F., Delage, F.P., 2011. Changes in the South Pacific Convergence Zone in IPCC AR4 future climate projections. Clim. Dyn. 39, 1–19. doi:10.1007/s00382-011-1192-0

Cai, W., Lengaigne, M., Borlace, S., Collins, M., Cowan, T., McPhaden, M.J., Timmermann, A., Power, S., Brown, J., Menkes, C., Ngari, A., Vincent, E.M., Widlansky, M.J., 2012. More extreme swings of the South Pacific convergence zone due to greenhouse warming. Nature 488, 365–369. doi:10.1038/nature11358

Cantrell, C.A., 2008. Technical Note: Review of methods for linear least-squares fitting of data and application to atmospheric chemistry problems. Atmos. Chem. Phys. Discuss. 8, 5477–5487.

Che, L.M., Andréfouët, S., Bothorel, V., Guezennec, M., Rougeaux, H., Guezennec, J., Deslandes, E., Trichet, J., Matheron, R., Le Campion, T., Payri, C., Caumette, P., 2001. Physical, chemical, and microbiological characteristics of microbial mats (kopara) in the South Pacific atolls of French Polynesia. Can. J. Microbiol. 47, 994–1012. doi:10.1139/cjm-47-11-994

Chivall, D., Boule, D.M., Sinke-Schoen, D., Sinninghe Damsté, J.S., Schouten, S., van der Meer, M.T.J., 2014. The effects of growth phase and salinity on the hydrogen isotopic composition of alkenones produced by coastal haptophyte algae. Geochim. Cosmochim. Acta 140, 381–390.

Combettes, C., Sémah, A., Wirrmann, D., 2015. High-resolution pollen record from Efate Island, central Vanuatu: Highlighting climatic and human influences on Late Holocene vegetation dynamics. Comptes Rendus Palevol 14, 251–261. doi:10.1016/j.crpv.2015.02.003

Conroy, J.L., Cobb, K.M., Noone, D., 2013. Comparison of precipitation isotope variability across the tropical Pacific in observations and SWING2 model simulations. J. Geophys. Res. Atmos. 118, 5867–5892. doi:10.1002/jgrd.50412

Dansgaard, W., 1964. Stable isotopes in precipitation. Tellus 16, 436–468.

Dirghangi, S.S., Pagani, M., 2013a. Hydrogen isotope fractionation during lipid biosynthesis by *Haloarcula marismortui*. Geochim. Cosmochim. Acta 119, 381–390. doi:10.1016/j.gca.2013.05.023

Dirghangi, S.S., Pagani, M., 2013b. Hydrogen isotope fractionation during lipid biosynthesis by *Tetrahymena thermophila*. Org. Geochem. 64, 105–111.

Englebrecht, A.C., Sachs, J.P., 2005. Determination of sediment provenance at drift sites using hydrogen isotopes and unsaturation ratios in alkenones. Geochim. Cosmochim. Acta 69, 4253–4265. doi:10.1016/j.gca.2005.04.011

Ferguson, P.R., 2007. Aqueous and isotope geochemistry of the Fly River, Papua New Guinea: Coupling of the water and carbon cycles in tropical rainforest biomes. doi:https://doi.org/10.1002/ejlt.201200414

Ferguson, P.R., Dubois, K.D., Veizer, J., 2011. Fluvial carbon fluxes under extreme rainfall conditions: Inferences from the Fly River, Papua New Guinea. Chem. Geol. 281, 283–292. doi:10.1016/j.chemgeo.2010.12.015

Garcin, Y., Schwab, V.F., Gleixner, G., Kahmen, A., Todou, G., Séné, O., Onana, J.M., Achoundong, G., Sachse, D., 2012. Hydrogen isotope ratios of lacustrine sedimentary n-alkanes as proxies of tropical African hydrology: Insights from a calibration transect across Cameroon. Geochim. Cosmochim. Acta 79, 106–126. doi:10.1016/j.gca.2011.11.039

Garrett-Jones, S., 1979. Evidence for changes in Holocene vegetation and lake sedimentation in the Markham Valley, Papua New Guinea. Australian National University.

Haberle, S.G., 2002. Impact and timing of catastrophic events in PNG. Part II: achieving a reliable tephrochronology from lake sediments. AINSE Report 02/51. Report to Australian Institute of Nuclear Science and Engineering, ANSTO, Sydney, Australia.

Hassall, J.D., 2017. Static or dynamic: Reconstructing past movement of the South Pacific Convergence Zone. University of Southampton.

Heinzelmann, S.M., Villanueva, L., Sinke-Schoen, D., Sinninghe Damsté, J.S., Schouten, S., van der Meer, M.T.J., 2015. Impact of metabolism and growth phase on the hydrogen isotopic composition of microbial fatty acids. Front. Microbiol. 6, 1–11. doi:10.3389/fmicb.2015.00408

Henderson, A.K., Shuman, B.N., 2009. Hydrogen and oxygen isotopic compositions of lake water in the western United States. Geol. Soc. Am. Bull. 121, 1179–1189. doi:10.1130/B26441.1

Hildenbrand, A., Marlin, C., Conroy, A., Gillot, P.Y., Filly, A., Massault, M., 2005. Isotopic approach of rainfall and groundwater circulation in the volcanic structure of Tahiti-Nui (French Polynesia). J. Hydrol. 302, 187–208. doi:10.1016/j.jhydrol.2004.07.006

Hoffmann, G., Werner, M., Heimann, M., 1998. Water isotope module of the ECHAM atmoshperic general circulation model: A study on timescales from days to several years. J. Geophys. Res. 103, 871–896. doi:10.1029/98JD00423

Hogg, A.G., Hua, Q., Blackwell, P.G., Niu, M., Buck, C.E., Guilderson, T.P., Heaton, T.J., Palmer, J.G., Reimer, P.J., Reimer, R.W., Turney, C.S.M., Zimmerman, S.R.H., 2013. SHCal13 Southern Hemisphere calibration, 0–50,000 years cal BP. Radiocarbon 55, 1889–1903. doi:10.2458/azu_js_rc.55.16783

Hong, I., Pilarczyk, J.E., Horton, B.P., Fritz, H.M., Kosciuch, T.J., Wallace, D.J., Dike, C., Rarai, A., Harrison, M.J., Jockley, F.R., 2017. Sedimentological characteristics of the 2015 Tropical Cyclone Pam overwash sediments from Vanuatu, South Pacific. Mar. Geol. (in press). doi:10.1016/j.margeo.2017.05.011

Hope, G.S., 1996. Fieldwork Report: A reconnaissance survey of potential sites for pollen analysis in Southern Vanuatu. Unpublished report to Vanuatu Cultural Centre. (Corrections 2017).

Hope, G.S., Pask, J., 1998. Tropical vegetational change in the late Pleistocene of New Caledonia. Palaeogeogr. Palaeoclimatol. Palaeoecol. 142, 1–21. doi:10.1016/S0031-0182(97)00140-5

Hou, J., D'Andrea, W.J., Huang, Y., 2008. Can sedimentary leaf waxes record D/H ratios of continental precipitation? Field, model, and experimental assessments. Geochim. Cosmochim. Acta 72, 3503–3517. doi:10.1016/j.gca.2008.04.030

Hua, Q., Barbetti, M., Rakowski, A.Z., 2013. Atmospheric radiocarbon for the period 1950-2010. Radiocarbon 55, 2059–2072. doi:10.2458/azu_js_rc.v55i2.16177

Huang, Y., Shuman, B., Wang, Y., Webb, T., 2004. Hydrogen isotope ratios of individual lipids in lake sediments as novel tracers of climatic and environmental change: A surface sediment test. J. Paleolimnol. 31, 363–375. doi:10.1023/B:JOPL.0000021855.80535.13

IAEA/WMO, 2006. International Atomic Energy Agency/World Meteorological Organization Global Network for Isotopes in Precipitation, The GNIP Database, edited, Accessible at: http://www.iaea.org/water.

Issa, I., Aka Tongwa, F., Mouliom, A.G., Rouwet, D., Fantong, W.Y., Tchamabé, B.C., Ohba, T., Yoshida, Y., Sighomnou, D., Nkamdjou, S., Kusakabe, M., Chako Tchamabé, B., Ohba, T., Yoshida, Y., Sighomnou, D., Nkamdjou, S., Kusakabe, M., 2015. δ18O and δD variations in some volcanic lakes on the Cameroon Volcanic Line (West-Africa): generating isotopic baseline data for volcano monitoring and surveillance in Cameroon. J. Limnol. 74, 95–113. doi:10.4081/jlimnol.2014.966

Janouškovec, J., Gavelis, G.S., Burki, F., Dinh, D., Bachvaroff, T.R., Gornik, S.G., Bright, K.J., Imanian, B., Strom, S.L., Delwiche, C.F., Waller, R.F., Fensome, R.A., Leander, B.S., Rohwer, F.L., Saldarriaga, J.F., 2016. Major transitions in dinoflagellate evolution unveiled by phylotranscriptomics. Proc. Natl. Acad. Sci. 114, E171–E180. doi:10.1073/pnas.1614842114

Jeanpert, J., Genthon, P., Maurizot, P., Folio, J.L., Vendé-Leclerc, M., Sérino, J., Join, J.L., Iseppi, M., 2016. Morphology and distribution of dolines on ultramafic rocks from airborne LiDAR data: the case of southern Grande Terre in New Caledonia (SW Pacific). Earth Surf. Process. Landforms 41, 1854–1868. doi:10.1002/esp.3952

Kalnay, E., Kanamitsu, M., Kistler, R., Collins, W., Deaven, D., Gandin, L., Iredell, M., Saha, S., White, G., Woollen, J., Zhu, Y., Chelliah, M., Ebisuzaki, W., Higgins, W., Janowiak, J., Mo, K.C., Ropelewski, C., Wang, J., Leetmaa, A., Reynolds, R., Jenne, R., Joseph, D., 1996. The NCEP/NCAR 40-year reanalysis project. Bull. Am. Meteorol. Soc. doi:10.1175/1520-0477(1996)077<0437:TNYRP>2.0.CO;2

Kurita, N., Ichiyanagi, K., Matsumoto, J., Yamanaka, M.D., Ohata, T., 2009. The relationship between the isotopic content of precipitation and the precipitation amount in tropical regions. J. Geochemical Explor. 102, 113–122. doi:10.1016/j.gexplo.2009.03.002

Ladd, S.N., Dubois, N., Schubert, C.J., 2017. Interplay of temperature, productivity, and community assemblage on hydrogen isotope signatures of algal lipid biomarkers. Biogeosciences Discuss. 2017, 1–31. doi:10.5194/bg-2017-60

Le Cozannet, G., Garcin, M., Petitjean, L., Cazenave, A., Becker, M., Meyssignac, B., Walker, P., Devilliers, C., Brun, O. Le, Lecacheux, S., Baills, A., Bulteau, T., Yates, M., Wöppelmann, G., 2013. Exploring the relation between sea level rise and shoreline erosion using sea level reconstructions: an example in French Polynesia. J. Coast. Res. 2, 2137–2142. doi:10.2112/SI65-xxx.1

Leng, M.J., Marshall, J.D., 2004. Palaeoclimate interpretation of stable isotope data from lake sediment archives. Quat. Sci. Rev. 23, 811–831. doi:10.1016/j.quascirev.2003.06.012

Linsley, B.K., Kaplan, A., Gouriou, Y., Salinger, J., DeMenocal, P.B., Wellington, G.M., Howe, S.S., 2006. Tracking the extent of the South Pacific Convergence Zone since the early 1600s. Geochemistry, Geophys. Geosystems 7, 1–15. doi:10.1029/2005GC001115

Linsley, B.K., Zhang, P., Kaplan, A., Howe, S.S., Wellington, G.M., 2008. Interdecadal-decadal climate variability from multicoral oxygen isotope records in the South Pacific Convergence Zone region since 1650 A.D. Paleoceanography 23, 1–16. doi:10.1029/2007PA001539

Maloney, A.E., Shinneman, A.L.C., Hemeon, K., Sachs, J.P., 2016. Exploring lipid $^{2}H/^{1}H$ fractionation mechanisms in response to salinity with continuous cultures of the diatom *Thalassiosira pseudonana*. Org. Geochem. 101, 154–165. doi:10.1016/j.orggeochem.2016.08.015

Maupin, C.R., Partin, J.W., Shen, C.-C., Quinn, T.M., Lin, K., Taylor, F.W., Banner, J.L., Thirumalai, K., Sinclair, D.J., 2014. Persistent decadal-scale rainfall variability in the tropical South Pacific Convergence Zone through the past six centuries. Clim. Past 10, 1319–1332. doi:10.5194/cp-10-1319-2014

Mügler, I., Sachse, D., Werner, M., Xu, B., Wu, G., Yao, T., Gleixner, G., 2008. Effect of lake evaporation on δD values of lacustrine n-alkanes: A comparison of Nam Co (Tibetan Plateau) and Holzmaar (Germany). Org. Geochem. 39, 711–729. doi:10.1016/j.orggeochem.2008.02.008

Nelson, D.B., Sachs, J.P., 2014a. The influence of salinity on D/H fractionation in dinosterol and brassicasterol from globally distributed saline and hypersaline lakes. Geochim. Cosmochim. Acta 133, 325–339. doi:10.1016/j.gca.2014.03.007

Nelson, D.B., Sachs, J.P., 2014b. The influence of salinity on D/H fractionation in alkenones from saline and hypersaline lakes in continental North America. Org. Geochem. 66, 38–47. doi:10.1016/j.orggeochem.2013.10.013

Nelson, D.B., Sachs, J.P., 2013. Concurrent purification of sterols, triterpenols and alkenones from sediments for hydrogen isotope analysis using high performance liquid chromatography. Org. Geochem. 64, 19–28. doi:10.1016/j.orggeochem.2013.09.005

Osburn, M.R., Dawson, K.S., Fogel, M.L., Sessions, A.L., 2016. Fractionation of hydrogen isotopes by sulfate- and nitrate-reducing bacteria. Front. Microbiol. 7, 1–16. doi:10.3389/fmicb.2016.01166

Parkes, A., 1994. Holocene environments and vegetational change on four Polynesian islands.

Partin, J.W., Quinn, T.M., Shen, C.-C., Emile-Geay, J., Taylor, F.W., Maupin, C.R., Lin, K., Jackson, C.S., Banner, J.L., Sinclair, D.J., Huh, C.-A., 2013. Multidecadal rainfall variability in South Pacific Convergence Zone as revealed by stalagmite geochemistry. Geology 41, 1143–1146. doi:10.1130/G34718.1

Paul, H.A., 2002. Application of novel stable isotope methods to reconstruct paleoenvironments: Compound specific hydrogen isotopes and pore-water oxygen isotopes. Zürich: Swiss Federal Institute of Technology.

Polissar, P.J., D'Andrea, W.J., 2014. Uncertainty in paleohydrologic reconstructions from molecular δD values. Geochim. Cosmochim. Acta 129, 146–156. doi:10.1016/j.gca.2013.12.021

Polissar, P.J., Freeman, K.H., 2010. Effects of aridity and vegetation on plant-wax δD in modern lake sediments. Geochim. Cosmochim. Acta 74, 5785–5797. doi:10.1016/j.gca.2010.06.018

Power, S.B., Schiller, A., Cambers, G., Jones, D., Hennessy, K., 2011. The Pacific Climate Change Science Program. Bull. Am. Meteorol. Soc. 92, 1409–1411. doi:10.1175/BAMS-D-10-05001.1

Prebble, M., Anderson, A., Kennett, D.J., 2013. Forest clearance and agricultural expansion on Rapa, Austral Archipelago, French Polynesia. Holocene 23, 179–196. doi:10.1177/0959683612455551

Prebble, M., Wilmshurst, J.M., 2009. Detecting the initial impact of humans and introduced species on Island environments in Remote Oceania using palaeoecology. Biol. Invasions 11, 1529–1556. doi:10.1007/s10530-008-9405-0

R Core Team, 2017. R: A Language and Environment for Statistical Computing.

Read, J.L., Argument, D., Moseby, K.E., 2010. Initial conservation outcomes of the Tetepare Island Protected Area. Pacific Conserv. Biol. 16, 173–180. doi:10.1071/PC100173

Reed, C.B., 1989. Linear least-squares fits with errors in both coordinates. II: Comments on parameter variances. Am. J. Phys. 57, 642–646. doi:10.1119/1.17044

Risi, C., Bony, S., Vimeux, F., 2008. Influence of convective processes on the isotopic composition (δ18O and δD) of precipitation and water vapor in the tropics: 2. Physical interpretation of the amount effect. J. Geophys. Res. 113, D19306. doi:10.1029/2008JD009943

Risi, C., Bony, S., Vimeux, F., Jouzel, J., 2010. Water-stable isotopes in the LMDZ4 general circulation model: Model evaluation for present-day and past climates and applications to climatic interpretations of tropical isotopic records. J. Geophys. Res. Atmos. 115, 1–27. doi:10.1029/2009JD013255

Rozanski, K., Araguás-Araguás, L., Gonfiantini, R., 1993. Isotopic patterns in modern global precipitation, in: Swart, P.K. (Ed.), Climate Change in Continental Isotopic Records. American Geophysical Union, Washington DC, pp. 1–36. doi:10.1029/GM078p0001

Rull, V., Cañellas-Boltà, N., Margalef, O., Sáez, A., Pla-Rabes, S., Giralt, S., 2015. Late Holocene vegetation dynamics and deforestation in Rano Aroi: Implications for Easter Island's ecological and cultural history. Quat. Sci. Rev. 126, 219–226. doi:10.1016/j.quascirev.2015.09.008

Sachs, J.P., 2014. Hydrogen isotope signatures in the lipids of phytoplankton, in: Holland, H.D., Turekian, K.K. (Eds.), Treatise on Geochemistry. Elsevier Ltd, Oxford, pp. 79–94.

Sachs, J.P., Kawka, O.E., 2015. The influence of growth rate on $^{2}H/^{1}H$ fractionation in continuous cultures of the coccolithophorid *Emiliania huxleyi* and the diatom *Thalassiosira pseudonana*. PLoS One 10, e0141643. doi:10.1371/journal.pone.0141643

Sachs, J.P., Maloney, A.E., Gregersen, J., 2017. Effect of light on $^{2}H/^{1}H$ fractionation in lipids from continuous cultures of the diatom *Thalassiosira pseudonana*. Geochim. Cosmochim. Acta 209, 204–215. doi:10.1016/j.gca.2017.04.008

Sachs, J.P., Maloney, A.E., Gregersen, J., Paschall, C., 2016. Effect of salinity on $^{2}H/^{1}H$ fractionation in lipids from continuous cultures of the coccolithophorid *Emiliania huxleyi*. Geochim. Cosmochim. Acta 189, 96–109. doi:10.1016/j.gca.2016.05.041

Sachs, J.P., Schwab, V.F., 2011. Hydrogen isotopes in dinosterol from the Chesapeake Bay estuary. Geochim. Cosmochim. Acta 75, 444–459. doi:10.1016/j.gca.2010.10.013

Sachse, D., Billault, I., Bowen, G.J., Chikaraishi, Y., Dawson, T.E., Feakins, S.J., Freeman, K.H., Magill, C.R., McInerney, F.A., van der Meer, M.T.J., Polissar, P.J., Robins, R.J., Sachs, J.P., Schmidt, H.-L., Sessions, A.L., White, J.W., West, J.B., Kahmen, A., 2012. Molecular paleohydrology: Interpreting the hydrogen-isotopic composition of lipid

biomarkers from photosynthesizing organisms. Annu. Rev. Earth Planet. Sci. 40, 221–249. doi:10.1146/annurev-earth-042711-105535
Sachse, D., Radke, J., Gleixner, G., 2004. Hydrogen isotope ratios of recent lacustrine sedimentary n-alkanes record modern climate variability. Geochim. Cosmochim. Acta 68, 4877–4889. doi:10.1016/j.gca.2004.06.004
Sachse, D., Sachs, J.P., 2008. Inverse relationship between D/H fractionation in cyanobacterial lipids and salinity in Christmas Island saline ponds. Geochim. Cosmochim. Acta 72, 793–806. doi:10.1016/j.gca.2007.11.022
Sauer, P.E., Eglington, T.I., Hayes, J.M., Schimmelmann, A., Sessions, A.L., 2001. Compound-specific D/H ratios of lipid biomarkers from sediments as a proxy for environmental and climatic conditions. Geochim. Cosmochim. Acta 65, 213–222.
Schabetsberger, R., Drozdowski, G., Rott, E., Lenzenweger, R., Jersabek, C.D., Fiers, F., Traunspurger, W., Reiff, N., Stoch, F., Kotov, A. a., Martens, K., Schatz, H., Kaiser, R., 2009. Losing the bounty? Investigating species richness in isolated freshwater ecosystems of Oceania. Pacific Sci. 63, 153–179. doi:10.2984/049.063.0201
Schanze, J.J., Schmitt, R.W., Yu, L.L., 2010. The global oceanic freshwater cycle: A state-of-the-art quantification. J. Mar. Res. 68, 569–595. doi:10.1357/002224010794657164
Schmidt, G.A., LeGrande, A.N., Hoffmann, G., 2007. Water isotope expressions of intrinsic and forced variability in a coupled ocean-atmosphere model. J. Geophys. Res. Atmos. 112, 1–18. doi:10.1029/2006JD007781
Schouten, S., Ossebaar, J., Schreiber, K., Kienhuis, M.V.M., Langer, G., Benthien, A., Bijma, J., Burg, D., 2006. The effect of temperature, salinity and growth rate on the stable hydrogen isotopic composition of long chain alkenones produced by *Emiliania huxleyi* and *Gephyrocapsa oceanica*. Biogeosciences 3, 113–119.
Schwab, V.F., Garcin, Y., Sachse, D., Todou, G., Séné, O., Onana, J.M., Achoundong, G., Gleixner, G., 2015a. Dinosterol δD values in stratified tropical lakes (Cameroon) are affected by eutrophication. Org. Geochem. 88, 35–49. doi:10.1016/j.orggeochem.2015.08.003
Schwab, V.F., Garcin, Y., Sachse, D., Todou, G., Séné, O., Onana, J.M., Achoundong, G., Gleixner, G., 2015b. Effect of aridity on δ13C and δD values of C3 plant- and C4 graminoid-derived leaf wax lipids from soils along an environmental gradient in Cameroon (Western Central Africa). Org. Geochem. 78, 99–109. doi:10.1016/j.orggeochem.2014.09.007
Schwab, V.F., Sachs, J.P., 2011. Hydrogen isotopes in individual alkenones from the Chesapeake Bay estuary. Geochim. Cosmochim. Acta 75, 7552–7565. doi:10.1016/j.gca.2011.09.031
Sessions, A.L., Burgoyne, T.W., Hayes, J.M., 2001. Determination of the H3 factor in hydrogen isotope ratio monitoring mass spectrometry. Anal. Chem. 73, 200–207.
Sessions, A.L., Burgoyne, T.W., Schimmelmann, A., Hayes, J.M., 1999. Fractionation of hydrogen isotopes in lipid biosynthesis. Org. Geochem. 30, 1193–1200. doi:10.1016/S0146-6380(99)00094-7
Sichrowsky, U., Schabetsberger, R., Sonntag, B., Stoyneva, M., Maloney, A.E., Nelson, D.B., Richey, J.N., Sachs, J.P., 2014. Limnological characterization of volcanic crater lakes on Uvea Island (Wallis and Futuna, South Pacific). Pacific Sci. 68, 333–343. doi:10.2984/68.3.3

Southern, W., 1986. The Late Quaternary environmental histry of Fiji. Australia National University.
Southern, W., Ash, J., Brodie, J., Ryan, P., 1986. The flora, fauna and water chemistry of Tagimaucia crater, a tropical highland lake and swamp in Fiji. Freshw. Biol. 16, 509–520.
Stevenson, J., Hope, G.S., 2005. A comparison of late Quaternary forest changes in New Caledonia and northeastern Australia. Quat. Res. 64, 372–383. doi:10.1016/j.yqres.2005.08.011
Sturm, C., Zhang, Q., Noone, D., 2010. An introduction to stable water isotopes in climate models: benefits of forward proxy modelling for paleoclimatology. Clim. Past 6, 115–129. doi:10.5194/cpd-5-1697-2009
Thirumalai, K., Singh, A., Ramesh, R., 2011. A MATLAB^{TM} code to perform weighted linear regression with (correlated or uncorrelated) errors in bivariate data. J. Geol. Soc. India 77, 377–380. doi:10.1007/s12594-011-0044-1
Trichet, J., Hatté, C., Fontugne, M., 2013. Radiocarbon dating of recent Intertidal microbial mats on atoll rims. Radiocarbon 55, 1603–1616. doi:10.2458/azu_js_rc.55.16230
van der Meer, M.T.J., Benthien, A., French, K.L., Epping, E., Zondervan, I., Reichart, G.-J., Bijma, J., Sinninghe Damsté, J.S., Schouten, S., 2015. Large effect of irradiance on hydrogen isotope fractionation of alkenones in *Emiliania huxleyi*. Geochim. Cosmochim. Acta 160, 16–24. doi:10.1016/j.gca.2015.03.024
Vincent, D.G., 1994. The South Pacific Convergence Zone (SPCZ): A review. Mon. Weather Rev. 122, 1949–1970.
Volkman, J.K., 2005. Sterols and other triterpenoids: source specificity and evolution of biosynthetic pathways. Org. Geochem. 36, 139–159. doi:10.1016/j.orggeochem.2004.06.013
Volkman, J.K., Barrett, S.M., Blackburn, S.I., Mansour, M.P., Sikes, E.L., Gelin, F., 1998. Microalgal biomarkers: A review of recent research developments. Org. Geochem. 29, 1163–1179. doi:10.1016/S0146-6380(98)00062-X
Volkman, J.K., Barrett, S.M., Dunstan, G.A., Jeffrey, S.W., 1993. Geochemical significance of the occurrence of dinosterol and other 4-methyl sterols in a marine diatom. Org. Geochem. 20, 7–15. doi:10.1016/0146-6380(93)90076-N
Weiss, G.M., Pfannerstill, E.Y., Schouten, S., Sinninghe Damsté, J.S., van der Meer, M.T.J., 2017. Effects of alkalinity and salinity at low and high light intensity on hydrogen isotope fractionation of long-chain alkenones produced by *Emiliania huxleyi*. Biogeosciences Discuss. 14, 5693–5704. doi:10.5194/bg-2017-311
WHO, 2016. World Health Organization Western Pacific Region [WWW Document]. Data Stat. URL http://www.wpro.who.int/countries/en/ (accessed 12.26.17).
Widlansky, M.J., Webster, P.J., Hoyos, C.D., 2011. On the location and orientation of the South Pacific Convergence Zone. Clim. Dyn. 36, 561–578. doi:10.1007/s00382-010-0871-6
Wirrmann, D., Sémah, A.M., Chacornac-Rault, M., 2006. Late Holocene paleoenvironment in northern New Caledonia, southwestern Pacific, from a multiproxy analysis of lake sediments. Quat. Res. 66, 213–232. doi:10.1016/j.yqres.2006.04.002
Wolhowe, M.D., Prahl, F.G., Langer, G., Oviedo, A.M., Ziveri, P., Maria, A., Ziveri, P., 2015. Alkenone δD as an ecological indicator: A culture and field study of

physiologically-controlled chemical and hydrogen-isotopic variation in C37 alkenones. Geochim. Cosmochim. Acta 162, 166–182. doi:10.1016/j.gca.2015.04.034
Wolhowe, M.D., Prahl, F.G., Probert, I., Maldonado, M., 2009. Growth phase dependent hydrogen isotopic fractionation in alkenone-producing haptophytes. Biogeosciences 6, 1681–1694. doi:10.5194/bg-6-1681-2009
Xia, Z.H., Xu, B.Q., Mügler, I., Wu, G.J., Gleixner, G., Sachse, D., Zhu, L.P., 2008. Hydrogen isotope ratios of terrigenous n-alkanes in lacustrine surface sediment of the Tibetan Plateau record the precipitation signal. Geochem. J. 42, 331–338.
Xu, Y.-Y., Pearson, S., Kilbourne, H.K., 2015. Assessing coral Sr/Ca-SST calibration techniques using the species *Diploria strigosa*. Palaeogeogr. Palaeoclimatol. Palaeoecol. 440, 353–362. doi:10.1016/j.palaeo.2015.09.016
York, D., 1969. Least squares fitting of a straight line with correlated errors. Earth Planet. Sci. Lett. 5, 320–324. doi:10.1016/S0012-821X(68)80059-7
York, D., Evensen, N.M., Martı´nez, M.L., De Basabe Delgado, J., 2004. Unified equations for the slope, intercept, and standard errors of the best straight line. Am. J. Phys. 72, 367–375. doi:10.1119/1.1632486
Yoshimura, K., Kanamitsu, M., Noone, D., Oki, T., 2008. Historical isotope simulation using reanalysis atmospheric data. J. Geophys. Res. Atmos. 113, 1–15. doi:10.1029/2008JD010074
Yoshimura, K., 2015. Stable water isotopes in climatology, meteorology, and hydrology: A review. J. Meteorol. Soc. Japan 93, 513–533. doi:10.2151/jmsj.2015-036
Yu, L., Jin, X., Weller, R.A., 2008. Multidecade Global Flux Datasets from the Objectively Analyzed Air-sea Fluxes (OAFlux) Project: Latent and sensible heat fluxes, ocean evaporation, and related surface meteorological variables. OAFlux Proj. Tech. Rep. OA-2008-01 Woods Hole Oceanogr. Inst. doi:10.1007/s00382-011-1115-0
Zhang, X., Gillespie, A.L., Sessions, A.L., 2009. Large D/H variations in bacterial lipids reflect central metabolic pathways. Proc. Natl. Acad. Sci. U. S. A. 106, 12580–6. doi:10.1073/pnas.0903030106
Zhang, Z., Sachs, J.P., 2007. Hydrogen isotope fractionation in freshwater algae: I. Variations among lipids and species. Org. Geochem. 38, 582–608. doi:10.1016/j.orggeochem.2006.12.004
Zhang, Z., Sachs, J.P., Marchetti, A., 2009. Hydrogen isotope fractionation in freshwater and marine algae: II. Temperature and nitrogen limited growth rate effects. Org. Geochem. 40, 428–439. doi:10.1016/j.orggeochem.2008.11.002

Chapter 4: Precipitation changes in the South Pacific Convergence Zone during the last 2,000 years from $\delta^2H_{dinosterol}$ in freshwater lake sediments[3]

Abstract

Tropical moisture dynamics are centrally important to global climate, and precipitation in the tropics is undergoing large changes. It is unknown if these changes are unprecedented or within the range of natural variability since our observational records are short. The South Pacific Convergence Zone (SPCZ) is the southern hemisphere's most prominent precipitation feature extending 3000 km southeastwards from Papua New Guinea to French Polynesia. Seasonal and inter/intra-annual variability in SPCZ rainfall is well characterized by satellite data. Rainfall in the western tropical Pacific is difficult to reconstruct due to a dearth of archives that are both high-resolution and continuous. Here we present a spatially and temporally extensive picture of Late Holocene precipitation variability in the SPCZ region using molecular fossil hydroclimate reconstructions from the hydrogen isotopic composition (δ^2H) of the algal lipid biomarker dinosterol (4a, 23, 24-trimethyl-5a-cholest-22E-en-3β-ol). The network of records consists of 14 freshwater lake sediment cores from 10 lakes on 6 islands in the Solomon Islands, Vanuatu, Wallis, and Samoa. Together the records indicate wet Modern (1850-present) hydroclimate conditions and widespread dry conditions during the LIA (1450-1850) and MCA (950-1250). Replicate records from each region generally agree with each other with the exception of $\delta^2H_{dinosterol}$ records from two lakes on Wallis. Calculated precipitation rates during the LIA were estimated from a $\delta^2H_{dinosterol}$ core-top transfer function and approximately 0.6 – 0.9 mm d^{-1} lower than

[3] *In preparation for submission*

Modern in the Solomon Islands, Vanuatu, and Samoa, potentially due to a less intense or equatorward-shifted SPCZ. During the MCA the SPCZ likely had a more spatially heterogeneous hydrological pattern. Calculated precipitation rates were approximately 3 mm d^{-1} lower than present in the Solomon Islands and 0.4 mm d^{-1} lower than present in Vanuatu. Wallis and Samoa also appeared drier during the MCA. These precipitation records are important for understanding SPCZ natural variability during the Late Holocene.

Introduction

The tropics are the Earth's heat engine with global connections (Chiang, 2009) and changes in tropical precipitation have major implications for ecosystems and food security (Power et al., 2017). The SPCZ is the Southern Hemisphere's most prominent precipitation feature extending southeastward 3000 km from Papua New Guinea to French Polynesia (**Fig. 1**). Seasonal variability results in greater SPCZ rainfall during the austral summer and a northeast shift to a more zonal position is observed during El Niño events (Vincent, 1994). Recent studies examining instrumental data and numerical models have led to an improved understanding of the factors that influence SPCZ strength, shape, and extent (Cai et al., 2012; Kidwell et al., 2016; Kiladis et al., 1989; Lintner and Neelin, 2008; Takahashi and Battisti, 2007a, 2007b, van der Wiel et al., 2016a, 2016b, 2015, Widlansky et al., 2011, 2013), however an understanding of its behavior prior to the instrumental record is lacking.

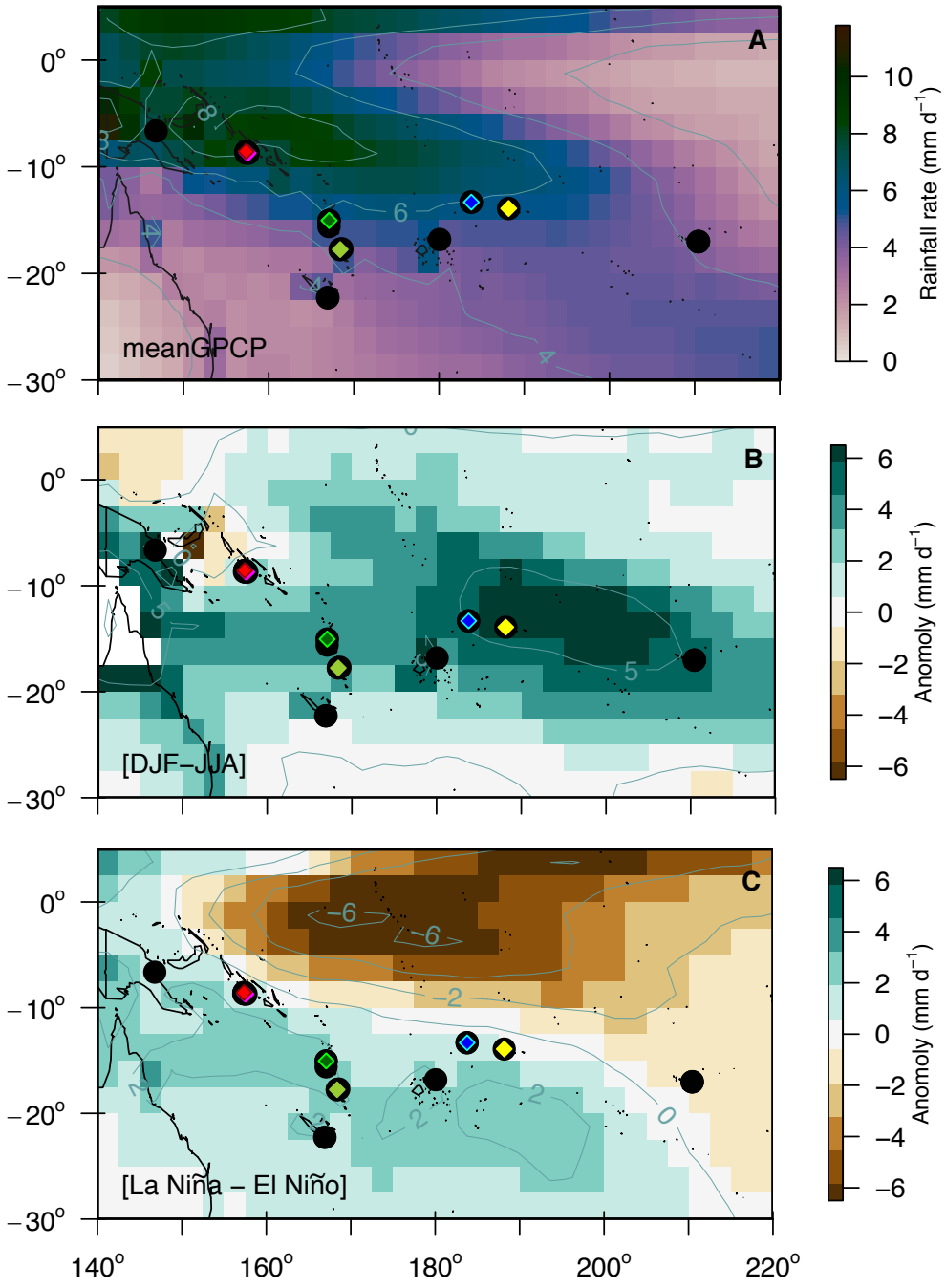

Fig. 1. Sample locations and rainfall rates. Black circles are 22 core-top calibration samples (Chapter 3), red diamonds are 4 lakes in the Solomon Islands (Rendova and Tetepare), green diamonds are 3 lakes in Vanuatu (Thion and Efate), blue diamonds are 2 lakes on Wallis, yellow diamond is 1 lake on Samoa. A) Contours and color scale show mean GPCPv2.3 rainfall rate (mm d^{-1}) on a 2.5° x 2.5° grid for the 1979-2016 period (http://www.esrl.noaa.gov/psd/), B) GPCP [DJF-JA] anomaly, C) GPCP [La Niña - El Niño] anomaly where La Niña (El Niño) conditions from ONI < 0.5°C (> 0.5°C).

Compiled paleoclimate records indicate that the past 2000 years have been marked by a warm MCA (950-1250), followed by cooler than normal temperatures of the LIA (1450-1850) as defined by the IPCC (Masson-Delmotte et al., 2013). Geochemical evidence indicates that the mean annual position of the Northern Hemisphere's most prominent rain feature, the Inter Tropical Convergence Zone (ITCZ), responded to the LIA and MCA in the central Pacific (Newton et al., 2006; Sachs et al., 2009; Schneider et al., 2014) and in the Indo-Pacific Warm Pool (Yan et al., 2015). It is likely that the SPCZ also experienced changes in mean annual position or intensity.

Changes in tropical precipitation in a warming climate will have profound implications for the global hydrologic balance and for societies that depend on rain to support subsistence lifestyles. Recent works have used global and regional climate models to examine how the SPCZ will respond to increased greenhouse warming. Future model projections of SPCZ behavior remain uncertain. Ensemble means result in little change in mean SPCZ position (Brown et al., 2012, 2011; Evans et al., 2016). Decreased precipitation was predicted for low levels of warming, and increased precipitation at higher levels of warming (Widlansky et al., 2013). Some studies suggest the SPCZ will have a more extreme zonal structure in a warmer climate (Borlace et al., 2014; Cai et al., 2012).

Accurately determining how the SPCZ responded to climate variations before the instrumental record requires the use of indirect indicators of rainfall. $\delta^{18}O$ coral records from the southwestern SPCZ region indicate colder and saltier ocean conditions during the LIA, potentially attributable to an equatorward shift of the SPCZ (Linsley et al., 2008, 2006). However the predominant influence on sea surface salinity in this region may be ocean circulation (Dassié et al., 2014; Wu et al., 2013). Speleothems from Vanuatu (Partin

et al., 2013) and the Solomon Islands (Maupin et al., 2014) revealed substantial multi-decadal variability but these records do not extend beyond 1600 AD, missing the MCA.

The main goal of this study is to determine how the SPCZ has changed in extent and/or intensity during the Late Holocene. To reconstruct past hydrological change, we measure hydrogen isotope ratios ($^2H/^1H$) of the algal lipid biomarker dinosterol, expressed as $\delta^2H_{dinosterol}$ ($\delta = [R_{sample}/R_{VSMOW}] - 1$, where R is $^2H/^1H$ and VSMOW is Vienna Standard Mean Ocean Water). These hydroclimate reconstructions rely on the link between the hydrogen isotopic composition of environmental waters, fluxes of water though the hydrologic cycle (Craig, 1961; Craig and Gordon, 1965; Dansgaard, 1964; Gat, 1996), and changes in lake water $^2H/^1H$ ratios that reflect hydrologic balance. In the tropics, the isotopic composition of precipitation is primarily influenced by the "amount effect" where higher precipitation rates are correlated with ^2H-depleted rain (Bony et al., 2008; Conroy et al., 2013; Dansgaard, 1964; Risi et al., 2008). The isotopic composition of lake water is determined by precipitation isotopes as well as evaporation, and in turn governs the isotopic composition of algal lipids (Englebrecht and Sachs, 2005; Zhang and Sachs, 2007). A core-top calibration between Global Precipitation Climatology Project (GPCP) (Adler et al., 2017, 2003) precipitation rates and $\delta^2H_{dinosterol}$ for the SPCZ region offers the opportunity to estimate quantitative changes in rainfall during the Late Holocene (Chapter 3). These calculations afford the opportunity to extend the GPCP record back prior to the instrumental record.

Magnetic susceptibility signals can independently confirm interpretations of hydrological change since they often reflect changes in runoff (Hodell et al., 2008; Liu et al., 2011; Rodysill et al., 2012). However, in anoxic environments magnetic susceptibility can

be degraded and may instead reflect preservation of magnetic minerals (Nowaczyk et al., 2007; Roy et al., 2017). Together, algal lipid $^{2}H/^{1}H$ ratios and magnetic susceptibility records can help paint a picture of past hydrological change in the understudied SPCZ region. In this study, we apply these techniques to several lake sites in each region.

Site descriptions

Details about the 14 cores presented in this study are listed in **Table 1**. All of these sites were lakes visited as part of the core-top study described in Chapter 3. Rendova and Tetepare are volcanic islands in the Western Province of the Solomon Islands located at the heart of the modern SPCZ (**Fig. 1**) with mean annual GPCP precipitation rates of ~8 mm d^{-1} at the lake sites. Compare to other regions in this study, the Solomon Islands has the smallest seasonal rainfall variation where austral summers (December-February) are on average 1.5 mm d^{-1} wetter than winter (June-August). The Solomon Islands also have a small response to ENSO variations of ~1 mm d^{-1} between La Niña's and relatively drier El Niño's (**Table 2**). (El Niño conditions are taken as seasons when the Oceanic Niño Index, derived from sea surface temperature anomalies in the Niño 3.4 region, were above 0.5°C (www.esrl.noaa.gov/psd/data/climateindices/list)). Tetepare Island is the largest uninhabited island in the South Pacific and has enforced marine and terrestrial protected areas (Read et al., 2010). Barora Pond is on the north-eastern side of Tetepare adjacent to mountainous terrain with a maximum depth of 2.4m. Lake Tavara is a near-coastal lake on the western side of Tetepare surrounded by flat topography with a maximum depth of 3.7m. On Rendova island, Harai Lake #1 is located farther north with a maximum water depth of 3.4m

and Lake Rano is the largest lake from the Solomon Islands in this study located at the south end with a maximum water depth of 11m.

The country of Vanuatu is located in the southern region of the SPCZ (**Fig. 1**) with GPCP precipitation rates around 4.8-5.5 mm d^{-1} at the lake sites. Austral summers are on average 3.5 mm d^{-1} wetter than winters. Vanuatu has the largest ENSO rainfall variations where La Niña's are >2 mm d^{-1} wetter than El Niño's (**Table 2**). Red Lake and White Lake are nearby lakes on Thion Island (also called Dauphin or Dionn Island), just off of the east coast of Espiritu Santo. The Eastern portion of Espiritu Santo is raised Quaternary reefs, including Thion Island which has a 180m raised plateau to the east of the lakes (Sémah and Wirrmann, 2006). Lake Emoatul (also sometimes referred to as "Lac aux Canards") is further to the south on the volcanic Efate Island (Ash et al., 1978; Raos and Crawford, 2004). It is ~131m above sea level and experiences fluctuating lake levels between 0 and 10m (Hope, 1996; Schabetsberger et al., 2009) and was mostly dry between 1994 and 1997 (Sémah and Wirrmann, 2006).

TABLE 1. Sediment cores sites.

Site Name	Latitude	Longitude	Water depth at core site (m)	Core ID	Collection date	Sediment length (cm)	$\delta^2H_{dinosterol}$ range (‰)	$\delta^2H_{dinosterol}$ (n)	Sample technique*
Barora Pond, Tetepare, Solomon Islands	-8.72232	157.600450	2.4	SBAR UC2	110617	143	26	42	UC
Lake Tavara Tetepare, Solomon Islands	-8.70277	157.450167	3.7	STAV UC4	110615	129	24	31	UC
Harai Lake #1, Rendova, Solomon Islands	-8.56218	157.355550	3.4	SHAR1 UC2	110623	121	61	24	UC
Lake Rano, Rendova, Solomon Islands	-8.68793	157.324267	11.8	SRANUC1	110620	135	NA	0	UC
Red Lake, Thion, Vanuatu	-15.03283	167.089917	2.5	VTR UC3	120627	176	41	44	UC
White Lake, Thion, Vanuatu	-15.04105	167.089133	17.1	VTW UC2	120626	111	45	55	UC
Emaotul Lake, Efate, Vanuatu	-17.72989	168.415462	6	VAN	150910	347	35	40	GC + L
Lac Lalolalo, Wallis	-13.30108	183.765917	88	LALO UC13	110516	161.5	56	36	UC
Lac Lalolalo, Wallis	-13.30048	183.766000	88	LALO UC14	110517	168	42	30	UC
Lac Lalolalo, Wallis	-13.30168	183.768083	23	LALO UC22	110519	38	42	7	UC
Lac Lalolalo, Wallis	-13.30168	183.768039	24	LALO UC24	110519	27	45	6	UC
Lac Lanutavake, Wallis	-13.32118	183.786033	23.3	LATVK UC1	110518	143	16	24	UC
Lac Lanutavake, Wallis	-13.32115	183.786133	23.2	LATVK UC4	110519	77.5	20	29	UC
Lake Lanoto'o, Upolu, Samoa	-13.91088	188.172600	16.4	LAN14 U2 + U1-1	140930	302	35	22	GC + L

*UC = Universal Corer, GC = UWITEC gravity core, L = Livingston

Wallis is located in the southern region of the SPCZ (**Fig. 1**) with GPCP precipitation rates around 6 mm d^{-1} at the lake sites. GPCP precipitation varies by 5.2 mm d^{-}

[1] between austral summer (December-February) and relatively drier winter (June-August) and by 0.8 mm d^{-1} between La Niña's and relatively drier El Niño's (**Table 2**). Lac Lalolalo (88ft deep) and Lac Lanutavake (25ft deep) are crater lakes that formed from collapse after eruption of lava, and enlarged by phreatomagmatic explosions. The craters are thought to have formed as recently as the Holocene based on thin soil layers along the rims (Stearns, 1945).

Samoa is located to the southeast of Wallis (**Fig. 1**) with GPCP precipitation rates around 5.6 mm d^{-1} at the lake sites. Samoa has the largest seasonal rainfall variations of 5.6 mm d^{-1}, and the smallest ENSO rainfall variations where the average La Niña is 0.7 mm d^{-1} wetter than El Niño (**Table 2**). Lake Lanoto'o is situated in a volcanic crater at 760 m above sea level. It has been previously described in detail (Hassall, 2017; Parkes, 1994).

TABLE 2. Mean GPCPv2.3 precipitation rates (mm d^{-1}) for the 1979-2017 period during specified intervals at lake sites

Lake site	Mean	SD	DJF	SD	JJA	SD	[DJF-JJA]	El Niño	SD	La Niña	SD	[Niña-Niño]
Barora Pond, Tetepare, Solomon Islands	7.7	3.0	9.2	3.7	7.1	2.4	2.1	7.2	3.2	8.2	3.2	1.1
Lake Tavara Tetepare, Solomon Islands	8.2	3.3	9.3	4.0	8.1	2.9	1.2	7.4	3.7	8.7	3.2	1.3
Lake Rano, Rendova, Solomon Islands	8.2	3.3	9.3	4.0	8.1	2.9	1.2	7.4	3.7	8.7	3.2	1.3
Harai Lake #1, Rendova, Solomon Islands	8.2	3.3	9.3	4.0	8.1	2.9	1.2	7.4	3.7	8.7	3.2	1.3
Red Lake, Thion, Vanuatu	5.0	3.3	6.5	3.7	3.0	2.0	3.5	4.1	3.0	6.5	3.6	2.4
White Lake, Thion, Vanuatu	5.0	3.3	6.5	3.7	3.0	2.0	3.5	4.1	3.0	6.5	3.6	2.4
Emaotul Lake, Efate, Vanuatu	5.0	3.2	6.8	3.5	3.1	1.6	3.7	4.2	2.8	6.3	3.6	2.1
Lac Lalolalo, Wallis	5.9	3.7	8.5	4.3	3.2	1.8	5.3	5.6	3.5	6.6	4.3	1.0
Lac Lanutavake, Wallis	5.9	3.7	8.5	4.3	3.2	1.8	5.3	5.6	3.5	6.6	4.3	1.0
Lake Lanoto'o, Upolu, Samoa	5.6	3.4	8.5	3.5	2.8	1.3	5.7	5.7	3.1	6.2	3.8	0.6

Methods

Field sampling

Sediment cores from Wallis, Solomon Islands, and Vanuatu were collected in 2011-2012 with a universal corer device (Aquatic Research) with 2-5/8" diameter core liners. The uppermost portion (typically 20-90 cm) was sectioned in the field at 0.5 or 1 cm intervals to

a depth at which the sediment was sufficiently consolidated to transport and store without disturbance to stratigraphy. These cores were split at the University of Washington or at the LacCore facility at the Limnological Research Center (LRC), University of Minnesota (USA). Cores were imaged with a DMT CoreScan and analyzed for magnetic susceptibility at 0.5-cm intervals using a high-resolution point sensor (MS2E) mounted on a GEOTEK XYZMSCL. Collection details about sediment from Lake Lanoto'o on Samoa can be found in Hassall (2017). Collection and scanning details about sediment from Lake Emaotul on Efate, Vanuatu can be found in Sear et al. (*in prep*).

Chronology

Age models for select cores were developed using radiocarbon and Lead-210 (^{210}Pb) analysis. Terrestrial leaf fossils from the top 70 cm of 13 sediment cores were analyzed for radiocarbon ages with accelerator mass spectrometry. Leaf fossils were pre-treated with an acid-base-acid procedure (Brock et al., 2010) at the University of Washington before analyses at Direct AMS (Seattle, WA), or pretreated and analyzed at Australian National University or CAMS (LLNL, Livermore, CA) (**Table S14**). Radiocarbon ages were calibrated using SHCAL13 (Hogg et al., 2013) and the SH1-2 bomb curve extension (Hua et al., 2013).

Selected sediment intervals from the uppermost portion (12 to 90cm) of eight sediment cores were analyzed for abundance of atmosphere derived ^{210}Pb at Flett Research Ltd. or ANTSO (Australian Nuclear Science and Organization) facilities (results in Chapter 3 Appendix A). Detailed procedures are available in Atahan et al., (2014). Alpha spectrometry was used to measure total ^{210}Pb indirectly from Polonium-210 (^{210}Po) (the

granddaughter of ^{210}Pb which is in secular equilibrium with ^{210}Pb within two years of deposition). Supported ^{210}Pb was measured indirectly from Radium-226 measurements. Atmospheric-derived unsupported ^{210}Pb was calculated by subtracting supported ^{210}Pb from total ^{210}Pb. A constant rate of supply (CRS) model (Appleby and Oldfield, 1978) was used to construct ^{210}Pb chronologies by relating exponential ^{210}Pb decay profiles to the cumulative dry mass-depth profiles as determined using bulk density measurements. Uncertainty in ages from the CRS model were conservatively estimated to be 20% of the age in years (Binford, 1990), with a minimum uncertainty of ±1 yr. The ^{210}Pb models were not validated with the independent tracer Cesium-137 due to limited sediment in these cores.

Age-depth relationships were constructed using CRS modeled ages and radiocarbon ages using BACON v2.2 software (Blaauw and Christen, 2011). For all cores the topmost 0 cm age was assumed to be the same as collection date.

Dinosterol hydrogen isotope analyses

Dinosterol was extracted, purified, identified, and quantified according to the methods detailed in Chapter 3. Briefly, sediments were freeze-dried then extracted with an Accelerated Solvent Extractor. Total lipid extracts (TLEs) were saponified then purified using column chromatography and High Performance Liquid Chromatography (HPLC) according to procedures in Nelson & Sachs (2013). HPLC fractions were checked to ensure full recovery of dinosterol in the target fraction(s) and for purity of dinosterol (Atwood and Sachs, 2012) using Gas Chromatography Mass Spectrometry (GCMS). Prior to HPLC, samples were acetylated using acetic anhydride with a known hydrogen isotopic composition (-123.8 ± 8.2‰). In preparation for isotopic measurements, HPLC-purified

dinosterol samples were quantified against a 5α-cholestane external standard. Quantifications were performed on an Agilent 6890N GC equipped with a Flame Ionization Detector (FID). $\delta^2H_{dinosterol}$ values were measured via gas-chromatography isotope-ratio mass spectrometry (GC-IRMS). Dinosterol δ^2H values were then corrected for hydrogen added during acetylation by a mass balance calculation as in (Nelson and Sachs, 2014). All $\delta^2H_{dinosterol}$ values and the standard deviations of multiple injections are reported in **Tables S1-S13**.

Precipitation calculations

Precipitation rates were calculated from $\delta^2H_{dinosterol}$ values using the $\delta^2H_{dinosterol}$–precipitation rate calibration generated from 44 core-top samples from 22 lakes (black circles **Fig. 1**) across the SPCZ region [$\delta^2H_{dinosterol}$ = -12.1(±2.6)*P-211(±15), R^2=0.59, p=0.0003, n=18] (see Figure 2 in Chapter 3). The Global Precipitation Climatology Project (GPCPv2.3) dataset (Adler et al., 2017, 2003) was used to compute long-term mean annual precipitation rates for the 1979-2016 period. Data are provided by the National Oceanic & Atmospheric Administration/Oceanic & Atmospheric Research/Earth System Research Laboratory Physical Sciences Division (NOAA/OAR/ESRL PSD), Boulder, Colorado, USA, from their Web site at http://www.esrl.noaa.gov/psd/. The dataset is based on gauge and satellite observations and is gridded at a 2.5° x 2.5° scale. Estimates of precipitation uncertainty (Adler et al., 2012) accompany precipitation data and resulted in large errors in independent variable of the calibration which required the use of a maximum likelihood estimate method (York et al., 2004) incorporating bivariate analytical uncertainty for all linear regressions (Cantrell, 2008; Reed, 1989; Thirumalai et al., 2011; York, 1969; York et

al., 2004), which were performed using published Matlab™ code (Thirumalai et al., 2011). To calculate precipitation rates, the calibration was used as a transfer function such that

$$Pp_1 = \delta^2H_{sample} + 211 / -12.1 \quad \text{[Eq. 1]}$$

where Pp_1 is the calculated paleorainfall, δ^2H_{sample} is a downcore measurement. The estimated uncertainty in Pp_1 from this transfer function ranges from ~1 to 3 mm d^{-1} (depending on the measured δ^2H_{sample} value) from the errors on the slope (±2.6) and intercept (±15) plus propagated analytical $\delta^2H_{dinosterol}$ uncertainties (Chapter 3). In Figures 2-5 in this Chapter, these uncertainties are shown as blocks of color on the right axis.

Results

Sedimentology

Sediment core images (**Fig. S1**), magnetic susceptibility levels, *b** (blue-yellow) and *a** (green-red) reflectance data (**Fig. S2-4**), and age models (**Fig. S5**) revealed heterogeneous depositional environments, sediment types, and accumulation rates between the ten lakes in this study. The 143 cm long sediment core SBARUC2 from Barora Pond (Tetepare, Solomon Islands) had the fastest accumulation rate with an average of 0.84 years contained in each 1 cm interval. The results of a 210-Pb CRS model (Chapter 3) from eight samples in the top 50 cm were used with three ^{14}C dates from fossil leaves to construct a BACON age model that extends back to 57 years BP (between 27 and 106 years BP), or 1893 calendar year CE (**Fig. S5**). This core was collected from 2.4 m water depth and was consistently laminated with brown, light brown, and dark brown layers. A large magnetic

susceptibility signal was measured in Barora Pond (Tetepare, Solomon Islands) in SBARUC2 which ranged from 16 to 483 SI*10^{-5} (**Fig. S2**).

On the same island the 129 cm long core STAVUC4 from Lake Tavara (Tetepare, Solomon Islands) was collected from 3.7 m water depth and had dark brown organic sediment above frequent layers of sandy material towards the base. The BACON age model from 210-Pb (Chapter 3) and 3 fossil leaves indicates that the upper 85 cm above the sand layers extends back to 357 ybp (between 283 and 483 ybp) (**Fig. S5**). The magnetic susceptibility signal in Lake Tavara STAVUC4 ranged from -1 to 3 SI*10^{-5} with the highest values from the sandy layers at the base of the core (**Fig. S2**).

SHAR1UC2 from Harai Lake #1 (Rendova, Solomon Islands) was 121 cm long and collected from 3.4 m water depth. The age model from eight fossil leaves indicates a very slow accumulation rate in the top 40 cm (average of 26 years per each 1 cm interval) and faster accumulation in the remaining 81 cm. There was almost no magnetic susceptibility signal, values ranged from -1.9 to 0.8 SI*10^{-5}, indicating primarily organic material (**Fig. S2**). Also on Rendova Island, the larger and deeper Lake Rano had visible layering throughout and a high magnetic susceptibility signal ranging from -8 to 981 SI*10^{-5} in SRANUC1 (**Fig. S2**). The BACON age model for SRANUC1 was made from eight ^{14}C dates from fossil leaves, and had two were outliers (**Fig. S5**).

Sediment cores collected from Red Lake and White Lake on Thion Island (Vanuatu) consisted of dark brown algal gytta throughout with no laminations, and both had substantial (8 to 30 cm) sandy layers near the base of the cores. VTRUC3 from Red Lake was 176 cm collected from a water depth of 2.5 m. Eight fossil leaves from the upper 121.5 cm of sediment above the sandy layer produced a BACON age model that extends back ~1310 ybp

(between 1291 and 1629 ypb) (**Fig. S5**). VTWUC2 collected in 17 m water depth from White Lake had a similar stratigraphy and age-depth relationship. Seven fossil leaves from the upper 100 cm of sediment above the sandy layer produced a BACON age model that extends back ~1240 ybp (between 1128 and 1472 ypb) (**Fig. S5**). Sediments in both Red Lake and White Lake (Thion Island, Vanuatu) were mainly composed of organic material and had very small magnetic susceptibility that ranged from -3 to 9 SI*10^{-5} with the highest values from the white sandy portion at the base of the cores (**Fig. S3**).

Sediment cores collected from Lac Lanutavke (Wallis Island) had laminations of tan and brown sediment interspersed with thick layers of dark algal gytta (**Fig. S1**). LATVKUC1 collected from 23 m water depth had a total core length of 143 cm and the oldest fossil leaf from 133 cm had a calibrated age of 1560 ybp (between 1474 and 1684 ypb). LATVKUC4 collected 12 m away from the same water depth had a total core length of 77.5 cm, the oldest fossil leaf from 67 cm had a calibrated age of 1231 ybp (between 1115 and 1321 ypb) (**Fig. S5**). The magnetic susceptibility ranges measured in these cores were 226 and 316 SI*10^{-5} in LATVKUC1 and LATVKUC4 and coincided with color variations and reflectance data where dark (negative *b**) algal gytta sediment layers had the lowest values, and regions with light brown laminations of lithogenic material had high and variable values (**Fig. S4**). The similarities in color and magnetic susceptibility facilitated hand-tuning the longer core LATVKUC1 to the depth scale of LATVKUC4, which experienced less compression during core collection. Using the modified depth scale of LATCKUC1 (**Fig. S6**), a total of 10 ^{14}C dates from both cores were used to create a single BACON age model (**Fig. S5**).

All sediment cores collected from Lac Lalolalo (Wallis Island) had large amounts of terrestrial plant litter interspersed with dark brown algal gytta and no visible laminations. LALOUC13 from ~88 m water depth at the lake center had a total core length of 161.5 cm. The BACON age model from eight fossil leaves extends back to ~1393 ybp (between 1312 and 1529 ypb) at 155 cm. Collected 68 m away, LALOUC14 also from ~88 m water depth had a total core length of 168 cm. Two of the five fossil leaves in this core had radiocarbon ages that BACON found to be outliers, both being too old and the deepest fossil leaf from the 12 5cm interval had a calibrated age of 1837 ybp (between 1717 and 1923 ypb) (**Fig. S5**). Both cores displayed vigorous degassing upon collection mixing the top 10 cm of sediment, therefore the first 15-20 cm were sampled into one bag. Collected near the shore without degassing-mixed sediment, LALOUC22 from 24 m water depth had a total core length of 38 cm, the oldest fossil leaf from the 13-14 cm interval had a calibrated age of 50 ybp (between 26 and 86 ypb) (Chapter 3). LALOUC24 from 24 m water depth had a total core length of 38 cm, the oldest 210-Pb CRS model age from 8 cm was 54 ybp (between 28 and 84 ypb) (Chapter 3). Lalolalo cores had magnetic susceptibility levels nearly an order of magnitude lower than Lac Lanutavake with ranges of 25 or 26 $SI*10^{-5}$ in LALOUC13 and LALOUC14. The cores collected from shallow water depths near the shore of Lac Lalolalo were either completely sectioned (LALOUC24), or consisted of only rock and wood material below the sectioned material (so no magnetic susceptibility or reflectance profiles are shown). Despite the large differences in absolute ranges between the two lakes on Wallis, the general pattern in magnetic susceptibility between the sites was similar through time (**Fig. S4**), however since the signals were small and distinct color patterns were not present, hand tuning of the cores from Lalolalo to the same depth scale was not attempted.

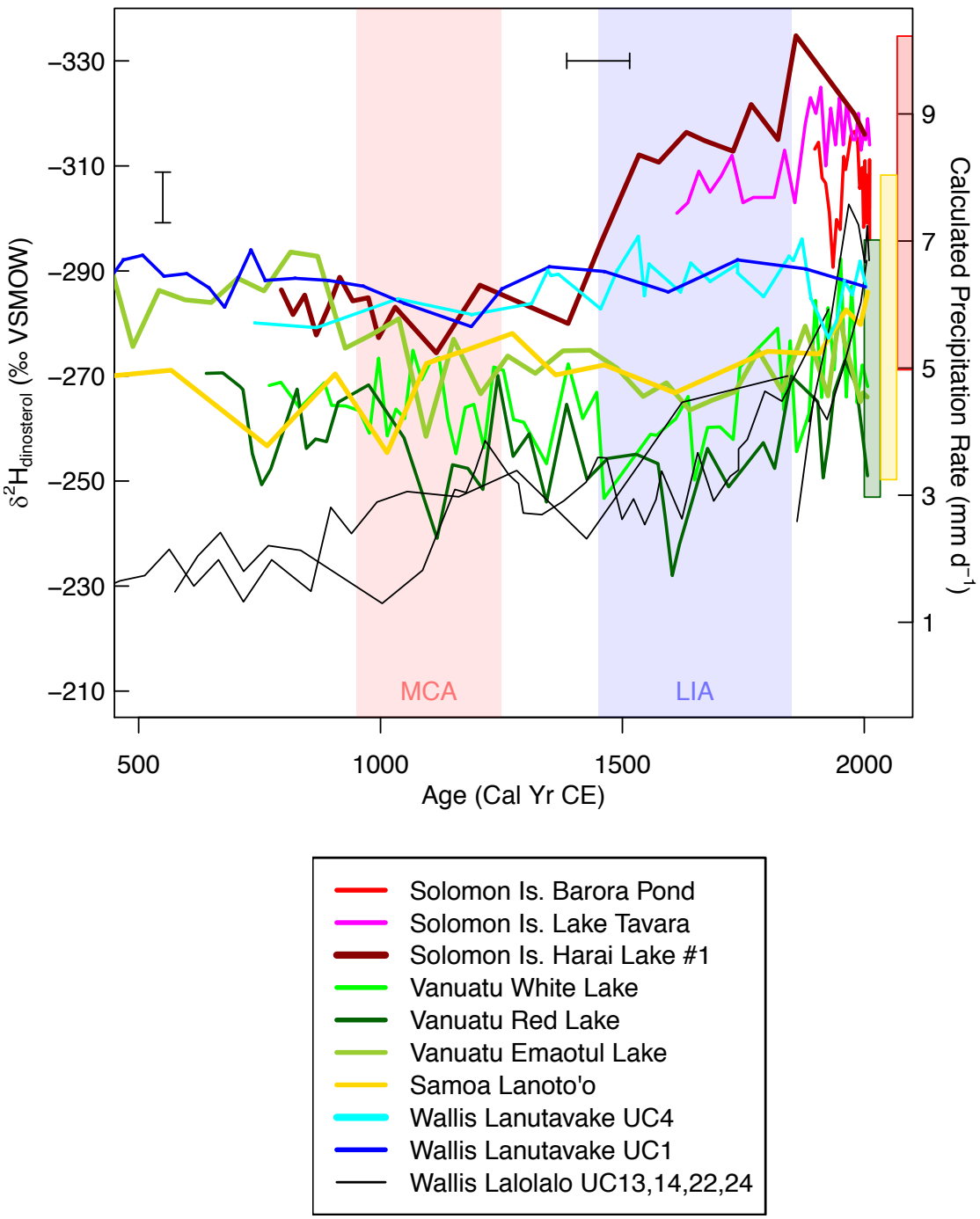

FIG. 2. All freshwater lake $\delta^2H_{dinosterol}$ records (left axis) and calculated precipitation rates (right axis). Records are more ^2H-enriched as mean island precipitation rates decrease from the Solomon Islands (reds) to Vanuatu (greens). During the MCA the Solomon Islands may have been as dry as Wallis, Samoa, and Vanuatu. Blue and red bands indicate LIA and MCA and colored bars on the right axis indicate average estimated uncertainty in calculated precipitation for each region. The think black vertical bar indicates average $\delta^2H_{dinosterol}$ uncertainty (±4.8 ‰) and the thin black horizontal bar indicates average age model uncertainty (±65 yrs).

TABLE 3. Average and standard deviations of d2H_dinosterol values during select time periods: modern (1850-present), LIA (1450-1850), MCA (950-1250). Values were combined for all four Lac Lalolalo cores and for both Lac Lanutavake cores.

		1850-present					1450-1850					950-1250				
		Modern d2H_dino.	SD	Modern rain	SD	n	LIA d2H_dino.	SD	LIA rain	SD	n	MCA d2H_dino.	SD	MCA rain	SD	n
Site	Core	‰	‰	mm d^{-1}	mm d^{-1}		‰	‰	mm d^{-1}	mm d^{-1}		‰	‰	mm d^{-1}	mm d^{-1}	
Barora Pond, Tetepare, Solomon Islands	SBARUC2	-306	6	7.8	0.48	42	NA	NA	NA	NA	NA	NA	NA	NA	NA	NA
Lake Tavara Tetepare, Solomon Islands	STAVUC4	-317	5	8.7	0.42	20	-306	4	7.8	0.32	11	NA	NA	NA	NA	NA
Harai Lake #1, Rendova, Solomon Islands	SHAR1UC2	-324	10	9.3	0.81	3	-312	8	8.4	0.63a	8	-281	5	5.8	0.44	5
Red Lake, Thion, Vanuatu	VTRUC3	-261	9	4.2	0.73	7	-251	10	3.3	0.83	12	-256	11	3.7	0.9	7
White Lake, Thion, Vanuatu	VTWUC2	-273	11	5.1	0.93	12	-262	9	4.2	0.74	14	-265	6	4.5	0.53	16
Emaotul Lake, Efate, Vanuatu	VAN	-272	7	5	0.6	7	-268	4	4.7	0.3	8	-272	9	5.1	0.77	5
Lac Lalolalo, Wallis	LALOUC13,14,22,24	-280	18	5.7[a]	1.5[a]	14	-253	8	3.5[a]	0.70[a]	19	-245	9	2.8[a]	0.78[a]	9
Lac Lanutavake, Wallis	LATVKUC1,4	-287	5	6.4	0.4	11	-289	4	6.5	0.3	15	-283	3	6	0.24	5
Lake Lanoto'o, Upolu, Samoa	SAMOA	-281	5	5.8	0.41	4	-271	4	5	0.33	3	-268	11	4.7	0.88	3

[a]Note, the calculation of precipitation rates from d2H_dinosterol data may not be appropriate since this record may be heavilty influenced by other environmental factors

$\delta^2H_{dinosterol}$

$\delta^2H_{dinosterol}$ values from all freshwater lakes in the tropical South Pacific are shown in **Figure 2** and available in **Tables S1-S13**. Mean $\delta^2H_{dinosterol}$ values for specific time periods are in **Table 3** and anomalies between time periods in **Table 4**. $\delta^2H_{dinosterol}$ values from the three lakes in the Solomon Islands had the most ^2H-depeleted values compare to $\delta^2H_{dinosterol}$ values from other islands (**Table S1 – S3; Fig. 2; Fig. 3**). From Barora Pond on Tetepare $\delta^2H_{dinosterol}$ values in SBARUC2 do not extend back to the LIA and had a 26 ‰ range from -317 to -291 ‰, 42 samples were injected on average 3.5 times and had a pooled uncertainty of 4.9 ‰. The $\delta^2H_{dinosterol}$ values in SBARUC2 were well correlated with magnetic susceptibility in this core (**Fig. S7**). $\delta^2H_{dinosterol}$ values and magnetic susceptibility data show high frequency changes that resemble instrumental rainfall data from nearby stations in the Solomon Islands, 2003-2011 data from Tetepare (Read et al., 2010), and GPCP data (**Fig. S8**). Also on Tetepare, STAVUC4 from Tavara Lake had $\delta^2H_{dinosterol}$ values with a 24 ‰ range from -325 to -301 ‰, 31 samples were injected on average 3.4 times and had a pooled uncertainty of 7.0 ‰. Data from this core extended back to the LIA where it was more ^2H-enriched (**Fig. 2; Fig. 3; Table S2**).

On Rendova Island, $\delta^2H_{dinosterol}$ values in SHARIUC2 from Lake Harai #1 had a 61 ‰ range from -335 to -274 ‰, 24 samples were injected on average 2.8 times and had a pooled uncertainty of 4.0 ‰. Low dinosterol concentrations and large quantities of an unidentified compound in samples from core SRANUC1 in Lake Rano (Rendova Island) prohibited measurements of $\delta^2H_{dinosterol}$ values.

$\delta^2H_{dinosterol}$ records from Red Lake and White Lake (Thion Island, Vanuatu) (**Fig. 2; Fig. 4; Tables S4-5**) had good inter-lake agreement, although the average $\delta^2H_{dinosterol}$ value in White Lake (-268 ‰) was ~11 ‰ ^{2}H-depleted compare the average value in Red Lake (-257 ‰). In Red Lake $\delta^2H_{dinosterol}$ values in VTRUC3 had a 41 ‰ range from -273 to -232 ‰, 44 samples were injected on average 2.4 times and had a pooled uncertainty of 7.3 ‰. Similarly, White Lake $\delta^2H_{dinosterol}$ values from VTWUC2 had a 45 ‰ range from -292 to -247 ‰, 55 samples were injected on average 3.4 times and had a pooled uncertainty of 5.6 ‰. In addition to the cores from Vanuatu described in this paper, $\delta^2H_{dinosterol}$ measurements from sediment core VAN collected in Lake Emaotul on Efate Island (Vanuatu) had a 35 ‰ range from -294 to -258 ‰, 40 samples were injected on average 3.4 times and had a pooled uncertainty of 4.0 ‰. Details about this core and its sedimentological properties are described in Sear et al. (*in prep*).

Both lakes on Wallis Island had two independent $\delta^2H_{dinosterol}$ records with good intra-lake agreement, but the duplicate records had very different inter-lake results (**Fig. 2; Fig. 5; Tables S7-12**). From Lac Lanutavake, $\delta^2H_{dinosterol}$ values in LATVKUC1 had a 16 ‰ range from -295 to -279 ‰, 24 samples were injected on average 3.4 times and had a pooled uncertainty of 4.5 ‰. Similarly, $\delta^2H_{dinosterol}$ values in LATVKUC4 had a 20 ‰ range from -

297 to -277 ‰, 29 samples were injected on average 2.5 times and had a pooled uncertainty of 6.4 ‰.

The older samples from Lac Lalolalo had the most ^{2}H-enriched $\delta^{2}H_{dinosterol}$ values of all cores in this study. In Lac Lalolalo $\delta^{2}H_{dinosterol}$ values in LALOUC13 had a 56 ‰ range from -283 to -227 ‰, 36 samples were injected on average 3.8 times and had a pooled uncertainty of 4.2 ‰. Similarly, $\delta^{2}H_{dinosterol}$ values in LALOUC14 had a 42 ‰ range from -270 to -227 ‰, 30 samples were injected on average 2.1 times and had a pooled uncertainty of 4.8 ‰. In the short cores collected from shallow water near the shore, $\delta^{2}H_{dinosterol}$ values in LALOUC22 had a 42 ‰ range from -303 to -261 ‰, 7 samples were injected on average 3.4 times and had a pooled uncertainty of 6.3 ‰. Similarly, $\delta^{2}H_{dinosterol}$ values in LALOUC24 had a 45 ‰ range from -288 to -242 ‰, 6 samples were injected on average 2.8 times and had a pooled uncertainty of 4.2 ‰. Taken together, the range in LALOUC13+LALOUC22 (76 ‰) or LALOUC14+LALOUC24 (60 ‰) was ~four times larger than the ranges in the $\delta^{2}H_{dinosterol}$ values from the smaller neighboring Lac Lanutavake.

In addition to the cores described in this study from Wallis, Vanuatu, and the Solomon Islands, the Late Holocene sections (LANU2 and LANU1-1) of a sediment core from Lake Lanoto'o (Samoa) were analyzed for $\delta^{2}H_{dinosterol}$ (**Fig. 2; Fig. 5; Tables S13**). A detailed description of this core and interpretation of several sedimentological parameters can be found in Hassall (2017). Lake Lanoto'o $\delta^{2}H_{dinosterol}$ values had a 35 ‰ range from -290 to -255 ‰, 22 samples were injected on average 4 times and had a pooled uncertainty of 7.2 ‰. Unlike other sediment cores, some LAN samples had a split dinosterol peak detected

on the GCFID (but had pure mass spectra (and no detectable split peak) on the GCMS) most likely due to a stereoisomer of dinosterol.

TABLE 4. Amomolies calculated from averages in **Table 3** of δ2H_dinosterol and corresponding precipitation rate

		[Modern-LIA]		[Modern-MCA]		[LIA-MCA]	
Site	Core	δ2H_dino. ‰	Rain mm d^{-1}	δ2H_dino. ‰	Rain mm d^{-1}	δ2H_dino. ‰	Rain mm d^{-1}
Barora Pond, Tetepare, Solomon Islands	SBARUC2	NA	NA	NA	NA	NA	NA
Lake Tavara Tetepare, Solomon Islands	STAVUC4	-11	0.90	NA	NA	NA	NA
Harai Lake #1, Rendova, Solomon Islands	SHAR1UC2	-11	0.93	-42	3.48	-31	2.56
Red Lake, Thion, Vanuatu	VTRUC3	-10	0.83	-6	0.50	4	-0.34
White Lake, Thion, Vanuatu	VTWUC2	-10	0.87	-7	0.62	3	-0.25
Emaotul Lake, Efate, Vanuatu	VAN	-4	0.31	0.4	-0.04	4	-0.34
Lac Lalolalo, Wallis	LALOUC13,14,22,24	-27	2.2[a]	-35	2.9[a]	8	0.68[a]
Lac Lanutavake, Wallis	LATVKUC1,4	2	-0.16	-4	0.33	-6	0.49
Lake Lanoto'o, Upolu, Samoa	SAMOA	-9	0.78	-13	1.10	-4	0.30

[a]Note, the calculation of precipitation rates from d2H_dinosterol data may not be appropriate since this record may be heavilty influenced by other environmental factors

Precipitation rates

Figures 3-5 show $\delta^2H_{dinosterol}$ records (left axis) and corresponding calculated precipitation rates (right axis) using the calibration Eq. 1 developed in Chapter 3. The short, high resolution record from Barora Pond (Tetepare, Solomon Islands) had a relatively ^2H-depleted average $\delta^2H_{dinosterol}$ value (-306 ‰) and a corresponding wet precipitation rate (7.8 mm d^{-1}) during the Modern period (42 samples) compare to other regions but was more ^2H-enriched compare to other Solomon Islands sites (**Table 3**). In Lake Tavara (Tetepare, Solomon Islands) the average $\delta^2H_{dinosterol}$ value (-317 ‰) and precipitation rate (8.7 mm d^{-1}) during the Modern period (20 samples) was more ^2H-depleted/wetter than the average $\delta^2H_{dinosterol}$ value (-306‰) and precipitation rate (7.8 mm d^{-1}) during the LIA (11 samples) (**Fig. 3D; Table 3**). In Lake Harai #1 (Rendova, Solomon Islands), the average $\delta^2H_{dinosterol}$ value (-324 ‰) and precipitation rate (9.3 mm d^{-1}) during the modern period (3 samples) was ^2H-depleted/wetter than the average $\delta^2H_{dinosterol}$ value (-312 ‰) and precipitation rate (8.4 mm d^{-1}) during the LIA (8 samples). The average $\delta^2H_{dinosterol}$ value and precipitation

rate during the MCA (5 samples) was (-281 ‰) and (5.8 mm d^{-1}), indicating drier MCA conditions (**Fig. 3D; Table 3**).

In Red Lake (Thion, Vanuatu) the average $\delta^2H_{dinosterol}$ value (-261 ‰) and precipitation rate (4.2 mm d^{-1}) during the modern period (7 samples) was more ^2H-depleted/wetter than the average $\delta^2H_{dinosterol}$ value (-251 ‰) and precipitation rate (3.3 mm d^{-1}) during the LIA (12 samples) and the MCA (7 samples) when the average $\delta^2H_{dinosterol}$ value was -256 ‰ and precipitation rate 3.7 mm d^{-1} (**Fig. 4D; Table 3**). In nearby White Lake, the average $\delta^2H_{dinosterol}$ value (-273 ‰) and precipitation rate (5.1 mm d^{-1}) during the modern period (12 samples) was also more ^2H-depleted/wetter than the average $\delta^2H_{dinosterol}$ value (-262 ‰) and precipitation rate (4.2 mm d^{-1}) during the LIA (14 samples) and was also more ^2H-depleted/wetter than the average $\delta^2H_{dinosterol}$ value (-265 ‰) and precipitation rate (4.5 mm d^{-1}) during the MCA (16 samples) (**Fig. 4D; Table 3**). This trend was similar but muted in Lake Emaotul (Efate, Vanuatu), the average $\delta^2H_{dinosterol}$ value (-272 ‰) and precipitation rate (5.0 mm d^{-1}) during the modern period (7 samples) was similar to the average $\delta^2H_{dinosterol}$ value (-268 ‰) and precipitation rate (4.7 mm d^{-1}) during the LIA (8 samples) and the average $\delta^2H_{dinosterol}$ value (-272 ‰) and precipitation rate (5.1 mm d^{-1}) during the MCA (5 samples) (**Fig. 4D; Table 3**).

In Lac Lanutavake (Wallis) combined UC1 and UC4 had an average $\delta^2H_{dinosterol}$ value (-287) and precipitation rate (6.4 mm d^{-1}) during the modern period (11 samples) similar to the average $\delta^2H_{dinosterol}$ value (-289 ‰) and precipitation rate (6.5 mm d^{-1}) during the LIA (15 samples) and the average $\delta^2H_{dinosterol}$ value (-283 ‰) and precipitation rate (6.0 mm d^{-1}) during the MCA (5 samples) (**Fig. 5D; Table 3**). In Lake Lanoto'o (Samoa), the average $\delta^2H_{dinosterol}$ value (-281 ‰) and precipitation rate (5.8 mm d^{-1}) during the modern

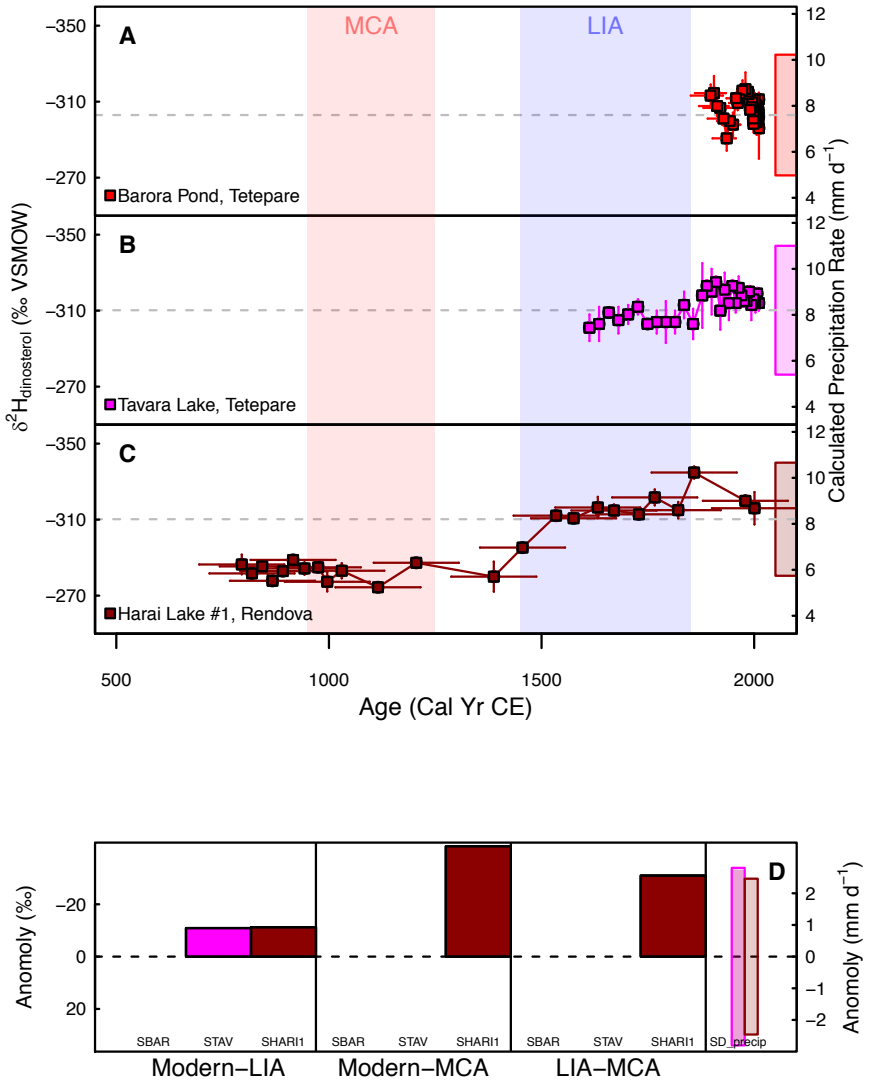

Fig. 3. Solomon Islands $\delta^2H_{dinosterol}$ (left axis) and calculated precipitation rate (right axis) versus age. Horizontal error bars are 95% prediction intervals from BACON age models and vertical error bars are the standard deviations of triplicate injections (or the pooled uncertainty if only one injection was made). Blue and red bands indicate LIA and MCA and colored bars on the right axis indicate average estimated uncertainty in calculated precipitation. Gray dashed lines indicate observed mean GPCP precipitation rate. Note inverse scale for $\delta^2H_{dinosterol}$ data. A) SBARUC2 from Barora Pond (Tetepare), B) STAVUC4 from Lake Tavara (Tetepare), and C) SHARIUC2 from Harai Lake #1 (Rendova). D) Calculated anomalies from all samples that fell within a defined time including Modern (1850-present), LIA (1450-1850), or MCA (950-1250).

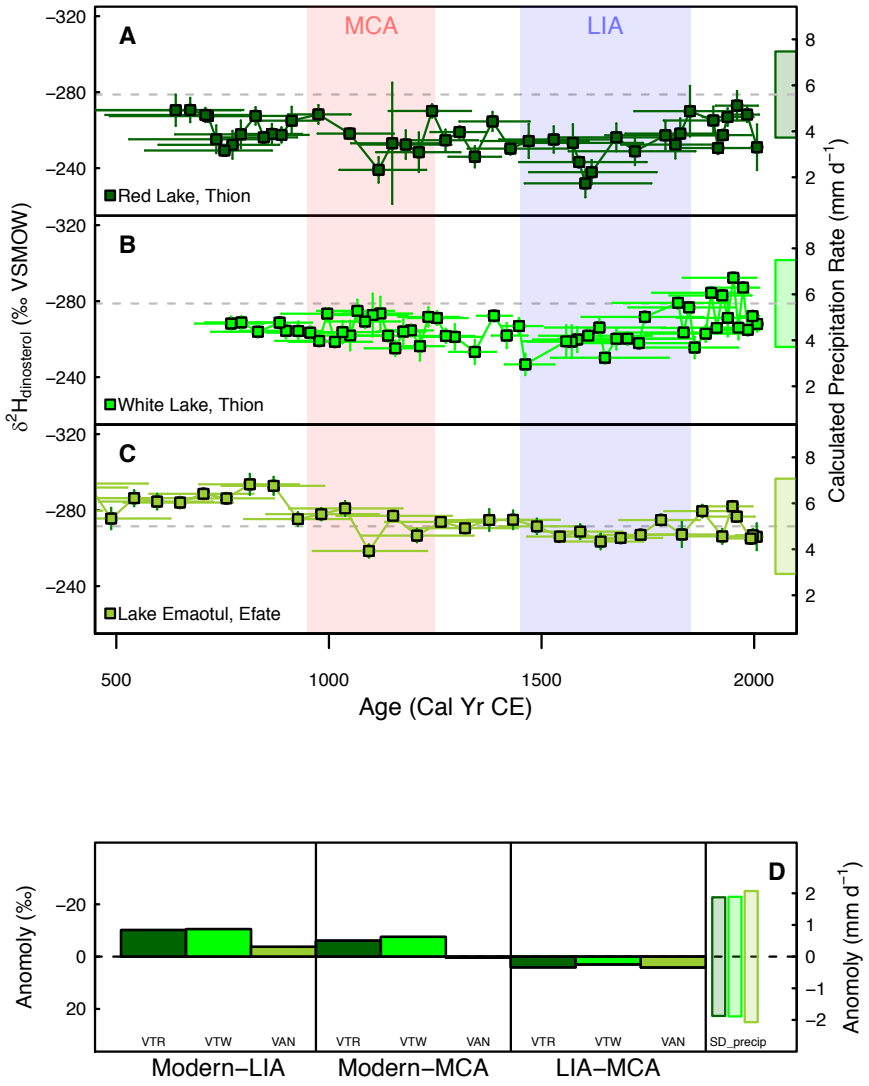

Fig. 4. Vanuatu $\delta^2H_{dinosterol}$ (left axis) and calculated precipitation rate (right axis) versus age. Horizontal error bars are 95% prediction intervals from BACON age models and vertical error bars are the standard deviations of triplicate injections (or the pooled uncertainty if only one injection was made). Blue and red bands indicate LIA and MCA and colored bars on the right axis indicate average estimated uncertainty in calculated precipitation. Gray dashed lines indicate observed mean GPCP precipitation rate. Note inverse scale for $\delta^2H_{dinosterol}$ data. A) VTWUC3 from Red Lake, (Thion), B) VTWUC2 from White Lake, (Thion), and C) VAN from Lake Emaotul, (Efate). D) Calculated anomalies from all samples that fell within a defined time including Modern (1850-present), LIA (1450-1850), or MCA (950-1250).

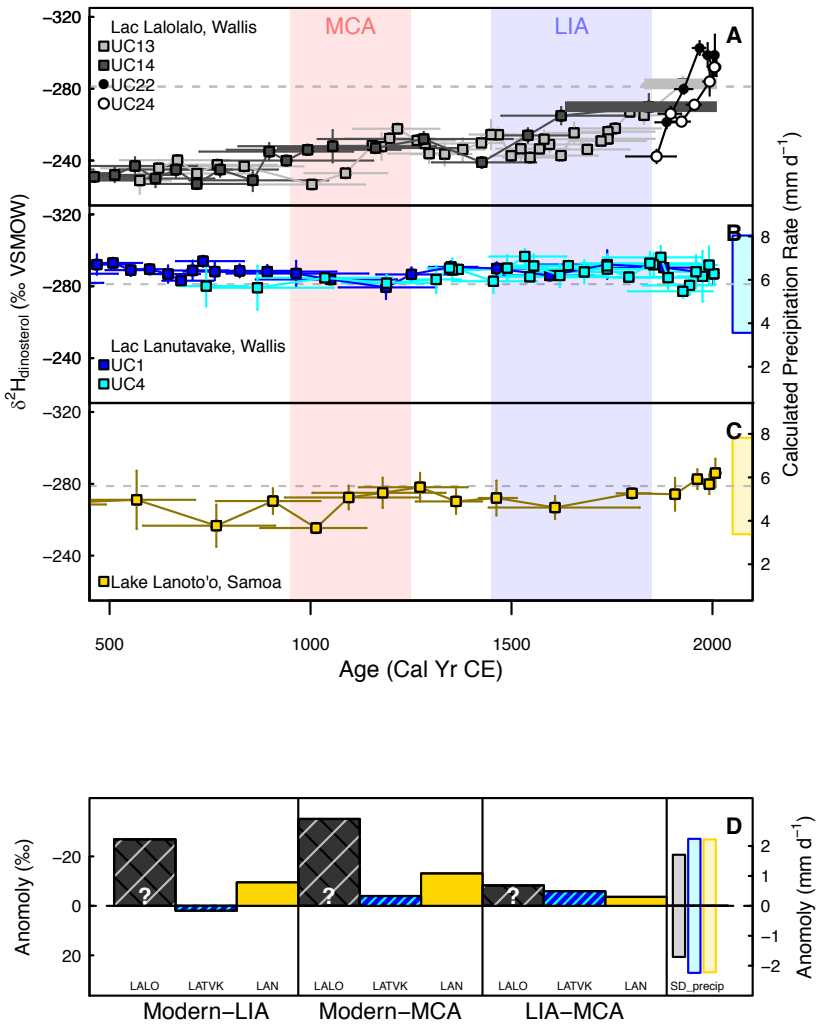

Fig. 5. Wallis and Samoa $\delta^2H_{dinosterol}$ (left axis) and calculated precipitation rate (right axis) versus age. Horizontal error bars are 95% prediction intervals from BACON age models and vertical error bars are the standard deviations of triplicate injections (or the pooled uncertainty if only one injection was made). Blue and red bands indicate LIA and MCA and colored bars on the right axis indicate average estimated uncertainty in calculated precipitation. Gray dashed lines indicate observed mean GPCP precipitation rate. Note inverse scale for $\delta^2H_{dinosterol}$ data. A) LALOUC13 (light gray squares), UC14 (dark gray squares), UC22 (black circles), UC24 (white circles) from Lac Lalolalo (Wallis), horizontal bars indicate value from the homogenized uppermost 0-10cm sample (LALOUC13) and 0-15cm sample (LALOUC14). B) LATCKUC1 (dark blue) and UC4 (cyan) from Lac Lanutavake (Wallis), and C) LAN from Lake Lanoto'o, (Samoa). D) Calculated anomalies from all samples that fell within a defined time including Modern (1850-present), LIA (1450-1850), or MCA (950-1250). The question marks in the anomalies of Lac Lalolalo indicate that $\delta^2H_{dinosterol}$ in this core is likely susceptible to non-hydrological processes and should be interpreted with caution.

period (4 samples) was more ^{2}H-depleted/wetter than the average $\delta^{2}H_{dinosterol}$ value (-271 ‰) and precipitation rate (5.0 mm d^{-1}) during the LIA (3 samples) and the average $\delta^{2}H_{dinosterol}$ value (-268 ‰) and precipitation rate (4.7 mm d^{-1}) during the MCA (3 samples) (**Fig. 5D; Table 3**).

Discussion

The $\delta^{2}H_{dinosterol}$ and magnetic susceptibility data presented here offer a spatially broad picture of Late Holocene precipitation variability in the SPCZ region. The records show wet hydroclimate conditions in the Modern period (1840-present), and widespread dry conditions during the LIA (1450-1850) and MCA (950-1250) discussed in detail below (**Fig. 3-5; Table 4**). Records that extend back prior to the MCA (-850-1250) indicate generally wetter conditions.

The high-resolution record from Barora Pond (Tetepare, Solomon Islands) shows large inter-annual variability in precipitation rates that are well aligned with changes in magnetic susceptibility data during the Modern period. Compared to available instrumental data from three nearby rain gauges and GPCP data (**Fig. S8**) precipitation rates calculated from $\delta^{2}H_{dinosterol}$ values and magnetic susceptibility generally follow major hydrologic trends within age model uncertainties, demonstrating the coherence between rain, $\delta^{2}H_{dinosterol}$, and magnetic susceptibility. FIG SBAR also reveals the disparate precipitation rates from different gauge stations around the Solomon Islands and GPCP data, which highlights how precipitation rates calculated in this study follow closely regional GPCP-like precipitation rather than extremely localized precipitation.

The assessment of moisture changes on Wallis is complicated by contradictory behavior of $\delta^2H_{dinosterol}$ records from Lac Lalolalo and Lac Lanutavake (**Fig. 5**). For instance, $\delta^2H_{dinosterol}$ values in Lac Lanutavake remained relatively stable from the LIA to Modern, but Lac Lalolalo had a very large Modern-LIA $\delta^2H_{dinosterol}$ anomaly of -27‰. The very different $\delta^2H_{dinosterol}$ ranges in duplicate records from both lakes imply that $\delta^2H_{dinosterol}$ in (at least) one of these lakes must have been influenced by non-climate environmental parameters. Lac Lalolalo exhibited changes in $\delta^2H_{dinosterol}$ values larger than two nearby freshwater lakes (Lac Lanutavake and Lac Lanoto'o on Samoa) and is therefore the most likely candidate to suffer from non-climate impacts on $\delta^2H_{dinosterol}$. Furthermore, Lac Lalolalo's multiple water inputs including rainwater (lake surface), groundwater (mid-depths), and ocean water (lake bottom) (**Fig. 6**), plus its uniquely great depth offer comparatively more opportunities for environmental impacts on $\delta^2H_{dinosterol}$. Given the outstanding differences between $\delta^2H_{dinosterol}$ in the two Wallis lakes, and the similarities between the records from Lac Lanutavake and Lake Lanoto'o (Samoa), extreme caution should be used before making interpretations about precipitation from the Lac Lalolalo $\delta^2H_{dinosterol}$ values. The reason why $\delta^2H_{dinosterol}$ records in Lac Lalolalo were so different than Lac Lanutavake remains unanswered. Several possibilities include biological impacts such as ^2H-enrichment due to increased surface salinity (Maloney et al., 2016; Nelson and Sachs, 2014; Sachs et al., 2016; Sachs and Schwab, 2011; Sachse and Sachs, 2008; Schouten et al., 2006; Weiss et al., 2017), a shift in species composition (Sessions et al., 1999; Zhang and Sachs, 2007), or a change in preferred metabolism (a shift from heterotrophy to photoautotrophy) (Dawson et al., 2015; Heinzelmann et al., 2015; Osburn et al., 2016; Zhang et al., 2009). Additionally, post

depositional alterations to the isotope signature of dinosterol have been suggested to take place in highly eutrophic lakes (Schwab et al., 2015).

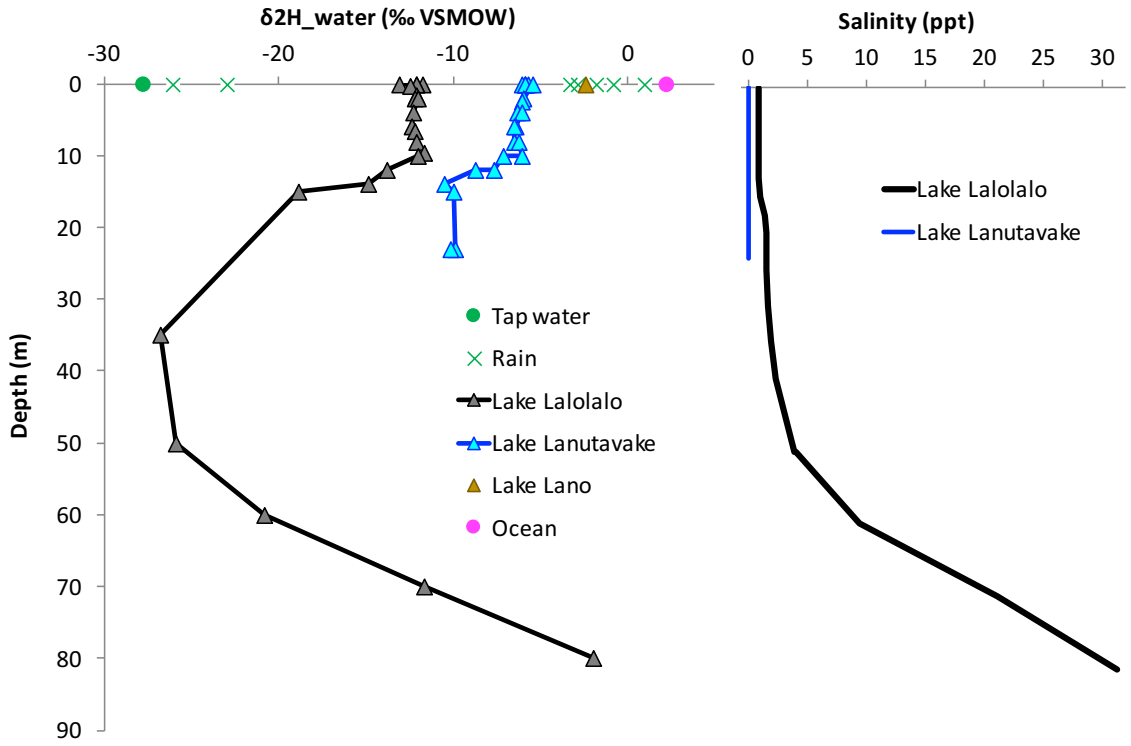

Fig. 6. Hydrogen isotope ratios of environmental water samples (left) and salinity profiles (right) from Wallis Island lakes. The most ^{2}H-depleted sample is tap water (green circle), which is sourced from groundwater and reflects the long term mean rain water isotopic composition. Lac Lalolalo (black diamonds and black line), Lac Lanutavake (blue diamonds and blue line), and Lake Lano (brown diamond) are all ^{2}H-depleted compare to ocean water (pink circle). Individual rain events shown (green crosses).

Dry conditions during the Little Ice Age

The most coherent result from the $\delta^{2}H_{dinosterol}$ data is the widespread agreement for a dry LIA compare to Modern throughout SPCZ islands with rainfall rates 0.3 – 0.9 mm d^{-1} lower (**Table 4**). $\delta^{2}H_{dinosterol}$ values were more ^{2}H-depleted in the Modern (1840-present) compare to the LIA (1450-1850) in the Solomon Islands (2 of 2 cores), Vanuatu (3 of 3 cores), and Samoa (1 of 1 core), and slightly ^{2}H-enriched on Wallis Island (considering only combined Lac Lanutavake cores which had a slight negative anomaly whereas the large

positive anomaly in Lac Lalolalo cores may be sensitive to environmental change) (**Fig. 3-5; Table 4**). The widespread [Modern-LIA] $\delta^2H_{dinosterol}$ anomalies (between -9 to -11‰) provides strong evidence for decreased precipitation and/or increased evaporation during the LIA at all locations except potentially Wallis. Precipitation rates from the GPCP-$\delta^2H_{dinosterol}$ core-top calibration (Chapter 3) gave [Modern-LIA] calculated precipitation anomalies of 0.90 – 0.93 mm d^{-1} on Tetepare and Rendova (Solomon Islands), 0.31 – 0.87 mm d^{-1} on Thion and Efate (Vanuatu), and 0.78 mm d^{-1} on Samoa (**Fig. 3-5; Table 4**).

A dry SPCZ LIA is also evident in nearby speleothem records that have slightly more ^{18}O-depleted samples in the Modern versus late-LIA from Efate (Vanuatu) (Partin et al., 2013) and Guadalcanal (Solomon Islands) (Maupin et al., 2014). A drier LIA climate is consistent with decreased runoff detected across the SPCZ from Australia (Lough, 2011) to French Polynesia (Toomey et al., 2016) and more saline LIA sea surface salinities in coral records extending into part of the LIA from Fiji and Rarotonga (Linsley et al., 2006, 2004), Vanuatu (Quinn et al., 1993), New Caledonia (Quinn et al., 1998), and the nearby Great Barrier Reef (Druffel and Griffin, 1993; Hendy et al., 2002) and Coral Sea (Calvo et al., 2007); for a synthesis see (Smerdon et al., 2017).

Possible causes of widespread LIA dryness include a less expansive/intense SPCZ or an equatorward shift of the SPCZ. Linsley et al. (2006) interpreted high LIA salinities from coral records to indicate a more "La Niña-like" Modern period since observed La Niñas result in increased SPCZ rainfall (**Fig. 1**). Quantitative estimates of rainfall from the SPCZ region can help inform if comparisons to ENSO can appropriately describe past rainfall regimes. To test the analogy, observed ENSO shifts during the 1979-2017 GPCP period

caused [La Niña - El Niño] anomalies of 1.3 mm d^{-1} in the Solomon Islands, 2.4 mm d^{-1} on

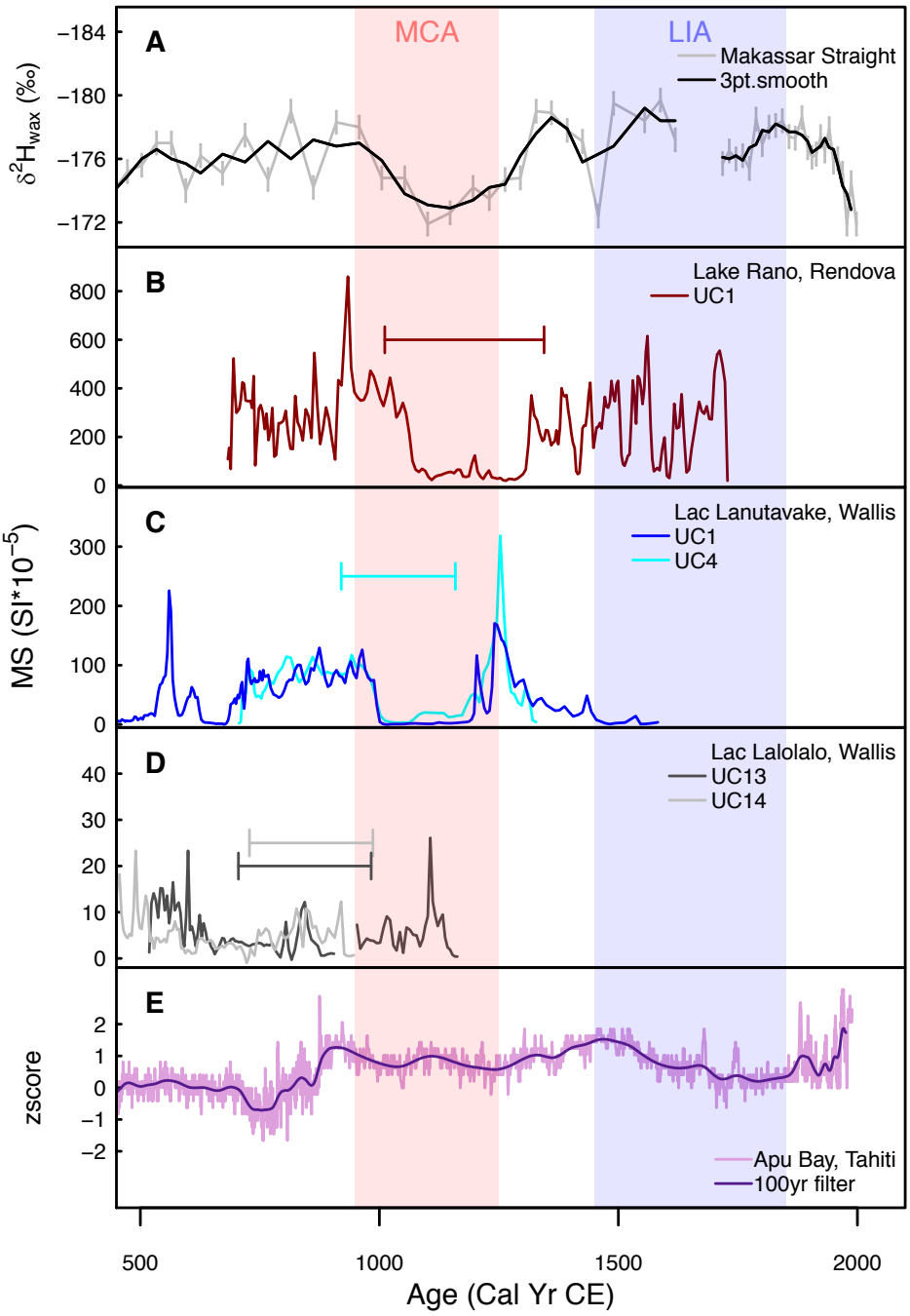

Fig. 7. Comparison of magnetic susceptibility records from the Solomon Islands and Wallis to nearby records that indicate the extent of the MCA drought. Horizontal bars indicate the average BACON modelled maximum and minimum ages. A) Makassar Straight leaf wax isotopes (Tierney et al. 2010) inverted, B) MS from SRANUC1, Lake Rano, Rendova, Solomon Islands, C) MS records from two sediment cores LATVKUC1 and LATVKUC4 from Lac Lanutavake (Wallis Island), D), MS records from two sediment cores LALOUC13 and LALOUC14 from Lac Lalolalo (Wallis Island), E) Ti/Ca record from French Polynesia (Toomey et al. 2016).

Thion Island (Vanuatu), 0.6 mm d^{-1} on Samoa, and 1 mm d^{-1} on Wallis (**Fig. 1; Table 2**). Compared to our calculated paleoprecipitation rates, dinosterol hydrogen isotope derived [Modern-LIA] precipitation anomalies were smaller than ENSO anomalies in the Solomon Islands, Vanuatu, and Wallis, but larger than Samoa. If correct, this suggests that precipitation associated with a "La Niña-like" mean state had a different spatial expression than actual modern La Niña's, or that the centennial-scale variability that caused LIA dryness is different than ENSO. However, the actual magnitudes of both observed [La Niña - El Niño] and calculated [Modern-LIA] anomalies remain tentative due to GPCP uncertainties of ~1.4 mm d^{-1} (Adler et al., 2012), and estimated calculated rainfall uncertainties of ~1-3 mm d^{-1} (Chapter 3) which are shown as blocks of color on the right axis in Figures 2-5.

It is not clear why a dry LIA was detected in the Solomon Islands, Vanuatu, and Samoa, but not on Wallis (**Table 4**) and if it is a result of spatial heterogeneity of past hydrologic change or to unknown influence on the $\delta^2H_{dinosterol}$ record in Lac Lanutavake. Lac Lalolalo indicates a very large change, but it is likely that this signal is not due to climate. Unfortunately, the magnetic susceptibility signals that offer insight into older hydrologic changes (**Fig. S9**) are not available for the upper portions of these cores since they were sectioned in the field. It is noteworthy that Wallis has the deepest lakes in this study (25 and 88 m). Thus, they should be slower to respond to hydrologic changes due to the longer residence time of water. Presently, both Lac Lanutavake and Lac Lalolalo have strong oxyclines at 10m, suggesting that the effective depths of these lakes are comparable to other lakes in the study. But if the Wallis lakes were not always been meromictic, then it is possible that the amplitudes of past hydrologic change were muted as a function of lake

depth, precipitation rate (**Fig. S10**), and their connection to the slow-responding water table. Indicators of lake stratification could help constrain how these unique lake sites may have changed during the past.

Drought during the Medieval Climate Anomaly

$\delta^2H_{dinosterol}$ values were also ^2H-depleted during the Modern (1840-present) compare to the MCA (950-1250) in the Solomon Islands (1 core), Vanuatu (2 of 3 cores), Wallis (1 core, considering only Lake Lanutavake), and Samoa (1 core) (**Fig. 2; Fig. 3; Table 3**). The [LIA- MCA] anomaly indicates that MCA was not as dry as the LIA in Vanuatu, but the MCA was drier than the LIA in the Solomon Islands, Wallis, and Samoa (**Fig. 3-5; Table 4**). Calculated precipitation rates from the GPCP-$\delta^2H_{dinosterol}$ core-top calibration Eq. 1 (Chapter 3) gave [Modern- MCA] precipitation anomalies as large as 3.48 mm d^{-1} in Harai Lake #1 on Rendova (Solomon Islands), 1.10 mm d^{-1} in Lake Lanoto'o on Samoa, and 0.62 mm d^{-1} in White Lake on Thion (Vanuatu) (**Table 4**).

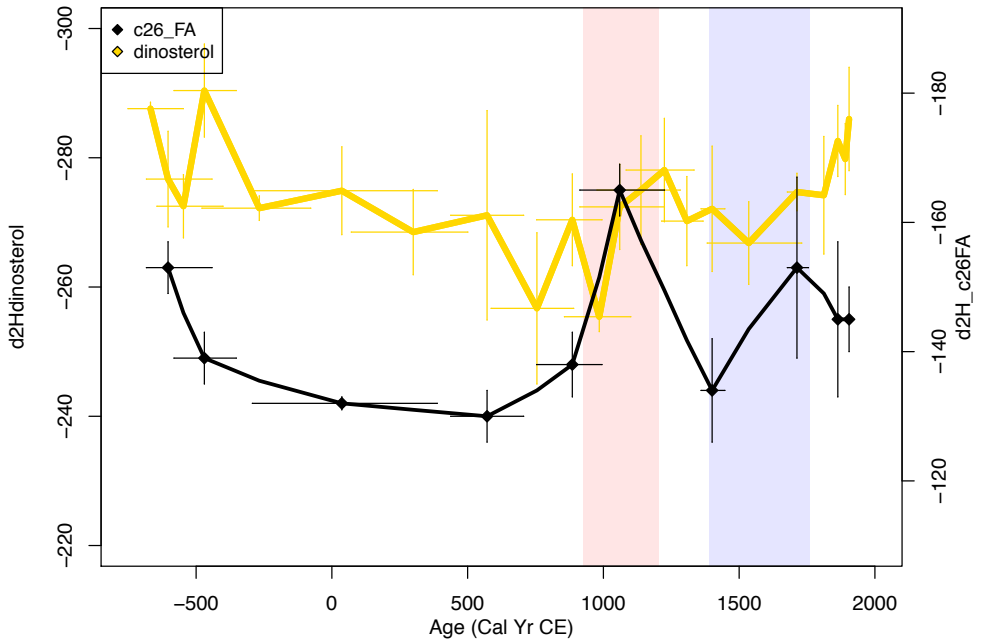

Fig. 8. Comparison of $\delta^2H_{dinosterol}$ (this study: left axis in yellow) to $\delta^2H_{nc26fattyacid}$ from Hassall (2017) (right axis in black). X-axis error bars represent min and max ages from BACON age model and y-axis errors are standard deviations from multiple injections.

The striking 3.1 mm d^{-1} change on Rendova is more than two times larger than the mean observed [La Niña - El Niño] anomaly and three times larger than the mean seasonal [DJF-JJA] anomaly calculated from GPCP data at this location. A large and persistent drought in the region of the Solomon Islands would be required to produced such a remarkable change. Magnetic susceptibility signals may offer independent confirmation of precipitation change since they often reflect changes in runoff (Hodell et al., 2008; Liu et al., 2011; Rodysill et al., 2012). The magnetic susceptibility signal in Lake Harai #1 was small (**Fig. S2**) since the core primarily consisted of organic matter. But nearby Lake Rano's sediments had highly variable magnetic susceptibility with a distinctly low magnetic susceptibility response during the MCA that coincides with Lake Harai #1 ^{2}H-enrichement/drying. If this low magnetic susceptibility signal was not caused by changes in

preservation of magnetic minerals, then it qualitatively confirms a drier MCA than the LIA in the Solomon Islands (**Fig. 7**).

A similar low MCA magnetic susceptibility signal was observed in both cores from Lac Lanutavake on Wallis Island (**Fig. 7; Fig. S9**), and while the algal lipid isotope response was small, it agrees in sign with the magnetic susceptibility data, and is especially evident when comparing the z-scores of Lac Lanutavake magnetic susceptibility and $\delta^2H_{dinosterol}$. This suggests that magnetic susceptibility primarily reflects hydrological change (**Fig. S9**) and supports a dry MCA on Wallis. However, data from nearby Samoa are less clear, only three $\delta^2H_{dinosterol}$ values span the MCA in Lake Lanoto'o and a particularly ^2H-enriched sample during the early MCA indicates that Samoa may have been dry during part of this time interval (**Fig. 5**). However, comparison of $\delta^2H_{dinosterol}$ values to the leaf wax hydrogen isotope and magnetic susceptibility records (Hassall, 2017) suggests that Samoa was relatively wet during the MCA (**Fig. 8**). Since Samoa and Wallis are so close to each other, this is a key location to further investigate hydrological changes in during this time interval, especially if the two locations did experience opposite trends.

How extensive were drought conditions during the MCA? **Figure 7** compares magnetic susceptibility records from Rendova (Solomon Islands) and Wallis to a hydrological record east of the SPCZ in Indonesia which also shows a dry MCA (Tierney et al., 2010). This indicates that a drought in the Solomon Islands may be caused by the same mechanism responsible for dry climate in Indonesia during the MCA. Meanwhile a runoff record from French Polynesia shows a wet MCA (Toomey et al., 2016) suggesting that the spatial limit of the MCA drought was somewhere between Wallis and French Polynesia. Interestingly, as noted in Toomey et al., 2016, the start of dry conditions in the east Pacific

and wet conditions in French Polynesia coincided with the first human migrations from Samoa to the remote islands of French Polynesia between ~1025 and 1120 (Wilmshurst et al., 2011).

Conclusion

This study combined replicate records of paleohydrology generated from algal lipid biomarker hydrogen isotope ratios from across the SPCZ region. Many of the isotope records are supported by similar trends in the magnetic susceptibility records in the same or in nearby lakes. The driest time in the Solomon Islands was during the MCA as evidenced by the $\delta^2H_{dinosterol}$ record from Harai Lake #1 and magnetic susceptibility record from Lake Rano. The Solomon Islands Modern and LIA periods experienced wetter conditions where the Modern was likely wetter than the LIA as inferred by Lake Tavara and Harai Lake #1 $\delta^2H_{dinosterol}$ records.

Three records from 2 islands on Vanuatu suggest a wet Modern and dry past where LIA was possibly drier than the MCA (unlike the Solomon Islands and possibly Wallis). This suggests that the dry conditions evident in the Solomon Islands during the MCA may have extended eastward to Wallis but did not extend southeastward to Vanuatu.

On Samoa the $\delta^2H_{dinosterol}$ record from Lake Lanoto'o suggests that the Modern was wetter than the past and that conditions may have been dry just prior to the MCA, but a low resolution record of leafwax hydrogen isotopes and magnetic susceptibility data (Hassall, 2017) suggests that the MCA was relatively wet. Interpretations of paleohydrology from the records on Wallis Island are limited since $\delta^2H_{dinosterol}$ records that have very good intra-lake agreement show very different inter-lake patterns. Independent proxies of hydroclimate such

as magnetic susceptibility can help clarify past change; the coherent (although small) variations in $\delta^2H_{dinosterol}$ suggests that magnetic susceptibility in Lac Lanutavake primarily reflects runoff rather than preservation, indicating that the MCA was dry.

Taken together and compared to nearby records, it appears that the SPCZ was more expansive/intense or shifted equator-wards during the LIA causing widespread dry conditions. The MCA was even drier in the Solomon Islands and possibly Wallis during the MCA but not as dry in Vanuatu. Samoa and French Polynesia appear to be wetter during the MCA.

Acknowledgements

This work was supported by the U.S. National Science Foundation [grant #1502417] to J.P.S; a University of Washington Program on Climate Change Fellowship and IGERT Ocean Change Fellowship [grant #NSF1068839] provided partial support for A.E.M; radiometric dating was supported by AINSE (The Australian Institute of Nuclear Science and Engineering) [Award No ALNGRA14513] to M.P.; IGERT Ocean Change mini-research awards and a University of Washington Quaternary Research Center research award to A.E.M; The Explorers Club Exploration Fund Grant, Gilchrist Expedition Grant and Royal Geographical Society (with IBG) Monica Cole Grant assisted with travel to Samoa. Sediment from Lake Emaotul, Efate, Vanuatu were provided as part of funding from NERC Grant NE/N006674/1 by the NERC Radiocarbon Facility NRCF010001 (allocation number 2009.0416) awarded to PI David Sear. We are grateful for permission from all civic and traditional authorities and assistance on Wallis Island from J.N. Richey, U. Sichrowsky, J.-Y. Meyer, A. Malau, K. Manufeki, S. Tauvale, C. Manry and others from Service de

L'Environment, M. Fotuaika, J.-F. Poncet, P. Nicomette, S. Felomaki, P. Tauvale, C. Chauvet, and the planning assistance from R. Schabetsberger, C. Lique, M. Bridoux, and C. Altman. We would like to thank T. Thomas and the Tetepare Descendants' Association Rangers for helping with sample collection in the Solomon Islands. We thank Cerillo Balo from the Vanuatu Kaljarol Senta at Port Olry for assisting with sample collection in Vanuatu (2012)**.** Field work in Upolu, Samoa was kindly permitted by Taule'ale'ausmai Laavasa Malua, Chief Executive Officer, Niualuga Evaimalo and staff in Ministry Natural Resources and Environment. Field assistance was provided by Josie Hill, Lucy, Tinifu, Solomano and Ai. In Vanuatu (2015 & 2017) we would like to thank Esline Garaebiti and Philip Malsale of the Geo-Hazards Division, Government of Vanuatu for permission to undertake fieldwork in Efate, Lake Emoatul, and to Fabienne, Maurice and Hugo for assistance with construction of the coring platform. S. Hing, E. Baldwin, A. Witt, and P Sobeck provided careful assistance in the lab. M. Wolfshorndl, T. Magee, and S. N. Ladd, assisted with splitting cores at LacCore. We thank C. Kaapu-Lyons, N. Wallsgrove, and B. Popp for analyzing Wallis Island water samples. Conversations with L. Thompson, C. Maupin, D. Nelson, N. Ladd, J. Richey, A. Atwood, and constructive comments from A.E. Ingalls and P. Quay greatly improved this chapter.

Chapter 4 Appendix A. Supplementary data

TABLE S1. SBARUC2 from Barora Pond (Tetepare, Solomon Islands) BACON age model, δ^2H dinosterol, and z-score. Depths indicate midpoint of 1cm intervals.

Modeled age (yrs C.E.)	Depth (cm)	Min modeled age (yrs BP)	Max modeled age (yrs BP)	Mean modeled age (yrs BP)	W.Mean modeled age (yrs BP)	δ^2H dinosterol (‰)	LATVKUC1 Analytical SD (‰)**	n	Z-score
2011.2	0.5	-63.4	-59.4	-61.1	-61.2	-295.8*	16*	2*	1.6722
2011.0	1.5	-63.0	-59.3	-60.9	-61.0	-311.2	3.5	3	-0.9430
2010.5	2.5	-62.1	-59.1	-60.5	-60.5	-302.0	4.5	3	0.6300
2010.1	3.5	-61.5	-58.7	-60.1	-60.1	-303.3	2.9	3	0.4172
2009.6	4.5	-61.1	-58.2	-59.7	-59.6	-303.4	4.4	3	0.3891
2009.2	5.5	-60.9	-57.5	-59.2	-59.2	-306.0	7.0	3	-0.0466
2008.7	6.5	-60.4	-56.9	-58.8	-58.7	-306.7	2.8	3	-0.1806
2008.2	7.5	-59.9	-56.4	-58.2	-58.2	-304.8	5.1	3	0.1566
2007.7	8.5	-59.6	-55.7	-57.7	-57.7	-301.6	3.4	3	0.7017
2007.1	9.5	-59.3	-54.8	-57.2	-57.1	-307.6	2.9	3	-0.3353
2006.6	10.5	-59.1	-53.9	-56.7	-56.6	-303.3	3.6	3	0.4099
2006.0	11.5	-58.5	-53.3	-56.1	-56.0	-299.1	6.6	3	1.1426
2004.7	13.5	-57.0	-52.4	-54.8	-54.7	-301.9	7.1	3	0.6600
2004.1	14.5	-56.6	-51.6	-54.2	-54.1	-308.3	4.1	3	-0.4522
2003.5	15.5	-56.3	-50.5	-53.6	-53.5	-307.1	4.3	3	-0.2374
2002.8	16.5	-55.7	-49.6	-52.9	-52.8	-300.0	4.9	3	0.9751
2002.1	17.5	-55.0	-49.0	-52.2	-52.1	-304.5	6.2	6	0.2006
2001.4	18.5	-54.5	-48.3	-51.4	-51.4	-311.0	3.5	6	-0.9141
2000.7	19.5	-54.2	-47.3	-50.7	-50.7	-303.8	8.2	4	0.3328
2000.0	20.5	-53.8	-46.1	-50.0	-50.0	-305.1	1.0	3	0.1073
1999.3	21.5	-53.0	-45.3	-49.4	-49.3	-300.0	1.6	4	0.9795
1998.5	22.5	-51.9	-44.9	-48.6	-48.5	-298.3	4.5	3	1.2830
1997.8	23.5	-51.0	-44.5	-47.9	-47.8	-301.1	2.8	4	0.7999
1997.1	24.5	-50.4	-43.9	-47.1	-47.1	-304.9	4.4	3	0.1404
1995.7	26.5	-49.2	-42.3	-45.8	-45.7	-309.7	1.7	3	-0.6869
1993.2	30.5	-46.9	-39.4	-43.2	-43.2	-307.1	5.4	5	-0.2391
1990.6	34.5	-44.8	-36.2	-40.6	-40.6	-305.7	2.7	3	-0.0090
1986.7	40.5	-41.5	-31.6	-36.8	-36.7	-313.9	3.1	3	-1.4165
1985.3	42.5	-40.2	-30.2	-35.4	-35.3	-315.2	2.8	8	-1.6473
1979.5	50.5	-35.8	-22.0	-29.7	-29.5	-316.6	8.8	3	-1.8873
1972.5	58.5	-31.5	-10.0	-23.2	-22.5	-315.8	5.4	3	-1.7482
1965.0	66.5	-27.5	3.2	-16.3	-15.0	-311.3	1.6	3	-0.9617
1961.3	70.5	-25.1	9.1	-12.7	-11.3	-309.3	3.8	5	-0.6282
1957.5	74.5	-22.6	15.1	-9.1	-7.5	-311.8	2.8	3	-1.0564
1950.1	82.5	-17.7	25.9	-2.0	-0.1	-297.9	6.3	3	1.3399
1942.7	90.5	-12.8	37.4	5.1	7.3	-299.8	1.7	3	1.0162
1935.4	98.5	-6.9	47.8	12.0	14.6	-290.7	6.5	3	2.5827
1927.8	106.5	-1.3	59.4	19.2	22.2	-301.1	3.6	3	0.7839
1920.2	114.5	4.6	69.3	26.4	29.8	-306.7	1.4	3	-0.1702
1912.8	122.5	10.2	79.5	33.4	37.2	-307.7	5.3	4	-0.3488
1905.4	130.5	16.4	89.3	40.5	44.6	-314.5	9.0	3	-1.5183
1897.7	138.5	23.4	99.0	47.8	52.3	-313.2	5.8	5	-1.2933

*Coretop value and SD are average and SD of two 0-1cm samples (SBARUC2 and SBARUC3) from Chapter 3

**The pooled analytical uncertainty for these samples was 4.9‰

TABLE S2. STAVUC4 from Lake Tavara (Tetepare, Solomon Islands) BACON age model, δ^2H dinosterol, and z-score. Depths indicate midpoint of 1cm intervals.

Modeled age (yrs C.E.)	Depth (cm)	Min modeled age (yrs BP)	Max modeled age (yrs BP)	Mean modeled age (yrs BP)	W.Mean modeled age (yrs BP)	δ^2H dinosterol (‰)	LATVKUC1 Analytical SD (‰)**	n	Z-score
2011	0.5	-64	-59	-61	-61	-314.4*	4.1*	2*	-0.1358
2007	2.5	-59	-55	-57	-57	-318.6	2.8	3	-0.7906
2003	4.5	-56	-50	-53	-53	-315.5	6.1	3	-0.3447
1999	6.5	-52	-45	-49	-49	-315.7	2.6	3	-0.3731
1993	8.5	-48	-38	-44	-43	-313.1	8.2	3	-0.0102
1988	10.5	-44	-31	-38	-38	-320.4	3.1	3	-1.0388
1982	12.5	-40	-24	-33	-32	-315.1	3.1	3	-0.2975
1976	14.5	-35	-16	-27	-26	-315.1	3.3	3	-0.2940
1970	16.5	-29	-10	-21	-20	-317.9	4.5	3	-0.6907
1964	18.5	-24	-2	-14	-14	-322.5	5.7	3	-1.3346
1957	20.5	-18	6	-7	-7	-313.7	5.2	5	-0.0923
1949	22.5	-12	16	1	1	-323.3	3.2	3	-1.4565
1941	24.5	-5	26	9	10	-314.1	8.7	5	-0.1432
1931	26.5	2	39	19	19	-321.1	9.2	4	-1.1411
1920	28.5	9	52	29	30	-309.7	10.4	3	0.4673
1910	30.5	17	63	40	40	-324.5	3.5	3	-1.6221
1900	32.5	25	75	50	50	-319.6	12.1	3	-0.9290
1889	34.5	33	87	62	61	-323.4	2.8	3	-1.4645
1878	36.5	42	100	72	72	-317.7	16.5	3	-0.6600
1856	40.5	61	124	94	94	-303.2	8.1	3	1.3931
1835	44.5	81	146	115	115	-313.1	7.5	3	-0.0143
1814	48.5	102	167	136	136	-303.5	6.2	4	1.3446
1792	52.5	123	188	158	158	-303.9	10.9	5	1.2887
1771	56.5	145	207	180	179	-304.4	6.0	3	1.2236
1749	60.5	165	228	202	201	-303.0	2.0	3	1.4175
1727	64.5	188	254	224	224	-311.7	3.9	4	0.1948
1704	68.5	210	279	247	246	-307.9	5.2	3	0.7327
1681	72.5	233	301	269	269	-305.2	6.9	4	1.1075
1658	76.5	257	324	292	292	-308.8	2.5	4	0.5974
1635	80.5	281	346	315	315	-303.5	9.4	4	1.3518
1613	84.5	306	368	337	337	-300.9	7.2	4	1.7143

*Coretop value and SD are average and SD of two 0-1cm samples (STAVUC1 and STAVUC4) from Chapter 3

**The pooled analytical uncertainty for these samples was 7.0‰

TABLE S3. SHARIUC2 from Lake Harai#1 (Rendova, Solomon Islands) BACON age model, δ^2H dinosterol, and z-score. Depths indicate midpoint of 1cm intervals.

Modeled age (yrs C.E.)	Depth (cm)	Min modeled age (yrs BP)	Max modeled age (yrs BP)	Mean modeled age (yrs BP)	W.Mean modeled age (yrs BP)	δ^2H dinosterol (‰)	LATVKUC1 Analytical SD (‰)**	n	Z-score
2001	0.5	-62	-34	-50	-51	-316.0*	8.5*	3*	-1.0171
1979	1.5	-61	20	-25	-29	-319.9	3.0	2	-1.2322
1859	7.5	-12	221	85	91	-334.8	3.2	3	-2.0556
1821	9.5	11	269	123	129	-315.0	4.3	3	-0.9585
1766	12.5	56	321	180	184	-321.7	4.2	3	-1.3295
1729	14.5	89	355	219	221	-312.8	2.5	3	-0.8385
1670	17.5	148	400	281	280	-314.8	3.2	3	-0.9511
1632	19.5	196	427	319	318	-316.4	5.6	4	-1.0401
1575	22.5	265	464	378	375	-310.7	2.5	2	-0.7217
1534	24.5	315	489	421	416	-312.1	2.7	3	-0.8021
1455	27.5	402	583	495	495	-295.3	0.6	2	0.1305
1388	29.5	462	656	561	562	-280.0	7.9	3	0.9772
1205	32.5	664	815	746	745	-287.3	1.4	3	0.5757
1115	34.5	752	901	835	835	-274.4	1.2	3	1.2897
1030	37.5	809	991	923	920	-283.1	4.0	3	0.8068
996	39.5	836	1019	960	954	-277.3	5.1	4	1.1290
975	41.5	865	1039	980	975	-284.9	1.1	3	0.7036
943	45.5	927	1074	1006	1008	-284.3	3.3	3	0.7372
916	49.5	970	1104	1031	1034	-288.8	2.3	3	0.4922
892	53.5	990	1136	1054	1058	-282.9	1.9	2	0.8189
867	57.5	1009	1169	1079	1083	-277.8	1.2	2	1.0984
843	61.5	1030	1199	1103	1107	-285.4	2.4	3	0.6809
819	65.5	1051	1227	1126	1131	-281.7	0.8	2	0.8839
795	69.5	1073	1255	1150	1155	-286.4	5.2	3	0.6222

*Coretop value from Chapter 3

**The pooled analytical uncertainty for these samples was 4.0‰

TABLE S4. VTRUC3 from Red Lake (Thion Island, Vanuatu) BACON age model, δ^2H dinosterol, and z-score. Ages below 121cm are linearly interpolated. Depths indicate midpoint of 1cm sample intervals.

Modeled age (yrs C.E.)	Depth (cm)	Min modeled age (yrs BP)	Max modeled age (yrs BP)	Mean modeled age (yrs BP)	W.Mean modeled age (yrs BP)	δ^2H dinosterol (‰)	Analytical SD (‰)**	n	Z-score
2007	0.5	-63	-51	-57	-57	-251.3*	12*	3*	0.6356
1984	2.5	-61	-5	-32	-34	-268.2	3.9	3	-1.1724
1960	4.5	-59	40	-7	-10	-272.9	7.7	3	-1.6590
1938	6.5	-48	71	12	13	-266.9	4.6	4	-1.0355
1926	7.5	-44	99	20	24	-257.4	1.8	2	-0.0393
1915	8.5	-39	130	29	35	-250.6	3.2	2	0.6734
1904	9.5	-36	163	38	46	-265.1	(7.3)	1	-0.8435
1849	14.5	2	232	91	101	-270.0	13.3	2	-1.3542
1826	16.5	22	253	113	124	-258.2	8.0	3	-0.1197
1815	17.5	29	263	124	135	-252.4	(7.3)	1	0.4836
1791	19.5	41	300	145	159	-257.3	(7.3)	1	-0.0208
1720	24.5	88	386	221	230	-248.9	(7.3)	1	0.8520
1676	27.5	132	424	268	274	-256.2	(7.3)	1	0.0941
1618	31.5	180	479	332	332	-237.9	6.4	3	2.0091
1603	32.5	192	490	348	347	-232.0	(7.3)	1	2.6249
1588	33.5	203	503	364	362	-243.2	1.3	3	1.4566
1574	34.5	211	519	379	376	-253.3	9.8	3	0.3954
1529	37.5	272	550	424	421	-255.1	6.9	3	0.2081
1470	41.5	340	593	483	480	-254.3	8.9	3	0.2926
1427	44.5	387	624	528	523	-250.3	3.2	2	0.7119
1385	47.5	478	643	565	565	-264.6	5.0	2	-0.7962
1343	50.5	546	669	605	607	-246.0	5.6	4	1.1643
1307	53.5	581	711	641	643	-259.0	2.9	4	-0.2012
1274	56.5	600	764	674	676	-254.7	5.6	3	0.2514
1243	59.5	616	809	705	708	-270.1	3.5	3	-1.3724
1212	62.5	641	839	737	739	-248.4	10.4	3	0.9086
1181	65.5	662	874	768	769	-252.4	7.5	3	0.4935
1149	68.5	691	898	803	801	-253.1	31.9	2	0.4126
1117	71.5	721	925	837	833	-239.1	6.7	5	1.8803
1049	77.5	798	977	909	901	-258.2	2.7	3	-0.1216
975	83.5	899	1046	974	975	-268.3	4.9	2	-1.1806
912	89.5	977	1109	1031	1038	-265.0	(7.3)	1	-0.8386
888	92.5	998	1139	1060	1062	-257.5	4.0	2	-0.0441
866	95.5	1013	1178	1087	1084	-258.0	5.3	3	-0.0982
847	98.5	1025	1211	1103	1103	-256.2	0.9	2	0.0905
828	101.5	1037	1248	1120	1123	-267.5	4.6	3	-1.1007
793	107.5	1055	1312	1150	1157	-257.8	(7.3)	1	-0.0739
773	110.5	1067	1351	1168	1177	-252.3	(7.3)	1	0.5034
754	113.5	1084	1382	1188	1196	-249.3	1.1	2	0.8093
735	116.5	1101	1420	1207	1215	-255.2	(7.3)	1	0.1936
716	119.5	1117	1465	1229	1234	-267.4	3.1	2	-1.0835
710	125.5	1123	1476	1235	1241	-268.0	3.7	3	-1.1511
674	131.5	1151	1555	1271	1276	-270.6	6.4	4	-1.4240
640	137.5	1158	1630	1292	1310	-270.5	8.2	2	-1.4143

*Coretop value and SD are average and SD of three 0-1cm samples (VTRUC1, VTRUC2, VTRUC5) from Chapter 3

**The pooled analytical uncertainty for these samples was 7.3‰, used for samples with only one injection

TABLE S5. VTWUC2 from White Lake (Thion Island, Vanuatu) BACON age model, δ^2H dinosterol, and z-score. Ages below 100cm are linearly interpolated. Depths indicate midpoint of 1cm sample intervals.

Modeled age (yrs C.E.)	Depth (cm)	Min modeled age (yrs BP)	Max modeled age (yrs BP)	Mean modeled age (yrs BP)	W.Mean modeled age (yrs BP)	δ^2H dinosterol (‰)	Analytical SD (‰)**	n	Z-score
2007	0.5	-63	-44	-58	-57	-268*	4*	3*	-0.2168
1996	1.5	-62	-10	-49	-46	-272.1	0.6	3	-0.6768
1985	2.5	-62	26	-40	-35	-264.9	0.6	2	0.1468
1974	3.5	-61	61	-31	-24	-287.1	2.3	3	-2.3820
1963	4.5	-61	96	-22	-13	-266.0	6.1	3	0.0185
1951	5.5	-55	118	-11	-1	-292.3	2.7	3	-2.9670
1938	6.5	-49	131	3	12	-271.2	9.7	5	-0.5734
1925	7.5	-44	149	16	25	-283.0	1.2	3	-1.9091
1912	8.5	-40	167	28	38	-265.9	2.8	3	0.0302
1899	9.5	-37	190	41	51	-284.4	2.3	4	-2.0652
1886	10.5	-29	206	53	64	-262.9	4.3	3	0.3745
1860	12.5	-12	230	81	90	-255.6	(5.6)	1	1.2055
1847	13.5	-6	246	95	103	-276.7	1.1	3	-1.1926
1834	14.5	0	268	108	116	-263.5	0.5	2	0.3056
1821	15.5	10	283	121	129	-279.1	1.5	3	-1.4670
1743	21.5	70	356	204	207	-271.7	2.2	3	-0.6239
1729	22.5	81	366	219	221	-257.9	0.5	3	0.9373
1702	24.5	99	392	246	248	-260.3	3.4	3	0.6656
1676	26.5	128	411	272	274	-260.2	(5.6)	1	0.6791
1649	28.5	151	428	296	301	-250.2	3.0	3	1.8149
1636	29.5	160	441	308	314	-266.1	4.5	3	0.0106
1610	31.5	191	456	331	340	-261.8	3.7	3	0.4932
1584	33.5	215	470	357	366	-259.8	6.6	3	0.7284
1571	34.5	227	483	377	379	-258.7	8.6	3	0.8545
1558	35.5	248	493	393	392	-258.9	8.5	3	0.8313
1462	42.5	420	536	492	488	-246.7	(5.6)	1	2.2177
1447	43.5	448	543	505	503	-266.9	4.3	3	-0.0837
1418	45.5	483	567	534	532	-261.9	6.6	3	0.4879
1388	47.5	520	602	560	562	-272.3	1.5	3	-0.7012
1343	50.5	557	667	599	607	-253.3	6.4	3	1.4629
1296	54.5	589	726	653	654	-261.2	6.7	3	0.5638
1275	56.5	608	747	674	675	-261.7	3.8	3	0.5092
1254	58.5	624	765	696	696	-271.1	3.6	2	-0.5565
1234	60.5	644	787	715	716	-271.7	5.0	3	-0.6265
1214	62.5	679	798	735	736	-256.3	7.6	6	1.1265
1193	64.5	706	816	757	757	-264.6	3.2	3	0.1798
1175	66.5	723	837	775	775	-264.0	6.5	3	0.2516
1156	68.5	732	866	792	794	-255.2	4.0	3	1.2486
1139	70.5	741	899	808	811	-261.8	3.1	4	0.4997
1121	72.5	755	916	827	829	-273.5	8.8	9	-0.8366
1103	74.5	765	941	844	847	-272.7	11.3	9	-0.7420
1085	76.5	783	958	862	865	-269.3	3.5	4	-0.3518
1067	78.5	797	978	881	883	-274.9	5.9	5	-0.9861
1050	80.5	811	1003	899	900	-261.9	7.8	4	0.4830
1032	82.5	833	1023	915	918	-263.7	5.9	5	0.2841
1014	84.5	849	1045	932	936	-258.6	1.4	3	0.8549
996	86.5	878	1062	949	954	-273.4	3.0	6	-0.8161
977	88.5	907	1076	965	973	-259.1	2.5	3	0.7987
956	90.5	937	1095	984	994	-263.4	3.6	3	0.3124
928	92.5	968	1120	1013	1022	-264.3	5.0	5	0.2166
899	94.5	979	1160	1040	1051	-264.4	4.0	3	0.1975
884	95.5	990	1177	1056	1066	-268.7	1.0	2	-0.2924
833	98.5	1024	1227	1111	1117	-263.9	2.9	3	0.2626
794	101	1080	1241	1153	1156	-268.8	3.3	3	-0.2987
770	103	1104	1265	1177	1180	-268.2	3.7	3	-0.2269

*Coretop value and SD are average and SD of three 0-1cm samples (VTWUC1, VTWUC2, VTWUC5) from Chapter 3

**The pooled analytical uncertainty for these samples was 5.6‰, used for samples with only one injection

TABLE S6. VAN from Lake Emaotul (Efate Island, Vanuatu) BACON age model, δ^2H dinosterol, and z-score. Depths indicate base of 1cm intervals. Ages below 273cm are linearly interpolated.

Modeled age (yrs C.E.)	Depth (cm)	Min modeled age (yrs BP)	Max modeled age (yrs BP)	Mean modeled age (yrs BP)	δ^2H dinosterol (‰)	Analytical SD (‰)**	n	Z-score
2006	1	-50	-69	-61	-266.2*	6.6	3	-1.6965
1997	4	-7	-67	-47	-266.8	3.3	6	-1.6979
1992	5	7	-67	-42	-265.1	1.7	4	-1.6950
1959	12	56	-51	-9	-276.6	2.8	3	-1.7143
1949	14	71	-46	1	-282.0	2.0	3	-1.7232
1925	19	105	-31	25	-266.2	3.9	3	-1.6968
1878	29	161	0	72	-279.5	3.3	3	-1.7192
1830	39	216	37	121	-267.2	6.6	3	-1.6986
1781	49	267	78	169	-274.8	2.9	3	-1.7113
1733	59	317	120	217	-267.0	2.1	3	-1.6981
1686	69	363	166	265	-265.4	2.4	3	-1.6955
1639	79	404	211	311	-263.5	4.1	6	-1.6924
1591	89	445	260	359	-268.7	3.9	3	-1.7011
1543	99	484	310	407	-266.1	2.3	3	-1.6967
1489	109	548	359	461	-271.5	4.0	3	-1.7057
1433	119	623	407	517	-274.9	4.9	4	-1.7114
1377	129	691	455	573	-274.8	5.7	6	-1.7112
1320	139	758	506	630	-270.5	1.8	2	-1.7040
1263	149	818	558	687	-273.8	2.2	3	-1.7096
1207	159	874	610	743	-266.6	3.5	4	-1.6976
1151	169	932	661	799	-277.0	0.5	2	-1.7149
1094	179	988	719	856	-258.5	3.4	3	-1.6840
1038	189	1044	777	912	-280.9	3.9	3	-1.7214
982	199	1097	833	968	-277.9	3.2	3	-1.7164
927	209	1149	897	1023	-275.3	3.6	3	-1.7120
870	219	1202	961	1080	-292.8	4.7	3	-1.7412
814	229	1255	1021	1136	-293.6	5.5	3	-1.7426
759	239	1310	1079	1191	-286.2	2.3	3	-1.7302
705	249	1372	1128	1245	-288.6	1.0	3	-1.7343
650	259	1433	1176	1300	-284.0	3.0	3	-1.7266
596	269	1491	1223	1354	-284.5	4.1	5	-1.7275
542	279	1547	1272	1408	-286.3	4.2	4	-1.7304
488	289	1602	1323	1462	-275.6	5.6	3	-1.7126
433	299	1658	1376	1517	-294.0	1.4	3	-1.7433
383	308	1706	1424	1567	-291.9	3.9	3	-1.7398
329	318	1752	1483	1621	-279.7	6.1	6	-1.7194
273	328	1801	1540	1678	-289.4	3.3	3	-1.7356
217	338	1834	1648	1732	-293.3	2.2	3	-1.7422
161	348	1889	1706	1788	-292.1	4.2	3	-1.7402

*Coretop value and SD are average and SD of two 0-2cm samples (VAN G5 and VAN G7) and one 0-1cm sample (VTEFVR) from Chapter 3.

**The pooled analytical uncertainty for these samples was 4.0‰

Age model from Sear et al. (*in prep*)

TABLE S7. LATVKUC1 from Lac Lanutavake (Wallis Island) BACON[a] age model, δ^2H dinosterol, and z-score. Core depths indicate midpoint of 1cm sample intervals.

Modeled age (yrs C.E.)	Core Depth (cm)	Adjusted[a] Depth (cm)	Min modeled age (yrs BP)	Max modeled age (yrs BP)	Mean modeled age (yrs BP)	W.Mean modeled age (yrs BP)	δ^2H dinosterol (‰)	Analytical SD (‰)**	n	Z-score
2002	0.5	0.6	-62	-34	-54	-52	-286.9*	6*	4*	0.2480
1879	6.5	8.1	-30	220	61	71	-290.4	3.2	3	-0.7317
1738	12.5	15.7	78	384	207	212	-292.1	7.9	3	-1.1950
1595	18.5	23.2	246	470	352	355	-286.0	1.0	3	0.5440
1463	24.5	30.7	383	587	493	487	-289.9	3.4	3	-0.5892
1350	30.5	38.2	535	656	605	601	-290.8	3.2	4	-0.8228
1251	36.5	44.8	595	787	701	699	-286.6	3.9	4	0.3518
1188	42.5	48.4	637	880	765	762	-279.4	6.5	4	2.4114
1050	48.5	55.3	735	1086	893	900	-283.8	0.8	4	1.1487
964	54.5	59.5	806	1159	986	986	-287.1	7.1	4	0.2164
892	60.5	63.1	886	1202	1060	1058	-288.2	3.6	5	-0.0970
824	66.5	66.7	983	1238	1126	1126	-288.6	3.6	4	-0.2049
762	72.5	70	1056	1266	1182	1188	-288.2	4.8	5	-0.1056
732	78.5	73.9	1116	1285	1222	1218	-294.0	3.0	3	-1.7428
706	84.5	77.5	1154	1300	1250	1244	-288.8	5.5	3	-0.2649
678	90.5	81.1	1192	1318	1278	1272	-283.1	2.7	3	1.3562
645	96.5	84.4	1225	1352	1308	1305	-286.8	4.8	3	0.3083
600	102.5	88	1302	1402	1349	1351	-289.5	1.4	3	-0.4570
553	108.5	91.6	1350	1460	1394	1397	-289.0	3.3	3	-0.3322
508	114.5	95.2	1369	1534	1437	1442	-293.0	0.5	2	-1.4565
468	120.5	98.8	1396	1583	1479	1482	-292.1	5.6	3	-1.1904
429	126.5	102.4	1430	1634	1519	1522	-287.0	3.8	3	0.2392
389	132.5	106	1466	1687	1558	1561	-281.9	8.2	3	1.6985
351	138.5	109.6	1500	1738	1595	1599	-285.5	2.7	3	0.6676

[a]Core depths tuned to LATVKUC4 using magnetic susceptibility to find adjusted depths; fossil leaves from both cores were used to make a single LATVK age model.

*Coretop value and SD are average and SD of four 0-1cm samples (LATVKUC1, UC3, UC4, UC6) from Chapter 3

**The pooled analytical uncertainty for these samples was 4.5‰

TABLE S8. LATVKUC4 from Lac Lanutavake (Wallis Island) BACON[a] age model, δ^2H dinosterol, and z-score. Depths indicate midpoint of 1cm sample intervals.

Modeled age (yrs C.E.)	Depth (cm)	Min modeled age (yrs BP)	Max modeled age (yrs BP)	Mean modeled age (yrs BP)	W.Mean modeled age (yrs BP)	δ^2H dinosterol (‰)	Analytical SD (‰)**	n	Z-score
2004	0.5	-62	-39	-55	-54	-286.9*	6*	4*	1.3623
1991	1.25	-60	-7	-45	-41	-291.8	10.3	3	-0.9380
1975	2.25	-58	36	-32	-25	-285.5	14.1	2	0.2983
1959	3.25	-57	80	-18	-9	-288.1	9.2	5	-0.2088
1943	4.25	-55	123	-5	7	-280.5	5.3	4	1.2834
1926	5.25	-50	160	10	24	-277.2	3.5	3	1.9480
1890	7.25	-30	196	50	60	-284.8	(6.4)	1	0.4487
1871	8.25	-24	223	68	79	-296.1	(6.4)	1	-1.7913
1853	9.25	-19	259	86	97	-292.0	(6.4)	1	-0.9655
1844	9.75	-17	279	94	106	-292.8	(6.4)	1	-1.1232
1792	12.75	32	329	151	158	-285.1	3.4	3	0.3929
1738	15.75	76	386	209	212	-289.6	4.0	3	-0.4938
1738	15.75	76	386	209	212	-291.3	(6.4)	1	-0.8416
1681	18.75	148	425	284	269	-288.0	(6.4)	1	-0.1909
1642	20.75	188	452	318	309	-291.5	3.0	4	-0.8683
1620	21.75	212	460	332	330	-286.0	(6.4)	1	0.2007
1555	24.75	270	492	406	395	-291.3	(6.4)	1	-0.8286
1546	25.25	284	501	418	405	-285.3	2.5	4	0.3415
1533	26	314	505	434	417	-296.6	4.1	3	-1.8802
1489	28.6	362	548	475	461	-290.1	7.2	3	-0.6005
1455	30.75	387	594	503	495	-282.8	(6.4)	1	0.8344
1368	36.75	497	648	586	583	-289.4	3.1	5	-0.4619
1353	37.75	526	655	602	597	-289.1	(6.4)	1	-0.4050
1346	38.25	538	658	610	604	-290.1	2.8	2	-0.5973
1313	40.5	576	688	644	637	-283.8	7.5	4	0.6376
1189	48.5	643	872	763	761	-281.7	4.6	3	1.0580
1036	56.5	746	1085	913	914	-284.7	2.6	3	0.4714
868	64.5	893	1216	1088	1082	-279.2	12.3	3	1.5456
741	72.5	1107	1277	1211	1210	-280.1	11.3	3	1.3720

[a]Fossil leaves from both cores (UC1 and UC4) were used to make a single LATVK age model after UC1 was tuned to UC4 depths using magnetic suseptibility.

*Coretop value and SD are average and SD of four 0-1cm samples (LATVKUC1, UC3, UC4, UC6) from Chapter 3

**The pooled analytical uncertainty for these samples was 6.4‰, used for samples with only one injection

TABLE S9. LALOUC13 from Lac Lalolalo (Wallis Island) BACON age model, δ^2H dinosterol, and z-score. Italics indicate first sample was from the top 0-20cm, all other depths indicate midpoint of 1cm sample intervals.

Modeled age (yrs C.E.)	Depth (cm)	Min modeled age (yrs BP)	Max modeled age (yrs BP)	Mean modeled age (yrs BP)	W.Mean modeled age (yrs BP)	δ^2H dinosterol (‰)	Analytical SD (‰)**	n	Z-score
2011 to 1835	*0-20*	*-91 to 11*	*-33 to 224*	*-61.4 to 112*	*-61.4 to 115*	*-282.7*	*4.0*	*4*	*-3.1736*
1830	20.5	14	228	118	120	-265.2	4.7	6	-1.5777
1795	24.5	43	257	156	156	-267.1	2.7	3	-1.7519
1758	28.5	78	280	197	192	-257.9	1.5	4	-0.9091
1740	30.5	94	295	218	210	-256.1	0.5	3	-0.7462
1740	30.5	94	295	218	210	-252.1	2.5	4	-0.3836
1723	32.5	116	302	242	227	-250.9	2.7	4	-0.2697
1689	36.5	156	323	283	261	-246.2	3.2	7	0.1566
1656	40.5	192	361	308	294	-255.4	5.8	3	-0.6802
1623	44.5	235	394	331	327	-242.8	2.8	4	0.4692
1595	48.5	278	422	356	356	-249.0	4.4	3	-0.0963
1581	50.5	293	438	368	369	-251.9	4.8	5	-0.3636
1570	52.5	308	448	380	380	-246.5	2.4	5	0.1340
1546	56.5	337	471	402	404	-241.7	2.4	3	0.5694
1523	60.5	361	488	427	427	-246.6	7.3	3	0.1245
1499	64.5	386	502	452	451	-242.7	1.8	3	0.4832
1467	68.5	420	526	485	483	-254.4	3.5	3	-0.5908
1449	70.5	439	554	502	501	-254.5	8.1	4	-0.5953
1425	72.5	468	578	524	525	-249.8	3.2	3	-0.1740
1379	76.5	516	635	564	572	-246.2	6.3	4	0.1616
1334	80.5	550	700	610	616	-243.6	6.3	6	0.3967
1295	84.5	570	757	651	655	-243.9	5.3	4	0.3725
1285	85.5	577	772	661	665	-249.5	4.0	4	-0.1427
1265	87.5	592	790	681	685	-251.2	0.7	3	-0.2954
1216	92.5	630	844	731	734	-257.7	2.6	3	-0.8927
1197	94.5	642	865	750	753	-252.3	1.8	4	-0.3937
1177	96.5	668	880	770	773	-247.8	7.3	4	0.0103
1154	98.75	690	896	792	796	-248.4	2.3	3	-0.0457
1087	104.75	759	965	861	863	-233.0	2.9	3	1.3663
1003	110.75	814	1092	947	947	-226.7	3.0	3	1.9366
835	122.75	968	1268	1110	1115	-236.8	0.5	3	1.0195
768	128.75	1034	1335	1175	1182	-237.7	3.1	3	0.9363
717	134.75	1091	1380	1233	1233	-232.8	5.1	3	1.3819
669	140.75	1153	1424	1279	1281	-240.2	2.5	4	0.7109
622	146.75	1218	1470	1323	1328	-235.7	4.7	4	1.1171
575	152.75	1298	1510	1364	1375	-228.9	7.3	3	1.7358

**The pooled analytical uncertainty for these samples was 4.2‰

TABLE S10. LALOUC14 from Lac Lalolalo (Wallis Island) BACON age model, δ^2H dinosterol, and z-score. Italics indicate the first sample was from the top 0-15cm. All other depths indicate midpoint of 1cm sample intervals. Ages below 121cm were linearly interpolated.

Modeled age (yrs C.E.)	Depth (cm)	Min modeled age (yrs BP)	Max modeled age (yrs BP)	Mean modeled age (yrs BP)	W.Mean modeled age (yrs BP)	δ^2H dinosterol (‰)	Analytical SD (‰)**	n	Z-score
2011 to 1633	*0-15*	*129*	*478.6*	*-61.4 to 317.4*	*-61.4 to 316.6*	*-269.8*	*7.0*	*2*	*-2.9358*
1624	15.5	149	475	327	326	-265.4	(4.8)	1	-2.5198
1541	18.5	292	506	413	409	-254.5	4.3	3	-1.4685
1426	21.5	389	648	525	524	-239.3	3.2	2	-0.0223
1282	24.5	447	932	657	669	-251.6	4.0	3	-1.1918
1162	27.5	566	1031	776	788	-247.5	0.9	2	-0.8030
1055	30.5	638	1130	892	895	-247.8	8.9	2	-0.8305
993	33.5	726	1158	961	957	-245.8	2.2	3	-0.6389
940	36.5	794	1193	1016	1010	-240.4	2.3	3	-0.1242
897	39.5	844	1226	1057	1053	-244.8	(4.8)	1	-0.5409
856	42.5	906	1251	1095	1094	-228.6	6.0	2	1.0004
775	48.5	1031	1300	1166	1175	-235.1	3.8	2	0.3838
717	54.5	1098	1362	1228	1233	-227.4	1.3	2	1.1214
665	60.5	1146	1426	1282	1285	-234.6	(4.8)	1	0.4319
614	66.5	1189	1483	1333	1336	-229.6	(4.8)	1	0.9053
563	72.5	1232	1533	1385	1387	-236.9	(4.8)	1	0.2090
513	78.5	1280	1584	1437	1437	-231.9	4.0	3	0.6875
462	84.5	1328	1635	1488	1488	-230.7	1.1	3	0.8060
411	90.5	1382	1685	1541	1540	-228.6	(4.8)	1	1.0008
360	96.5	1434	1729	1592	1590	-233.4	(4.8)	1	0.5456
308	102.5	1490	1774	1644	1642	-235.5	(4.8)	1	0.3445
255	108.5	1548	1816	1697	1695	-232.4	5.6	3	0.6364
204	114.5	1610	1857	1749	1746	-233.9	4.0	3	0.4990
152	120.5	1676	1890	1797	1798	-231.3	6.2	3	0.7450
96	126.5	1715	1969	1857	1854	-229.1	(4.8)	1	0.9557
44	132.5	1769	2019	1910	1906	-235.9	1.6	2	0.3021
-9	138.5	1823	2069	1963	1959	-235.3	5.3	2	0.3671
-61	144.5	1877	2118	2016	2011	-236.8	3.6	3	0.2211
-114	150.5	1931	2168	2069	2064	-238.9	6.0	3	0.0146
-166	156.5	1985	2218	2122	2116	-240.2	5.4	3	-0.1014

**The pooled analytical uncertainty for these samples was 4.8‰, used for samples with only one injection

TABLE S11. LALOUC22 from Lac Lalolalo (Wallis Island) BACON age model, δ^2H dinosterol, and z-score. Depths indicate midpoint of 1cm sample intervals.

Modeled age (yrs C.E.)	Depth (cm)	Min modeled age (yrs BP)	Max modeled age (yrs BP)	Mean modeled age (yrs BP)	W.Mean modeled age (yrs BP)	δ^2H dinosterol (‰)	Analytical SD (‰)**	n	Z-score
2010	0.5	-66	-55	-60	-60	-292.2*	4.8*	4*	-0.1913
2006	1.5	-62	-49	-56	-56	-298.6	11.5	4	-0.6791
2001	2.5	-57	-43	-51	-51	-291.6	6.9	3	-0.1913
1988	4.5	-48	-26	-39	-38	-298.8	6.6	2	-0.6926
1968	6.5	-32	-1	-19	-18	-302.7	3.8	2	-0.9677
1929	8.5	0	43	20	21	-279.8	2.5	4	0.6314
1886	10.5	36	92	64	64	-261.3	3.3	3	1.9201

*Coretop value and SD are average and SD from four 0-1cm samples (LALOUC5, LALOUC16, LALOUC22, and LALOUC24) from Chapter 3

**The pooled analytical uncertainty for these samples was 6.3‰

TABLE S12. LALOUC24 from Lac Lalolalo (Wallis Island) BACON age model, δ^2H dinosterol, and z-score. Depths indicate midpoint of 1cm sample intervals.

Modeled age (yrs C.E.)	Depth (cm)	Min modeled age (yrs BP)	Max modeled age (yrs BP)	Mean modeled age (yrs BP)	W.Mean modeled age (yrs BP)	δ^2H dinosterol (‰)	Analytical SD (‰)**	n	Z-score
2005.0	0.5	-62	-45	-56	-55	-292.2*	4.8*	4*	-1.2834
1993.0	1.5	-55	-27	-44	-43	-284.0	8.3	3	-0.9152
1955.0	4.5	-21	14	-5	-5	-271.1	2.6	3	-0.1341
1923.0	6.5	6	51	26	27	-261.7	2.9	6	0.4319
1896.0	8.5	28	84	53	54	-266.1	(4.2)	1	0.1667
1861.0	10.5	41	165	83	89	-242.3	(4.2)	1	1.6089

*Coretop value and SD are average and SD from four 0-1cm samples (LALOUC5, LALOUC16, LALOUC22, and LALOUC24) from Chapter 3

**The pooled analytical uncertainty for these samples was 4.2‰, used for samples with only one injection

TABLE S13. LANU2 and U1-1 from Lake Lanoto'o (Samoa) BACON age model[a], δ^2H dinosterol, and z-score. Depths indicate base of 1cm intervals.

Modeled age (yrs C.E.)	Depth (cm)	Min modeled age (yrs BP)	Max modeled age (yrs BP)	Mean modeled age (yrs BP)	W.Mean modeled age (yrs BP)	δ^2H dinosterol (‰)	LATVKUC1 Analytical SD (‰)**	n	Z-score
2007	1	-58.5	-56	-57	-57	-285.6*	8.5*	3*	-1.8117
1992	4	-43.2	-41	-42	-42	-279.8	5.5	4	-0.6405
1963	8	-13.9	-11	-13	-13	-282.6	5.5	8	-0.9521
1907	12	36.2	50	43	43	-274.2	9.1	6	0.0028
1800	16	104.2	188	152	150	-274.7	2.9	6	-0.0534
1608	20	131	507	356	342	-266.8	6.4	4	0.8420
1463	24	436.8	532	489	488	-272.1	9.7	5	0.2357
1362	28	523.4	688	580	588	-270.2	6.9	5	0.4581
1273	32	559.3	830	670	678	-278.1	8.0	7	-0.4425
1179	36	614.4	945	766	771	-275.0	8.4	4	-0.0881
1095	40	677	1014	857	855	-272.4	6.6	5	0.2027
1014	44	811	1075	929	936	-255.4	2.3	2	2.1349
906	48	925.5	1186	1040	1044	-270.4	7.1	2	0.4357
766	52	1038.1	1367	1179	1184	-256.7	11.7	3	1.9872
567	56	1237.2	1527	1378	1383	-271.1	16.2	2	0.3542
274	60	1459.2	1923	1672	1676	-268.5	6.6	3	0.6486
-10	64	1580.7	2316	1967	1960	-274.9	6.8	5	-0.0748
-339	68	2084.1	2517	2282	2289	-272.2	1.9	3	0.2277
-557	72	2380.1	2628	2521	2507	-290.4	(7.2)	1	-1.8481
-640	76	2432.9	2696	2600	2590	-272.5	4.9	5	0.1946
-702	80	2476.6	2738	2665	2652	-276.7	7.4	5	-0.2810
-772	84	2590.8	2811	2726	2722	-287.6	1.0	2	-1.5320

*Coretop value and SD are average and SD of three 0-1cm (0-2cm for LAN-U1) samples (LAN-U1, LAN14 U1, LAN14 U2) from Chapter 3

**The pooled analytical uncertainty for these samples was 7.2‰, used for the sample with only one injection

[a]Age model from Hassall 2017

Table S14. Radiocarbon dates for SPCZ cores. Note Pb-210 data can be found in Chapter 3

Sample	Core	SAMPLE ID	f modern	±	Δ14C	±	14C Age	±
CAMS 154213	SBAR UC2	SBAR UC2 0-2cm (Solomons, Tetepare)	1.1326	0.0043	132.6	4.3	>Modern	
D-AMS 009280	SBAR UC2	SBAR UC2 142 cm (Solomons, Tetepare)	99.31	0.3			56	24
CAMS 154214	SBAR UC2	SBAR UC2 126 cm (Solomons, Tetepare)	0.9632	0.0035	-36.8	3.5	300	30
D-AMS 022808	STAV UC4	STAVUC4 3-4cm (Tetepare Solomon Is)	100.53	0.37			Modern	
D-AMS 013113	STAV UC4	STAV UC4 59cm (Lake Tavara, Tetepare, Solomons)	96.94	0.33			250	27
D-AMS 009281	STAV UC4	STAV UC4 33-34cm (Solomons, Tetepare)	96.67	0.26			272	22
D-AMS 013114	STAV UC4	STAV UC4 85cm (Lake Tavara, Tetepare, Solomons)	94.77	0.31			432	26
CAMS 154217	SHARI UC2	SHAR1 UC2 1-3cm (Solomons, Rendova)	1.0113	0.0045	11.3	4.5	>Modern	
D-AMS 009278	SHARI UC2	SHAR1 UC2 24-25cm (Solomons, Rendova)	95.52	0.34			368	29
D-AMS 009279	SHARI UC2	SHAR1 UC2 30-31cm (Solomons, Rendova)	91.21	0.3			739	26
D-AMS 017999	SHARI UC2	SHAR1 UC2 34cm (Rendova Solomon Is)	88.03	0.31			1024	28
D-AMS 013116	SHARI UC2	SHAR1 UC2 47cm (Rendova, Solomons)	86.13	0.29			1199	27
D-AMS 007000	SHARI UC2	SHAR1 UC2 39-40cm (Solomons, Rendova)	85.14	0.25			1292	24
S-ANU 37225	SHARI UC2	SHAR1 UC2 99-100cm (Solomons, Rendova)	83.66		-163.4		1435	25
CAMS 154218	SHARI UC2	SHAR1 UC2 181cm (Solomons, Rendova)	0.8162	0.0031	-183.8	3.1	1630	35
CAMS 154215	SRAN UC1	SRAN UC1 0-2cm (Solomons, Rendova)	1.0398	0.0056	39.8	5.6	>Modern	
D-AMS 013115	SRAN UC1	SRAN UC1 15cm (Lake Rano, Rendova, Solomons)	97.55	0.3			199	25
D-AMS 022793	SRAN UC1	SRANUC1 73-74cm (Rendova Solomon Is)	93.87	0.64			508	55
D-AMS 007001	SRAN UC1	SRAN UC1 40cm (Solomons, Rendova)	90.08	0.42			839	37
S-ANU 37233	SRAN UC1	SRAN UC1 89-90 (Solomons, Rendova)			-108.5		920	25
S-ANU 37237	SRAN UC1	SRAN UC1 133-134cm (Solomons, Rendova)					1350	25
D-AMS 022794	SRAN UC1	SRANUC1 121-122cm (Rendova Solomon Is)	82.49	0.45			1546	44
CAMS 154216	SRAN UC1	SRAN UC1 113cm (Solomons, Rendova)	0.788	0.0029	-212	2.9	1915	30
D-AMS 022802	VTR UC3	VTR UC3 17-18cm (Thion Vanuatu)	100.69	0.45			Modern	
D-AMS 022801	VTR UC3	VTR UC3 5-6cm (Thion Vanuatu)	122.8	1.2			Modern	
D-AMS 009271	VTR UC3	VTR_UC3 4-5cm (Thion Is. Vanuatu)	100.54	0.23			Modern	
D-AMS 013106	VTR UC3	VTR UC3 50cm (Red Lake, Thion Is., Vanuatu)	91.99	0.31			671	27
D-AMS 022803	VTR UC3	VTR UC3 74-75cm (Thion Vanuatu)	89.22	0.7			916	63
D-AMS 013107	VTR UC3	VTR UC3 85cm (Red Lake, Thion Is., Vanuatu)	86.63	0.27			1153	25
D-AMS 009272	VTR UC3	VTR_UC3 121-121.5cm (Thion Is. Vanuatu)	86.37	0.22			1177	20
D-AMS 022804	VTR UC3	VTR UC3 92-93cm (Thion Vanuatu)	85.79	0.33			1231	31
D-AMS 009273	VTW UC2	VTW_UC2 3-4cm (Thion Is. Vanuatu)	139.09	0.31			Modern	
D-AMS 022800	VTW UC2	VTW UC2 31-32cm (Thion Vanuatu)	96.53	0.64			284	53
D-AMS 009274	VTW UC2	VTW_UC2 42-43cm (Thion Is. Vanuatu)	94.42	0.26			461	22
D-AMS 013108	VTW UC2	VTW UC2 48-49cm (White Lake, Thion Is., Vanuatu)	92.24	0.32			649	28
D-AMS 018000	VTW UC2	VTW UC2 62cm (Thion Vanuatu)	89.79	0.28			865	25
D-AMS 018001	VTW UC2	VTW UC2 87cm (Thion Vanuatu)	87.55	0.25			1068	23
D-AMS 013109	VTW UC2	VTW UC2 100cm (White Lake, Thion Is., Vanuatu)	85.21	0.28			1286	26
D-AMS 022790	LATVK UC1	LATVKUC1 14-15cm (Wallis Is)	96.88	0.52			255	43
D-AMS 022791	LATVK UC1	LATVKUC1 36-37cm (Wallis Is)	92.34	0.35			640	30
D-AMS 017995	LATVK UC1	Latvk UC1a 88.5cm (Wallis Is)	85.19	0.24			1288	23
D-AMS 022792	LATVK UC1	LATVKUC1 102-103cm (Wallis Is)	82.82	0.33			1514	32
D-AMS 017996	LATVK UC1	Latvk UC1b 133cm (Wallis Is)	81.21	0.25			1672	25
CAMS 153012	LATVK UC4	LATVK UC4 2-4.5 cm (Wallis Island)	1.4238	0.0051	423.8	5.1	>Modern	
D-AMS 006998	LATVK UC4	LATVK UC4 26 cm (Wallis Island)	94.9	0.25			420	21
D-AMS 006999	LATVK UC4	LATVK UC4 38-38.5 cm (Wallis Island)	92.3	0.28			644	24
CAMS 153013	LATVK UC4	LATVK UC4 44.5 cm (Wallis Island)	0.8933	0.0032	-106.7	3.2	905	30
D-AMS 009275	LATVK UC4	LATVK UC4 67.5cm (Wallis Island)	84.48	0.24			1355	23
D-AMS 009276	LALO UC22	LALO UC22 1-2cm (Wallis Island)	106.45	0.26			Modern	
D-AMS 009277	LALO UC22	LALO UC22 13-14cm (Wallis Island)	99.3	0.24			56	19
CAMS 153008	LALO UC13	Lalo UC13 36.5 cm (Wallis Island)	0.9673	0.0035	-32.7	3.5	265	30
D-AMS 022797	LALO UC13	LaloUC13 66-67cm (Wallis Is)	95.39	0.36			379	30
D-AMS 022796	LALO UC13	LaloUC13 56-57cm (Wallis Is)	94.84	0.54			426	46
D-AMS 022795	LALO UC13	LaloUC13 46-47cm (Wallis Is)	94.39	0.87			464	74
D-AMS 022798	LALO UC13	LaloUC13 76-77cm (Wallis Is)	92.41	0.4			634	35
D-AMS 017993	LALO UC13	Lalo UC13 104cm (Wallis Is)	89.18	0.41			920	37
D-AMS 022799	LALO UC13	LaloUC13 127-128cm (Wallis Is)	83.48	0.47			1450	45
CAMS 153009	LALO UC13	Lalo UC13 155 cm (Wallis Island)	0.8292	0.003	-170.8	3	1505	30
D-AMS 022805	LALO UC14	LaloUC14 18-19cm (Wallis Is.)	95.25	0.56			391	47
D-AMS 017997	LALO UC14	Lalo UC14a 53cm (Wallis Is)	84.96	0.29			1309	27
D-AMS 022806	LALO UC14	LaloUC14 27-28cm (Wallis Is.)	81.08	0.35			1685	35
D-AMS 017998	LALO UC14	Lalo UC14b 125cm (Wallis Is)	79.37	0.21			1856	21
D-AMS 022807	LALO UC14	LaloUC14 33-34cm (Wallis Is.)	78.1	0.48			1986	49

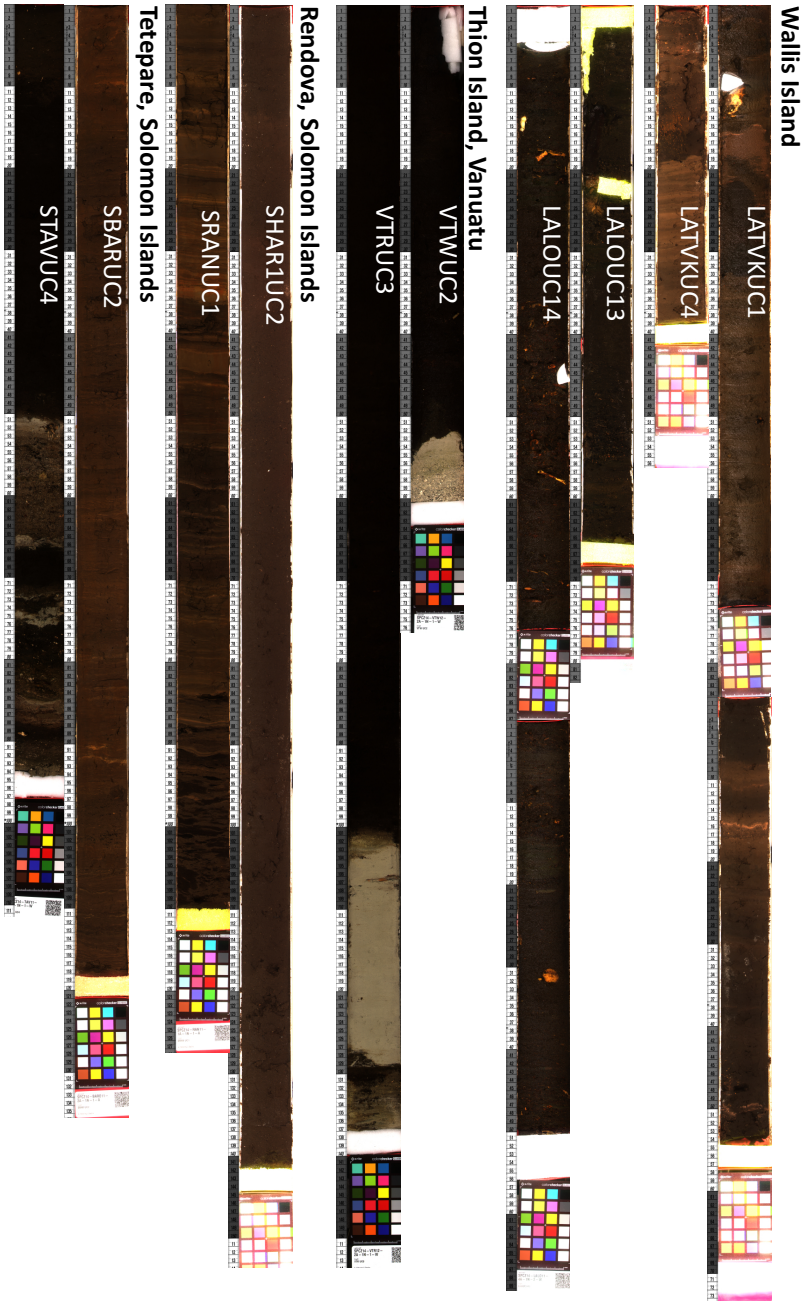

Fig. S1. Images of sediment cores. The uppermost portion of these cores was sectioned in the field as follows: STAVUC4=35cm, SBARUC2=25cm, SRANUC1=25cm, SHAR1UC2=40cm, VTRUC3=40cm, VTWUC2=50cm, LALOUC13=97cm, LALOUC14=40cm, LALOUC24=16cm (not shown, remaining core was rock and wood), LALOUC24=27cm (not shown, entire core was sectioned), LATVKUC1=18cm, LATVKUC4=38.5cm. The cores from Lake Emaotul (Efate, Vanuatu) (Sear et al. *in prep*) and Lake Lanoto'o (Samoa) (Hassall 2017) are not shown.

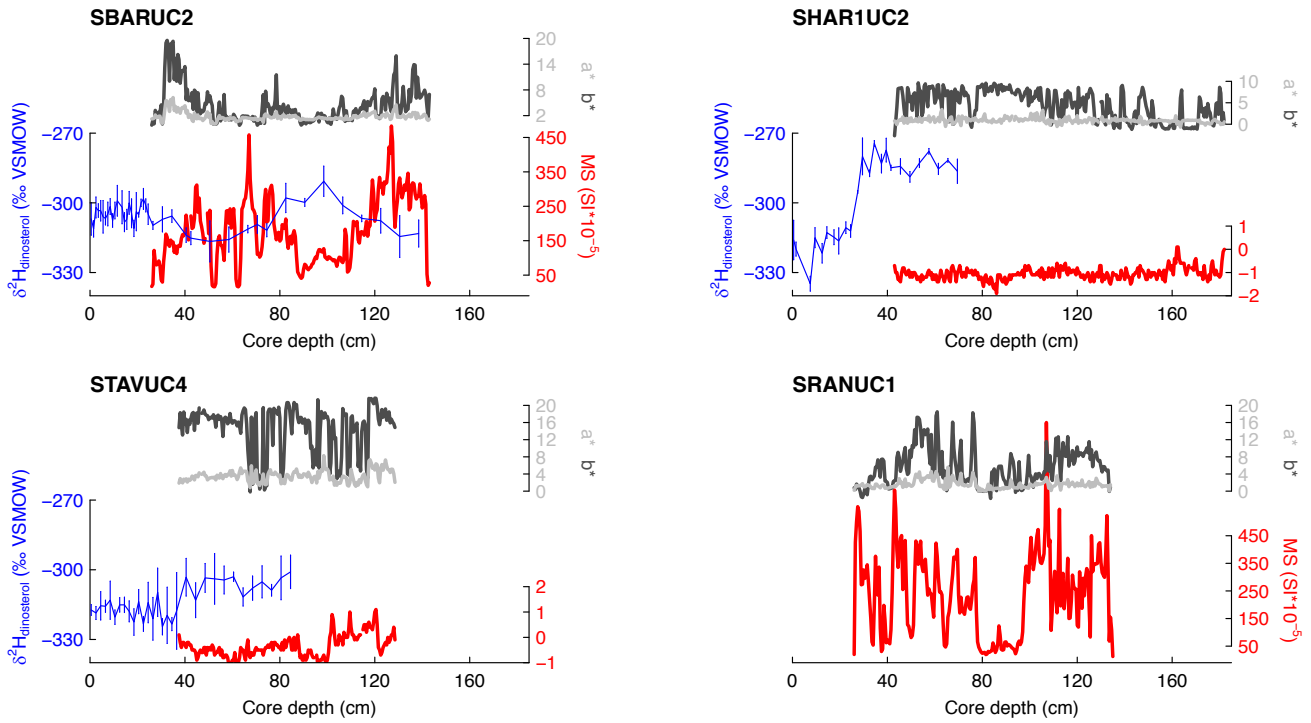

Fig. S2. Magnetic susceptibility (red line), $\delta^2H_{dinosterol}$ (blue line with analytical uncertainty), *a** green (negative) and red (positive) reflectance (light gray line), and *b** blue (negative) and yellow (positive) reflectance (dark gray line) versus core depth (cm) for sediment cores from Tetepare (SBARUC2 and STAVUC4) and Rendova (SHAR1UC2 and SRANUC1) in the Solomon Islands. Dinosterol was not analyzed in the deeper sections of STAVUC4 or SHAR1UC2 due to major changes in stratigraphy or accumulation rate that signified shifts in lake status. MS signal not available for the uppermost portion of the cores that were sampled in the field.

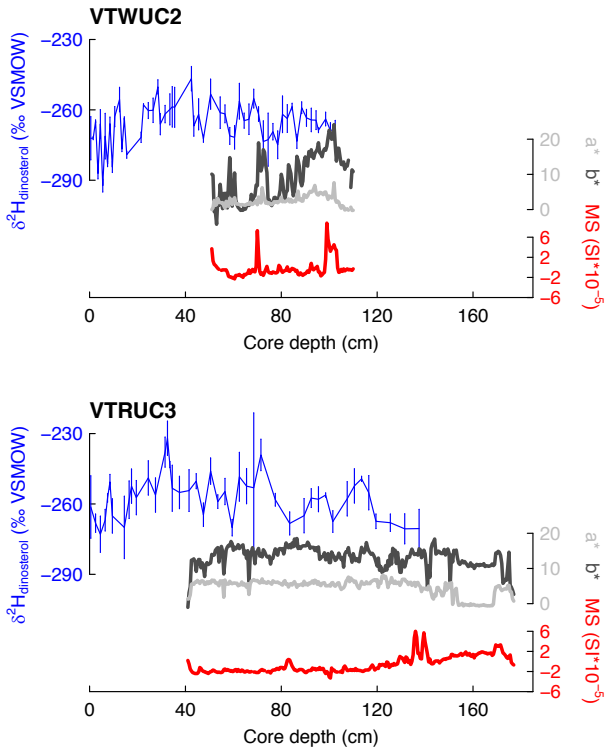

Fig. S3. Magnetic susceptibility (red line), $\delta^2H_{dinosterol}$ (blue line with analytical uncertainty), *a** green (negative) and red (positive) reflectance (light gray line), and *b** blue (negative) and yellow (positive) reflectance (dark gray line) versus core depth (cm) for sediment cores from Thion Island (Vanuatu). MS signal not available for the uppermost portion of the cores that were sampled in the field.

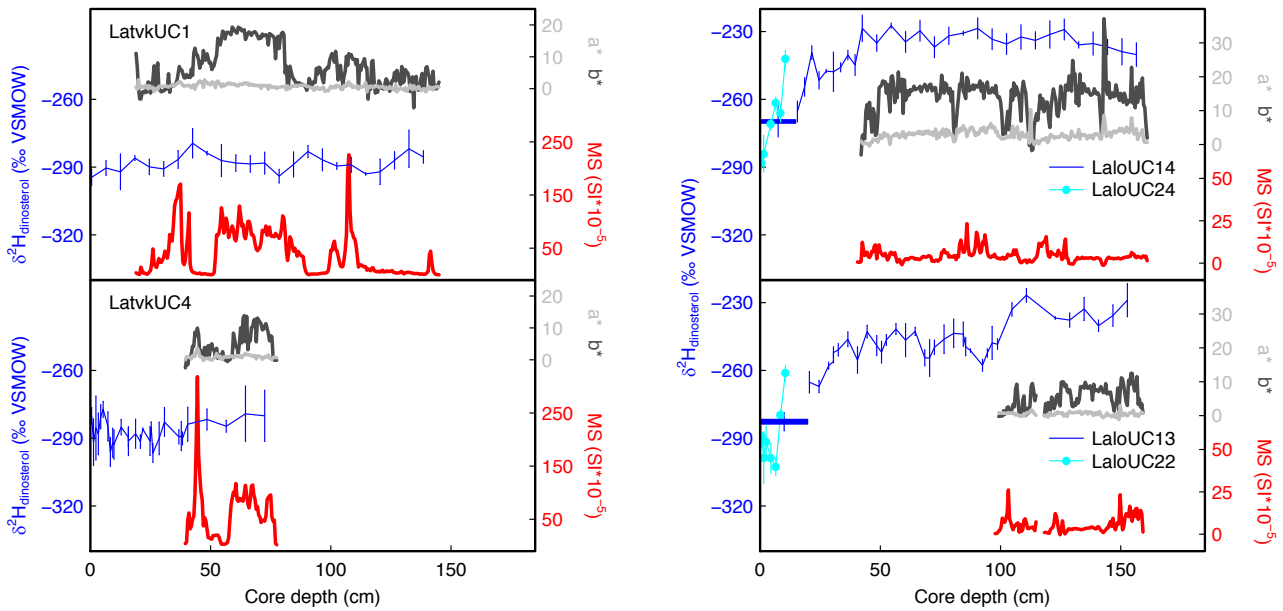

Fig. S4. Magnetic susceptibility (red line), $\delta^2H_{dinosterol}$ (blue line with analytical uncertainty), *a** green (negative) and red (positive) reflectance (light gray line), and *b** blue (negative) and yellow (positive) reflectance (dark gray line) versus core depth (cm) for sediment cores from Wallis. Both Lalolalo dinosterol records were from a short core collected in shallow water and a longer core collected from the deepest part of the lake (~88m). The horizontal blue bar indicates the value of the 10cm core-top sample (LaloUC14) and 15cm core-top sample (LaloUC13). MS signal not available for the uppermost portion of the cores that were sampled in the field.

A) Wallis Island

Lac Lanutavake

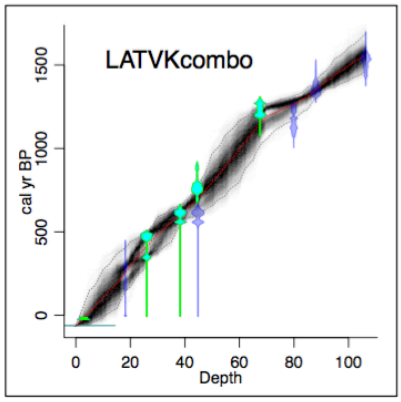

Lac Lalolalo

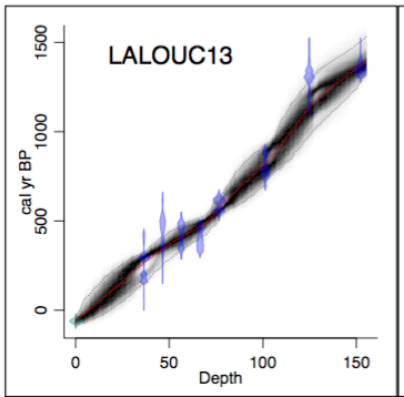

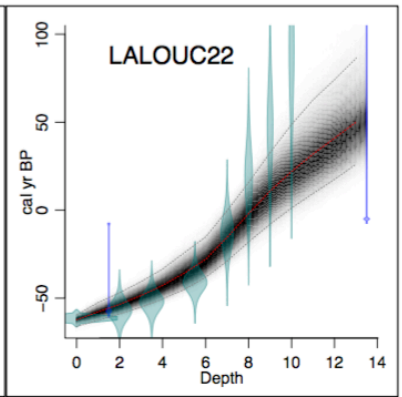

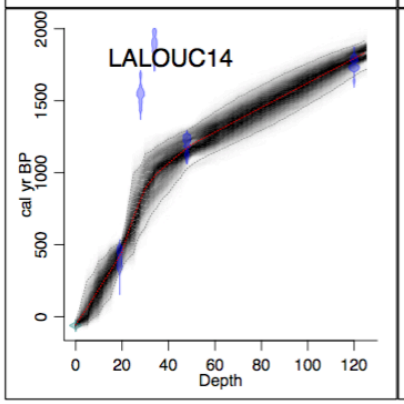

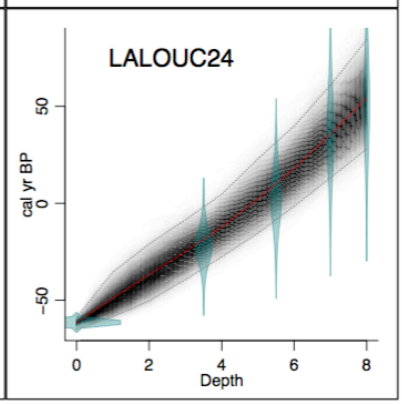

B) Thion Island, Vanuatu

Red Lake

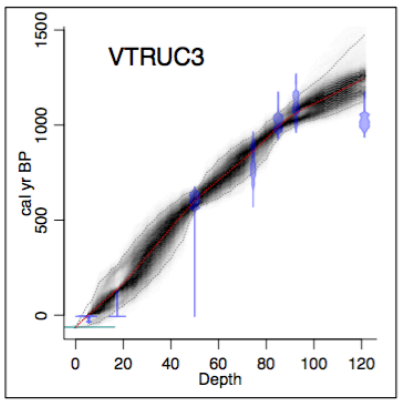

White Lake

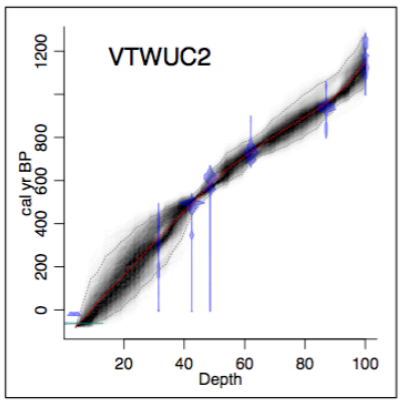

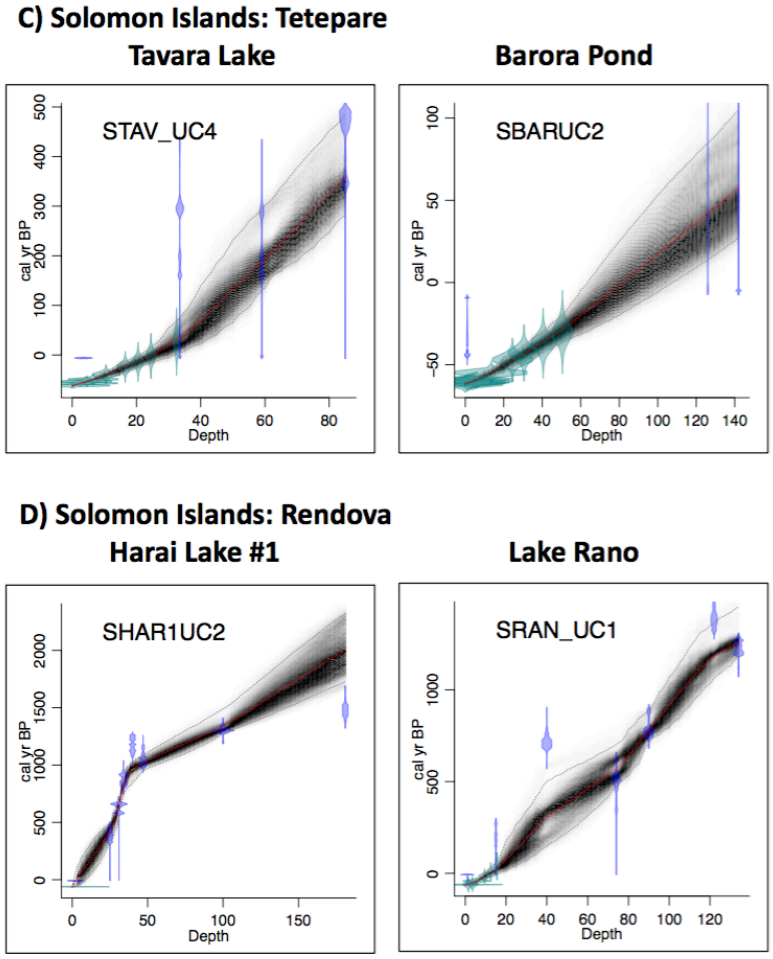

Fig. S5. BACON age models (Blaauw and Christen, 2011) from a) Wallis Island, b) Thion Island (Vanuatu), Tetepare (Solomon Islands), and Rendova (Solomon Islands). The age model for LATVK was made by first tuning the LATVKUC1 depth scale to the LATVK UC4 depth scale using magnetic susceptibility and color and using fossil leaves from both cores (^{14}C dates from LATVKUC4 shown in cyan with green border and 14C dates from LATVK UC1 shown in blue). Age model for LAN (Samoa) can be found in Hassall (2017). The age model for VAN (Emoatul, Vanuatu) Sear et al. (*in prep*) consists of three bulk ^{14}C dates at 95, 225, and 335 cm.

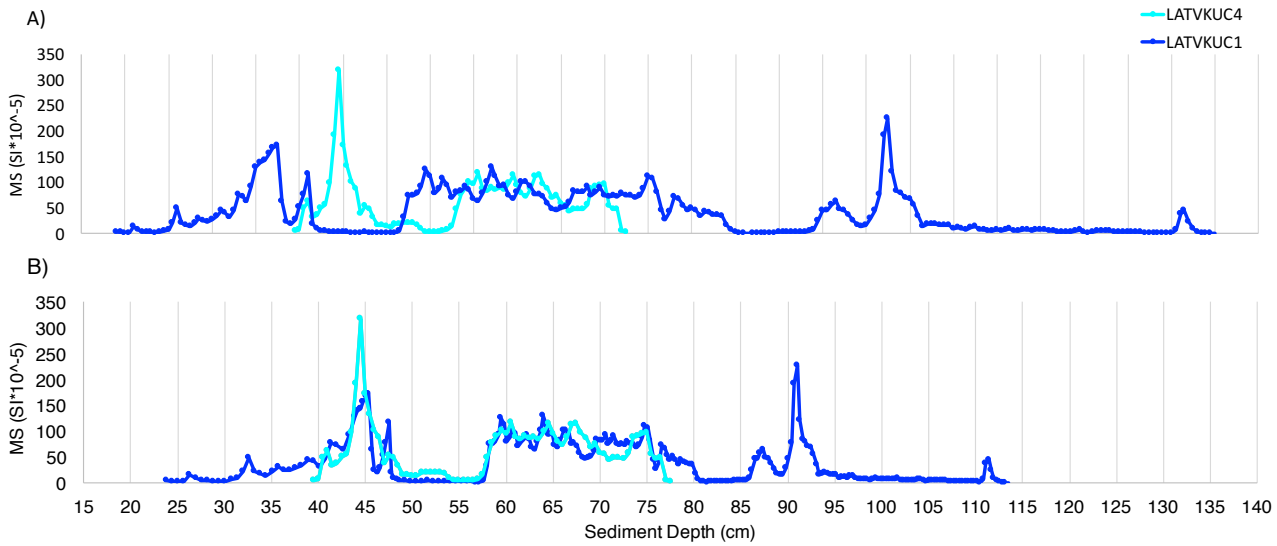

Fig. S6. Magnetic susceptibility versus core depth (cm) in two cores from Lac Lanutavake (Wallis). A) Both LATVKUC4 and LATVKUC1 are plotted on their own respective depth scale, clear minimums and maximums that coincide with obvious color variations are slightly offset. B) Since the longer core (LATVKUC1) experienced more hammering that led to increased compression of sediments with the UCore device, it is set to the depth scale of the shorter core LATVKUC4 by visually tuning the MS maxima and minima. Once on the same depth scales, ^{14}C ages on fossil leaves from both cores were used to make a single Lac Lanutavake age model.

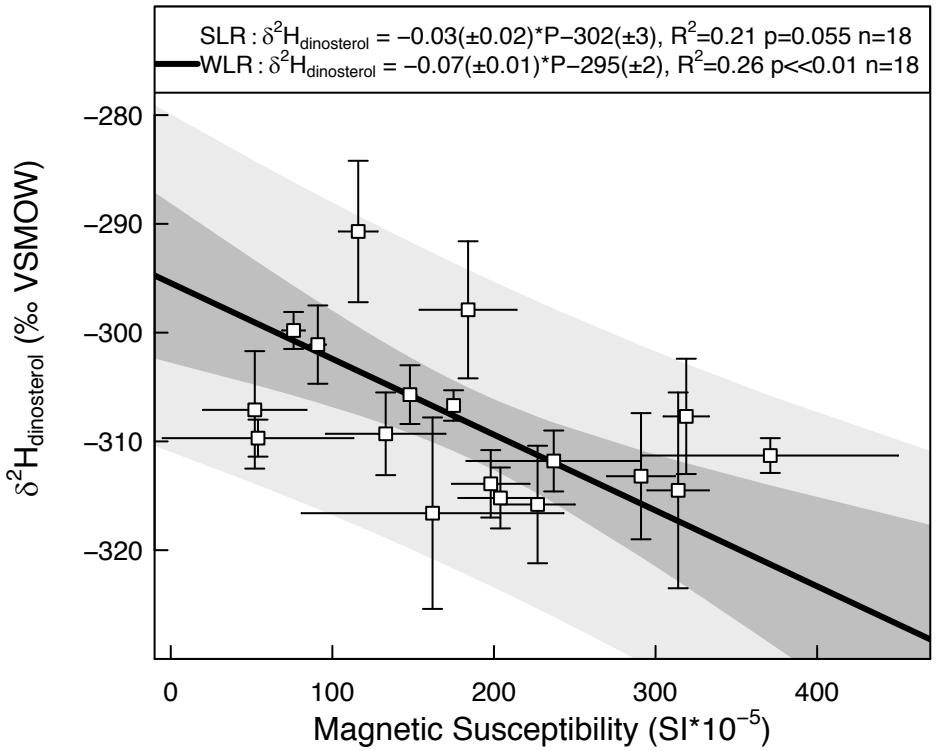

Fig. S7. SBARUC2 (Tetepare, Solomon Islands) $\delta^2H_{dinosterol}$ plotted vs magnetic susceptibility. $\delta^2H_{dinosterol}$ samples were taken every ~5cm and had a thickness of 1cm, MS data (0.5cm intervals) was averaged over the same 1cm depth as its partner $\delta^2H_{dinosterol}$ sample. The x-axis error bars are the SD from the 3 MS measurements over a 1cm sample interval, the y-axis error bars are the SD from triplicate measurements. To account for large errors in both axes, linear fits were determined using the maximum likelihood estimate method (York et al., 2004) incorporating bivariate analytical uncertainty (Thirumalai et al., 2011).

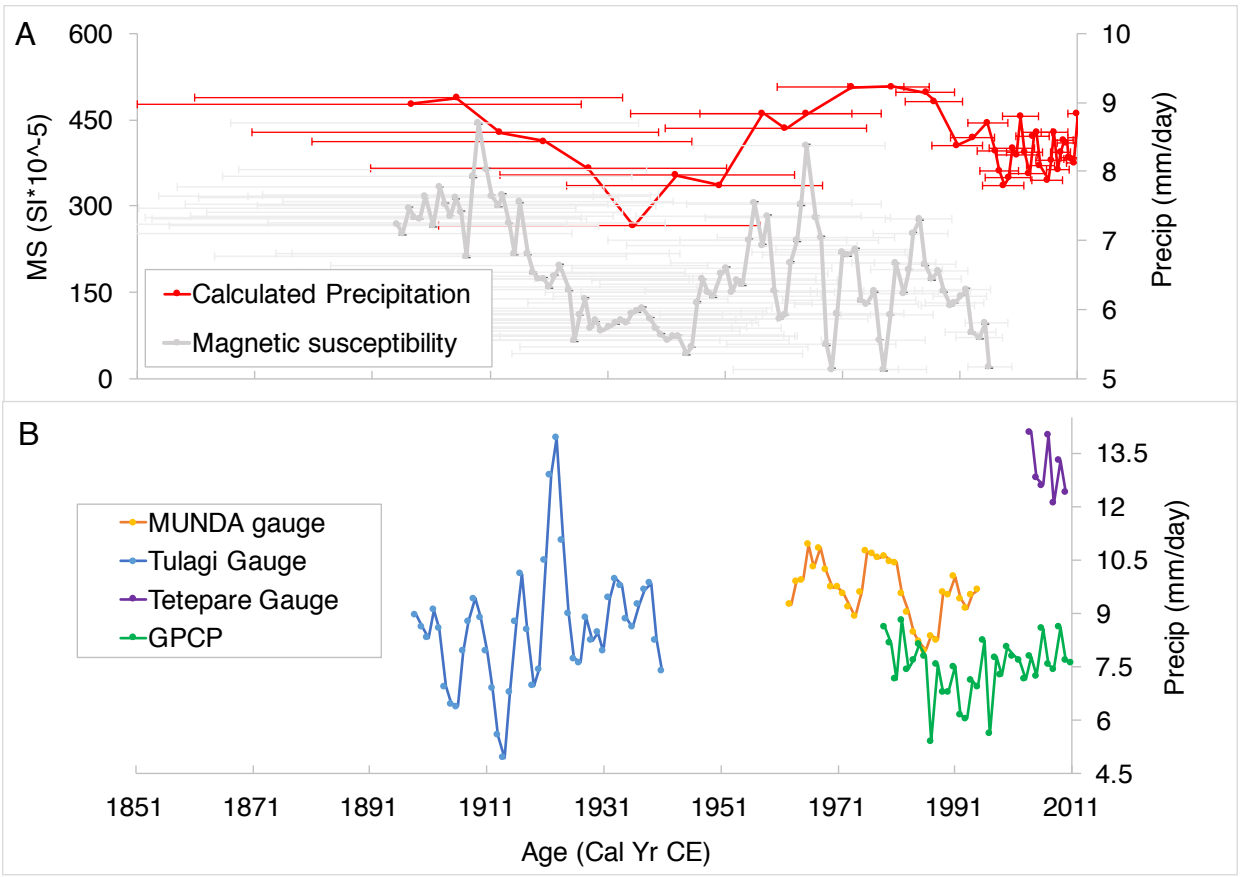

Fig. S8. A) Rainfall rate calculated from $\delta^2H_{dinosterol}$ values in SBARUC2 from Barora Pond (Rendova, Solomon Islands) (red, right axis) and magnetic susceptibility (gray, left axis). X-axis error bars show maximum and minimum ages determined from BACON age model. Y-axis error bars are omitted for clarity: they are on average ±4.6‰ for $\delta^2H_{dinosterol}$ and ±2.6 mm d^{-1} for calculated precipitation rates. B) Instrumental precipitation records: Munda rain gauge (orange), Tulagi rain gauge (blue), Tetepare rain gauge (purple) (Read et al. 2010), and GPCP rainfall rate (green) (GPCP errors are ±1.5 mm d^{-1}, not shown).

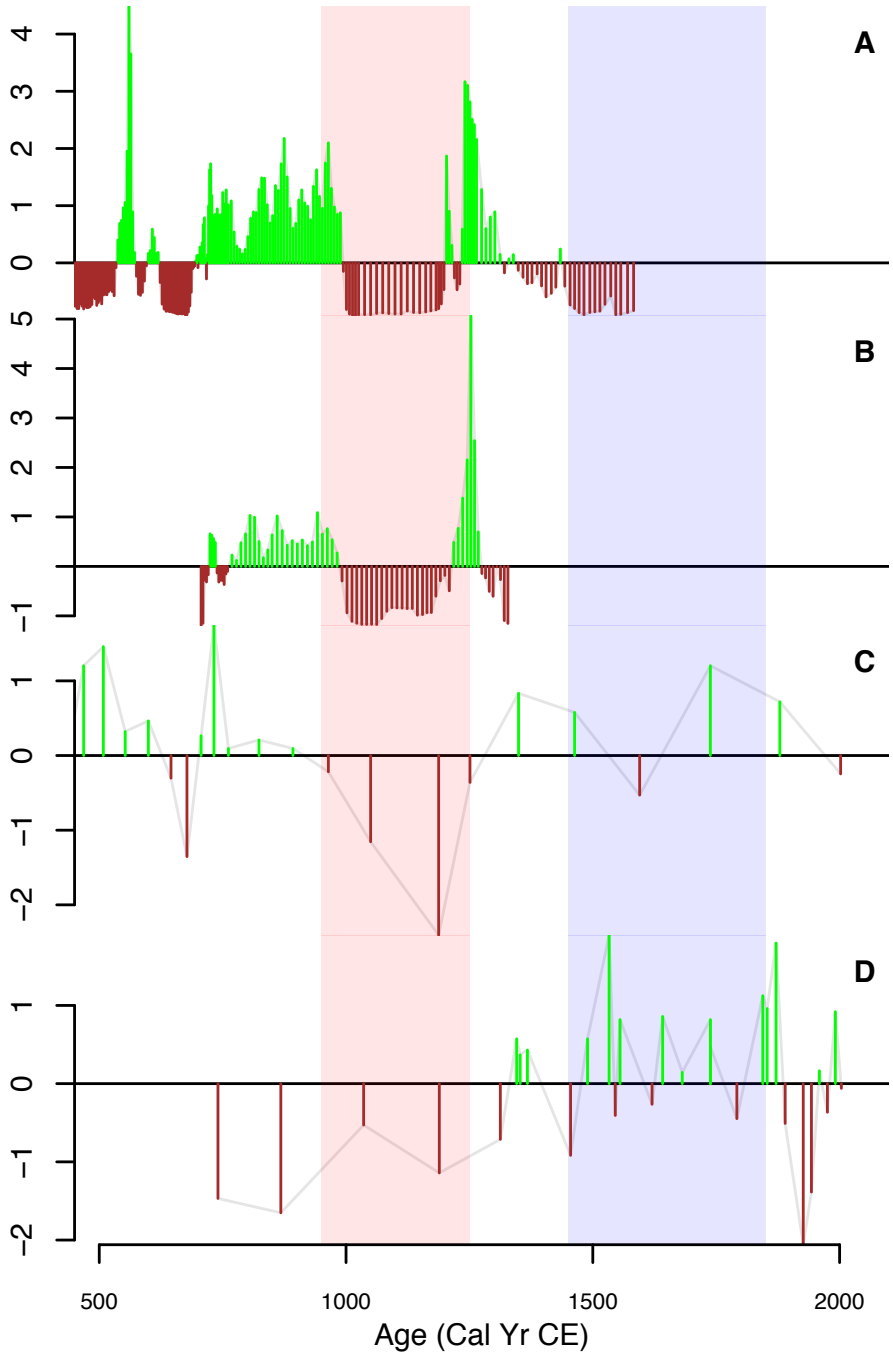

Fig. S9. Z scores ([data-mean] / SD) of sediment core data from Lac Lanutavake (Wallis) versus age. A) Magnetic susceptibility from LATVKUC1, B) Magnetic susceptibility from LATVKUC4, C) Calculated rainfall from $\delta^2H_{dinosterol}$ in LATVKUC1, D) Calculated rainfall from $\delta^2H_{dinosterol}$ in LATVKUC4. Brown segments indicate drier periods and green segments indicate wetter periods. Blue and red bands indicate LIA (1450-1850) or MCA (950-1250).

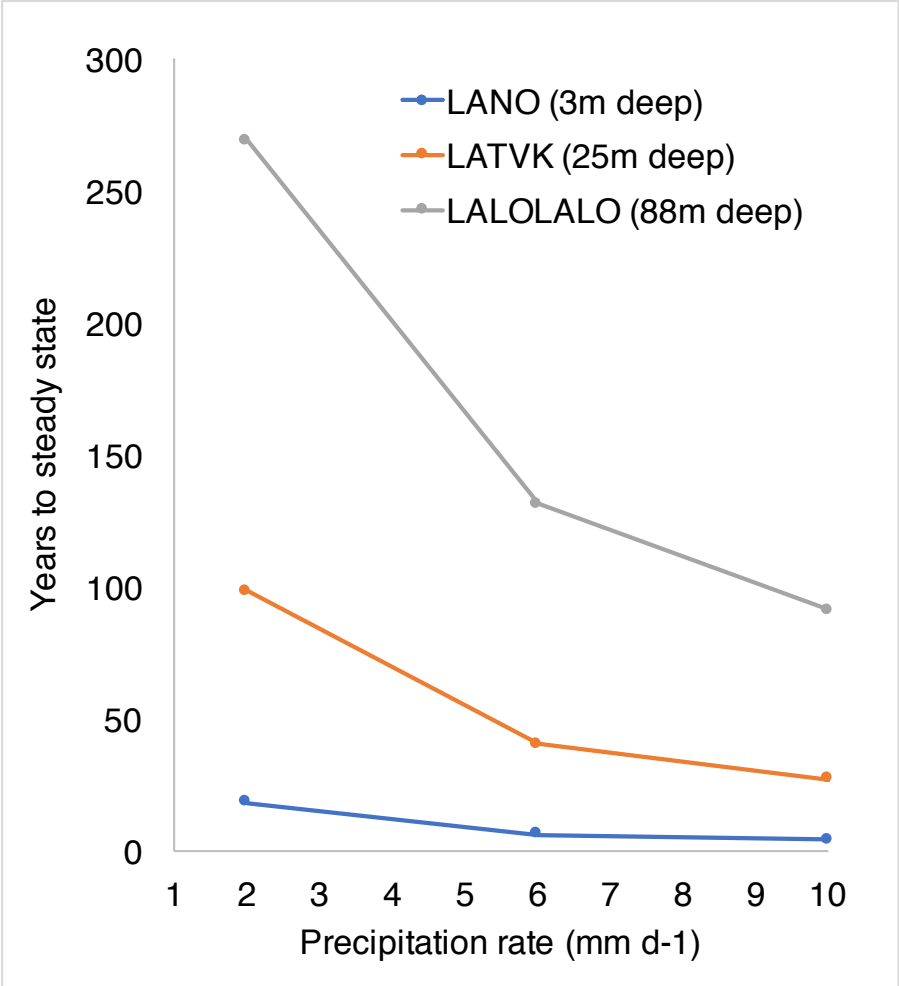

Fig. S10. Hypothetical maximum response time of 3 model lakes on Wallis to changes in precipitation rate. Simple model lakes were held at constant depths and lake water isotopes were determined by mass balance. Isotope compositions of precipitation were determined from the SPCZ "amount effect" (Chapter 3) and were changed to test how long it took each lake to come to a new steady state (within 1‰ of the input). Precipitation isotopes used were -21‰ for 2 mm d^{-1}, -36‰ for 5 mm d^{-1}, and -51‰ for 10 mm d^{-1}. The time to steady state in LALO and LATVK is likely overestimated since the lakes are highly stratified with a strong chemocline/thermocline at 10m (see Fig. A.1 in Chapter 3 Appendix A).

Chapter 4 References

Adler, R.F., Gu, G., Huffman, G.J., 2012. Estimating climatological bias errors for the global precipitation climatology project (GPCP). J. Appl. Meteorol. Climatol. 51, 84–99. doi:10.1175/JAMC-D-11-052.1

Adler, R.F., Gu, G., Sapiano, M., Wang, J.J., Huffman, G.J., 2017. Global precipitation: Means, variations and trends during the Satellite Era (1979–2014). Surv. Geophys. 38, 679–699. doi:10.1007/s10712-017-9416-4

Adler, R.F., Huffman, G.J., Chang, A., Ferraro, R., Xie, P.-P., Janowiak, J., Rudolf, B., Schneider, U., Curtis, S., Bolvin, D., Gruber, A., Susskind, J., Arkin, P., Nelkin, E., 2003. The Version-2 Global Precipitation Climatology Project (GPCP) Monthly Precipitation Analysis (1979–Present). J. Hydrometeorol. 4, 1147–1167. doi:10.1175/1525-7541(2003)004<1147:TVGPCP>2.0.CO;2

Appleby, P.G., Oldfield, F., 1978. The calculation of lead-210 dates assuming a constant rate of supply of unsupported 210Pb to the sediment. Catena 5, 1–8. doi:10.1016/S0341-8162(78)80002-2

Ash, R.P., Carney, J.N., Macfarlane, A., 1978. Geology of Efate and offshore islands. Regional Report, New Hebrides Condominium Geological Survey. British Service.

Atahan, P., Heijnis, H., Dodson, J., Grice, K., Le Métayer, P., Taffs, K., Hembrow, S., Woltering, M., Zawadzki, A., 2014. Pollen, biomarker and stable isotope evidence of late Quaternary environmental change at Lake McKenzie, southeast Queensland. J. Paleolimnol. 53, 139–156. doi:10.1007/s10933-014-9813-3

Atwood, A.R., Sachs, J.P., 2012. Purification of dinosterol from complex mixtures of sedimentary lipids for hydrogen isotope analysis. Org. Geochem. 48, 37–46. doi:10.1016/j.orggeochem.2012.04.006

Binford, M.W., 1990. Calculation and uncertainty analysis of 210Pb dates for PIRLA project lake sediment cores. J. Paleolimnol. 3, 253–267.

Blaauw, M., Christen, J.A., 2011. Flexible paleoclimate age-depth models using an autoregressive gamma process. Bayesian Anal. 6, 457–474. doi:10.1214/11-BA618

Bony, S., Risi, C., Vimeux, F., 2008. Influence of convective processes on the isotopic composition (δ 18 O and δ D) of precipitation and water vapor in the tropics: 1. Radiative-convective equilibrium and Tropical Ocean–Global Atmosphere–Coupled Ocean-Atmosphere Response Experiment (TOGA-CO. J. Geophys. Res. 113, D19305. doi:10.1029/2008JD009942

Borlace, S., Santoso, A., Cai, W., Collins, M., 2014. Extreme swings of the South Pacific Convergence Zone and the different types of El Niño events. Geophys. Res. Lett. 41, 4695–4703. doi:10.1002/2014GL060551

Brock, F., Higham, T., Ditchfield, P., Ramsey, C.B., 2010. Current pretreatment methods for AMS radiocarbon dating at the Oxford Radiocarbon Accelerator Unit (ORAU). Radiocarbon 52, 103–112. doi:10.1017/S0033822200045069

Brown, J.R., Moise, A.F., Colman, R.A., 2012. The South Pacific Convergence Zone in CMIP5 simulations of historical and future climate. Clim. Dyn. 41, 2179–2197. doi:10.1007/s00382-012-1591-x

Brown, J.R., Moise, A.F., Delage, F.P., 2011. Changes in the South Pacific Convergence Zone in IPCC AR4 future climate projections. Clim. Dyn. 39, 1–19. doi:10.1007/s00382-011-1192-0

Cai, W., Lengaigne, M., Borlace, S., Collins, M., Cowan, T., McPhaden, M.J., Timmermann, A., Power, S., Brown, J., Menkes, C., Ngari, A., Vincent, E.M., Widlansky, M.J., 2012. More extreme swings of the South Pacific convergence zone due to greenhouse warming. Nature 488, 365–369. doi:10.1038/nature11358

Calvo, E., Marshall, J.F., Pelejero, C., McCulloch, M.T., Gagan, M.K., Lough, J.M., 2007. Interdecadal climate variability in the Coral Sea since 1708 A.D. Palaeogeogr. Palaeoclimatol. Palaeoecol. 248, 190–201. doi:10.1016/j.palaeo.2006.12.003

Cantrell, C.A., 2008. Technical Note: Review of methods for linear least-squares fitting of data and application to atmospheric chemistry problems. Atmos. Chem. Phys. Discuss. 8, 5477–5487.

Chiang, J.C.H., 2009. The tropics in paleoclimate. Annu. Rev. Earth Planet. Sci. 37, 263–297. doi:10.1146/annurev.earth.031208.100217

Conroy, J.L., Cobb, K.M., Noone, D., 2013. Comparison of precipitation isotope variability across the tropical Pacific in observations and SWING2 model simulations. J. Geophys. Res. Atmos. 118, 5867–5892. doi:10.1002/jgrd.50412

Craig, H., 1961. Isotopic variations in meteoric waters. Science (80-.). 133, 1702–1703.

Craig, H., Gordon, L., 1965. Deuterium and oxygen 18 variations in the ocean and the marine atmosphere, in: Tongiori, E. (Ed.), Proceedings of a Conference on Stable Isotopes in Oceanographic Studies and Paleotemperatures. CNR-Laboratorio di Geologia Nucleare, Pisa, pp. 9–130.

Dansgaard, W., 1964. Stable isotopes in precipitation. Tellus 16, 436–468.

Dassié, E.P., Linsley, B.K., Corrège, T., Wu, H.C., Lemley, G.M., Howe, S., Cabioch, G., 2014. A Fiji multi-coral δ18O composite approach to obtaining a more accurate reconstruction of the last two-centuries of the ocean-climate variability in the South Pacific Convergence Zone region. Paleoceanography 29, 1196–1213. doi:10.1002/2013PA002591

Dawson, K.S., Osburn, M.R., Sessions, A.L., Orphan, V.J., 2015. Metabolic associations with archaea drive shifts in hydrogen isotope fractionation in sulfate-reducing bacterial lipids in cocultures and methane seeps. Geobiology 13, 462–477. doi:10.1111/gbi.12140

Druffel, E.R.M., Griffin, S., 1993. Large variations of surface ocean radiocarbon: Evidence of circulation changes in the southwestern Pacific. J. Geophys. Res. 98, 20249–59. doi:10.1029/93JC02113

Englebrecht, A.C., Sachs, J.P., 2005. Determination of sediment provenance at drift sites using hydrogen isotopes and unsaturation ratios in alkenones. Geochim. Cosmochim. Acta 69, 4253–4265. doi:10.1016/j.gca.2005.04.011

Evans, J.P., Bormann, K., Katzfey, J., Dean, S., Arritt, R., 2016. Regional climate model projections of the South Pacific Convergence Zone. Clim. Dyn. 47, 817–829. doi:10.1007/s00382-015-2873-x

Gat, J.R., 1996. Oxygen and hydrogen isotopes in the hydrologic cycle. Annu. Rev. Earth Planet. Sci. 24, 225–262. doi:10.1146/annurev.earth.24.1.225

Hassall, J.D., 2017. Static or dynamic: Reconstructing past movement of the South Pacific Convergence Zone. University of Southampton.

Heinzelmann, S.M., Villanueva, L., Sinke-Schoen, D., Sinninghe Damsté, J.S., Schouten, S., van der Meer, M.T.J., 2015. Impact of metabolism and growth phase on the hydrogen isotopic composition of microbial fatty acids. Front. Microbiol. 6, 1–11. doi:10.3389/fmicb.2015.00408

Hendy, E.J., Gagan, M.K., Alibert, C.A., McCulloch, M.T., Lough, J.M., Isdale, P.J., 2002. Abrupt decrease in tropical Pacific sea surface salinity at end of Little Ice Age. Science (80-.). 295, 1511–1514. doi:10.1126/science.1067693

Hodell, D.A., Anselmetti, F.S., Ariztegui, D., Brenner, M., Curtis, J.H., Gilli, A., Grzesik, D.A., Guilderson, T.J., Müller, A.D., Bush, M.B., Correa-Metrio, A., Escobar, J., Kutterolf, S., 2008. An 85-ka record of climate change in lowland Central America. Quat. Sci. Rev. 27, 1152–1165. doi:10.1016/j.quascirev.2008.02.008

Hogg, A.G., Hua, Q., Blackwell, P.G., Niu, M., Buck, C.E., Guilderson, T.P., Heaton, T.J., Palmer, J.G., Reimer, P.J., Reimer, R.W., Turney, C.S.M., Zimmerman, S.R.H., 2013. SHCal13 Southern Hemisphere calibration, 0–50,000 years cal BP. Radiocarbon 55, 1889–1903. doi:10.2458/azu_js_rc.55.16783

Hope, G.S., 1996. Fieldwork Report: A reconnaissance survey of potential sites for pollen analysis in Southern Vanuatu. Unpublished report to Vanuatu Cultural Centre. (Corrections 2017).

Hua, Q., Barbetti, M., Rakowski, A.Z., 2013. Atmospheric radiocarbon for the period 1950-2010. Radiocarbon 55, 2059–2072. doi:10.2458/azu_js_rc.v55i2.16177

Kidwell, A., Lee, T., Jo, Y.H., Yan, X.H., 2016. Characterization of the variability of the South Pacific convergence zone using satellite and reanalysis wind products. J. Clim. 29, 1717–1732. doi:10.1175/JCLI-D-15-0536.1

Kiladis, G.N., von Storch, H., van Loon, H., 1989. Origin of the South Pacific Convergence Zone. J. Clim. 2, 1185–1195.

Linsley, B.K., Kaplan, A., Gouriou, Y., Salinger, J., DeMenocal, P.B., Wellington, G.M., Howe, S.S., 2006. Tracking the extent of the South Pacific Convergence Zone since the early 1600s. Geochemistry, Geophys. Geosystems 7, 1–15. doi:10.1029/2005GC001115

Linsley, B.K., Wellington, G.M., Schrag, D.P., Ren, L., Salinger, M.J., Tudhope, A.W., 2004. Geochemical evidence from corals for changes in the amplitude and spatial pattern of South Pacific interdecadal climate variability over the last 300 years. Clim. Dyn. 22, 1–11. doi:10.1007/s00382-003-0364-y

Linsley, B.K., Zhang, P., Kaplan, A., Howe, S.S., Wellington, G.M., 2008. Interdecadal-decadal climate variability from multicoral oxygen isotope records in the South Pacific Convergence Zone region since 1650 A.D. Paleoceanography 23, 1–16. doi:10.1029/2007PA001539

Lintner, B.R., Neelin, J.D., 2008. Eastern margin variability of the South Pacific Convergence Zone. Geophys. Res. Lett. 35, L16701. doi:10.1029/2008GL034298

Liu, J.B., Chen, F.H., Chen, J.H., Xia, D.S., Xu, Q.H., Wang, Z.L., Li, Y.C., 2011. Humid medieval warm period recorded by magnetic characteristics of sediments from Gonghai Lake, Shanxi, North China. Chinese Sci. Bull. 56, 2464–2474. doi:10.1007/s11434-011-4592-y

Lough, J.M., 2011. Great Barrier Reef coral luminescence reveals rainfall variability over northeastern Australia since the 17th century. Paleoceanography 26, 1–14. doi:10.1029/2010PA002050

Maloney, A.E., Shinneman, A.L.C., Hemeon, K., Sachs, J.P., 2016. Exploring lipid $^{2}H/^{1}H$ fractionation mechanisms in response to salinity with continuous cultures of the diatom *Thalassiosira pseudonana*. Org. Geochem. 101, 154–165. doi:10.1016/j.orggeochem.2016.08.015

Masson-Delmotte, V., Schulz, M., Abe-Ouchi, A., Beer, J., Ganopolski, A., González Rouco, J., Jansen, E., Lambeck, K., Luterbacher, J., Naish, T., Osborn, T., Otto-Bliesner, B., Quinn, T., Ramesh, Rojas, M., Shao, X., Timmermann, A., 2013. Information from Paleoclimate Archives, in: Stocker, T.F., Qin, D., Plattner, G.-K., Tignor, M., Allen, S., Boschung, J., Nauels, A., Xia, Y., Bex, V., Midgely, P.M. (Eds.), Climate Change 2013 - The Physical Science Basis. Contribution of Working Group 1 to the Fifth Assessment Report of the Intergovernnmental Panel on Climate Change. Cambridge University Press, Cambridge, United Kingdom and New York, NY, USA, pp. 383–464. doi:10.1017/CBO9781107415324.013

Maupin, C.R., Partin, J.W., Shen, C.-C., Quinn, T.M., Lin, K., Taylor, F.W., Banner, J.L., Thirumalai, K., Sinclair, D.J., 2014. Persistent decadal-scale rainfall variability in the tropical South Pacific Convergence Zone through the past six centuries. Clim. Past 10, 1319–1332. doi:10.5194/cp-10-1319-2014

Nelson, D.B., Sachs, J.P., 2014. The influence of salinity on D/H fractionation in dinosterol and brassicasterol from globally distributed saline and hypersaline lakes. Geochim. Cosmochim. Acta 133, 325–339. doi:10.1016/j.gca.2014.03.007

Nelson, D.B., Sachs, J.P., 2013. Concurrent purification of sterols, triterpenols and alkenones from sediments for hydrogen isotope analysis using high performance liquid chromatography. Org. Geochem. 64, 19–28. doi:10.1016/j.orggeochem.2013.09.005

Newton, A., Thunell, R., Stott, L., 2006. Climate and hydrographic variability in the Indo-Pacific Warm Pool during the last millennium. Geophys. Res. Lett. 33, L19710. doi:10.1029/2006GL027234

Nowaczyk, N.R., Melles, M., Minyuk, P., 2007. A revised age model for core PG1351 from Lake El'gygytgyn, Chukotka, based on magnetic susceptibility variations tuned to northern hemisphere insolation variations. J. Paleolimnol. 37, 65–76. doi:10.1007/s10933-006-9023-8

Osburn, M.R., Dawson, K.S., Fogel, M.L., Sessions, A.L., 2016. Fractionation of hydrogen isotopes by sulfate- and nitrate-reducing bacteria. Front. Microbiol. 7, 1–16. doi:10.3389/fmicb.2016.01166

Parkes, A., 1994. Holocene environments and vegetational change on four Polynesian islands.

Partin, J.W., Quinn, T.M., Shen, C.-C., Emile-Geay, J., Taylor, F.W., Maupin, C.R., Lin, K., Jackson, C.S., Banner, J.L., Sinclair, D.J., Huh, C.-A., 2013. Multidecadal rainfall variability in South Pacific Convergence Zone as revealed by stalagmite geochemistry. Geology 41, 1143–1146. doi:10.1130/G34718.1

Power, S.B., Delage, F.P.D., Chung, C.T.Y., Ye, H., Murphy, B.F., 2017. Humans have already increased the risk of major disruptions to Pacific rainfall. Nat. Commun. 8, 14368. doi:10.1038/ncomms14368

Quinn, T.M., Crowley, T.J., Taylor, F.W., Henin, C., 1998. A multicentury stable isotope record from a New Caledonia coral : Interannual and decadal sea surface temperature variability in the Southwest Pacific since 1657 AD. Paleoceanography 13, 412–426.

Quinn, T.M., Taylor, F.W., Crowley, T.J., 1993. A 173 year stable isotope record from a tropical South Racific coral. Quat. Sci. Rev. 12, 407–418. doi:10.1016/S0277-3791(05)80005-8

Raos, A.M., Crawford, A.J., 2004. Basalts from the Efate Island Group, central section of the Vanuatu arc, SW Pacific: geochemistry and petrogenesis. J. Volcanol. Geotherm. Res. 134, 35–56. doi:10.1016/j.jvolgeores.2004.12.004

Read, J.L., Argument, D., Moseby, K.E., 2010. Initial conservation outcomes of the Tetepare Island Protected Area. Pacific Conserv. Biol. 16, 173–180. doi:10.1071/PC100173

Reed, C.B., 1989. Linear least-squares fits with errors in both coordinates. II: Comments on parameter variances. Am. J. Phys. 57, 642–646. doi:10.1119/1.17044

Risi, C., Bony, S., Vimeux, F., 2008. Influence of convective processes on the isotopic composition (δ18O and δD) of precipitation and water vapor in the tropics: 2. Physical interpretation of the amount effect. J. Geophys. Res. 113, D19306. doi:10.1029/2008JD009943

Rodysill, J.R., Russell, J.M., Bijaksana, S., Brown, E.T., Safiuddin, L.O., Eggermont, H., 2012. A paleolimnological record of rainfall and drought from East Java, Indonesia during the last 1,400 years. J. Paleolimnol. 47, 125–139. doi:10.1007/s10933-011-9564-3

Roy, P.D., Torrescano-Valle, N., Islebe, G.A., Gutiérrez-Ayala, L.V., 2017. Late Holocene hydroclimate of the western Yucatan Peninsula (Mexico). J. Quat. Sci. 32, 1112–1120. doi:10.1002/jqs.2988

Sachs, J.P., Maloney, A.E., Gregersen, J., Paschall, C., 2016. Effect of salinity on $^{2}H/^{1}H$ fractionation in lipids from continuous cultures of the coccolithophorid *Emiliania huxleyi*. Geochim. Cosmochim. Acta 189, 96–109. doi:10.1016/j.gca.2016.05.041

Sachs, J.P., Sachse, D., Smittenberg, R.H., Zhang, Z., Battisti, D.S., Golubic, S., 2009. Southward movement of the Pacific intertropical convergence zone. Nat. Geosci. 2, 519–525. doi:10.1038/NGEO554

Sachs, J.P., Schwab, V.F., 2011. Hydrogen isotopes in dinosterol from the Chesapeake Bay estuary. Geochim. Cosmochim. Acta 75, 444–459. doi:10.1016/j.gca.2010.10.013

Sachse, D., Sachs, J.P., 2008. Inverse relationship between D/H fractionation in cyanobacterial lipids and salinity in Christmas Island saline ponds. Geochim. Cosmochim. Acta 72, 793–806. doi:10.1016/j.gca.2007.11.022

Schabetsberger, R., Drozdowski, G., Rott, E., Lenzenweger, R., Jersabek, C.D., Fiers, F., Traunspurger, W., Reiff, N., Stoch, F., Kotov, A. a., Martens, K., Schatz, H., Kaiser, R., 2009. Losing the bounty? Investigating species richness in isolated freshwater ecosystems of Oceania. Pacific Sci. 63, 153–179. doi:10.2984/049.063.0201

Schneider, T., Bischoff, T., Haug, G.H., 2014. Migrations and dynamics of the intertropical convergence zone. Nature 513, 45–53. doi:10.1038/nature13636

Schouten, S., Ossebaar, J., Schreiber, K., Kienhuis, M.V.M., Langer, G., Benthien, A., Bijma, J., Burg, D., 2006. The effect of temperature, salinity and growth rate on the stable hydrogen isotopic composition of long chain alkenones produced by *Emiliania huxleyi* and *Gephyrocapsa oceanica*. Biogeosciences 3, 113–119.

Schwab, V.F., Garcin, Y., Sachse, D., Todou, G., Séné, O., Onana, J.M., Achoundong, G., Gleixner, G., 2015. Dinosterol δD values in stratified tropical lakes (Cameroon) are affected by eutrophication. Org. Geochem. 88, 35–49. doi:10.1016/j.orggeochem.2015.08.003

Sémah, A.-M., Wirrmann, D., 2006. Mission Vanuatu - du 9 septembre au 2 décembre 2005 (Rapport de missions No. 67). Sci. la Terre Géologie-Géophysique, IRD.

Sessions, A.L., Burgoyne, T.W., Schimmelmann, A., Hayes, J.M., 1999. Fractionation of hydrogen isotopes in lipid biosynthesis. Org. Geochem. 30, 1193–1200. doi:10.1016/S0146-6380(99)00094-7

Smerdon, J.E., Luterbacher, J., Phipps, S.J., Anchukaitis, K.J., Ault, T., Coats, S., Cobb, K.M., Cook, B.I., Colose, C., Felis, T., Gallant, A., Jungclaus, J.H., Konecky, B., LeGrande, A., Lewis, S., Lopatka, A.S., Man, W., Mankin, J.S., Maxwell, J.T., Otto-Bliesner, B.L., Partin, J.W., Singh, D., Steiger, N.J., Stevenson, S., Tierney, J.E., Zanchettin, D., Zhang, H., Atwood, A.R., Andreu-Hayles, L., Baek, S.H., Buckley, B., Cook, E.R., D'Arrigo, R., Dee, S.G., Griffiths, M., Kulkarni, C., Kushnir, Y., Lehner, F., Leland, C., Linderholm, H.W., Okazaki, A., Palmer, J., Piovano, E., Raible, C.C., Rao, M.P., Scheff, J., Schmidt, G.A., Seager, R., Widmann, M., Williams, A.P., Xoplaki, E., 2017. Comparing proxy and model estimates of hydroclimate variability and change over the Common Era. Clim. Past Discuss. 1–70. doi:10.5194/CP-2017-37

Stearns, H.T., 1945. Geology of the Wallis Islands. Bull. Geol. Soc. Am. 56, 849–860. doi:10.1130/0016-7606(1945)56[849:GOTWI]2.0.CO;2

Takahashi, K., Battisti, D.S., 2007a. Processes controlling the mean tropical Pacific precipitation pattern. Part I: The Andes and the eastern Pacific ITCZ. J. Clim. 20, 3434–3451. doi:10.1175/JCLI4198.1

Takahashi, K., Battisti, D.S., 2007b. Processes controlling the mean tropical Pacific precipitation pattern. Part II: The SPCZ and the southeast Pacific dry zone. J. Clim. 20, 5696–5706. doi:10.1175/2007JCLI1656.1

Thirumalai, K., Singh, A., Ramesh, R., 2011. A MATLAB^{TM} code to perform weighted linear regression with (correlated or uncorrelated) errors in bivariate data. J. Geol. Soc. India 77, 377–380. doi:10.1007/s12594-011-0044-1

Tierney, J.E., Oppo, D.W., Rosenthal, Y., Russell, J.M., Linsley, B.K., 2010. Coordinated hydrological regimes in the Indo-Pacific region during the past two millennia. Paleoceanography 25, 1–7. doi:10.1029/2009PA001871

Toomey, M.R., Donnelly, J.P., Tierney, J.E., 2016. South Pacific hydrologic and cyclone variability during the last 3,000 years. Paleoceanography 31, 491–504. doi:10.1002/2015PA002870

van der Wiel, K., Matthews, A.J., Joshi, M.M., Stevens, D.P., 2016a. Why the South Pacific Convergence Zone is diagonal. Clim. Dyn. 46, 1683–1698. doi:10.1007/s00382-015-2668-0

van der Wiel, K., Matthews, A.J., Joshi, M.M., Stevens, D.P., 2016b. The influence of diabatic heating in the South Pacific Convergence Zone on Rossby wave propagation and the mean flow. Q. J. R. Meteorol. Soc. 142, 901–910. doi:10.1002/qj.2692

van der Wiel, K., Matthews, A.J., Stevens, D.P., Joshi, M.M., 2015. A dynamical framework for the origin of the diagonal South Pacific and South Atlantic Convergence Zones. Q. J. R. Meteorol. Soc. 141, 1997–2010. doi:10.1002/qj.2508

Vincent, D.G., 1994. The South Pacific Convergence Zone (SPCZ): A review. Mon. Weather Rev. 122, 1949–1970.

Weiss, G.M., Pfannerstill, E.Y., Schouten, S., Sinninghe Damsté, J.S., Marcel, T.J., 2017. Effects of alkalinity and salinity at low and high light intensity on hydrogen isotope fractionation of long-chain alkenones produced by *Emiliania huxleyi*. Biogeosciences Discuss. (under review).

Widlansky, M.J., Timmermann, A., Stein, K., Mcgregor, S., Schneider, N., England, M.H., Lengaigne, M., Cai, W., 2013. Changes in South Pacific rainfall bands in a warming climate. Nat. Clim. Chang. 3, 417–423. doi:10.1038/nclimate1726

Widlansky, M.J., Webster, P.J., Hoyos, C.D., 2011. On the location and orientation of the South Pacific Convergence Zone. Clim. Dyn. 36, 561–578. doi:10.1007/s00382-010-0871-6

Wilmshurst, J.M., Hunt, T.L., Lipo, C.P., Anderson, A.J., 2011. High-precision radiocarbon dating shows recent and rapid initial human colonization of East Polynesia. Proc. Natl. Acad. Sci. 108, 1815–1820. doi:10.1073/pnas.1015876108

Wu, H.C., Linsley, B.K., Dassié, E.P., Schiraldi, B., DeMenocal, P.B., 2013. Oceanographic variability in the South Pacific Convergence Zone region over the last 210 years from multi-site coral Sr/Ca records. Geochemistry, Geophys. Geosystems 14, 1435–1453. doi:10.1029/2012GC004293

Yan, H., Wei, W., Soon, W., An, Z., Zhou, W., Liu, Z., Wang, Y., Carter, R.M., 2015. Dynamics of the intertropical convergence zone over the western Pacific during the Little Ice Age. Nat. Geosci. 6–11. doi:10.1038/ngeo2375

York, D., 1969. Least squares fitting of a straight line with correlated errors. Earth Planet. Sci. Lett. 5, 320–324. doi:10.1016/S0012-821X(68)80059-7

York, D., Evensen, N.M., Martı´nez, M.L., De Basabe Delgado, J., 2004. Unified equations for the slope, intercept, and standard errors of the best straight line. Am. J. Phys. 72, 367–375. doi:10.1119/1.1632486

Zhang, X., Gillespie, A.L., Sessions, A.L., 2009. Large D/H variations in bacterial lipids reflect central metabolic pathways. Proc. Natl. Acad. Sci. U. S. A. 106, 12580–6. doi:10.1073/pnas.0903030106

Zhang, Z., Sachs, J.P., 2007. Hydrogen isotope fractionation in freshwater algae: I. Variations among lipids and species. Org. Geochem. 38, 582–608. doi:10.1016/j.orggeochem.2006.12.004